UNIVERSITY OF CALIFORNIA
SANTA CRUZ

TESTING, OPTIMIZATION AND DESIGN OF A BIPV/T SOLAR AIR COLLECTOR

A dissertation submitted in partial satisfaction
of the requirements for the degree of

DOCTOR OF PHILOSOPHY

in

ELECTRICAL ENGINEERING

by

Andrea Chialastri

June 2019

The Dissertation of Andrea Chialastri
is approved:

_____
Professor Michael Isaacson, Chair

_____
Professor Patrick E. Mantey

_____
Professor Brent Haddad

_____
Lori Kletzer
Vice Provost and Dean of Graduate Studies

Table of Contents

List of Figures viii

List of Tables xv

Abstract xvi

Dedication xviii

Acknowledgement xix

1 Introduction 1

1.1 Research Rationale 1
1.2 Aim and methodology 2
1.3 Thesis Outline 3

2 Background 6

2.1 Energy Consumption in Buildings 6
2.2 Brief History of Windows 9
2.3 Window Energy Performance 12
2.3.1 Thermal Insulation 12
2.3.2 Solar Heat Gain 15
2.3.3 Air Leakage 16
2.4 Glass and Solar Radiation 17
2.4.1 The Solar Spectrum 17
2.4.2 Radiative Properties 18
2.4.3 Selective Surfaces 22
2.4.4 Glass Interaction with Solar Radiation 26
2.5 Components of Window Assemblies 29
2.5.1 Frame materials 30

2.5.2 Glazing Technology 34
2.5.2.1 Tinted Glass 36
2.5.2.2 Reflective Coatings 38
2.5.2.3 Low-Emissivity (Low-e) Coatings 38
2.5.2.4 Multiple Panes 41
2.5.2.5 Low Conductance Gas Fills and Gap Width 43
2.5.2.6 Warm Edge Spacers 45
2.6 Ventilated Double-Skin Façades and Air-Flow Windows 48
2.6.1 Airflow Windows 49
2.6.2 Advantages of Airflow Windows over Regular Windows 52
2.7 Solar PV and Thermal Collectors 54
2.7.1 Crystalline Silicon Solar Cells and Modules 54
2.7.2 Flat-Plate Solar Thermal Collectors 59
2.7.2.1 Liquid-based Collectors 60
2.7.2.2 Air-based Collectors 61
2.7.2.3 Hybrid PV/T Collectors 63
2.8 BIPV and BIPV/T Systems 66
2.8.1 Market 66
2.8.2 Literature Review 68

3 BIPV/T Prototype: Concept and Implementation 72

3.1 The Solar Window Concept 72
3.2 Prototype Description 74

4 Experimental Evaluation of Thermal and Electrical Performance 82

4.1 Thermal Measurement Instrumentation 82
4.2 Electrical Measurement Set-up 85
4.2.1 PV Module Testing 85
4.2.2 PV System Design and Implementation 89
4.3 Thermal and Electrical Parameters 98

4.3.1 Thermal Output 98
4.3.2 Electrical Output 101
4.4 Results and Discussion 106
4.4.1 Summer Measurements 106
4.4.2 Fall Measurements 111
4.4.3 Winter Measurements 115
4.4.4 Comparison for the Vertical South-Facing Case 120
4.4.4.1 Thermal Results 120
4.4.4.2 Electrical Results 123
4.4.4.3 Efficiency 124

5 CFD Modeling in COMSOL 126

5.1 Introduction 126
5.2 Overview of Finite Element Analysis 127
5.3 COMSOL Model 128
5.3.1 Global Parameters 128
5.3.2 Geometry 131
5.3.3 Materials 131
5.3.4 Heat Transfer Interface 133
5.3.4.1 Heat Transfer in Solids 133
5.3.4.2 Heat Transfer in Fluids 134
5.3.4.3 Radiation Settings 135
5.3.4.4 Solar Radiation Modeling 136
5.3.4.5 Radiative Boundary Conditions 136
5.3.4.6 Convective Heat Flux Boundary Conditions 139
5.3.4.7 Inlet and Outlet Boundary Conditions 141
5.3.5 Fluid Flow Interface 142
5.3.5.1 Fluid Flow and Heat Transfer Coupling 143
5.3.5.2 Compressibility 143
5.3.5.3 Turbulent Flow Modeling 144

5.3.5.4 Initial Values 146
5.3.5.5 Wall Boundary Condition 146
5.3.5.6 Inlet and Outlet Boundary Conditions 147
5.3.5.7 Meshing 147
5.3.5.8 Study Steps 150
5.3.5.9 Results 151

6 Optimization **156**

6.1 Introduction 156
6.2 Thermal Insulation 157
6.2.1 Glazing System Optimization 158
6.2.2 Frame Heat Losses 166
6.3 Heat Transfer Enhancement 169
6.3.1 Increase of *h* - Air Velocity Augmentation 169
6.3.1.1 Increased airflow rate 170
6.3.1.2 Reduced Glass – Glass Spacing 173
6.3.2 Increased *A* – Extended Surfaces (Finned PV/T Absorber) 179
6.3.3 Increased *k* – PV layers thermal conductivity 185

7 Prototype Design **190**

7.1 Preliminary Analysis 190
7.1.1 Effects of a Whole Array of PV Blinds 190
7.1.2 Effects of a Wood Frame 192
7.1.3 Hybrid Configuration 194
7.1.4 Effects of Increased Blind Spacing 196
7.2 Design Variations 198
7.2.1 Frame Material 198
7.2.2 Blinds Layout 199
7.2.3 Blinds Composition 199
7.2.4 Glazing system 200

7.3 Prototypes Overview 202
7.3.1 Prototype 1 203
7.3.2 Prototype 2 206
7.3.3 Prototype 3 209
7.3.4 Prototype 4 209
7.3.5 Prototype 5 212
7.3.6 Prototype 6 212

8 Conclusion and Summary of Results **214**

Bibliography **218**

List of Figures

Fig. 2.1: U.S. energy consumption: (a) total energy consumption by end-use sector; (b) residential sector and (c) electric power sector energy consumption by major sources [3]. 7

Fig. 2.2: Residential energy consumptions in the U.S. in 2015 [4]. 8

Fig. 2.3: Heat losses and heat gain through the building envelope [5]. 8

Fig. 2.4: Window heat transfer components related to insulating value [16]. 13

Fig. 2.5: Cross section of a window assembly showing convective currents in the frame cavities and within the double-glazing, conduction through the frame and radiation through the glass, assuming a cold exterior [17]. 14

Fig. 2.6: Solar radiation incident on a window (left) and components of solar heat gain coefficient (right) [16][[18]. 16

Fig. 2.7: Solar energy in the electromagnetic spectrum [19]. 18

Fig. 2.8: Solar radiation spectral distribution at the top of the atmosphere, attenuation by the earth's atmosphere and radiation of a blackbody at 5778K [20]. 18

Fig. 2.9: Variation of the total directional emissivity (a) with an angle θ measured from the normal to the surface [22], and comparison of the total spectral emissivity (b) for a blackbody, a real and a gray surface [18]. 19

Fig. 2.10: Reflection, absorption and transmission of incident radiation for semitransparent medium [22]. 20

Fig. 2.11: Solar spectrum and radiation emitted by black bodies at various temperatures close to the earth's surface temperature [24]. 23

Fig. 2.12: Solar absorptivity and infrared emissivity approximation by a step function [25]. 24

Fig. 2.13: Spectral emissivities for different surfaces: (a) gray absorber, (b) gray reflector, (c) selective absorber and (d) selective reflector [18]. 24

Fig. 2.14: Spectral hemispherical emissivity of some selective surfaces [26]. 25

Fig. 2.15: Spectral transmissivity of various 6-mm thick glass panels with different iron contents: regular clear glass (0.10% Fe_2O_3), low-iron glass (0.02% Fe_2O_3) and high iron glass (0.5% Fe_2O_3). 27

Fig. 2.16: Transmissivity variation with thickness for soda-lime glass [27]. 28

Fig. 2.17: Effects of the incident angle on the transmissivity of 6-mm glass [16].....29

Fig. 2.18: Double glazed window components (left) and insulated glass unit detail (right) [28],[29]...30

Fig. 2.19: Different frame types [30].....31

Fig. 2.20: (*a*) Improvements in modern high-performance windows and (*b*) components of an IGU [15], [17].....35

Fig. 2.21: Ideal spectral transmittances of glass for hot (curve 1) and cold (curve 2) climates [16].....36

Fig. 2.22: Transmittance curves of tinted and low-e glazings for solar control [6]. 37

Fig. 2.23: (a) Surface labeling for IGUs and (b) example of the effects of low-e coatings applied to both surfaces #2 and #4. The U-factor is expressed in BTU/(hr ft^2 °F) [30], [33].....40

Fig. 2.24: (Top) spectral transmittances of various low-e glazings and (bottom) center-of-glass properties for double glazings with (a) high-solar gain low-e, (b) moderate-solar-gain low-e and (c) low-solar-gain low-e coatings. The U-factors are expressed in BTU/(hr ft^2 °F). 42

Fig. 2.25: Center-of-glass U-factors for double- and triple-glazings with different gas fills and emissivity, as a function of gap width [35]. 44

Fig. 2.26: Schematic representation of center-of-glass and edge-of-glass regions (left) and thermogram comparison between double-glazed clear window with aluminum spacer (middle) and double-glazed window with a low-e coating and insulated spacer (right) [15], [18]. 46

Fig. 2.27: Different types of metal and non-metal spacer systems [30].....47

Fig. 2.28: Schematic of mechanically ventilated multiple-skin facades [38]. 48

Fig. 2.29: Modes of airflow windows operation [40]. 50

Fig. 2.30: Example of an indoor circulation airflow window [42] 51

Fig. 2.31: Variation of effective U-vale of an exhaust air window for different airflow rates [39].....53

Fig. 2.32: Single junction solar cell operating principle [49]. 55

Fig. 2.33: Layers in a c-Si PV module [53]. 56

Fig. 2.34: Components of a stand-alone (left) and a grid-connected (right) PV system [57]. 58

Fig. 2.35: I-V characteristics for different irradiation levels and operating temperatures for a mc-Si module.[56].....58

Fig. 2.36: Solar water collector [60].....61

Fig. 2.37: Different airflow patterns in solar air collectors [62]. 62

Fig. 2.38: Schematics of a solar air collector (Source: Grammer Solar GmbH, Germany) 63

Fig. 2.39: Hybrid PV/T solar collector (source: Solimpeks). 65

Fig. 3.1: Solar window concept [104] 73

Fig. 3.2: Solar window prototype. 75

Fig. 3.3: Photograph of the top vent. 76

Fig. 3.4: Fans and heat exchanger at the top of the unit 78

Fig. 3.5: Parallax XHHOO1-4 module: front (top left) and back (top right), and its electrical characteristics 79

Fig. 3.6: Air passages and tilting of the PV array 80

Fig. 3.7: Cross section and airflow schematic. 81

Fig. 4.1: Thermocouples placement (marked with red circles) at the bottom vent. 82

Fig. 4.2: Thermocouple setup on the back at the output vent and on 2 PV modules (red circles). 83

Fig. 4.3: Hot wire anemometer for air velocity readings. 84

Fig. 4.4: I-V characteristics for the PV module tested outside (top graph) and inside (bottom graph) of the double glazing. 87

Fig. 4.5: PV connection schematics: series connection (green) and parallel connections (red and black). 91

Fig. 4.6: Ambient temperature correction factors. Source: NEC Table 310.15(B)(2)(a). 92

Fig. 4.7: Photograph showing the charge controller, the battery and the connections with the PV array (left conductors) and DC fans (right conductors). 93

Fig. 4.8: MPPT operation [107]. 95

Fig. 4.9: PV array, load and battery monitoring. 96

Fig. 4.10: Schematic of the PV/T system 97

Fig. 4.11: Energy transfer and mass flow rate conservation in a control volume in steady-state conditions [18]. 99

Fig. 4.12: Incident and normal radiation on the window [109]. 100

Fig. 4.13: Example of thermal measurements data worksheet and parameters computation. 102

Fig. 4.14: Fill factor representation on the I-V curve [109]. 103

Fig. 4.15: Example of electrical testing. 105

Fig. 4.16: Schematic showing the tilt angles for the prototype (black) and PV array (red). 106

Fig. 4.17: Tilting of the prototype by 20°. 107

Fig. 4.18: Location for outside measurements. 108

Fig. 4.19: Normal irradiance (top) and output temperature (bottom) for summer measurements. 109

Fig. 4.20: Temperature rise (top) and heat transfer rate (bottom)..... 110

Fig. 4.21: Schematics of the 4 different tilting conditions. 113

Fig. 4.22: Performance testing in fall: temperature, thermal power output and temperature difference for the south-facing (top) and tracking (bottom) conditions. 113

Fig. 4.23: PV array power output and temperature in different tilting conditions, for the south-facing (top) and tracking (bottom) cases. 114

Fig. 4.24: Air velocity increment with the fans voltage. 116

Fig. 4.25: Temperature difference, electrical and thermal power output for different voltage levels: 6V (top left), 7.5V (top right), 9V (bottom left) and 12V (bottom right). 117

Fig. 4.26: Thermal (top) and electrical (bottom) efficiency. 119

Fig. 4.27: Hourly data of the solar radiation, temperature output, temperature rise and generated heat for the days of July 10th, November 25th and February 24th. 121

Fig. 4.28: Hourly variation of average modules temperature and PV power output for November 25 (left) and February 24 (right). 123

Fig. 4.29: Thermal efficiency (left) and electrical efficiency (right) for the tested seasons. 124

Fig. 5.1: Model tree (left), with expanded physics interface nodes (right)..... 129

Fig. 5.2: 2D model geometry: close-up views for the bottom, middle and top parts (left), and whole geometry (right). 132

Fig. 5.3: Incoming (left) and outgoing radiation (right) at a point *P* on a surface [112]. 137

Fig. 5.4: Convective heat flux settings in COMSOL. 141

Fig. 5.5: Coupling of the energy and momentum equation for the fluid domain [115]. 143

Fig. 5.6: Meshes for the top (top left), bottom (bottom left) and middle (bottom right) parts of the geometry, and close-up (top right) of the frame showing the boundary layers. 148

Fig. 5.7: Mesh of part of the channel hosting the PV domains (left) and close-ups showing the boundary layers at the glass (top right) and PV (bottom right) boundaries..... 149

Fig. 5.8: Computed air velocity (left) and temperature field (right). 152

Fig. 5.9: Temperature (top row) and velocity (bottom row) profiles along the channel cross-section at different heights: before the PV array (y=1.9m), past the PV array (y=2.7m), middle and top of the frame (y=2.8m and y=2.9m). 153

Fig. 5.10: Air temperature (left) along the vertical axis (1.9 m < y < 2.9 m), evaluated at x= -1 cm, and representation of the cut line (right). 154

Fig. 6.1: Total heat flux in the direction normal to the boundaries interfacing with the outdoor environment, evaluated on the back side of the window at the top frame (top) and top glass (bottom) surfaces..... 158

Fig. 6.2: Temperature field for 2-panes with Low-e on surface #3 (a), #2-3 (b), 3-panes with Low-e on surface #2-3 (c), #2-3-5 (d), #2-3(NIR absorbing)-5 (e), and 4-panes with Low-e on surface #4-5-7 (f). 160

Fig. 6.3: Output temperature profile and average values before (left) and after (right) the optimization. 165

Fig. 6.4: 3D temperature field for Aluminum (top left) and Wood frame (top right), and their relative temperature (bottom) on a x-z plane at half of the frame length (y=0.41 m). 167

Fig. 6.5: Temperature profile comparison between Aluminum and Wood frame, along a line at z=0.1 m on the x-z plane at half of the frame length (y=0.41 m), for a plate thickness of 3.175mm (left) and 2.54 cm (right). 167

Fig. 6.6: Effects of a doubled flow rate, for a double-glazing with Low-e on surface #3 (left), and for triple-glazing with Low-e on surfaces #2-3-5 (right)..... 170

Fig. 6.7: Air velocity (top) and temperature (bottom) profiles along a cut line at y=2.5 m, for both velocities for a double-glazing configuration with Low-e on surface 3..... 171

Fig. 6.8: Definition of geometrical parameters..... 175

Fig. 6.9: Results for the PV temperature, heat and air temperature output, as a function of d, for d/w=1.14. 177

Fig. 6.10: Model setup for decreasing *d*, with 3, 4 and 6 blinds, for *d/w*=1.14. 177

Fig. 6.11: Temperature profile at mid-height in the direction normal to the glazing surfaces, for d/w=1.14 and w = 6.3 cm, 4.725 cm and 3.15 cm. 178

Fig. 6.12: PV temperature and heat output as a function of the ratio *d/w*, for w=3.15 cm. 178

Fig. 6.13: Cut plane for data selection (top) and temperature field for the no-fins (bottom left), 1 cm fins (bottom center) and 2 cm fins (bottom right) cases. 180

Fig. 6.14: PV tilting by 20 º in the case of 3.15 cm blinds and 1 cm fins. The straight lines represent the solar radiation beam, incident at an angle of 32 º. 181

Fig. 6.15: Velocity field for 25 (top left) and 14 fins (top right) on a plane parallel to the PV module, at middle-length of the fins, and related velocity profiles along the central line of the plane (bottom plots) 182

Fig. 6.16: Comparison of PV (T_PV) and air output temperature (T_out) for different number of fins. The constant profiles represent the values for the no-fins situation. 183

Fig. 6.17: Temperature field (ºC) for the module without fins (top) and with 14 fins (bottom). 184

Fig. 6.18: Structure of a PV module and layers properties [134]–[135]. 185

Fig. 6.19: PV module layers for current (a) and new (b) configurations, where Silicon and Teflon are applied to the displayed boundaries as thin layers. 187

Fig. 6.20: Conductive heat flux in the direction perpendicular to the PV module's surface (x-direction). 188

Fig. 6.21: Temperature profiles within the module's layers for the reference case (top) and for the new setup (bottom). 189

Fig. 7.1: Reference configuration (a), extended blinds to the bottom section (b) and whole PV array with 3.15 cm wide blinds and d/w=1.1 (c). 191

Fig. 7.2: Modified frame geometry (highlighted in blue). 193

Fig. 7.3: Temperature field for 3-pane system with Low-e on surfaces # 2-3-5, with Aluminum frame (left) and Wood frame (right). 193

Fig. 7.4: Results for the temperature of the top portions of the Aluminum and PV blinds for a 3-pane (left) and 4-pane (right) system. 195

Fig. 7.5: Temperature field and output temperature for vertical blinds with spacing of 0.635 cm (left), 1.27 cm without tilting (center) and with 15° tilting (right). 197

Fig. 7.6: Blinds layout configurations. 199

Fig. 7.7: Different arrangements of the blind's layers. 200

Fig. 7.8: Triple (left) and quadruple (right) glazing configurations. 201

Fig. 7.9: Frontal, rear and side view of Prototype 1. 203

Fig. 7.10: Prototype 1 cross-sectional view. 204

Fig. 7.11: 3D cross sectional view and close-ups showing the frame openings. 205

Fig. 7.12: Prototype 2 front, rear and side views. 206

Fig. 7.13: Prototype 2 2D and 3D cross sectional view. 207

Fig. 7.14: 3D details for Prototype 2. 208

Fig. 7.15: Prototype 3 2D and 3D front view. 210

Fig. 7.16: 3D cross-section of Prototype 3 (left) and Prototype 4 (right). 211

Fig. 7.17: Details of a PV blinds with fins used for Prototype 5. 212

Fig. 7.18: 3D cross-sectional views of Prototype 6. 213

List of Tables

Table 2.1: Properties of different gases used in windows gaps. The optimal gap thickness is given for inside to outside temperature difference of 20K [34]. 44

Table 3.1: Prototype geometrical characteristics. 76

Table 4.1: Air velocity reading (in m/s) at 9 data points at different times. 85

Table 4.2: Testing conditions and data for I-V curve measurements 86

Table 4.3: Charge controller specifications 94

Table 4.4: Average parameters under different voltage configurations: Air speed, temperature difference, electrical and thermal powers, input and output temperatures and power consumed by the fans 118

Table 5.1: Global parameters. 130

Table 5.2: Material properties. 133

Table 5.3: Comparison between experimental data and simulation results. 155

Table 6.1: Simulation results for different glazing system configurations. 159

Table 6.2: Comparison between Aluminum and Wood frame for different thicknesses 168

Table 6.3: Summary of the strategies pursued to improve heat removal from the PV 169

Table 6.4: Comparison between several glazing configurations for two air velocity values 172

Table 6.5: PV layer properties for the reference case and for the new configuration. 188

Table 7.1: Comparison between cases *a*) - *c*) for the air output temperature T_{out}, maximum PV temperature $T_{PV,max}$ and total PV length 191

Table 7.2: Comparison between the reference case (PV array at the top and large module at the bottom) and the modified frame configurations. 194

Table 7.3: Performance of triple and quadruple glazing with 3 Low-e coatings, wood frame and hybrid blinds arrangement. 196

Table 7.4: Details of monolithic glass products by Guardian Glass. 201

Table 7.5: Overview of the different prototypes, where the variations are highlighted in bold. 202

Abstract

Testing, Optimization and Design of a BIPV/T Solar Air Collector

Andrea Chialastri

Integrated building elements, which combine their structural, control and architectural functions with that of energy generation, are expected to become increasingly important in the future scenario of energy efficient buildings, and they could significantly contribute to the thermal behavior of the building envelope in order to provide energy savings. A prototype of a building-integrated photovoltaic thermal (BIPV/T) solar air collector was built, consisting of a double-glazed airflow window wall with photovoltaic (PV) louvers embedded in it. The collector is intended to either be used as a modular window wall unit that would form a ventilated double-skin façade, or as an independent airflow window, and it provides combined heat and power generation, while still allowing light transmission, shading control and thermal insulation as a conventional window.

In this work, the prototype's thermal and electrical performance have been tested, and the experimental data served to develop and validate a thermo-fluid dynamic model in COMSOL Multiphysics. This served as a first reference model and starting point to build more expanded 2D models, as well as to develop 3D models of some portions of the window, which were used for optimization and design by editing the prototype’s features, such as geometrical layout, material properties and operational parameters. CFD simulations were used to enhance PV cooling and thermal insulation, in order to

optimize both the thermal and electrical efficiency. The optimization of the glazing system, frame heat losses minimization and several strategies for PV-to-air heat transfer enhancement are discussed. These included parametric analysis of the effects of airflow rate and glass spacing on PV temperature and thermal generation, the use of extended surfaces and a new layer structure of the PV absorbers. The field measurements on existing prototype determined a maximum temperature rise of 31 °C and average thermal and electrical efficiency of 31% and 7%, respectively. The optimization showed that significant increases in air temperature rise and thermal efficiency by up to 70% and 60%, respectively, as well as up to 25% decrease in PV temperature can be achieved. Lastly, the design of new prototypes in SolidWorks, which were developed based on the simulation results, are presented.

To my wife and my daughter, my source of inspiration

Acknowledgements

First and foremost, I wish to express my sincerest gratitude to my advisor, Dr. Michael Isaacson, who has supported me throughout my thesis with his patience and knowledge and steered me in the right the direction whenever he thought I needed it, whilst allowing me the room to work in my own way. His guidance helped me in all the time of research and writing of this thesis, and I could not have imagined having a better advisor and mentor.

A very special thanks goes to Dr. Narinder Singh Kapany, for his continuous motivation and enthusiasm towards my research. I considered it an honor working with him, and his teaching represented for me a source of both professional and personal growth, for which I am deeply grateful.

I would like to thank my colleagues and friends from SolarPath: Jake, Josh and Larry Tarter, Andrei Manoliu, Mark Hintzke and Raj Kapany, for the construction of the prototype and the many stimulating and helpful discussions. I would also like to thank the Hartnell College staff for providing the space for the equipment, especially Mike Thomas for his support and friendship that persisted even after my work there.

I am highly grateful to my parents and my brother and sister, for their constant love and encouragement throughout my entire life, and to my parents-in-law for their optimism. The most special thanks goes to my greatest supporter and life partner, my wife, who completes and inspires me, and without whom I would not be the person I am.

Chapter 1
Introduction

1.1 Research Rationale

Buildings constitute a remarkable fraction of the global energy demand, accounting for about 40% of the total energy consumption, a large part of which is being used for space heating and cooling in both the residential and commercial sector. The improvement of buildings energy efficiency is of crucial importance to reduce buildings energy needs, and therefore the amount of fossil fuels used to supply the required energy. Moreover, distributed energy generation can further reduce fossil fuel consumptions by providing on-site heat and electricity from renewable energy sources. The different elements of the building envelope such as facades, roofs and windows play a central role in the thermal behavior and energy efficiency of buildings, and new technologies that integrate their structural and architectural functions with energy generation are emerging.

Among the various strategies and construction systems for sustainable design, the use of multiple-skin facades has proven to be effective in reducing heating and cooling loads, by means of a ventilated cavity between the building inner and outer skins.

A particular type of ventilated faced is known as an airflow window, where the same concept is applied to a window-sized element, which could either be a modular unit of a larger ventilated facade or be used as an independent smaller-scale module. Airflow windows consist of a ventilated double-glazed cavity, with shading devices embedded

inside, which serve as thermal absorbers of solar radiation. They can therefore be regarded as a building-integrated version of a solar thermal collector, with the back element being transparent, thus allowing for light transmittance.

However, while some new designs of double-skin facades involve the use of photovoltaic (PV) modules [73]–[74], with the advantage of providing combined heat and power (CHP) generation with the same glazed area, much like hybrid PV/T (PV/Thermal) solar collectors, the same cannot be said for airflow windows. Furthermore, the modules used in BIPV (building-integrated PV) façade systems are generally regular PV modules, which do not provide light transmission and shading control.

This research work aims to address these limitations, by investigating a novel PV/T airflow window collector, consisting of a double-glazed ventilated cavity with PV blinds integrated. The concept was developed and patented by Dr. Narinder S. Kapany, and a first prototype has been built by SolarPath Inc., in Palo Alto, CA.

1.2 Aim and methodology

The purpose of this work was to evaluate the performance of such airflow window collector, and to investigate its thermo-fluid behavior through numerical modeling and simulation, aimed at optimizing the energy efficiency and designing the next generation of prototypes.

In order to achieve this goal, the following steps were taken. The project was divided into three main phases, which are:

- Field-testing;
- Modeling and optimization;
- Prototype design.

First, an assessment of the current prototype thermal and electrical performance was carried out, by testing the prototype in outdoor conditions under mechanical ventilation. The experimental measurements served to evaluate the unit energy generation capabilities and energy efficiency, as well as to provide the data to validate a numerical model, which was developed in COMSOL Multiphysics [25]. In the second phase, the model was used to identify possible strategies for improvement, and served as a starting point to build more complete models, which were used for thermal optimization. In the last phase of the project, additional CFD models were developed, which have been used to design new prototypes in SolidWorks, together with the results from the optimization.

1.3 Thesis Outline

The dissertation is structured into the following chapters:

- **Chapter 2** sets the background on the main topics covered in the thesis, such as window technology and energy performance parameters, solar radiation through glass and solar technologies, as well as introducing the concepts of ventilated facades and airflow window and providing. Lastly, both the research and commercial status of BIPV and BIPV/T systems are discussed.

- **Chapter 3** illustrates the concept of the solar window and its implementation into a prototype, whose characteristics and various components are described.

- **Chapter 4** deals with the first phase of field testing, describing the electrical and thermal experimental setup and methodology for performance evaluation. This included the design and implementation of a stand-alone PV system, as well as measurements of the output air temperature, air velocity and PV power. From these, the thermal and electrical generation and efficiency were evaluated. The experimental results under different testing conditions and over different seasons are then presented and compared.

- **Chapter 5** describes the setup of a two-dimensional model in COMSOL Multiphysics, where the software workflow was followed to illustrate the different modeling steps, such as geometry, materials, physics interfaces and meshing. The experimental data were used as the model's boundary conditions, and they were compared to the results provided by the simulation.

- **Chapter 6** presents several strategies to improve the collector energy efficiency. The optimization of the glazing system layout is first addressed, where different combinations of multiple-glass panes and low-emissivity coatings, along with tinted glass and Argon filling are simulated, in order to increase thermal insulation. A 3-D model is also shown, to simulate the effects of a change in frame material on the heat losses. Next, the PV temperature and thermal generation were optimized by the use of heat transfer enhancement techniques, which include the increase in

mass flow rate, an optimal glass-to-glass distance, the use of extended surface on the back of the PV modules and a better layer composition of the PV modules.

- **Chapter 7** presents the design of several variations of prototypes, based on the obtained results from the optimization. Some preliminary CFD studies are also discussed, which include the effects of blinds' tilting, a wood frame, the use of blinds on the whole height of the collector, and a hybrid solution made of both aluminum and PV blinds.
- **Chapter 8** concludes the dissertation with a summary of the main findings.

Chapter 2
Background

2.1 Energy Consumption in Buildings

One of the XXI century's largest and most concerning issues is represented by the radical change and evolution that the world energy system is experiencing, characterized by a shift from a two-hundred-years-old energy system based on fossil fuels towards a more complex scenario, which involves the use of renewable energy sources, distributed generation and smart grids, as well as energy saving and energy efficiency approaches. Buildings account for about 40% of the global energy demand [1], a large part of which is being used for space heating and cooling in both the residential and commercial sector. They also represent a remarkable fraction of the global CO_2 emissions in developed countries. This is about 39% for the U.S., 36% for Europe and 20% for China [2]. Fig. 2.1*a* [3] shows the trend of the U.S. total energy consumption by sector from 1949 to 2016. In the past decade, the energy used by the residential and commercial sectors were around 21% and 18%, respectively. As of February 2017, the energy consumptions in the residential sector (Fig. 2.1*b*) came mainly from natural gas (56%) and electricity (32%), the latter being produced using fossil fuels (56%), nuclear energy (25%) and renewable sources (19%) such as solar, wind, hydroelectric, biomass and geothermal energy (Fig. 2.1*c*).

As shown in Fig. 2.2**,** in the residential sector about 50% of the total energy demand is used for space heating and cooling [4].

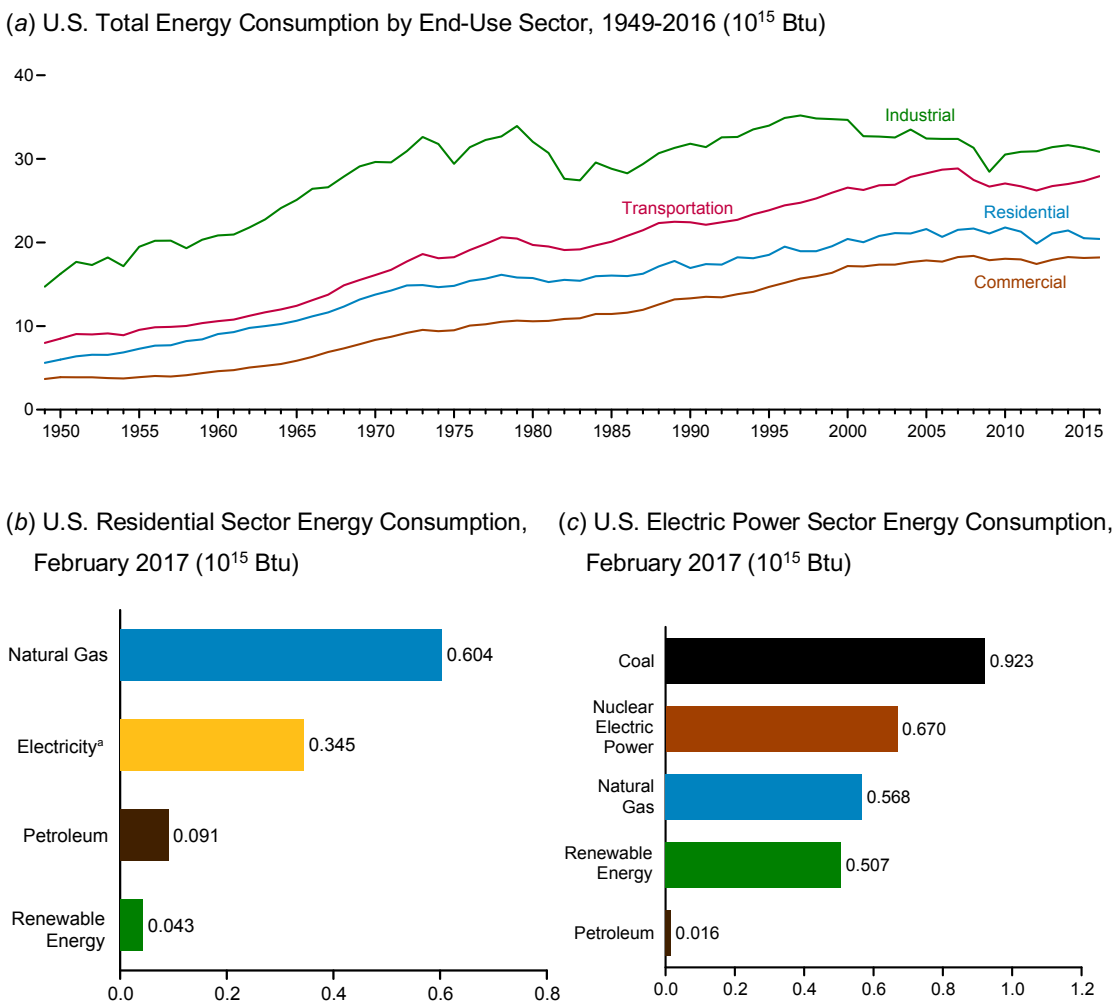

Fig. 2.1: U.S. energy consumption: (a) total energy consumption by end-use sector; (b) residential sector and (c) electric power sector energy consumption by major sources [3].

This is closely related to the degree of insulation between the building envelope and the environment, and any improvements to the different elements, such as ceiling, floors, walls and windows, would contribute to the overall thermal balance and provide energy savings. As shown in Fig. 2.3, between 35% and 55% of the energy transfer is from floors and ceilings both in summer and winter, 15% to 25% from walls and the remaining from fenestrations and possible air leakages [5].

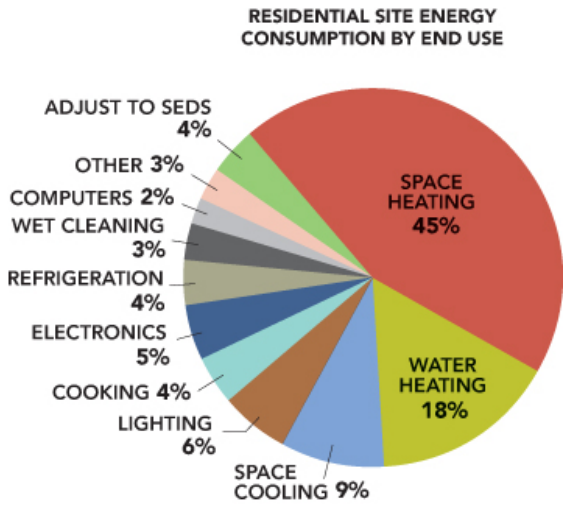

Fig. 2.2: Residential energy consumptions in the U.S. in 2015 [4].

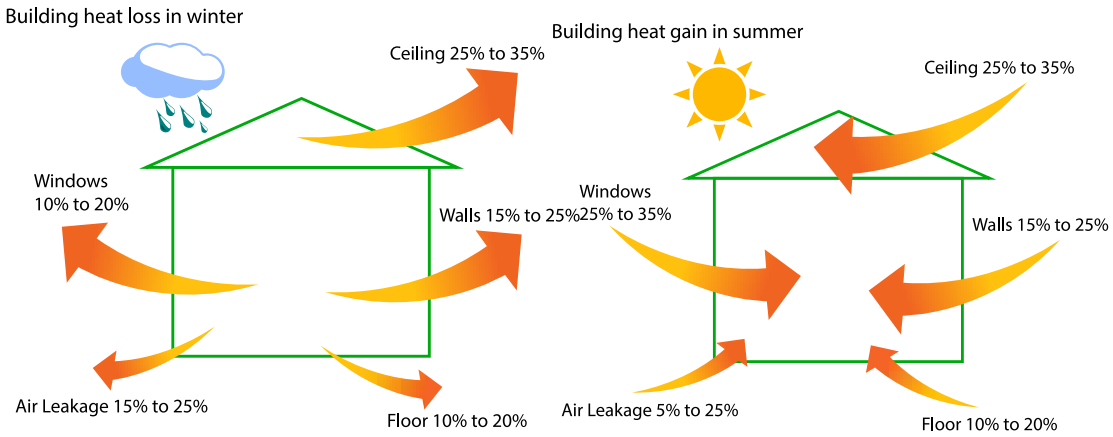

Fig. 2.3: Heat losses and heat gain through the building envelope [5].

Glazed openings such as windows, skylights and curtain walls account for 10% to 20% of the total thermal losses in winter, and about one third (25% - 35%) of the heat gain in summer, and the development of new window technologies has been historically a major factor in lowering heating or cooling requirements of buildings.

2.2 Brief History of Windows

The origins of the window concept date back to the very early stages of buildings history, when they were first introduced in primitive dwellings by cutting a hole in the wall [6]. This served as an opening connecting the interior of the house with the exterior environment by allowing sunlight and fresh air to reach the indoor space, thus improving its quality and liveability. The openings were also letting weathering, dust and insects in, and opaque or translucent covers were originally used to provide more control, until the Roman era, when transparent glass established as the primary cover material for windows in the most important buildings [7]. Glass enabled the benefits of daylight and solar gain, while providing protection from the external elements, but small pieces of irregular thickness and poor optical quality were manufactured. Around the 1st century BC [8], the invention of the glassblowing technique by Syrian and Palestinian craftsmen represented a turning point in the history of glass, and by the Middle Ages Venice had become the primary glassmaking center in Western Europe. Molten pieces of glass were inflated into bubbles or cylinders, cut while still hot and the resulting sheets were thinned and flattened. Blown glass was introduced in North America and used in windows of colonial houses, and in 1608 the first American glass factory was built in Jamestown, Virginia. In 1688 polished plate glass was produced in France [8], enabling larger, flatter and cleaner glass to be produced, allowing for larger windows to be used, and in 1773 this production process was adopted in England, which became the center of the glass industry during the XVIII and XIX centuries [8]. The demand for window glass grew rapidly and it was made increasingly available to

middle and lower classes, while larger, stronger and higher quality glass was manufactured. The first semi-automatic machine appeared in 1887 in Castelford, Yorkshire, which was able to produce 200 bottles per hour [10], and the following year, the machine rolled glass was introduced, allowing patterns to be created [9]. Mass production was eventually introduced in the United States with the development of the first fully automatic bottle blowing machine by Michael Owens in 1903, which had a production capacity of 2500 bottles per hour [11].

During the first half of the XX century, houses in the United States still had very inefficient clear single-pane windows [6], but buildings were designed to take advantage of the site's natural elements such as orientation, vegetation, sunlight and wind, so that the energy needs for light, heating, cooling and ventilation were kept as low as possible. The 1950s had seen a major event in glassmaking technology, with the development of the float glass technique by Sir Alastair Pilkington [12], which provided uniform, very flat surfaces, and became the standard process by which most of glass is still manufactured today. However, this decade was also characterized by larger energy consumptions in housing, mainly due to the lower cost of energy, and the site properties were not considered in buildings design. Later, the need for lower energy consumptions and more efficient buildings came in response to the energy crisis of the 1970s and the consequent increase in energy prices, along with a new environmental consciousness. Since then, strategies for improving building energy efficiency and promoting sustainability became increasingly common, and these included the attention to the environmental characteristics in the design phase, passive utilization

and storage of solar energy, storm water collection, better insulation materials used for the building envelope. Windows have undergone significant improvements, starting from a shift from single glazing to insulated glass units (IGU), with two or more panes of glass. Double-glazing reached a market share of 45% in 1980s, and today around 90% of windows manufactured are either double or triple-glazed units [6]. The reduction in heat losses provided by insulated glass made windows a primary instrument for capturing solar heat and keeping it inside the building. More recently [13], the use of less thermally conductive gases to fill the cavity, as well as the development of low-emissivity (low-e) coatings enabled a further reduction in heat losses, while tinted glass and solar control coatings reduced cooling loads by absorbing or reflecting solar heat outside. Many other approaches to enhance window insulating properties are being carried on, such as better spacer design to limit edge-of-glass losses and reduce condensation risks, newer frame materials for higher thermal resistance and improved weather-stripping to reduce air leakage. High-performance windows still have significant potential for decades to come, and the recent progress highlights a trend towards a significant change of the role of windows. From weak elements of the building envelope and major source of heat losses they are now very highly efficient components which are increasingly becoming a central element able to dynamically interface the interior with the exterior environment, by controlling the transmitted solar radiation depending on the building's needs. Furthermore, windows are gradually transforming into active elements, providing not just daylight and solar gain alone, but

also adding ventilation and energy generation capabilities, through the use of double-skin facades and building-integrated photovoltaic and thermal technologies.

2.3 Window Energy Performance

Fenestration products can have a big impact on the building energy performance, as they can reduce the heat lost or gained through them and can influence either the capture or the rejection of the solar radiation, thus reducing the need for space heating or cooling. The properties related to the first aspect are the window U-factor, or insulating value, and the air leakage, while the windows behavior with solar radiation is connected to the solar heat gain coefficient. Windows also affect several other human factors, such as glare and sound control, visible light transmittance and thermal comfort, when for instance they provide warmer glass and frame surface temperatures or protect from cold air drafts and overheating from the sun.

2.3.1 Thermal Insulation

Windows offer the least resistance to heat transfer among the different parts of the building envelope, and it is common use to characterize and compare them by their insulating value, which is called U-factor or overall window heat transfer coefficient, and it is measured in $W/m^2 \cdot K$ [6]. The total U-factor is a combination of heat losses through the frame, the main glass area (center of glass), where fully perpendicular heat flow is assumed, and the glass region in the proximity of the frame (edge of glass), where the tridimensional effects are predominant.

Typical values are between 5–5.8 W/m^2·K for single glazed windows, depending on the frame material, and between 2.4–4.7 W/m^2·K for uncoated double glazed units with air filling, depending on the width of the air cavity and on the type of spacers and frame used [14]. Values between 1.6–2.4 W/m^2·K are achieved for double glazed windows with argon filling and low-e coatings, which drop to 0.8–1.1 W/m^2·K for triple argon-filled glass and low-e coatings on two surfaces [15].

Heat transfer through windows occurs by a combination of all three heat transfer mechanisms, that is by conduction, convection and radiation (Fig. 2.4).

Conductive heat transfer takes place through all the components, such as the frame, the glazing, the spacer and all the hardware used in the whole assembly. More thermally conductive frame materials facilitate the heat path from inside to outside of the building in the cold months, and from outside to inside in the summer months, as is the case for aluminum framed windows. The same applies for single-glazed windows, since most of the insulating value is provided by the air layers on each glass surface, while glass

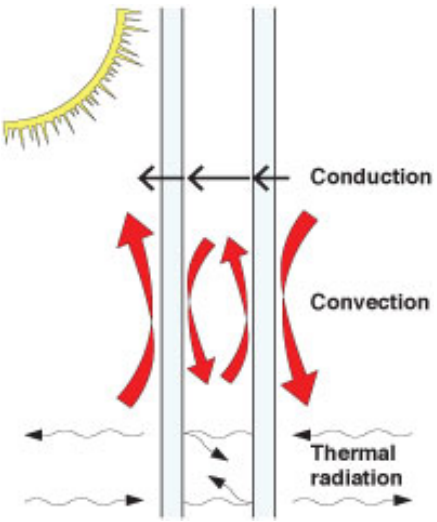

Fig. 2.4: Window heat transfer components related to insulating value [16].

has a relatively high thermal conductivity. Conduction in window frames is reduced by using lower conductivity materials, such as wood or plastics, or by adding insulating materials in aluminum frames, and within insulating glass units by using non metal spacers or lower conductivity metals.

Convection arises on the interior and exterior glass surfaces, due to the adjacent air movement caused by temperature-induced density gradients (interior of the building) or by wind blowing to the external surfaces. Convection currents can also develop in the hollow cavities of the frame structure and in the gaps of sealed glass units, although

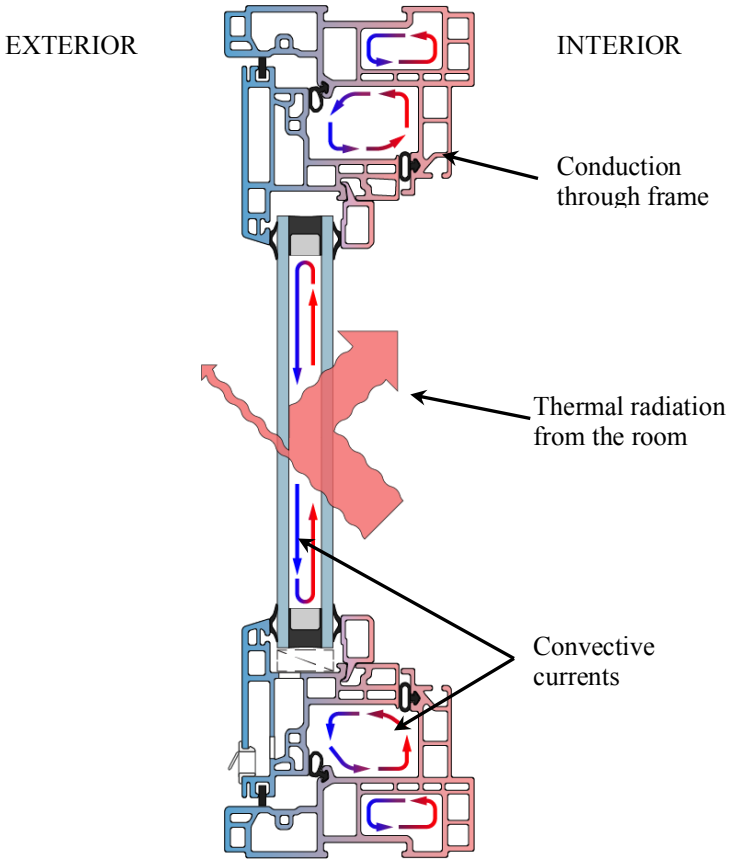

Fig. 2.5: Cross section of a window assembly showing convective currents in the frame cavities and within the double-glazing, conduction through the frame and radiation through the glass, assuming a cold exterior [17].

they are generally lower than those for external surfaces (Fig. 2.5). Convection losses in hollow window frames can be reduced by dividing larger cavities into smaller compartments or by filling the larger cavities with insulation. Within glass units, convection losses can be minimized by adjusting the glass spacing and using a more insulating and more viscous gas, such as argon or krypton.

Lastly, radiative heat transfer occurs between the glazing layers and between the exterior and interior window surfaces and the surrounding spaces. A cold interior glass surface would impact on the thermal comfort by mean of both convection and radiation. The air layer close to the glass surface will be cooled and consequently its lower density will generate a convection current, which will be perceived as a draft. At the same time, the cold surface will cool all the surrounding objects, including human bodies, because a net radiative heat exchange will take place from the surroundings towards the glass, which will generate discomfort even if the room temperature were at a comfortable level. This emphasizes the importance of having a window with a high U-factor, which could maximize the inner glass temperature. Radiative heat losses through glazing units can be reduced by applying low-emissivity coatings to the glass surfaces.

2.3.2 Solar Heat Gain

Direct and diffuse radiation coming from the sun and the sky, as well as reflected components from the ground and other objects (Fig. 2.6) are all taken into account in what is called solar heat gain coefficient (SHGC). This is defined as the ratio between the solar radiation that actually enters a building and the total incident radiation, and its

value ranges between 0, for a completely opaque surface (a wall), and 1 for a totally transparent surface (a hole in the wall). The heat gain includes both the directly transmitted radiation, as well as the component of the radiation absorbed by the glass, which is then indirectly transmitted inside, as shown in Fig. 2.6.

A high SHGC is desirable in heating dominated climates, in order to benefit from solar space heating during the winter, while the opposite is true in hot climates, where solar control windows that reject solar radiation are preferred.

2.3.3 Air Leakage

Unwanted infiltrations are considered a form of heat transfer, and thus an energy performance property, as they involve the exchange of air at different temperatures between the inside and outside of the building. In the case of a colder outside temperature, indoor air is replaced by colder outdoor air, which needs to be heated again, therefore increasing the overall heating needs of the room. Air leakage is

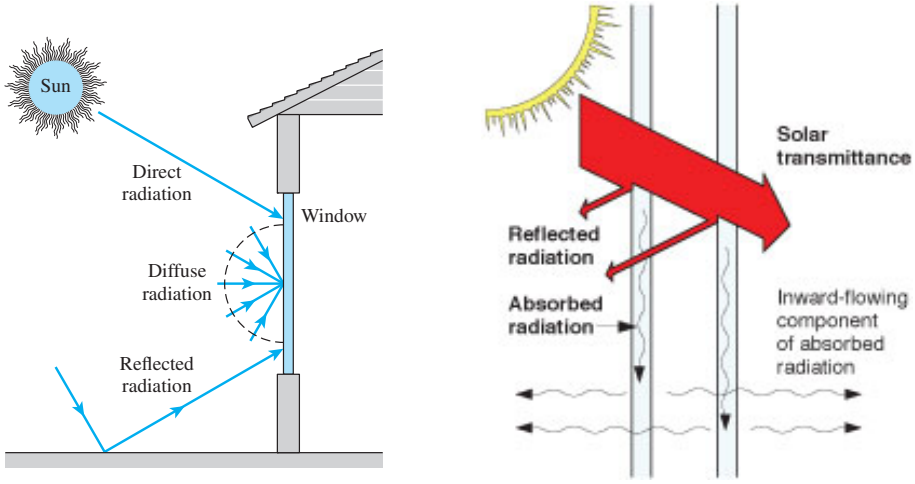

Fig. 2.6: Solar radiation incident on a window (left) and components of solar heat gain coefficient (right) [16][[18].

measured as the volume of air flowing per unit time, per unit area of the fenestration and can be expressed in $L/s \cdot m^2$. Most industry groups in the U.S. recommend air leakages below 1.5 $L/s \cdot m^2$ [6]. Operable windows are more susceptible to air leakages, and the compression-seal windows perform generally better than sliding windows. Fixed windows present the lowest air leakages, with values of around 0.2 $L/s \cdot m^2$.

2.4 Glass and Solar Radiation

2.4.1 The Solar Spectrum

Solar radiation is located between the ultraviolet (UV) and the near-infrared (NIR) range of the electromagnetic spectrum (Fig. 2.7). The spectral distribution of the extraterrestrial solar radiation can be very well approximated with that of a blackbody at nearly 5780 K [18], corresponding to the sun surface temperature (Fig. 2.8). Most of the energy is within the range of 0.25 to 3 μm: about 6.4% of the energy is within 250-380 nm (UV light), the largest fraction of around 48% is emitted as visible light in the range of 380-780 nm and the remaining 45.6% as near-infrared radiation, in a range of wavelengths ranging between 780nm and 3 μm [19].

As the sun's rays reach the earth atmosphere, they get absorbed and scattered by O_2, O_3, CO_2 and H_2O, as well as by dust, pollutants and other products of fossil fuel combustion, resulting in a considerable attenuation in solar radiation reaching the earth surface (red area in Fig. 2.8).

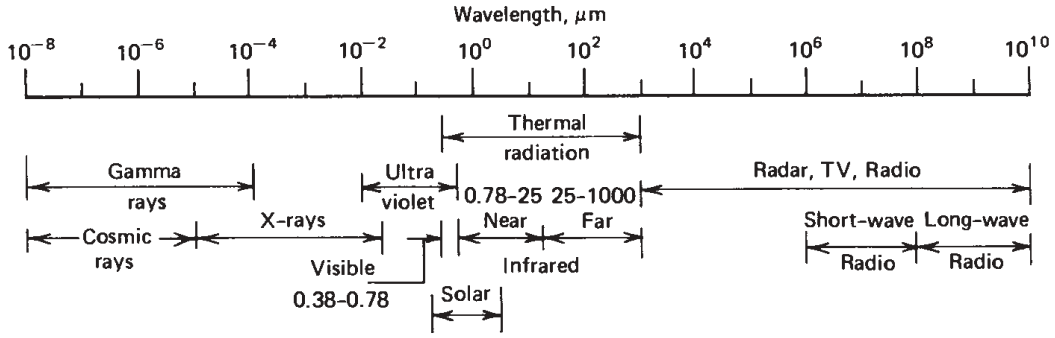

Fig. 2.7: Solar energy in the electromagnetic spectrum [19].

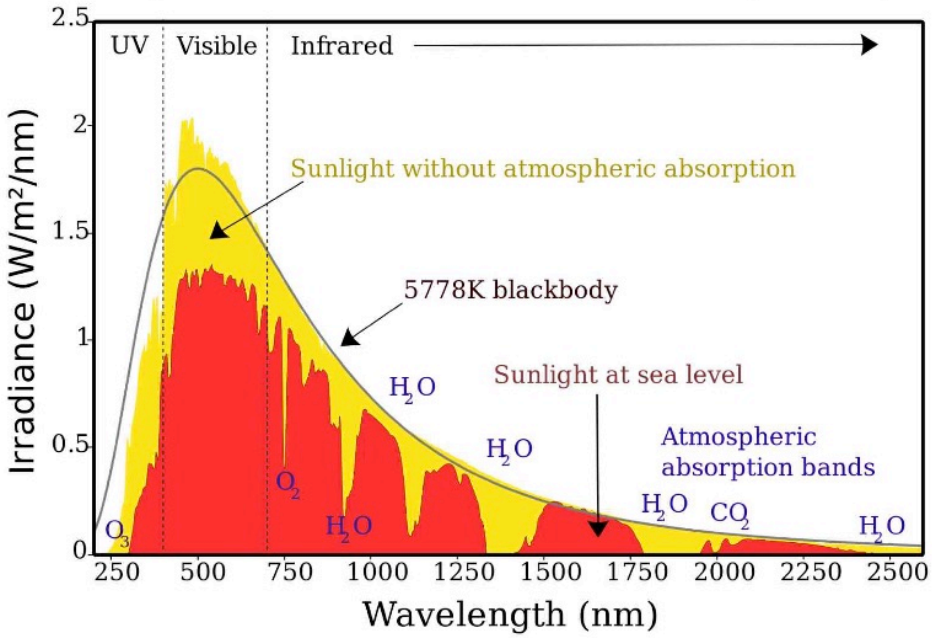

Fig. 2.8: Solar radiation spectral distribution at the top of the atmosphere, attenuation by the earth's atmosphere and radiation of a blackbody at 5778K [20].

The range of the solar energy received at the ground is therefore reduced to wavelength between 0.29 to 2.5 μm [19], with fractions in the UV, visible and NIR bands of 7%, 57% and 36%, respectively [21].

2.4.2 Radiative Properties

As mentioned above, extraterrestrial solar radiation can be approximated as that emitted by a blackbody at the same temperature. A blackbody is defined as an ideal

surface that absorbs all incident radiation, emits more energy than any other body at the same temperature and wavelength, and its emitted radiation is independent of direction. It is a perfect absorber and emitter and it is used as a standard to which radiative properties of real surfaces are compared. Any body emits radiation, and the ratio of the actual emitted radiation by the surface to the radiation emitted by a blackbody at the same temperature is defined as the emissivity, ε, of the surface. For a blackbody, $\varepsilon = 1$, while for real surfaces $0 < \varepsilon < 1$, and it is in general a function of temperature, wavelength and direction.

It is often useful to treat real surfaces as diffuse and gray surfaces, that is with their properties being independent of direction and wavelength, respectively [18]. While treating a surface as diffuse represents a reasonable approximation, due to the nearly constant emissivity for a good range of angles ($\theta < 40°$ for electrical conductors and θ

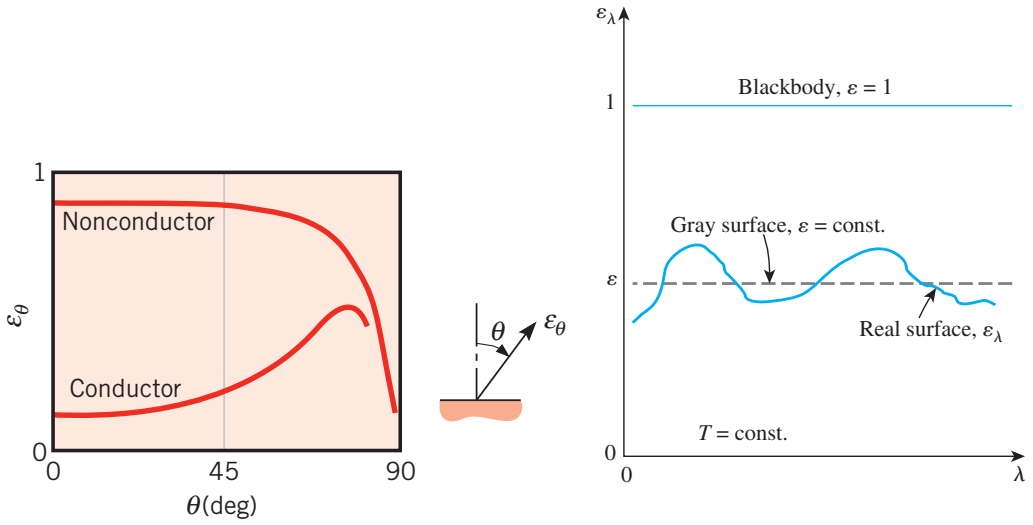

(*a*) (*b*)

Fig. 2.9: Variation of the total directional emissivity (a) with an angle θ measured from the normal to the surface [22], and comparison of the total spectral emissivity (b) for a blackbody, a real and a gray surface [18].

< 40° for non conductors, with θ measured from the surface normal, as shown in Fig. 2.9*a*), the gray surface approximation requires more caution as real surface emission may vary significantly with wavelength. If the spectral emissivity distribution of the surface is such that can be well approximated with a constant function (Fig. 2.9*b*), then it can be treated as a gray surface without losing too much accuracy.

When the solar radiation strikes the surface of any object, part of it is reflected, part is absorbed, and the remaining fraction, depending on the optical characteristics of the material, may be transmitted, as in the case of glass or other semitransparent materials. The fractions of reflected, absorbed and transmitted radiation are called reflectivity, (ρ), absorptivity (α) and transmissivity (τ), respectively. These are functions of direction and wavelength, but they are generally represented in terms of their directional averages (hemispherical properties) for an incoming radiation with wavelength λ, therefore the spectral hemispherical reflectivity, absorptivity and transmissivity are expressed as [18]:

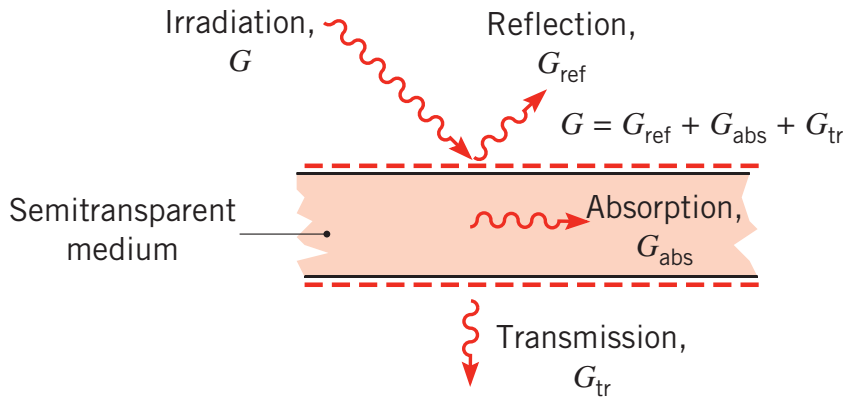

Fig. 2.10: Reflection, absorption and transmission of incident radiation for semitransparent medium [22].

$$\rho_{\lambda}(\lambda)=\frac{G_{\lambda,ref(\lambda)}}{G_{\lambda}(\lambda)} \tag{1}$$

$$\alpha_{\lambda}(\lambda)=\frac{G_{\lambda,abs(\lambda)}}{G_{\lambda}(\lambda)} \tag{2}$$

$$\tau_{\lambda}(\lambda)=\frac{G_{\lambda,tr(\lambda)}}{G_{\lambda}(\lambda)} \tag{3}$$

where G_{λ} (W/m^2·μm) is the radiation with wavelength λ incident on the surface, called spectral irradiance, and $G_{\lambda,ref}$, $G_{\lambda,abs}$ and $G_{\lambda,tr}$ are its reflected, absorbed and transmitted fractions, respectively, as shown in Fig. 2.10. If integrated over all wavelengths, the total hemispherical properties can be expressed as follows

$$\rho=\frac{\int_0^{\infty}\rho_{\lambda}(\lambda)G_{\lambda}(\lambda)d\lambda}{\int_0^{\infty}G_{\lambda}(\lambda)d\lambda}=\frac{G_{ref}}{G} \tag{4}$$

$$\alpha=\frac{\int_0^{\infty}\alpha_{\lambda}(\lambda)G_{\lambda}(\lambda)d\lambda}{\int_0^{\infty}G_{\lambda}(\lambda)d\lambda}=\frac{G_{abs}}{G} \tag{5}$$

$$\tau=\frac{\int_0^{\infty}\tau_{\lambda}(\lambda)G_{\lambda}(\lambda)d\lambda}{\int_0^{\infty}G_{\lambda}(\lambda)d\lambda}=\frac{G_{tr}}{G} \tag{6}$$

According to the first law of thermodynamics, the sum of the reflected, absorbed and absorbed components has to be equal to the irradiation G, and it can be found that

$$\alpha+\rho+\tau=1 \tag{7}$$

For blackbodies, which are perfect absorbers, $\rho = 0$ and $\tau = 0$, so that Eq. (4) reduces to $\alpha = 1$. For opaque surfaces, $\tau = 0$, which yields:

$$\alpha + \rho = 1 \tag{8}$$

According to Kirchhoff's law [23], the spectral hemispherical emissivity of a diffuse surface at temperature T is equal to its spectral hemispherical absorptivity at the same temperature:

$$\varepsilon_\lambda(T) = \alpha_\lambda(T) \tag{9}$$

and for a diffuse-grey surface, whose properties are independent from wavelength, Equation 9 can be further simplified as

$$\varepsilon(T) = \alpha(T) \tag{10}$$

Therefore, in radiation exchange phenomena between diffuse-grey opaque surfaces at similar temperatures (within a few hundred degrees difference), the total hemispherical properties can all be determined from the knowledge of one of them, by using the relations $\rho = 1 - \alpha$ and $\varepsilon = \alpha$.

2.4.3 Selective Surfaces

When the incident radiation comes from a source at very different temperature, as in the case of solar radiation, the spectral distribution of the source and the surface can be quite separated. As shown in Fig. 2.11 most of the solar energy is concentrated at wavelengths shorter than 2.5 μm, while most of the radiation emitted by blackbodies at temperatures close to that of the earth's surface lies at wavelengths longer than 2.5

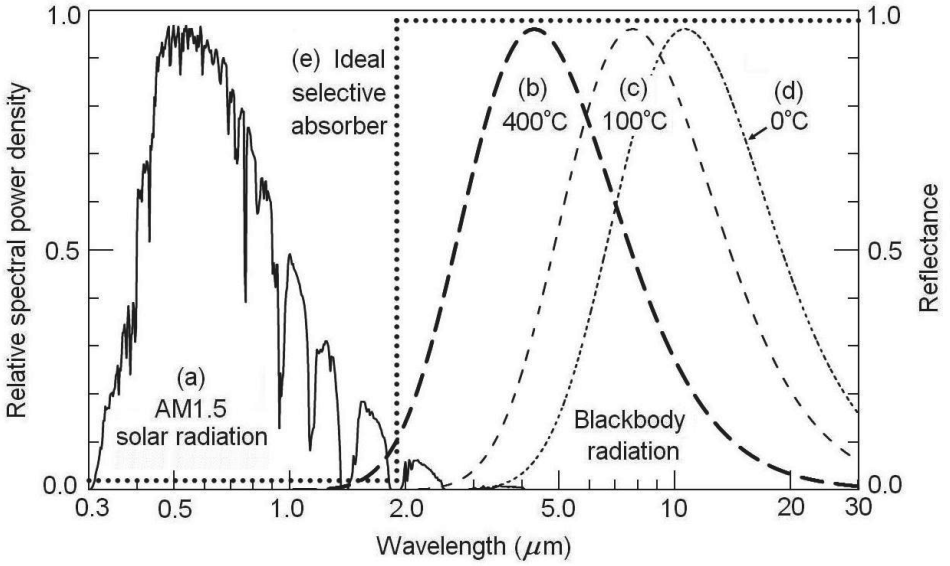

Fig. 2.11: Solar spectrum and radiation emitted by black bodies at various temperatures close to the earth's surface temperature [24].

μm, so that the range of wavelengths of the emitted radiation has almost no overlap with the solar spectrum [24].

Consequently, the radiation properties of many surfaces can be significantly different for incident and emitted radiation, and because of their spectral variation the surfaces cannot be approximated as gray. Even though ε_λ and α_λ are equal for each wavelength, according to Equation 9, if they are not constant over the entire spectral range then $\varepsilon \neq \alpha$, and Equation 10 will not be valid.

However, some surfaces, called selective surfaces, manifest a semi-gray behavior, that is they can be approximated as gray, but with different properties, for specific spectral bands, and in such a case the total absorptivity and emissivity are given as weighted average values for different spectral ranges [23]. When such surfaces can be considered semi-gray on two bands with a cutoff wavelength corresponding to the border between

the solar radiation spectrum and the infrared spectrum (around 3 μm), a step function can be defined as (Fig. 2.12):

$$\varepsilon_\lambda = \alpha_\lambda = \alpha_S \quad \text{for } \lambda < 3\ \mu\text{m} \tag{11}$$

$$\varepsilon_\lambda = \alpha_\lambda = \varepsilon_{IR} \quad \text{for } \lambda > 3\ \mu\text{m} \tag{12}$$

where α_S is the total absorptivity for solar radiation, and ε_{IR} is the total emissivity for

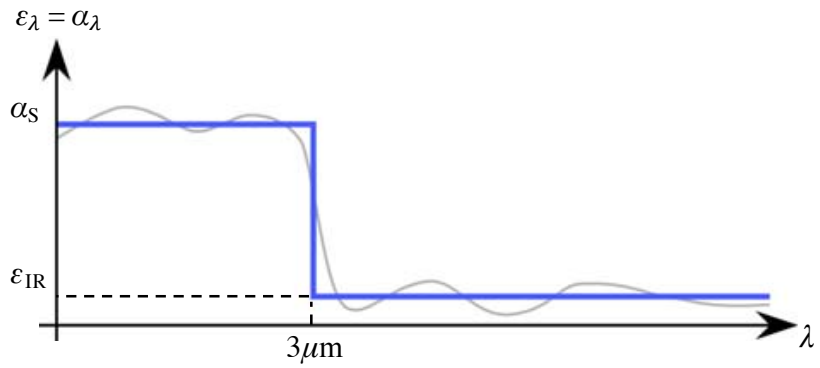

Fig. 2.12: Solar absorptivity and infrared emissivity approximation by a step function [25].

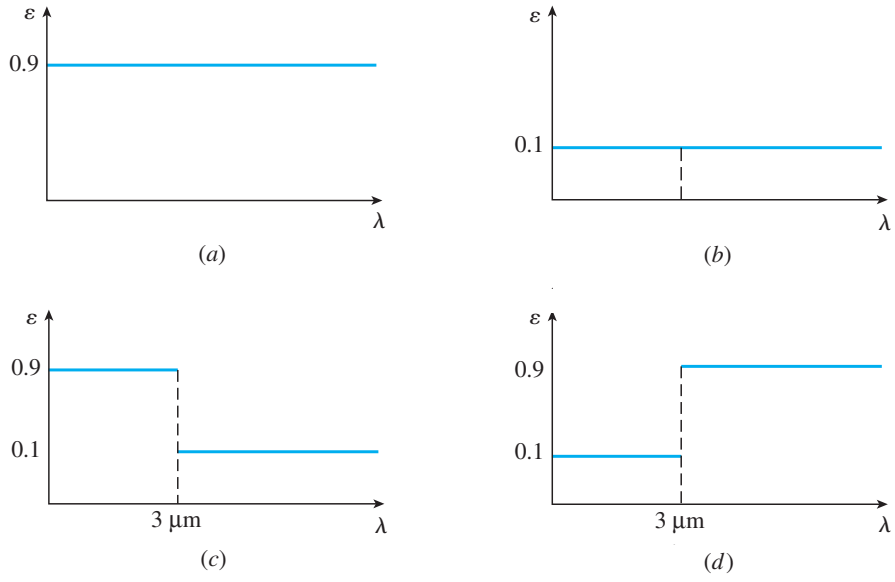

Fig. 2.13: Spectral emissivities for different surfaces: (a) gray absorber, (b) gray reflector, (c) selective absorber and (d) selective reflector [18].

long-wave infrared radiation. Surfaces which are highly absorbent in the solar spectrum and does not emit much in the infrared ($\alpha_S >> \varepsilon_{IR}$) are called selective absorbers, and they are commonly used as collector absorbers in solar thermal systems, while those reflecting most of solar radiation which are also good emitters in the long-wave infrared ($\alpha_S << \varepsilon_{IR}$) are called selective reflectors. In Fig. 2.13 are shown as a comparison the spectral emissivities of a gray absorber ($\alpha_S = 0.9$, $\varepsilon_{IR} = 0.9$) a gray reflector ($\alpha_S = 0.1$, $\varepsilon_{IR} = 0.1$), a selective absorber ($\alpha_S = 0.9$, $\varepsilon_{IR} = 0.1$) and a selective reflector ($\alpha_S = 0.1$, $\varepsilon_{IR} = 0.9$). For an ideal selective absorber (curve (e) in Fig. 2.11) $\alpha_S = 1$ and $\rho_S = 1 - \alpha_S = 0$, while $\varepsilon_{IR} = 0$ and, being $\varepsilon_{IR} = \alpha_{IR}$, the infrared reflectivity is $\rho_{IR} = 1 - \alpha_{IR} = 1 - \varepsilon_{IR} = 1$.

The behavior of real selective surfaces differs, of course, from the ideal case, and a few examples of some selective materials are given in Fig. 2.14. Black chrome and black

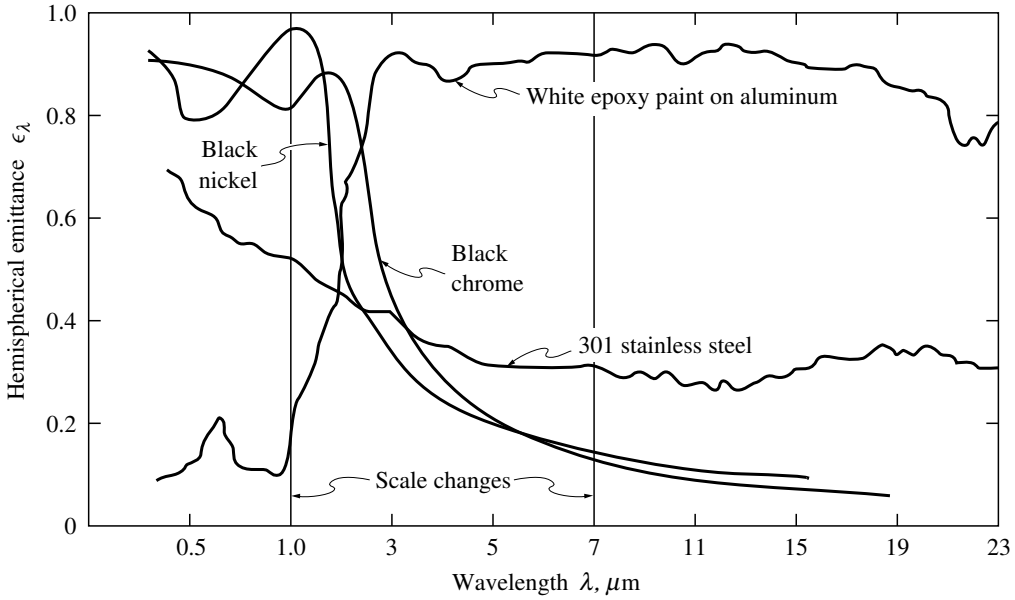

Fig. 2.14: Spectral hemispherical emissivity of some selective surfaces [26].

nickel are commonly utilized in solar collector absorbers for their highly selective properties, allowing for high solar absorptivity and low infrared emissivity, while epoxy paint represents a good solar reflector, due to its high reflectivity in the solar spectrum and high emissivity in the long-wave infrared.

2.4.4 Glass Interaction with Solar Radiation

Glass is a semitransparent medium, and as such it will partially reflect, absorb and transmit any incident solar radiation. For a typical 3-mm thick clear glass panel, about 8% of sunlight is reflected, 8% is absorbed (of which 6% convected away to the outside and 2% reradiated into the building) reflected and 84% is transmitted, for a total SHGC of 0.86 [15].

Glass behaves as a selective transmitter of solar radiation, that is, the transmittance is a function of wavelength of the incoming radiation, and τ_λ for normal incidence depends on the glass thickness and on its Fe_2O_3 content. In Fig. 2.15 [19] the spectral transmittance of 6-mm thick glass with different contents of iron oxide are reported. This shows that a glass with high iron content is a relatively poor transmitter, as it will absorb most of the NIR portion of the solar spectrum, while low-iron glass has the highest transmission.

Most importantly, it is shown how glass acts as a selective transmitter. For clear glass, and even more for low-iron glass, τ_λ does not vary significantly within the solar spectrum ($0.29 < \lambda < 2.5$ μm), and it ranges between 0.73–0.88% and 0.8–0.9%, respectively, for 6-mm thickness. In both cases, there are two sharp cutoff wavelengths

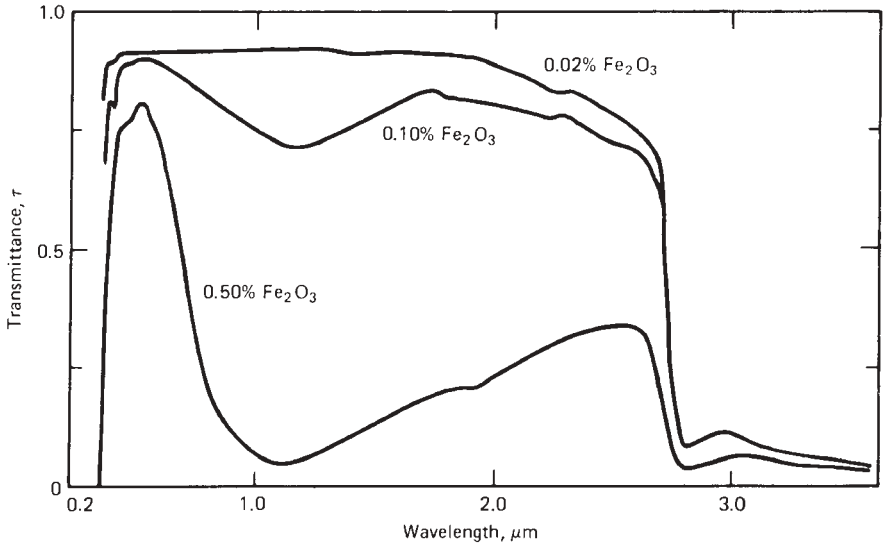

Fig. 2.15: Spectral transmissivity of various 6-mm thick glass panels with different iron contents: regular clear glass (0.10% Fe_2O_3), low-iron glass (0.02% Fe_2O_3) and high iron glass (0.5% Fe_2O_3).

in the far-UV and NIR fields, where the glass becomes highly absorbing: τ_λ drops close to zero for $\lambda < 0.17$ μm and beyond $\lambda \approx 2.5$ μm. This means that, apart from the low transmissivity in the UV range outside the solar spectrum, the glass becomes essentially opaque for long-wave infrared radiation. Its poor transmissivity (high absorptivity) for long wavelengths causes what is referred to as the "greenhouse effect", by which the far-infrared emission from objects at room temperature enclosed by the glass will be trapped inside by absorption and reflection at the glass surface. The percentage of absorbed and reflected fractions will depend on the glass emissivity. A regular uncoated glass has an emissivity of 0.84, therefore, being $\tau_{\lambda>2.5\mu m} \cong 0$, by means of Equations 8 and 9 it follows that:

$$\rho_{\lambda>2.5\mu m} = 1 - \alpha_{\lambda>2.5\mu m} = 1 - \varepsilon_{\lambda>2.5\mu m} = 1 - 0.84 = 0.16 \qquad (13)$$

so 84% the radiation emitted from the inside of the enclosed space will be absorbed by the glass and 16% will be reflected back. Similarly, in the case of a low-emissivity glass with $\varepsilon = 0.04$, only 4% of the radiation will be absorbed by the glass and the remaining 96% reflected back into the space.

The glass transmissivity will also vary with its thickness and angle of incidence of the incoming radiation, as shown in Fig. 2.16 and Fig. 2.17. With increasing thickness τ_λ is slightly reduced in the UV and visible bands and drops in a more pronounced way in the NIR. As shown in Fig. 2.17, the influence of the incident angle, that is the angle between the sunrays and the normal to the glass surface, is mainly seen after a certain point in the curve. The transmissivity is nearly unaffected until around 55°, after which it rapidly drops while the reflectance increases at the same rate.

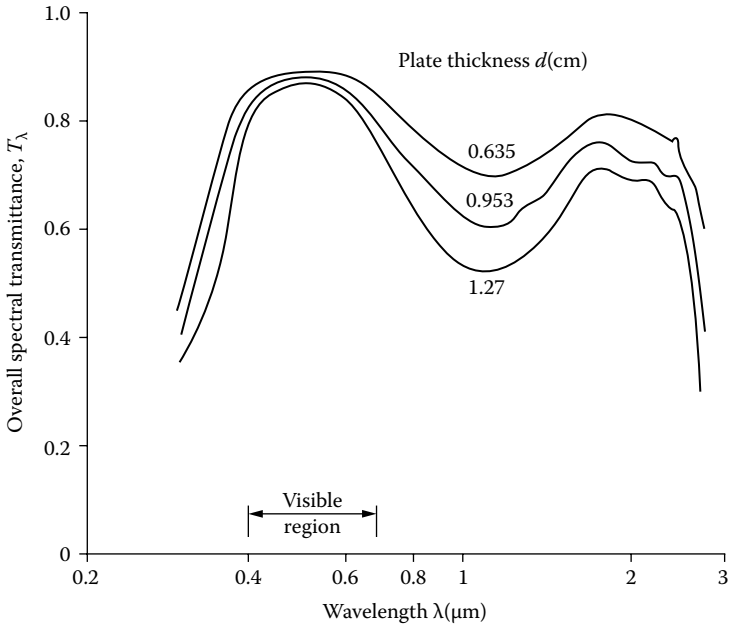

Fig. 2.16: Transmissivity variation with thickness for soda-lime glass [27].

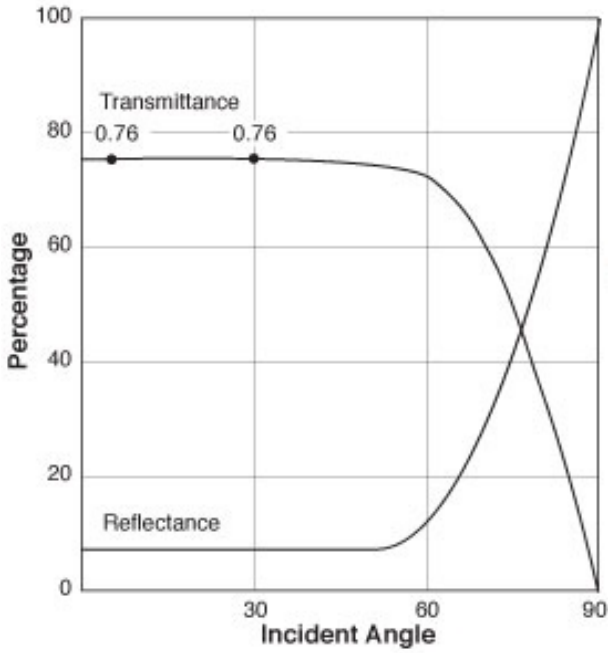

Fig. 2.17: Effects of the incident angle on the transmissivity of 6-mm glass [16].

2.5 Components of Window Assemblies

Modern window assemblies consist mainly of two parts: the outer frame, or casing, which is anchored to the building envelope, and could host the inner frame, or sash, in operable windows, and the glazing unit itself, which is held by the sash, or by the same frame in the case of fixed windows. For the purpose of this thesis, only fixed windows will be considered.

Nowadays, most windows for new constructions features double-pane glazing, and the standard glazing system consists of (Fig. 2.18) two glass panes which are sealed and spaced apart by spacer bars at the edges, forming what is referred to as an insulating glass unit (IGU).

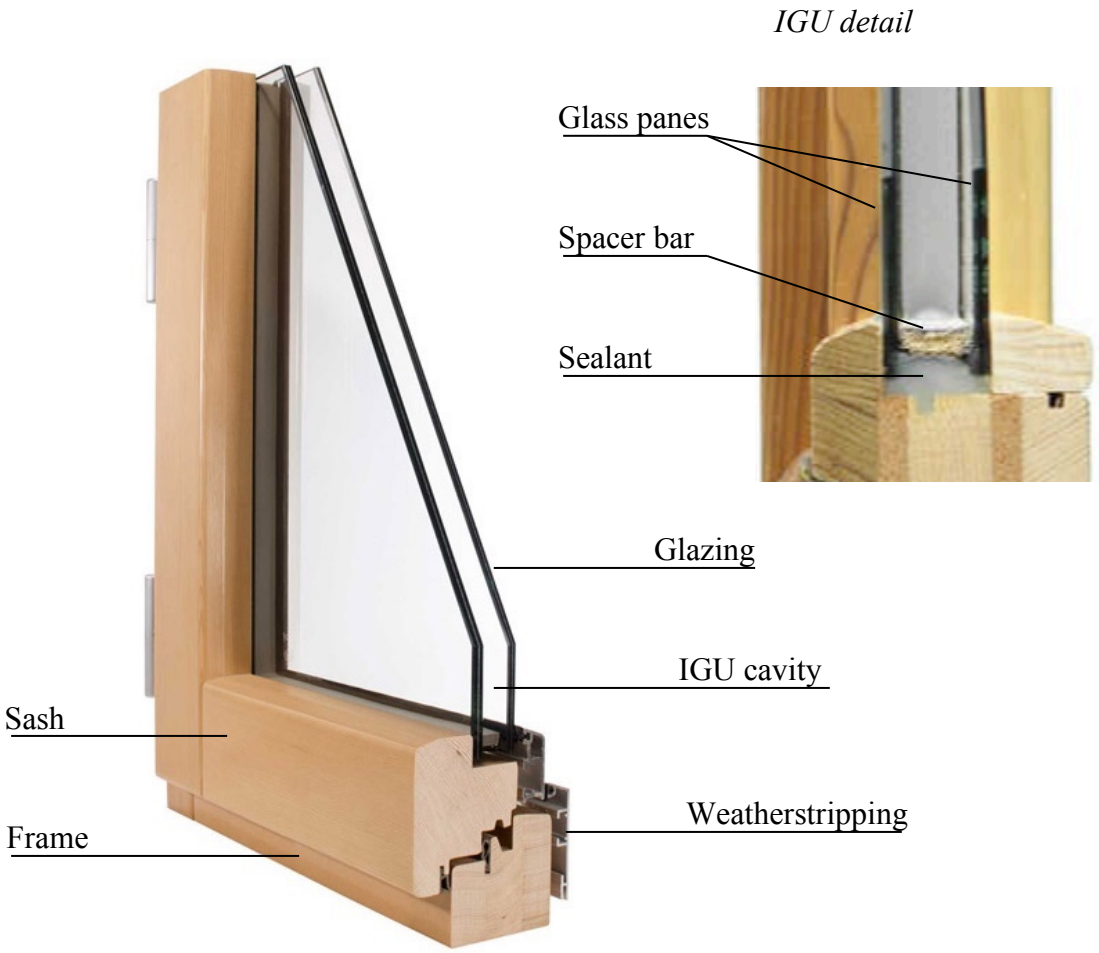

Fig. 2.18: Double glazed window components (left) and insulated glass unit detail (right) [28],[29].

2.5.1 Frame materials

The frame of common window units represents between 10% and 30% of the total area [30], and, together with the edge losses from the glazing, conduction losses through the frame account for 10-30% of the total heat losses from windows [13], thus improving the material thermal properties can contribute significantly to the overall window performances. The most commonly used frame materials are described below, and summarized in Fig. 2.19.

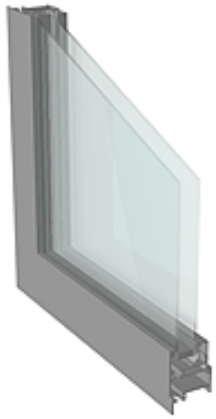

Aluminum frame

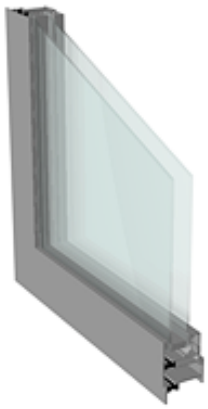

Aluminum frame with thermal break

Wood frame

Cladded wood frame

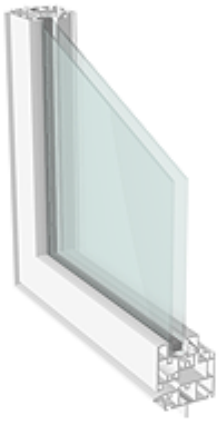

Vinyl frame

Insulated vinyl frame

Hybrid wood-vinyl frame

Fig. 2.19: Different frame types [30].

Aluminum frames

Aluminum had a widespread use during the second half of the XX century, and this was due to the fact that is a lightweight yet strong and durable material, it is easy to extrude and manufacture, and it requires minimal maintenance.

However, from a thermal point of view, it readily conducts heat, having a high thermal conductivity of about 237 W/m·K [31] (1500 times greater than that of wood), and it is therefore a major source of heat losses, which negatively contributes to the overall window U-factor.

Improvements are possible through the use of thermal breaks, by splitting the frame into several pieces connected with a less conductive material, typically cellular foam, PVC, polyurethane or wood, allowing for a reduction in the frame U-factor from about 5 - 7 to 2.5 - 4 $W/m^2 \cdot K$ [14].

Wood frames

Wood is a traditional frame material and has regained market share over aluminum framed windows since the last two decades of the last century. It is easy to adapt to complex shapes required for window frames and its thermal properties are excellent, with thermal conductivity in the range of 0.1-0.2 W/m·K [31] and U-factors between 1.5-2.6 $W/m^2 \cdot K$ [14].

The biggest disadvantage is its susceptibility to decay and it therefore requires high maintenance to protect from weather and insect attacks. A common and permanent weatherproof solution is the cladding of the exterior surface with either vinyl or aluminum, which acts as a barrier to the outside and lowers the required maintenance.

Vinyl frames

Vinyl is a relatively new plastic material, also known as PVC, which entered in the U.S. market in the 1960s [6] and became extremely popular. In 2007, its use as a frame material represented almost 60% of all residential windows sold [6].

Similarly to aluminum, vinyl is easy to extrude, it is resistant to moisture and requires very low maintenance. On the other hand, it is more susceptible to heat due to a higher thermal expansion coefficient than wood and aluminum, and it requires larger cross sections than aluminum to achieve the same structural strength.

Vinyl thermal performances are similar to wood, with frame U-factors between 2 and 2.8 $W/m^2 \cdot K$ [14], because of a thermal conductivity of about 0.17 $W/m \cdot K$, and filling the hollow cavities of the frame with a more insulating material can further increase its insulating value.

Fiberglass frames

Fiberglass represents a valid alternative to vinyl windows, as they share similar thermal properties with the same possibility to fill the hollow cavities with higher insulating material.

It is stronger and more durable than vinyl, allowing for smaller cross sections, and being composed for about 60% of glass it makes it a more sustainable choice.

Fiberglass has also a smaller thermal expansion coefficient than vinyl, and has a good resistance to rotting and corrosion, making it a low-maintenance material. The higher cost has however been the cause of a small market share for fiberglass windows [6].

Hybrid frames

Today, hybrid frames that use two or more frame materials are starting to become increasingly common. They have already been in the wood frame market with vinyl- and aluminum-clad frames for exterior maintenance reduction, and many vinyl manufacturers now offer interior wood veneers to make an interior wooden finish [30], which is generally more appealing to the customers. Hybrid frame designs will most likely open new ways of combining different materials that will make possible to achieve even higher energy performance and cost-effective window products.

2.5.2 Glazing Technology

The greatest advances towards energy-efficient windows have been related to improvements of the glazing system, and while glass was before the weakest element of a window assembly, it has now become more effective in increasing energy efficiency than the frame itself.

The main technological innovations that are included in current window products are shown in a Fig. 2.20*a*. These can be categorized into three approaches that are generally pursued:

1. Modify the glass chemical composition, as is the case for tinted glass.
2. Apply coatings to the glass surfaces, such as low-e and reflective coatings.
3. Change the glazing unit structure (Fig. 2.20*b*) by adding multiple panes of glass, filling the gaps in between with low-conductance gases and using thermally improved spacers to separate them.

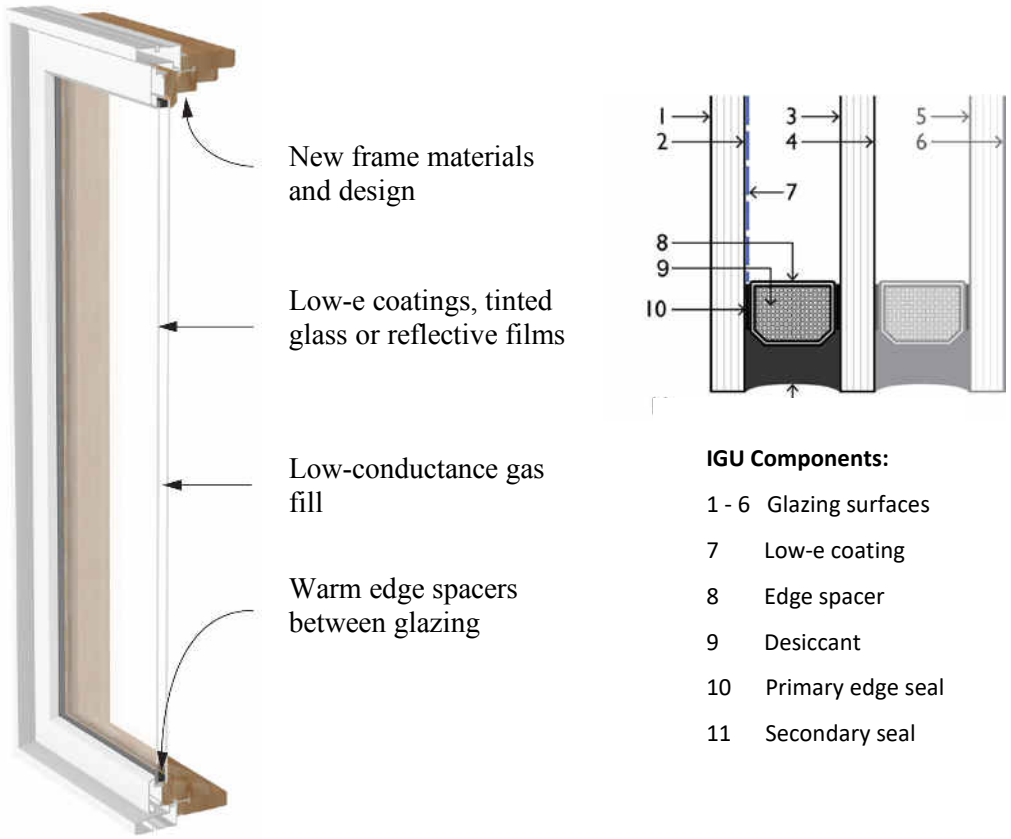

Fig. 2.20: (*a*) Improvements in modern high-performance windows and (*b*) components of an IGU [15], [17].

While the last approach is mainly related to improving window's insulating properties, by reducing the overall U-factor (which is beneficial both for hot and cold climates), the first two directly impact the glass spectral response to solar radiation. They can be used either to reduce heat gain during the summer or to allow more radiation to pass through the window during the cold season and to reduce heat losses at the same time. In Fig. 2.21 are shown the idealized glass transmittances for hot and cold climates. In cooling dominated climates (curve 1) the goal is to maximize visible light, essential for daylight, and minimize the solar NIR radiation, which only contributes to increase heat

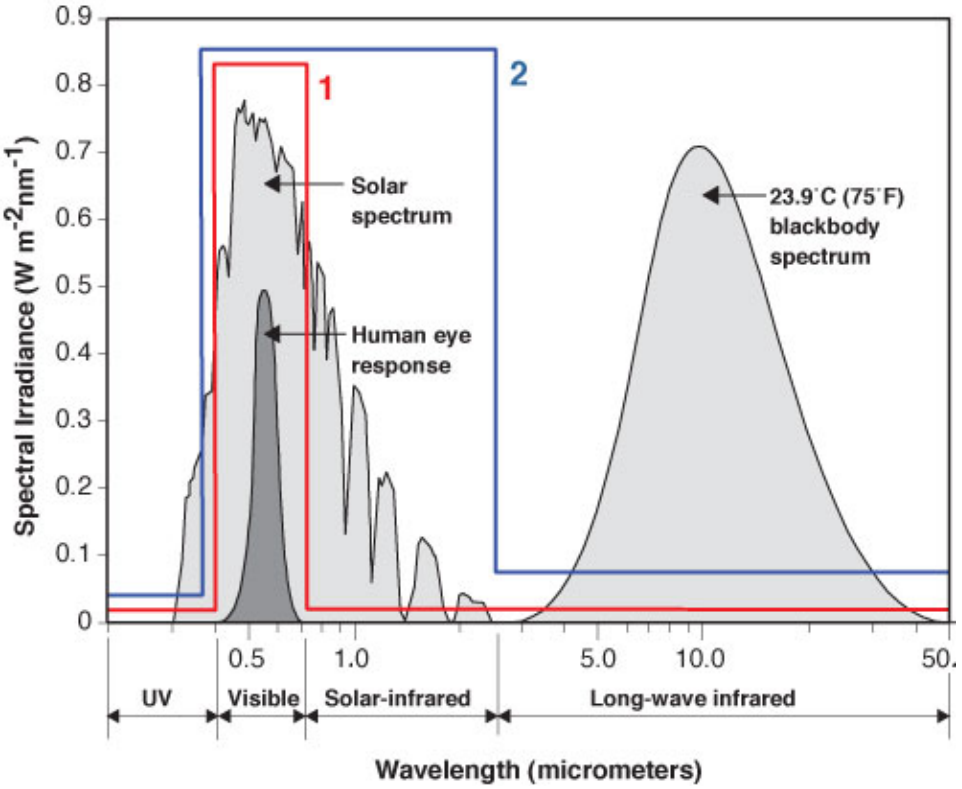

Fig. 2.21: Ideal spectral transmittances of glass for hot (curve 1) and cold (curve 2) climates [16].

gain. In heating dominated climates (curve 2) the whole solar spectrum should be allowed into the building, in order to maximize heat gains and reduce the need for space heating. In the first scenario, solar control can be realized through the use of tinted glass or by applying reflective or low-solar gain low-e coatings to the glass. In the second case, high and moderate-solar gain low-e glazings are generally used as the main spectrally selective option for glass units.

2.5.2.1 Tinted Glass

Tinted glazings are produced with special additives that alter their composition, affecting their radiative properties in such a way that solar absorption for certain

portions of the solar spectrum is maximized. In solar control applications this means that the glass will absorb the solar NIR while admitting visible light through it.

Conventional bronze or gray tints cause a moderate reduction in NIR transmittance, which drops up to 56%, but also a large drop in visible transmittance, as indicated in Fig. 2.22, while more advanced high performance green and blue tints are able to reduce the NIR transmittance to as low as 23%, with less effect on the visible transmittance.

Tinted glazing is also referred to as “heat-absorbing” glass, and since all the absorbed energy (up to 50-60% of the total incident radiation [32]) is transferred by convection and radiation to both sides of the glass, double-pane IGU are generally used, with the

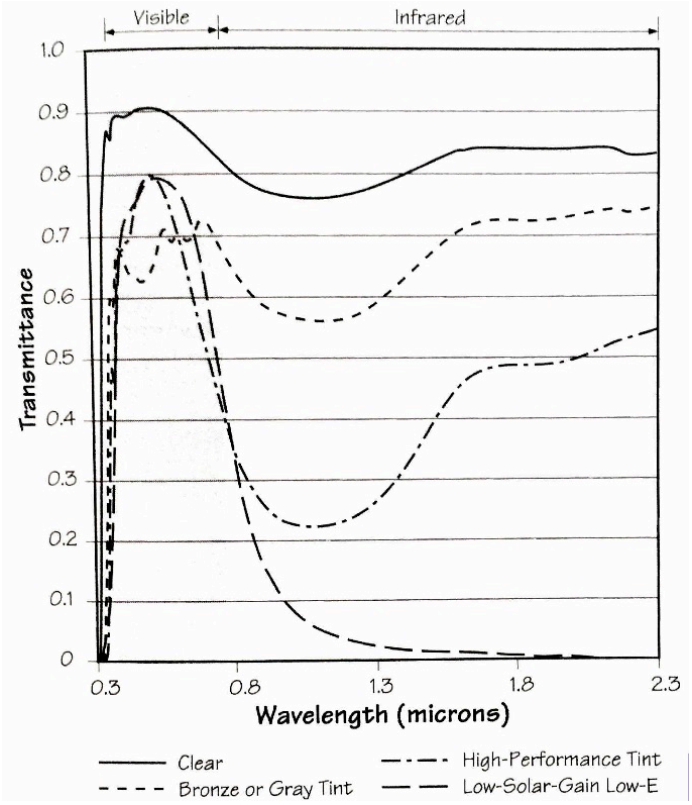

Fig. 2.22: Transmittance curves of tinted and low-e glazings for solar control [6].

tinted glass as the outer layer, in order to prevent the warm glass to transfer the heat inside the building. A low-e coating can also be applied to reduce the far-infrared (FIR) radiation emitted by the exterior glass.

2.5.2.2 Reflective Coatings

Another way to reject the solar NIR radiation is by the application of thin metallic or semiconductive layers with a high reflectance over the NIR band. Up to 70% of the incoming radiation is reflected back to the outside [32], therefore there is no heat gain associated with it as opposed to that originated by the absorbed fraction of the solar spectrum in heat-absorbing glazings.

However, the high solar reflectance is accompanied by a large reduction in visible transmittance, as in the case of tinted glass. They can be used in combination with the latter when the SHGC needs to be reduced beyond the capabilities of tinted glass. Reflective glazings are generally used for commercial buildings in hot climates, where high glazed areas are present or the solar heat gains needs to be substantially reduced.

2.5.2.3 Low-Emissivity (Low-e) Coatings

Among the various innovations in glazing technology, the development of low-e coatings has had the highest impact on improving of windows energy performance. The reason can be explained if we consider two large parallel planes with area $A_1 = A_2 = A$, at different temperatures T_1 and T_2, with emissivities of ε_1 and ε_2, respectively. The net rate of radiation transfer q_{12} between the two planes is given by [22]:

$$q_{12} = \frac{\sigma A\left(T_1^4 - T_2^4\right)}{\frac{1}{\varepsilon_1} + \frac{1}{\varepsilon_2} - 1} = \varepsilon_{eff}\sigma A\left(T_1^4 - T_2^4\right) \tag{14}$$

where ε_{eff} is the effective emissivity

$$\varepsilon_{eff} = \frac{1}{\frac{1}{\varepsilon_1} + \frac{1}{\varepsilon_2} - 1} \tag{15}$$

In the case of uncoated glass, $\varepsilon_1 = \varepsilon_2 = 0.84$, and $\varepsilon_{eff} = 0.72$. If the emissivity of one of the interior surfaces drops to 0.1, then $\varepsilon_{eff} = 0.1$, and the net radiation heat transfer rate would drop by a factor of 7. If both surfaces have the same emissivity of 0.1, the effective emissivity further reduces to 0.05 and q_{12} goes down by a factor of 14.

Therefore, applying low-e coatings to glazing surfaces facing the air gap significantly reduces the FIR radiation emitted by the glass, and this is critical to keep the heat inside the building in cold climates. The addition of a low-e coating has the same effect on the U-factor as adding another glass panel [6].

In terms of coating placement inside the air gap, the U-factor will be the same whether the low-e coating is applied to the #2 or #3 surface (Fig. 2.23*a*) but a different positioning will affect the SHGC. A coating on the #3 surface will minimize the radiative losses from that surface towards the outer glass, and it is therefore more suitable for heating-dominated climates. On the other hand, in cooling climates the coating is better placed on the #2 surface, which will radiate a minor fraction of the absorbed heat from the outside towards the building inside and so the solar heat gain will be reduced.

Since a low emissivity on the infrared spectrum also means high reflectivity, adding a second low-e coating on surface #4 ("4th surface" technology) causes most of the heat emitted by objects inside the building to be reflected back, therefore improving further the insulation value of the window Fig. 2.23*b*. However in this case, since the radiation is reflected back into the room before it can reach and warm the glass, the temperature of the latter will be lower than a similar glass with the low-e coating placed on surface 3, and more attention must be paid to avoid the risk of condensation.

In addition to reducing the winter heat losses, and therefore the window U-factor, low-e coatings can be made of different selectivity over the solar NIR spectrum. In Fig. 2.24 [6] are shown the solar transmittances and the energy properties of three types of low-e coated glazings. A glass with a high-solar-gain low-e has high transmittance over both the visible and the solar NIR wavelengths, making it more suitable to maximize

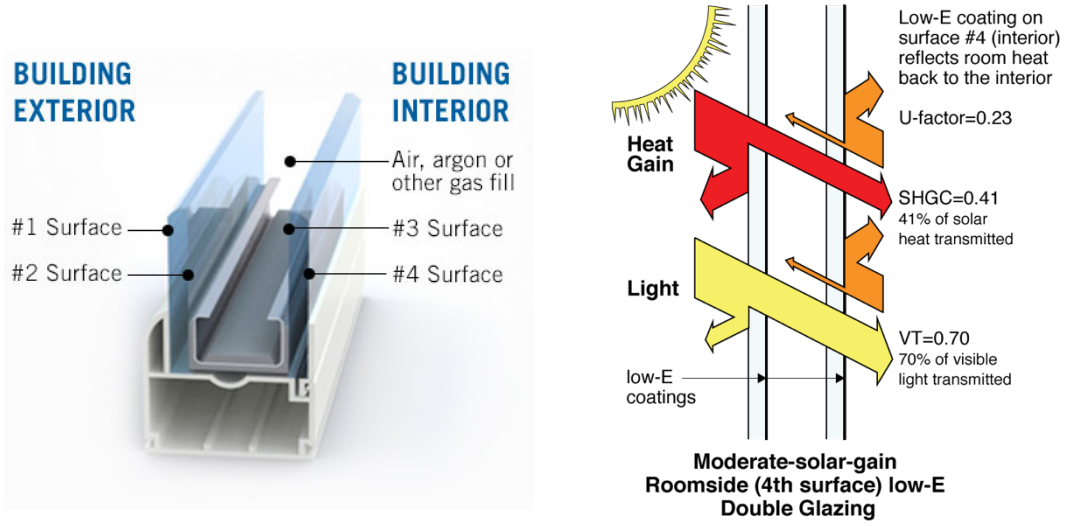

(*a*) (*b*)

Fig. 2.23: (a) Surface labeling for IGUs and (b) example of the effects of low-e coatings applied to both surfaces #2 and #4. The U-factor is expressed in BTU/(hr ft^2 °F) [30], [33].

winter solar gain while reducing heat losses due to the low-emissivity properties. Moderate and low-solar-gain low-e coatings will admit visible light but block solar infrared, thus reducing solar gain. Low-solar-gain glass is particularly suited to reduce summer cooling loads, while in cold climates will have a high insulation value (low U-factor) but it will reduce beneficial passive solar gain at the same time.

Low-e coatings can be manufactured using the sputtering and pyrolytic techniques. A sputtered (or soft) coating process consists of low-temperature vacuum chamber deposition of dielectric or metal (typically silver) layers, a few nanometers thick, on the glass. These coatings have very low emissivity values, from 0.15 to as low as 0.4, but also low solar transmittances (50-72%) [34] and are very fragile, so they must be protected from humidity and contact and can only be placed inside sealed glass units. They are mostly used to produce low-solar-gain low-e glass. A pyrolytic, or hard, coating is a thick metal oxide layer, typically 100-400nm, which is applied to the glass at high temperature (600-700 °C) by chemical vapor deposition (CVD), resulting in a strong covalent bond between the oxide and the glass surface. These types of coatings are therefore very durable and can be exposed to air, humidity and normal wear. They have emissivity values in the range of 0.15 – 0.4, as well as high solar transmittances, and are used for high-solar-gain low-e glass.

2.5.2.4 Multiple Panes

As already mentioned, adding multiple glass layers will increase the insulating value

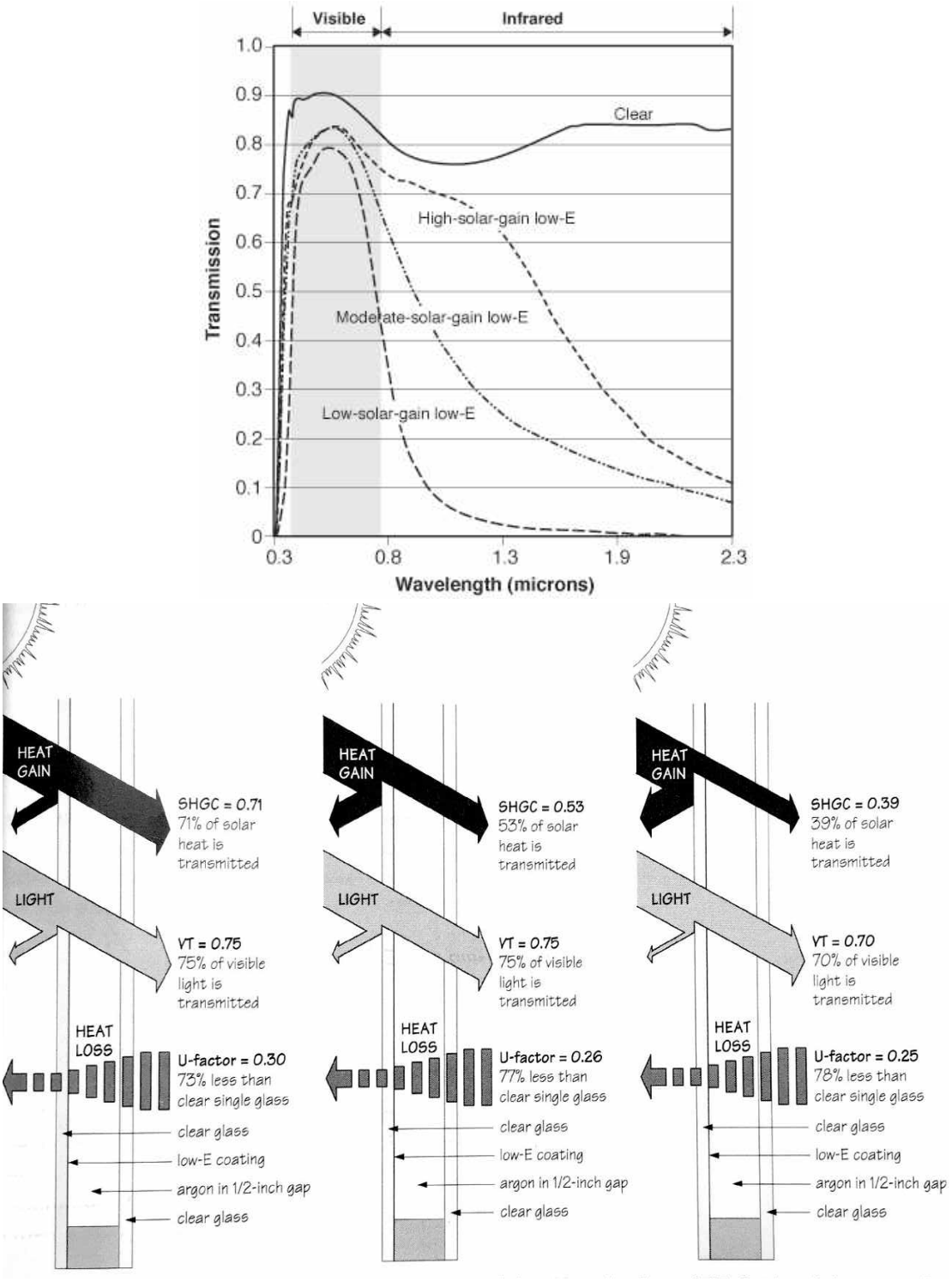

(*a*) (*b*) (*c*)

Fig. 2.24: (Top) spectral transmittances of various low-e glazings and (bottom) center-of-glass properties for double glazings with (a) high-solar gain low-e, (b) moderate-solar-gain low-e and (c) low-solar-gain low-e coatings. The U-factors are expressed in BTU/(hr ft^2 °F).

of the glazing system. Since the thermal resistance of glass is negligible, the increased thermal resistance is provided by the generated air layers between each couple of panes. On the other hand, each additional glass layer will also reduce visible light transmission and the SHGC, while adding more weight to the whole window assembly, and there are therefore practical and economic limits to the number of panes that can be added. Nevertheless, triple and quadruple glass units are commercially available, and are used when very low heat loss rates are required.

2.5.2.5 Low Conductance Gas Fills and Gap Width

With the use of low-e coatings, heat transfer through the IGU is mainly dominated by conduction and natural convection. These can be reduced by replacing the air with other inert, nontoxic and heavier (greater molecular mass) gases, such as argon and krypton, having lower thermal conductivity (Table 2.1). Argon and krypton have about two-thirds and one-third of the thermal conductivity of air, respectively, so the conduction losses within the gas-fill will be significantly reduced.

Another factor that impacts heat conduction in the gap of an IGU is the distance between the two glasses. By increasing the gap width, the thermal resistance to molecular heat conduction, equal to the ratio of the gap width to the gas thermal conductivity, will increase [34]. However, increasing the glass spacing beyond a critical point will initiate convective motions in the gap and the heat transfer coefficient will increase. This can be seen in Fig. 2.25, where the U-factors for both double- and triple-pane windows are represented as a function of the gap width, gas-fill type and

Table 2.1: Properties of different gases used in windows gaps. The optimal gap thickness is given for inside to outside temperature difference of 20K [34].

Gas	Molecular mass (g/mol)	Thermal conductivity (W/m·K)	Optimal gap width (mm)
Air	28.96	0.0250	20
Argon	39.95	0.0161	16
Krypton	83.8	0.0096	12

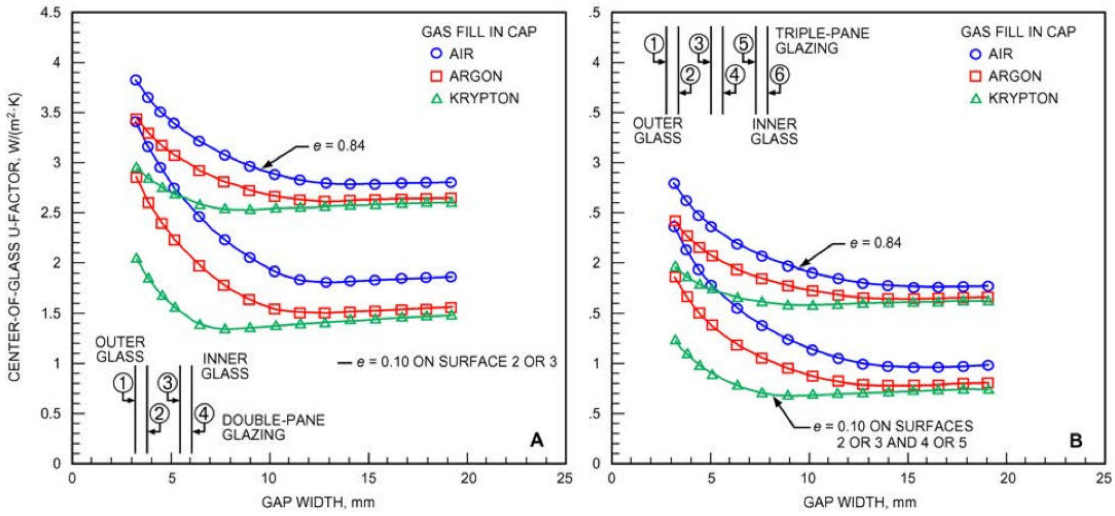

Fig. 2.25: Center-of-glass U-factors for double- and triple-glazings with different gas fills and emissivity, as a function of gap width [35].

low-e coatings. In the case of uncoated double-glazing with air filling the U-factor drops until a gap width of around 13 mm, after which it remains nearly constant as the increase in the heat transfer coefficient (caused by the rise of convection currents) offsets the benefits provided by the thicker air gap.

Convective currents are triggered by a large temperature difference between the inside and outside glasses and by large differences in the gas density, which increase with the gas molecular mass. As a result, the optimal gap spacing will be narrower for higher temperature differences and for heavier gases [13]. The latter represents an added

advantage of using argon- or krypton-filled windows, as to avoid convection their optimal gap thickness needs to be smaller than air-filled windows, and therefore the windows will be thinner and lighter, due to the reduced frame thickness. This is especially beneficial for tripe-glazed windows, allowing them to be fitted into framing systems conventionally used for double pane windows.

Manufacturers are able to achieve around 90-95% gas fill concentration, with less than 0.5% leakage per year with proper sealing, or 10% gas losses after 20 years, which results in only a few percent drop in U-value [6].

2.5.2.6 Warm Edge Spacers

Each pair of glasses in IGUs is kept apart at appropriate distance from spacer strips that run along the whole glass perimeter. In addition to separating the two panes of glass, the spacer system serves to mitigate the stress caused by thermal expansion and pressure differences, to seal the edges of the IGU and keep any low-conductance gas from being lost, as well as to provide a barrier against moisture and condensation. However, spacers also act as “thermal bridges” by short-circuiting the glasses, which can increase the window U-factor considerably, and they are therefore subject to continuous study to improve their performance [36].

Since the 1980s, spacer bars have traditionally been made of aluminum, and its high conductivity reduced the benefits of other improved window components. A high conductive spacer also means that under winter conditions the glass edges (left in Fig. 2.26) will be colder than the center-of-glass region, with a resulting increase of the risk

of condensation. The plots on the right of Fig. 2.26 show a temperature comparison between two double-glazed windows, one with uncoated glazing and aluminum spacer, and the other with a low-e coating and an insulated spacer. It can be noticed that the addition of a low-e coating increases the temperatures of all regions of the glass, and that the insulated spacer further contributes to increase the temperatures at the edges. The risk of condensation is substantially reduced, although it is not completely eliminated, and it can still occur around the bottom edge of the glass at low outdoor temperatures and high interior humidity levels.

Conventional aluminum spacers contain a desiccant to absorb residual moisture and can be of single-seal or double-seal design, both using butyl as primary sealant. In single-seal systems (Fig. 2.27*a*) the sealant is applied to the bottom of the metal spacer, providing moisture barrier and keeping the glass together, but it is not enough to prevent gas losses. These are instead significantly reduced in double-seal spacers (Fig.

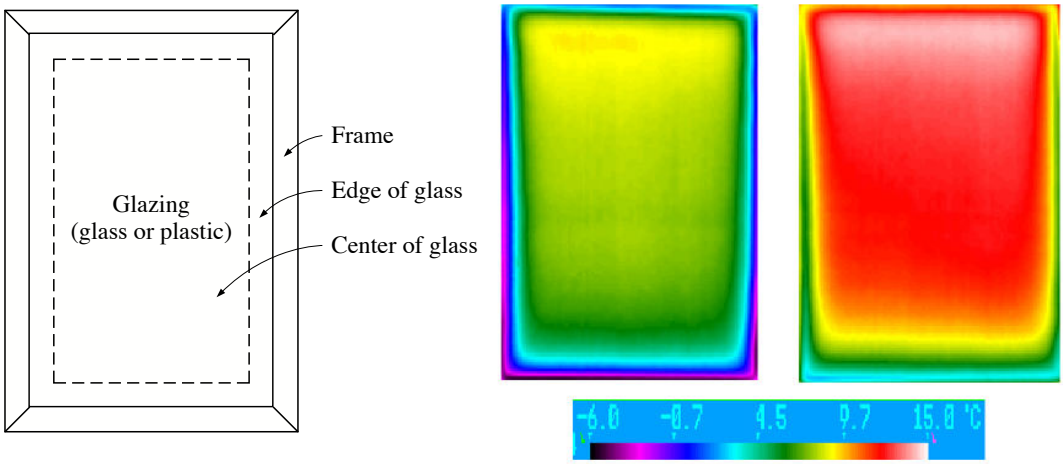

Fig. 2.26: Schematic representation of center-of-glass and edge-of-glass regions (left) and thermogram comparison between double-glazed clear window with aluminum spacer (middle) and double-glazed window with a low-e coating and insulated spacer (right) [15], [18].

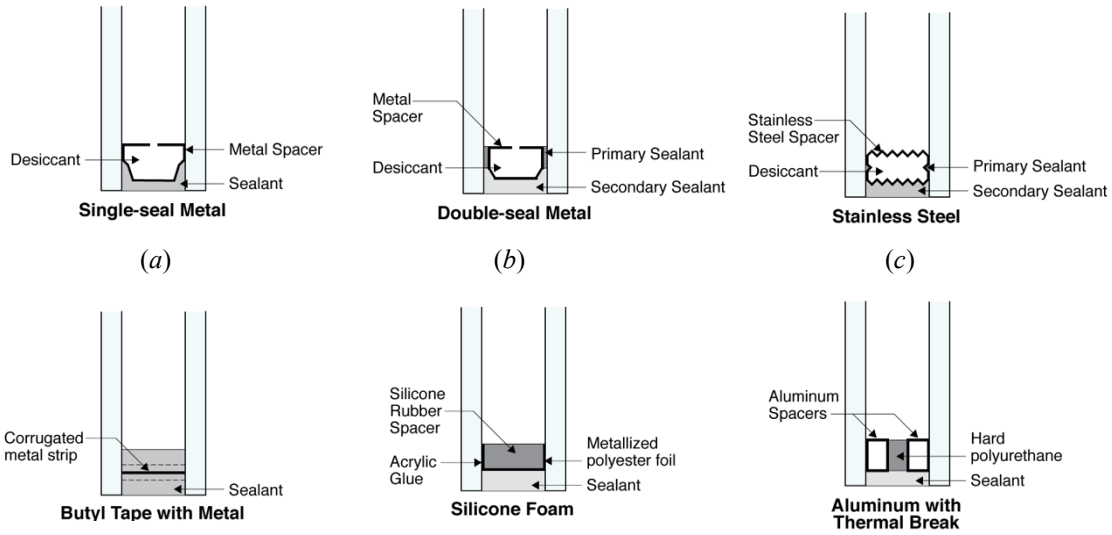

Fig. 2.27: Different types of metal and non-metal spacer systems [30].

2.27*b*), where a primary sealant prevents moisture and gas losses while a second sealant at the bottom, typically silicone, grants structural support.

Innovative spacer systems that perform better than conventional aluminum spacers are generally referred to as "warm-edge" spacers, and different approaches aimed to increase their thermal resistance are performed. These include using a less conducting metal, such as stainless steel, and altering the spacer cross-section (Fig. 2.27*c*), using a single element that incorporates sealant, desiccant and a higher insulating material (Fig. 2.27*d* and Fig. 2.27*e*), or interrupting the path for heat conduction by thermal breaks in metal spacers (Fig. 2.27*f*).

2.6 Ventilated Double-Skin Façades and Air-Flow Windows

Ventilation can contribute to improving the energy performance of the building's thermal envelope, as in the case of ventilated double-skin facades. These consist of an outer glazed (usually single or double) façade and an inner façade, which can also be single-, double- or triple-glazed or opaque [34]. An air space separates the two skins and fixed or operable openings are realized through both façades to allow for ventilation, which can either be forced or generated by exterior wind pressure or natural convection. Shading devices (generally motorized louvers) can be placed inside the air cavity, which will partially absorb and reflect solar radiation (Fig. 2.28). The absorbed radiation is then transferred to the air, contributing to the generation of the airflow by natural convection.

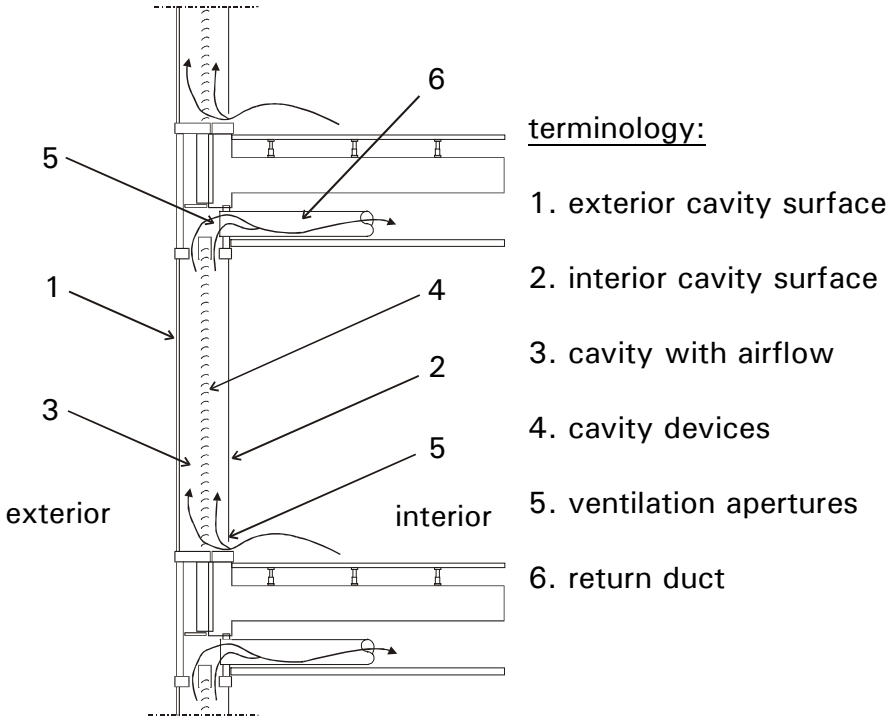

Fig. 2.28: Schematic of mechanically ventilated multiple-skin facades [38].

The heat generated between the two façades can be removed by venting the rising airflow to the outside during the summer, in which case the combined effect of direct reflection by the louvers and natural convection has the primary benefit of reducing the cooling load [37]. During winter, the heated air within the channel is directed to the inside of the building and contributes to preheat ventilation air and reduce heating requirements.

2.6.1 Airflow Windows

If ventilation is realized within two glass panes of a window, this will function like a smaller scale double-skin façade, where both the interior and the exterior layers are transparent. A ventilated, or "airflow window", consists of a pair of spaced glazings (either of which can be single- or double-glazed) where the air channel between the glass panes is connected to the inside or outside of the building through gaps at the bottom and at the top of the window [39]. A shading device, generally a venetian or roller blind, is placed between the inner and outer glasses and acts as a thermal absorber of solar radiation, collecting the heat and transferring it to the air flowing within the cavity, which warms up and rises to the top.

Airflow windows can be considered as a building-integrated version of solar air collectors, generating hot air while still providing view, daylight, shading and glare control like a traditional window with shades. The hot air generated can be used in a variety of ways, aimed to reduce energy consumptions: it can be ventilated directly into the building and used for space heating, as well as circulated outside during the summer

season to reduce cooling needs; or it can be transferred to a fluid circuit and used for radiant heating or to preheat domestic hot water; it can also be used to preheat fresh air which is further used by the building ventilation system.

Four operational modes exist for airflow windows, which depend on the flow configuration (Fig. 2.29. In the supply-air mode outside air is drawn through the window cavity and transferred into the building, thus providing fresh air and contributing to the building ventilation requirements. This mode is particularly suited for winter application, since the air passing through the window glazing, in addition to absorbing the heat from the glass, will also absorb part of the building heat that would otherwise be lost through the window, in a phenomenon known as dynamic insulation [34]. In the exhaust mode, inside air is circulated through the cavity to the outside, thus removing the heat accumulated between the glazings and rejecting it to the environment. This is best used for summer cooling to reduce building's cooling load.

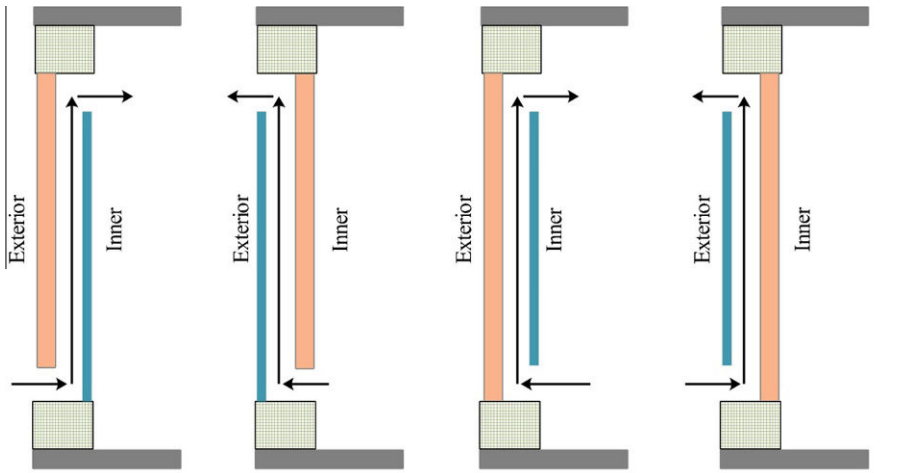

Fig. 2.29: Modes of airflow windows operation [40].

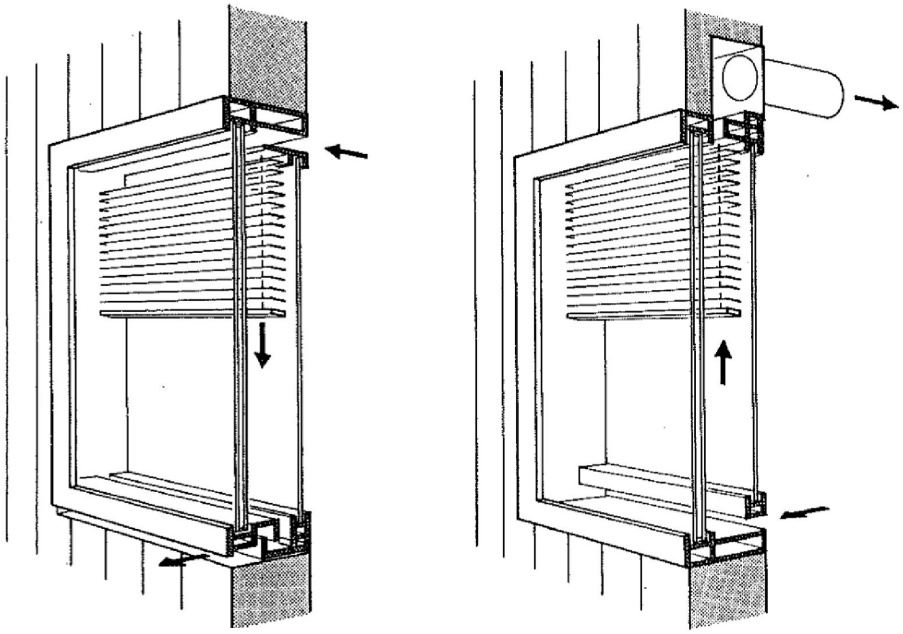

Fig. 2.30: Example of an indoor circulation airflow window [42]

The indoor circulation mode uses solar radiation to heat indoor air, which is circulated from the room up through the cavity and exhausted inside, therefore contributing to winter heating.

A schematic of the exhaust and indoor circulation window types is shown in Fig. 2.30. Lastly, another option for summer cooling is using solar radiation to produce a buoyancy effect inside the cavity, so that outside air is drawn through the window and exhausted outside and the accumulated heat is removed. In all four modes, venetian blinds placed between the glazings provide a better solar absorption than the glasses, and in naturally ventilated airflow windows they produce a larger buoyancy effect, thus increasing the airflow rate [40].

Airflow windows were originally used in Scandinavia in the 1950s, mainly for non-residential buildings [41]. The first related patent was filed in 1956 in Sweden and in

1967 the Finnish company EKONO built the first airflow window system for an office building in Helsinki [42][43].

Both air-supply and exhaust-air windows were developed and implemented in France, Switzerland and the Netherlands in the 1970s [44], and in the United States the first office building using airflow windows was built in 1973 in Pittsburgh, Pennsylvania [42].

2.6.2 Advantages of Airflow Windows over Regular Windows

Airflow windows show several advantages compared to conventional high-quality windows. The main effect of the presence of an airflow in the cavity is the added thermal insulation (dynamic insulation), which enables the air to recover part of the heat absorbed by the glass that in a similar window without airflow would be transferred and lost to the outside. This results in lower conductive losses of the window assembly, and studies have shown that the effective U-value of airflow windows can be reduced by 30 – 40%, compared to unventilated windows [45] [46], and it is strongly influenced by the air flow rate, as shown in Fig. 2.31. Haddad and Elmahdy [47] compared the thermal performance of a triple-pane supply-air window with a conventional triple glazed window. They reported a maximum reduction in conductive heat losses of 31% during the coldest month, when conductive losses are highest, corresponding to a decrease in U-values from 1.88 $W/m^2 \cdot K$ to 1.3 $W/m^2 \cdot K$ for the triple-glazed and airflow window, respectively.

A combined effect of the heat recovery by the airflow and the reduced U-value is that airflow windows also contribute to an increase in the net heat gain, which is the sum of the contribution of the solar radiation and the conductive losses or gains. Haddad and Elmahdy calculated an increase up to 56% with respect to a conventional triple-glazed window [47], with highest values during the coldest months (December and January), while Brandle and Boehm reported an annual improvement of using airflow windows over conventional windows of about 60% for heating and 55% for cooling loads [42]. An added benefit of using an airflow window in the supply mode is the opportunity to provide fresh air and improve indoor air quality (IAQ) [47]. Nowadays the construction of the building envelope tends to be increasingly tighter to limit infiltration losses and save energy, but this is often realized at the expense of IAQ. While commercial buildings rely on HVAC systems to meet ventilation requirements, the issue of the reduced IAQ due to the increased sealing particularly affects residential buildings, where air systems use 100% recirculated air and the only source of ventilation is through infiltrations [48].

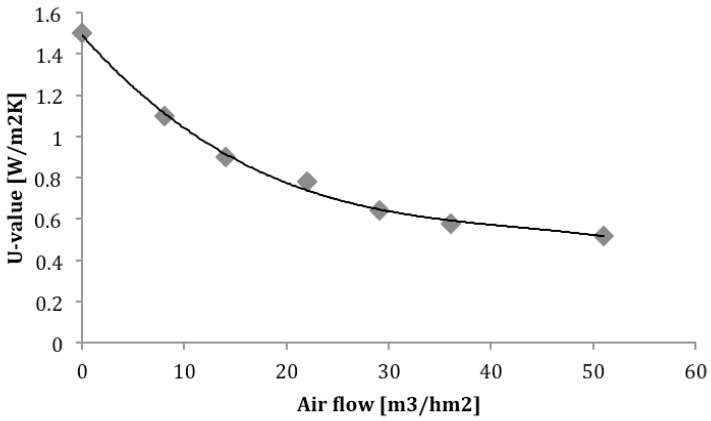

Fig. 2.31: Variation of effective U-vale of an exhaust air window for different airflow rates

Other advantages are those related to thermal comfort. During the cold season, the temperature of the inside glass surfaces of a fenestration system tend to be substantially lower than room air temperature. This temperature difference generates cold draft in the proximity of the window, and the lower glass temperature increases radiant losses from inside objects and people to the window, so both aspects are cause of thermal discomfort. Airflow windows in both exhaust and circulation modes have the advantage of providing an inner glass temperature that is closer to room air temperature, therefore increasing thermal comfort. Moreover, since most of the energy absorbed by the blinds is transferred to the airflow, an airflow window with blinds placed inside the air cavity reduce the amount of energy they reradiate and that is absorbed by the room [42].

2.7 Solar PV and Thermal Collectors

As it will be illustrated in the next chapter, the subject of this thesis involves the conversion of solar radiation into thermal and electrical energy, and the concept can be seen as a further development of PV and flat-plate solar thermal technologies, coupled with that of airflow windows. Therefore, this section will provide a brief overview of the different types of solar energy collectors.

2.7.1 Crystalline Silicon Solar Cells and Modules

Being the core element of a PV module, a solar cell directly converts solar radiation into electricity through the photovoltaic effect. When the device is struck by photons having a higher energy than the energy gap (E_g) of the semiconductor material the solar

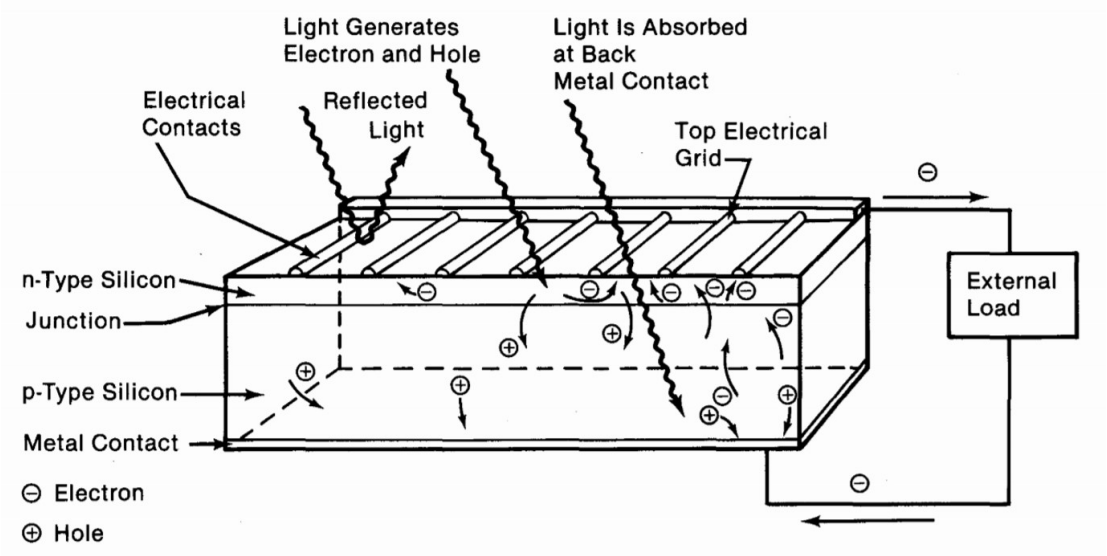

Fig. 2.32: Single junction solar cell operating principle [49].

cell is made of, electrons will transit from the valence band to the conduction band, and electron-hole couples are generated.

In a single-junction crystalline Silicon (c-Si) cell, two Silicon layers, one positively and the other negatively doped, are put in contact to form a p-n junction, and an electric field is generated, which acts like a potential barrier between the two layers, opposing the further flow of electrons and holes through the junction. The photogenerated electron-hole pairs are therefore separated across the p-n junction, and by adding metal contacts, both on the top n-type and the bottom p-type layers, and connecting them through an external circuit they can travel and recombine (Fig. 2.32), powering any connected load.

Today, the highest recorded c-Si solar cell efficiency is around 26.7% [50], while the theoretical limit for a single p-n junction solar cell, also known as Shockley-Queisser limit, was calculated to be 33.77% [51]. The main causes of energy losses are those

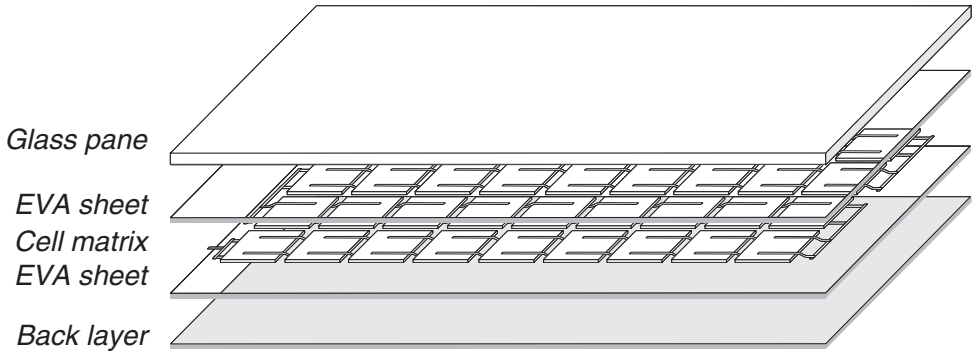

Fig. 2.33: Layers in a c-Si PV module [53].

related to the non-absorption of photons with energy level below E_g, the thermalization of carriers excited by photons with energy above E_g (process that generates heat), the casual recombination of the electron-hole pairs, and other minor losses such as optical and shading losses and internal cell resistance [52].

Traditional c-Si PV modules are built by interconnecting several solar cells with metal strips (Fig. 2.33), and laminating the cell array between two layers of encapsulant material, generally EVA, serving as a protection against mechanical stress, weathering and humidity, as well as providing electrical insulation and optical coupling between the cells and the front cover [54]. The lamination is usually done with a glass superstrate and a backfoil substrate (typically tedlar-based), the former providing structural strength and protection from weathering, and the latter acting as a barrier against humidity. The assembly is then hold together by an aluminum frame, which gives further mechanical support.

The efficiency of PV modules is slightly lower than the efficiency of a single cell, due to optical losses through the glass and the encapsulant, as well as resistive

interconnection losses and mismatch losses, the latter deriving from inhomogeneities occurred during manufacturing, for which the cells will have some differences in their current-voltage (I-V) characteristics.

Today, the best performing monocrystalline modules commercially available are produced by Sunpower and have an efficiency of 22.7% [55]. The module performance is then influenced during operation by the solar irradiance level and by the cell operating temperature (Fig. 2.35). The short circuit current is directly proportional to the irradiance, and therefore decreases with decreasing irradiance, whereas the open circuit voltage decreases only slightly.

The increase of the operating temperature leads instead to a minimal increase in the short circuit current, which is outweighed by the decrease in the open circuit voltage.

In addition to the solar panels, which are the core elements of a PV system, other components, often called Balance of System (BOS), are needed. PV systems can be divided into stand-alone and grid-connected systems (Fig. 2.34).

In stand-alone systems, the continuous operation during night or on cloudy days is provided by energy storage units, usually batteries, and a charge controller is placed between the PV array and the battery stack. This regulates the power flowing between the array, the batteries and the load, and ensures that the batteries are protected from overcharge (by disconnecting the PV array) and overdischarge (by disconnecting the batteries). Modern charge controllers have integrated maximum power point tracker (MPPT) functions to guarantee both a PV operation at MPP and a regulated voltage at

the battery level [57]. AC loads can also be connected to the charge controller, in which case an inverter for DC-AC conversion is used.

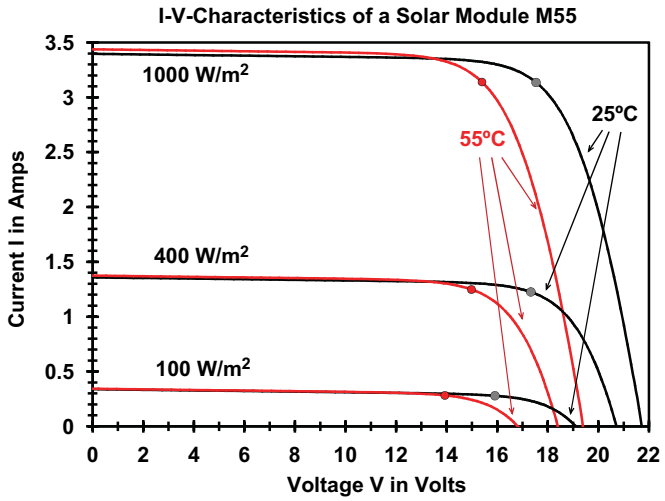

Fig. 2.35: I-V characteristics for different irradiation levels and operating temperatures for a mc-Si module.[56].

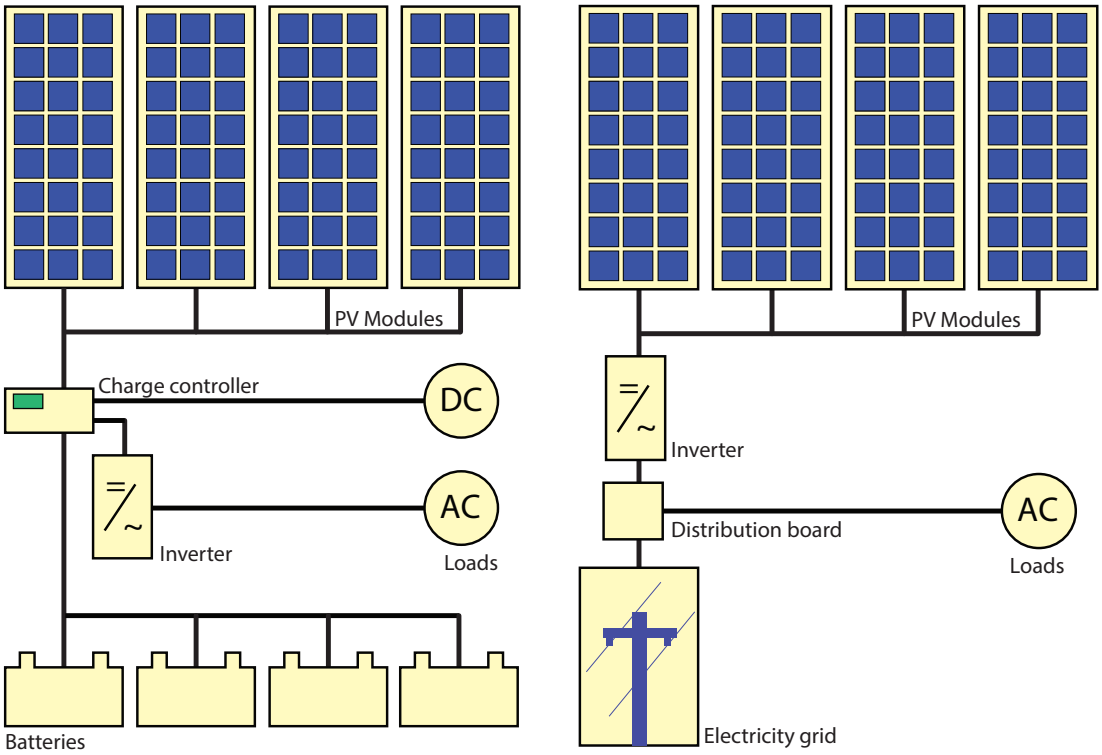

Fig. 2.34: Components of a stand-alone (left) and a grid-connected (right) PV system [57].

In grid-connected systems, the power from the PV array is converted into AC power by the power electronic system, which it is then fed into the grid. In PV systems for building applications, the building electrical distribution board interposes between the inverter and the grid, and connects them to the building AC load, so that PV power is fed to the grid in case of PV overgeneration, while the load is supplied by the grid when a compensation for insufficient PV power is needed.

2.7.2 Flat-Plate Solar Thermal Collectors

Solar thermal collectors can be classified into three main categories [58]: flat-plate collectors, consisting of a single encasement rectangular box, evacuated tube collectors, made of parallel glass tubes with vacuum created inside each tube, and concentrating collectors, which are of various shapes and configurations (such as compound parabolic connectors, parabolic trough, linear Fresnel and central tower receiver), and work by reflecting and concentrating the solar radiation to a focal point. Among the different types of collectors, the flat-plate one is the most widely used, as well as the most established and mature technology, especially with regard to domestic hot water heating and space heating applications.

Despite the use of different technologies, flat-plate collectors all share the same working principle, which is the conversion of solar radiation into thermal energy, or heat. This conversion is realized by the absorption of sunlight by a surface, called the absorber, that is in thermal contact with the working fluid (water or air) to which the heat is then transferred and carried out of the collector to be used or stored. The

absorber is generally a black-painted surface, to increase absorptivity and the fraction of solar radiation converted into heat. The use of spectrally selective materials would further increase the absorption by capturing more radiation in the solar wavelengths range (visible and near-infrared) while limiting the radiation reemitted from the absorber in the long-wave infrared range, that would otherwise be lost.

2.7.2.1 Liquid-based Collectors

Liquid-based flat plate solar collectors consist of a selective absorber plate, generally made of copper or aluminum, a parallel or serpentine tube structure where the heat-transfer fluid flows, a cover (glass or plastic) to reduce convective losses to the environment, a thermal-insulating material on the bottom and sides of the collector to limit conduction losses, and a sheet metal-case [59]. A schematic representation of a typical collector's cross-section is shown in Fig. 2.36. As the solar radiation reaches the absorber, it is converted into heat, which is then transferred through the pipes to the fluid, resulting in a temperature increase of the latter. The most commonly used liquid is water, which is mixed with glycol for applications in cold climates where the temperatures are likely to drop below freezing conditions.

Liquid flat-plate collectors are a simple and reliable technology, which is readily available, have no moving parts and are easy to install. Although they have a good cost-to-performance ratio, they are limited in temperature levels below 100 °C, as the efficiency drops significantly at higher temperatures due to increased heat losses.

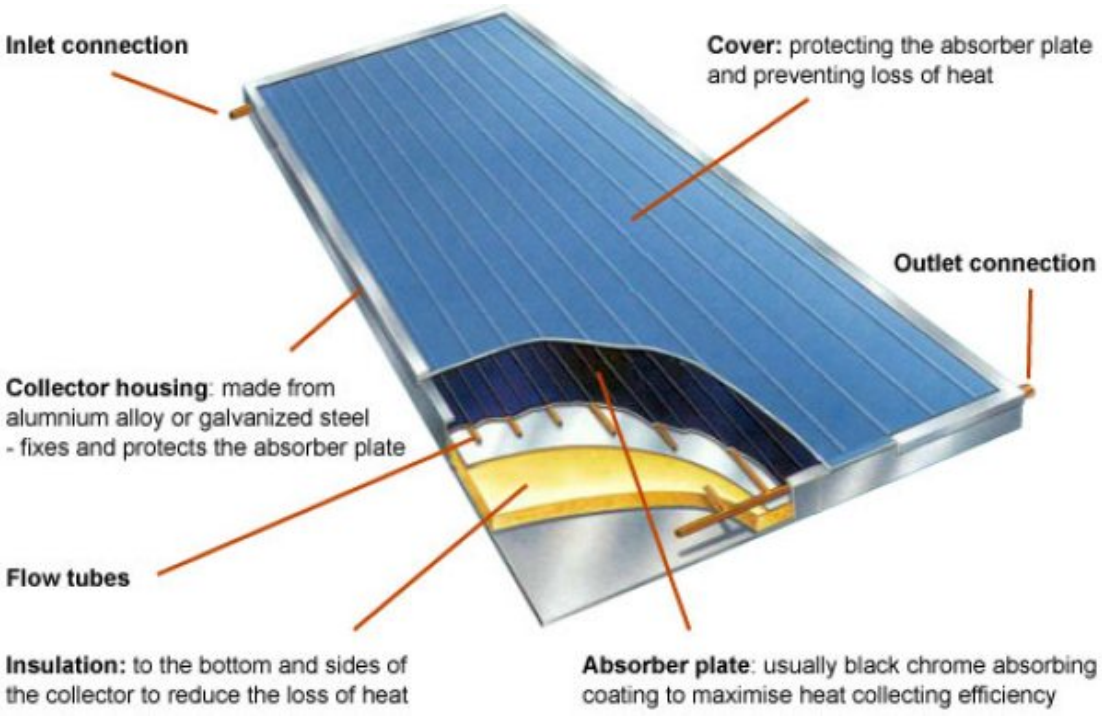

Fig. 2.36: Solar water collector [60].

Typical temperature range is 40 - 80 °C for regular collectors [61], which makes them well suited for domestic hot water generation applications.

2.7.2.2 Air-based Collectors

Solar air collectors have a similar construction to that of liquid flat plate collectors, but they use air as the heat transfer fluid instead of water. They can be classified depending on the different path the air enters in contact with the absorber (Fig. 2.37). The flow can be above the absorber, that is located down on the back insulation, and although it is the simplest design it is also the least efficient, since the air directly transfers the heat to the glass cover, and therefore the convective losses are higher.

This can be overcome by having the air flowing under the absorber, which can be manufactured with fins to increase the heat transfer area. Having the flow on both the top and the bottom side of the absorber further enhances the heat transfer from the absorber to the air [63], even if this would reintroduce thermal losses through the glass cover. A more recent design uses an absorber made of a porous plate, through which the air flows, and it represents the configuration with the highest heat transfer rate, but the downside is a higher pressure drop across the collector, which requires more power for the fans circulating the air. [62]. A schematic of a typical commercial air collector, with the absorber made of individual air channels, is shown in Fig. 2.38.

There are several advantages and disadvantages in using air as heat-transfer fluid instead of water [64]. Air collectors have generally a simpler construction, due to the fact that there are no water-leakage problems and no freezing or boiling problems, therefore no protection is necessary. Air is also non-corrosive, and that implies less maintenance and an increased collector life, as well as the possibility to safely feed the air directly into a heated room, in which case the air collector can also be integrated

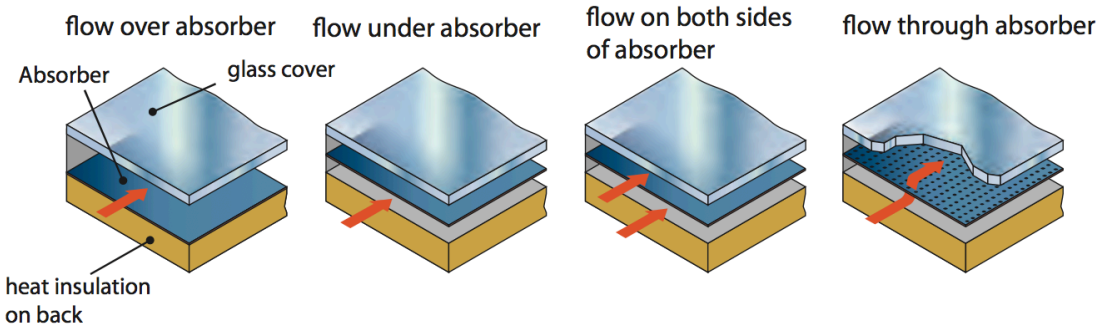

Fig. 2.37: Different airflow patterns in solar air collectors [62].

with the building ventilation system as a means of supplying fresh heated air from the outside.

On the other hand, air systems require larger ducts than water piping to be installed in a building, as well as more electricity consumption by fans or blowers for ventilation due to higher pressure drops. Furthermore, the poorer thermal properties involve lower collector efficiencies in comparison to water collectors, and also make the transfer of heat to another fluid, such as water for domestic hot water generation, more difficult and requiring larger exchanger surfaces [65].

2.7.2.3 Hybrid PV/T Collectors

A fairly recent development in solar energy technology is represented by a hybrid between photovoltaic modules and solar thermal collectors, in what are referred to as

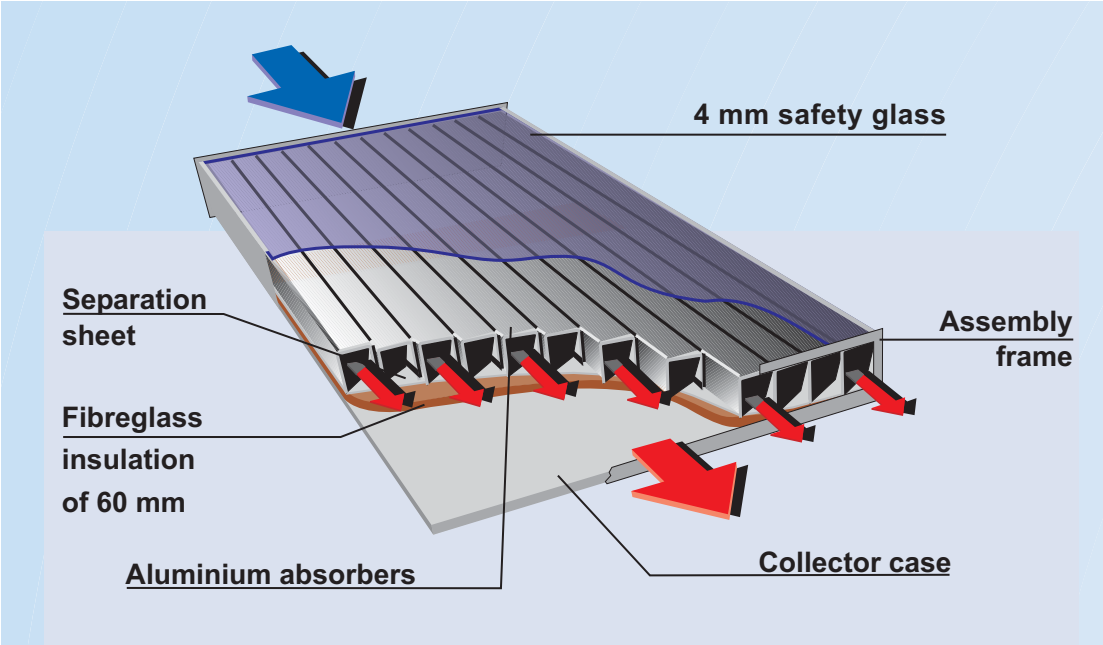

Fig. 2.38: Schematics of a solar air collector (Source: Grammer Solar GmbH, Germany).

photovoltaic-thermal solar collectors (PV/T) [66]. Here a photovoltaic (PV) module is embedded into a thermal collector, forming a single cogeneration unit for both electrical and thermal conversion.

Commercially available c-Si PV modules operate at efficiencies in the 12-20% range. Of the remaining portion of the non-converted solar radiation, a small fraction (5-10%) is reflected by the glass cover, while the rest (70-80%) is converted into heat, which constitutes the major energy output of a PV module. The heat generated contributes to raise the cell temperature by up to 50°C above the ambient [67], resulting in a decrease of PV conversion efficiency as the temperature deviates from the standard operating temperature of 25°C [68]. Removing the excess heat by circulating a fluid behind the panel and putting it to use has therefore two main effects: it cools the PV module, allowing it to operate at lower temperatures (and thus more efficiently), and it adds a thermal generation component [69]. When compared to a separate PV module and stand-alone thermal collector, a hybrid PV/T collector generates more energy per unit surface [70], due to the fact that the PV and thermal components share the same support, therefore the same energy (electrical + thermal) could be produced with less surface area, which implies some cost savings. This type of collector is then well-suited for applications requiring both electricity and heat, and where the available space for collectors' installation is limited.

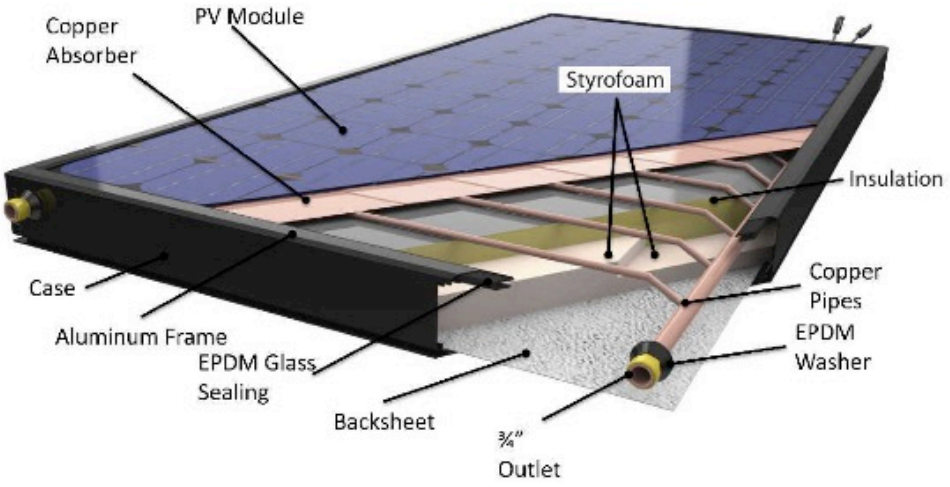

Fig. 2.39: Hybrid PV/T solar collector (source: Solimpeks).

The PV/T electrical efficiency can either be higher or lower with respect to a regular PV module, and this depends on the impact that additional glass layers have on the electrical generation (caused by additional absorption and reflection effects) as well as on the capacity that both the glazing and the heat transfer fluid (by providing insulation and heat removal, respectively) have to prevent the module temperature from rising [34]. The thermal efficiency is instead always lower than in the case of a regular thermal collector, and this is due to the non-optimal solar absorption coefficient of PV modules and to the fact that a part of the solar radiation is used to generate electricity.

Hybrid PV/T collectors can use water or air as the heat-transfer fluid, and have a similar construction to that of flat plate modules, with the difference that PV cells are directly pasted onto the absorber or a PV module can constitute the absorber itself [71]. For a water-based collector, copper pipes are generally placed below the absorber (Fig. 2.39), while in an air-based collector the absorber can be placed in the airflow in the same

way as previously discussed in Section 2.7.2.2, with an additional possibility to place the PV module in place of the outer glass cover.

2.8 BIPV and BIPV/T Systems

2.8.1 Market

The efforts that nowadays many countries are putting in trying to reduce buildings energy consumptions are raising a growing interest in new integrated energy generation technologies such as building-integrated photovoltaic (BIPV) and building-integrated photovoltaic/thermal systems (BIPV/T) [72]. The advantage of integrated systems is that they replace parts of the building envelope, such as roofs and façades, performing the same structural, architectural and aesthetic functions but integrating these with the generation of electricity, heat, or both.

BIPV technology is already a reality, with many companies selling PV integrated solutions for both the residential and commercial markets.

Schüco International KG (Germany) and Romag (UK) manufacture glass-glass PV modules for ventilated and unventilated façades, roofs, balconies, carports and solar shading applications [73],[74]. In the U.S., both Tesla and Dow Chemical Company are expected to begin volume production of PV shingles systems shortly, which would open a competitive solar tiles market in the U.S [75]. Onyx Solar (Spain) is one of the largest manufacturers of both c-Si and a-Si PV glass [76], while Soliculture (US) produces light-tuning PV glass for plant growth applications in greenhouses [77]. In 2016 Pilkington and Solaria Corporation partnered to produce a highly transparent PV

glass laminate with thin monocrystalline Si PV strips integrated [78], resulting in the Pilkington Sunplus™ BIPV product, which holds an efficiency of 8.8% and a visible light transmittance of 44% [79].

Although that of BIPV is now becoming a well-established and growing market, it does not seem to be the case for BIPV/T. While both the PV and the solar thermal sectors are currently seeing continuous growth, when it comes to the combined PV/T technology, the market is very small [80], and it is even more limited for building-integrated PV/T systems.

The Canadian company Conserval Engineering specializes in transpired solar air collectors (SolarWall®) for building facades, and also offers PV/T air system solutions for façade and rooftop integration, with many installations worldwide [80],[81]. In 2007, the company's first BIPV/T façade was developed and installed at Concordia University in Montreal, with a 25kW electrical and 75kW thermal power capacity. SolarWall PV/T generates up to 10% more energy than a same-size conventional PV module [82].

Other smaller companies are currently offering building-integrated PV/T products. DualSun (France) and Solator GmbH (Austria) produce roof-integrated PV/T modules and have several installations in central Europe [83][84]. Aesthetic Green Power, Inc, a small BIPV company in New York State producing PV roofing systems, BIPV canopy and façade solutions, also commercializes PV roof tiles with thermal recovery for domestic hot water heating [85]. An emerging Australian company, Tractile, is also

expanding the solar roof market by offering PV tiles with integrated hot water generation [86].

Despite these are good examples of BIPV/T commercialization, the market is still at its early stage, and much more effort needs to be made both on the research side and at the commercial level to make BIPV/T a competitive and accepted technology.

2.8.2 Literature Review

BIPV/T systems are a more recent development of the photovoltaic/thermal (PV/T) technology, whose research dates back to the 1970s [87], when combined PV/T collectors started to be studied and tested [66],[88][89]. The idea of solar cogeneration of electricity and heat with a single collector is related to the fact that PV modules have a large heat generation (up to 80%) component, resulting from the non converted portion of the solar radiation, and the removal of the excess heat has a positive effect on the PV electrical performance, while allowing the collection of thermal energy that would be otherwise lost. [90].

Kumar and Rosen [82] found that a PV/T collector produces more energy per unit area than individual PV and thermal collectors, and Fujisawa and Tani [91] came to a similar conclusion from an exergy evaluation, showing the potential that this technology has when both electricity and heat are needed with a limited installation area, as it is the case for the building sector.

The concept of BIPV/T was first introduced in 1996 by Clarke et al. [92], who performed laboratory tests and simulations of a PV ventilated façade with heat

recovery, which resulted in a lower operating cell temperature and higher electrical efficiency with an added thermal generation. Since then, the BIPV/T has attracted increasing attention and much research has been done all over the world.

Brinkworth et al. [93] validated a model for naturally ventilated PV façades, and Gaillard et al. [94] carried out an experimental evaluation of a naturally ventilated BIPV façade under real operating conditions, and demonstrated that the system can contribute to meet the building heating and ventilation demand, in addition to providing electrical generation.

PV façades have been also integrated with more conventional passive solar heating systems, such as Trombe walls [95], consisting of an exterior glazing pane and an interior thermal absorbing wall, with vents at the top and bottom of the latter to allow air circulation between the air cavity and the indoor. A BIPV/T Trombe wall was modeled by Jie et al. [96], finding that a room temperature increase of 12.3 ºC is possible, compared with a conventional wall, while Sun et al. [97] obtained a higher indoor air temperature for a BIPV/T Trombe wall façade with a window, compared to a same size conventional Trombe wall. Koyunbaba et al. [98] carried out experimental tests and modeling that showed a maximum electrical and thermal efficiency of 4.52% and 27.2%, respectively.

Many studies have been made on BIPV/T systems in forced ventilation. Nagano et al. [99] developed vertical exterior wallboards incorporating PV cells, and found that an increase in thermal efficiency from about 22% to 29% could be achieved with the addition of a glass cover in front of the wallboard. Athienitis et al. [100] constructed a

prototype of BIPV/T collector integrated with an unglazed transpired collector (UTC), which was further applied to a full-scale office building in Montreal, Canada. Pantic et al. [101] analyzed three different BIPV/T configurations integrated with roofing, showing that the addition of a vertical glazed solar air collector in series with the outlet of the roof system provides significant increase in the air temperature output, while adding a glazing cover on top of the PV would cause an increase of thermal generation but also a reduction in electrical performances, due to a lower solar radiation received and higher PV temperatures.

Agrawal and Tiwari [90] designed roof-integrated BIPV/T air channels able to be connected in series or in parallel, and developed a one-dimensional transient model to select an appropriate system suitable for cold conditions in India. Aste et al. [102] designed and implemented a BIPV/T system on a tilted façade using semi-transparent PV modules, reporting thermal and electrical efficiency varying from 20 to 40% and from 9 to 10%, respectively. Charron and Athienitis [103] carried out a theoretical study to optimize the performances of a ventilated double façade with integrated photovoltaics and motorized blinds, and found that PV modules placed within the air cavity can improve the thermal efficiency by 25% but at the expense of a 21% reduction in electrical generation.

The extensive interest in air-based BIPV/T systems is mainly driven by their flexibility and ease of integration with multiple building elements, due to the availability of air and its lightweight, to the reduced damages in case of fluid leakage as well as to the absence of freezing and corrosion problems, resulting in low installation and

maintenance costs [87]. However, there are some limitations and challenges that researchers and developers are currently facing, which are mainly related to the limited heat transfer coefficient of the air compared to water-based systems. This affects the ability to cool the PV panels, so that there is a conflict between generating thermal energy at high temperature and keeping the PV panels at low temperature for better electrical yields. Moreover, when the system operates at high temperatures, in addition to a lower electrical efficiency caused by high PV operating temperatures, higher heat losses will occur and the thermal efficiency tend to decrease further, as less heat is transported by the airflow.

Therefore, the design process will depend on the specific building requirements, the fraction of electrical and thermal energy needed and its intended use. Another constraint of BIPV/T collectors, when compared to conventional PV/T technology, is the fact that their installation, in terms of orientation and tilt angles, is strictly connected to the building itself and the design of its components.

Nevertheless, there are a number of factors that affect the performances of air-based BIPV/T systems and that can be optimized to improve the overall efficiency, such as the number of glass covers and glazing material, the use of anti-reflective or low-emissivity coatings, the thermal absorptivity and material composition of the PV panels, the radiative properties of the non-absorbing materials, the convective mode of the airflow, the flow regime and the mass flow rate.

Chapter 3
BIPV/T Prototype: Concept and Implementation

In the first phase of the project, the main objective has been to evaluate the performance of a newly developed BIPV/T air collector prototype. The concept is that of a PV/T window, patented in 2011 by Dr. Narinder Singh Kapany [104], and it was further developed into a first prototype by SolarPath, Inc., a startup company based in Palo Alto, California. An experimental investigation has been conducted in Salinas, California, which consisted of a series of electrical and thermal measurements performed under different testing conditions, with the aim of determining the energy performance and generation potential of the prototype.

In this chapter, a brief overview of the patent and a description of the window prototype will be provided.

3.1 The Solar Window Concept

The idea patented by the Indian-born American physicist Dr. Narinder Singh Kapany, further extends the concepts of building integrated photovoltaics (BIPV) and hybrid PV/T collectors to building fenestration elements, by coupling them with those of airflow windows and ventilated facades. Therefore, the concept belongs to the category of BIPV/T systems.

The invention is shown in Fig. 3.1. It consists of a double pane window, where a bottom and a top vent are realized to host fans and air filters (elements 170 and 175 in Fig.

3.1), allowing air to circulate through the cavity (120) between the two glass panes and be filtered [104].

Photovoltaic cells (140) mounted on louvers (145) can be placed in the cavity, which perform the multiple functions of providing shading control, generating electricity and converting the remaining absorbed fraction of the incoming solar radiation into heat. The latter is then transferred from the PV louvers to the air that circulates from bottom to top and carried out of the window through the top vent, so that it can be either put

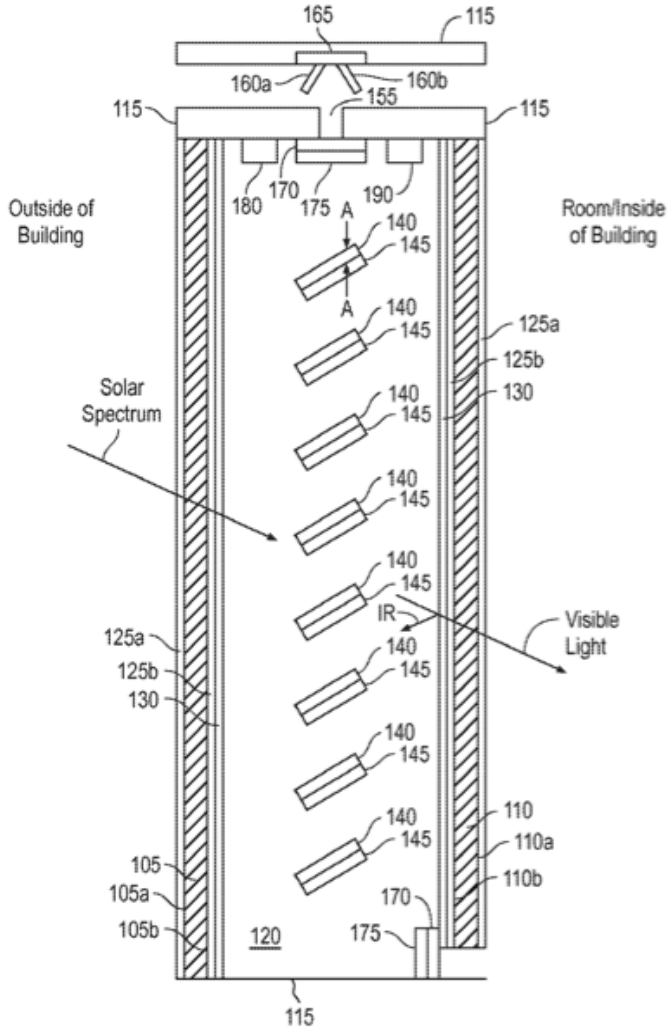

Fig. 3.1: Solar window concept [104].

into use or expelled outside by optional shutters (160a and 160b), which could be controlled by a thermostat (165) that determines whether to let the air entering or exiting the building, depending on the actual room temperature.

The two glass panels can be coated with anti-reflective layers (125a and 125b in Fig. 3.1) on both sides to reduce reflective losses, and infrared reflective coatings (130) could also be placed on the inner sides facing the cavity, in order to reach maximum heat gain within the air gap by reflecting back the long-wave infrared radiation emitted by the PV louvers.

The patent includes also the possibility of having a thermoelectric generator (180) at the top for additional conversion of heat into electricity, as well as a water heating unit (190) that transfers the heat to a water circuit which is fed from the outside of the window.

3.2 Prototype Description

A first prototype that is based on the aforementioned concept was constructed, featuring most of the elements included in Dr. Kapany's patent. The prototype is shown in Fig. 3.2, and consists of 2 double glazed window compartments with an air cavity in between, held together by an aluminum frame. The principal geometrical characteristics of the prototype are reported in Table 3.1. The first lower section of the frame hosts the input vent, which in this case is realized on the outer side of the window, allowing the window to operate in what is called "air-supply mode", where fresh ambient air is supplied to the inside of the building and therefore contributes to fulfill ventilation requirements.

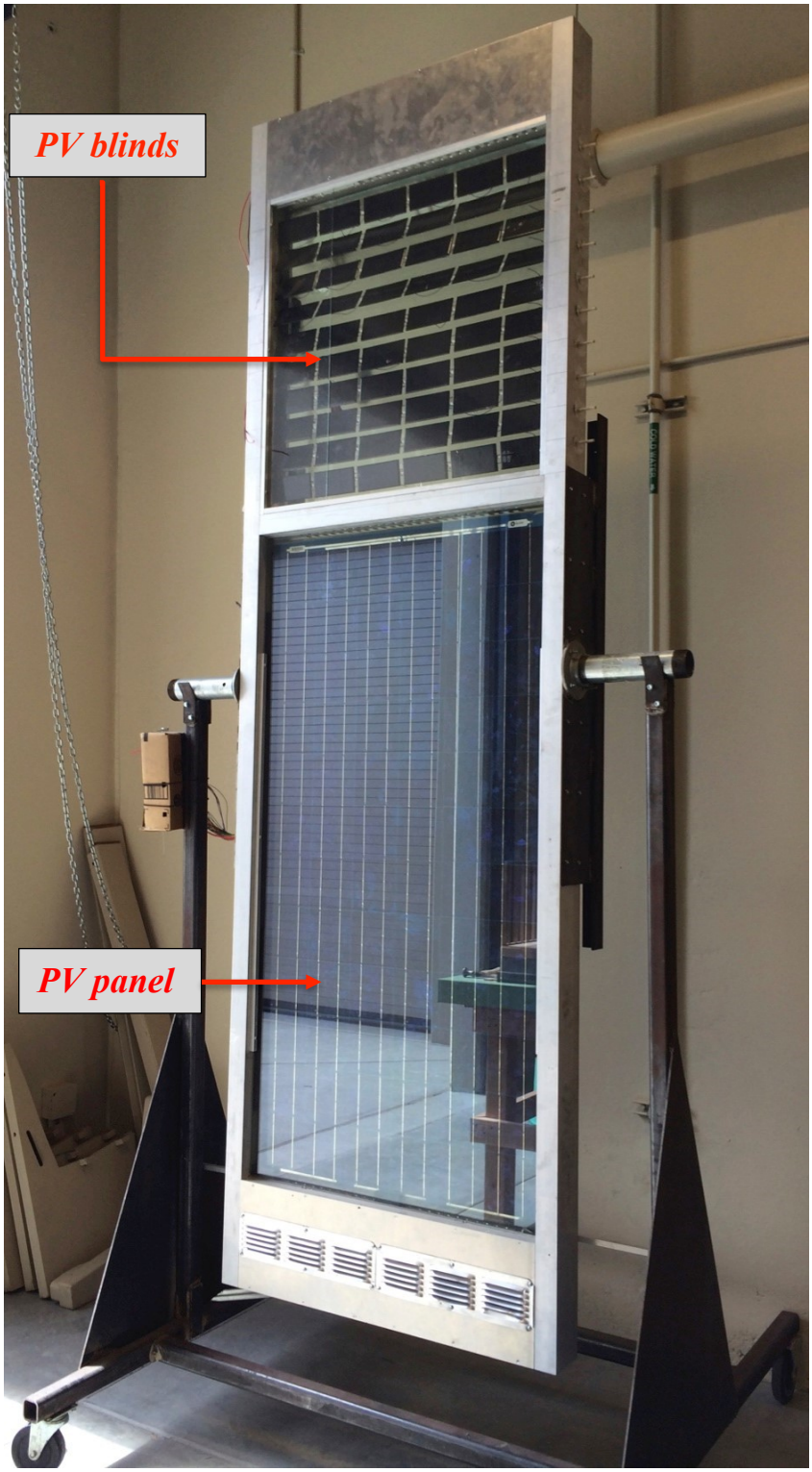

Fig. 3.2: Solar window prototype.

Table 3.1: Prototype geometrical characteristics.

Width	*0.91 m*	*Bottom vent area*	*411.78 cm^2*
Height	*2.92 m*	*Top vent area*	*248.5 cm^2*
Depth	*10.2 cm*	*Parallax module dimensions*	*12.5 x 6.3 cm*
Total gross area	*2.67 m^2*	*Parallax module area*	*78.75 cm^2*
Total glazed area	*1.958 m^2*	*Total top PV array area*	*0.4725 m^2*
Top glazing area	*0.658 m^2*	*BP Solar SX 170B area*	*1.258 m^2*

The vent consists of two apertures of 5.79 x 35.56 cm each, and a metal grid and aluminum fins act as an air filter, preventing dust from entering the window. The output vent, shown in Fig. 3.3, is located at the top section on the back of the unit, and it is a single aperture with dimensions of about 3.5 x 71 cm. The forced ventilation is realized by 10 Sunon KDE1208PTB1-6(OC) computer fans with an operating voltage range of

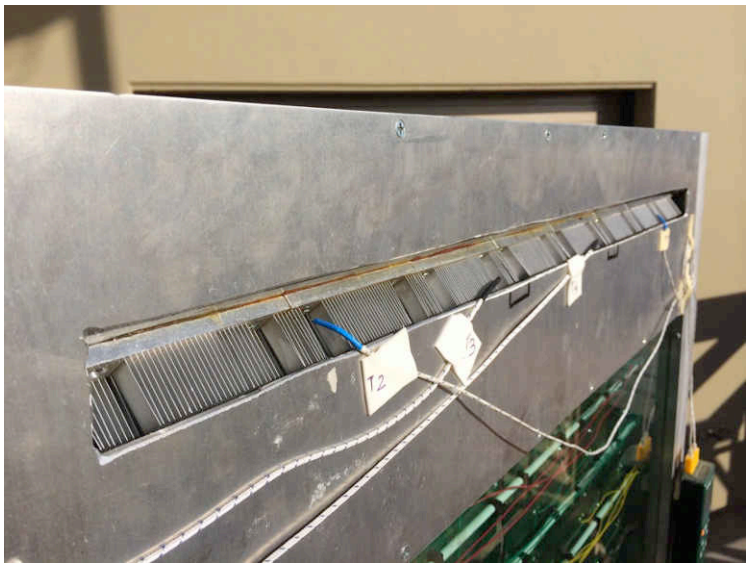

Fig. 3.3: Photograph of the top vent.

5-13.8 V and rated power of 2.6 W each at 12 VDC, which are placed inside the top section of the frame as well. A heat exchanger is located downstream of the fans, and it is composed of a U-shaped copper pipe and aluminum fins that are in thermal contact through a metal plate to which they are welded. The pipe runs down along the left side of the window (with respect to a front view) and ends in a storage tank containing glycol and a 65 W water pump to circulate it. This allows the heat to be transferred to a fluid circuit that could be used for radiant floor heating or to preheat water during the summer months when the heat is most needed for domestic hot water production. Fig. 3.4 shows two pictures of the fans and heat exchanger components.

The two main middle sections consist of the double-glazed air cavities, which enclose a fixed regular PV module at the bottom and a movable PV array at the top. In the bottom compartment, which has an aperture of 1.3 m^2, a BP Solar SX170B photovoltaic module has been installed, that is rated at 170 W with a nominal efficiency of 13.5%. The top double-glazing encloses an array of 60 Parallax XHHOO1-4 PV modules, which are mounted on 10 plastic rods (holding 6 modules each) that can be manually tilted up to 25° with respect to the normal to the modules. The Parallax modules' electrical specifications are reported in Fig. 3.5.

The PV array makes the top part of the prototype into what can be defined more properly as a window, as it allows visibility through it, while the bottom section enclosing a regular photovoltaic module looks more like a solar wall. The original reason of using this type of layout instead of a full PV array on the whole window was to test the maximum absorbing capability of the PV surfaces, which in this case

Fig. 3.4: Fans and heat exchanger at the top of the unit.

act as thermal absorbers, and are the central component of the system. The BP Solar module contributes to the overall thermal performances but it was not included in the electrical measurements, which were carried out on the PV array alone, as the final product is intended to look like a window on the entire height.

The transition between the different sections of the window is realized through the use of holes into the aluminum shell, in order to allow for air circulation and connect the two air cavities. The fans move the outside ambient air from the bottom vent into the double glazing, where it flows over the warm PV surfaces heated by the solar radiation, and carries the transferred heat up in its rising motion towards the top vent

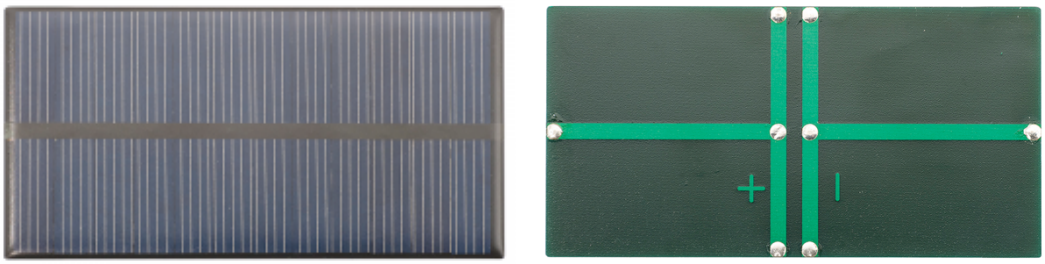

Electrical specifications - XHHOO1-4	
Rated power	*1 W*
Open circuit voltage	*7.2 V*
Short circuit current	*183 mA*
Max power voltage	*6 V*
Max power current	*166 mA*
Operating temperature	*0 – 70 ℃*
Number of cells	*12*

Fig. 3.5: Parallax XHHOO1-4 module: front (top left) and back (top right), and its electrical characteristics.

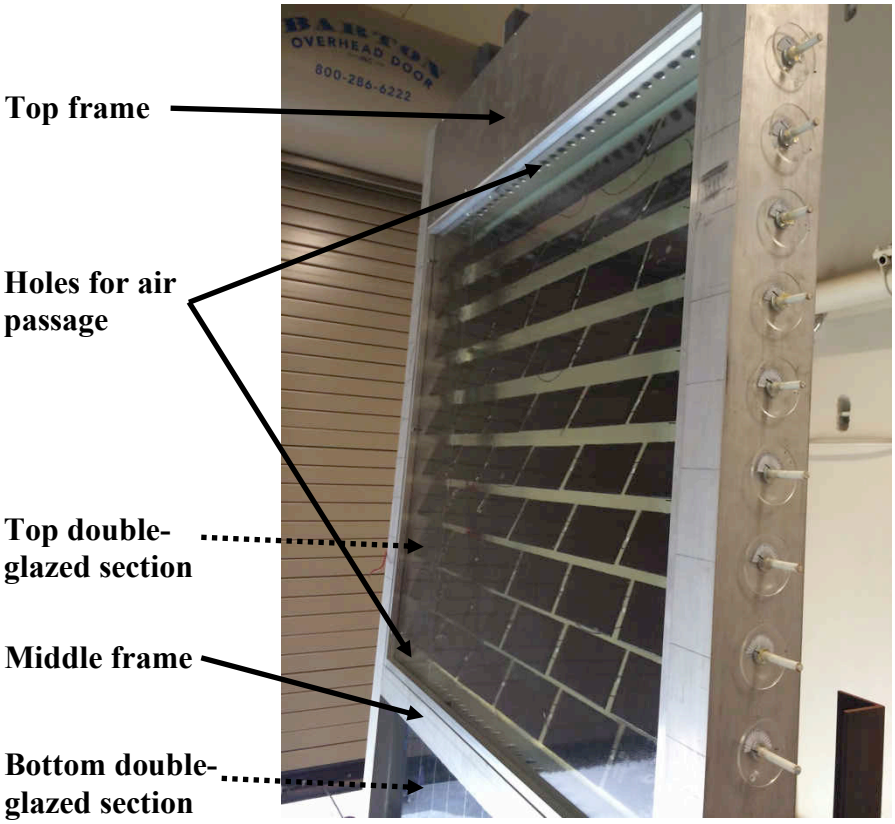

Fig. 3.6: Air passages and tilting of the PV array.

at the output. Fig. 3.6 shows a close-up of the PV array where the passages interconnecting the different sections can be seen, along with the tilting mechanism on one side of the window, while a schematic of the cross-sectional view of the window, with the airflow path represented, is represented in Fig. 3.7**.**

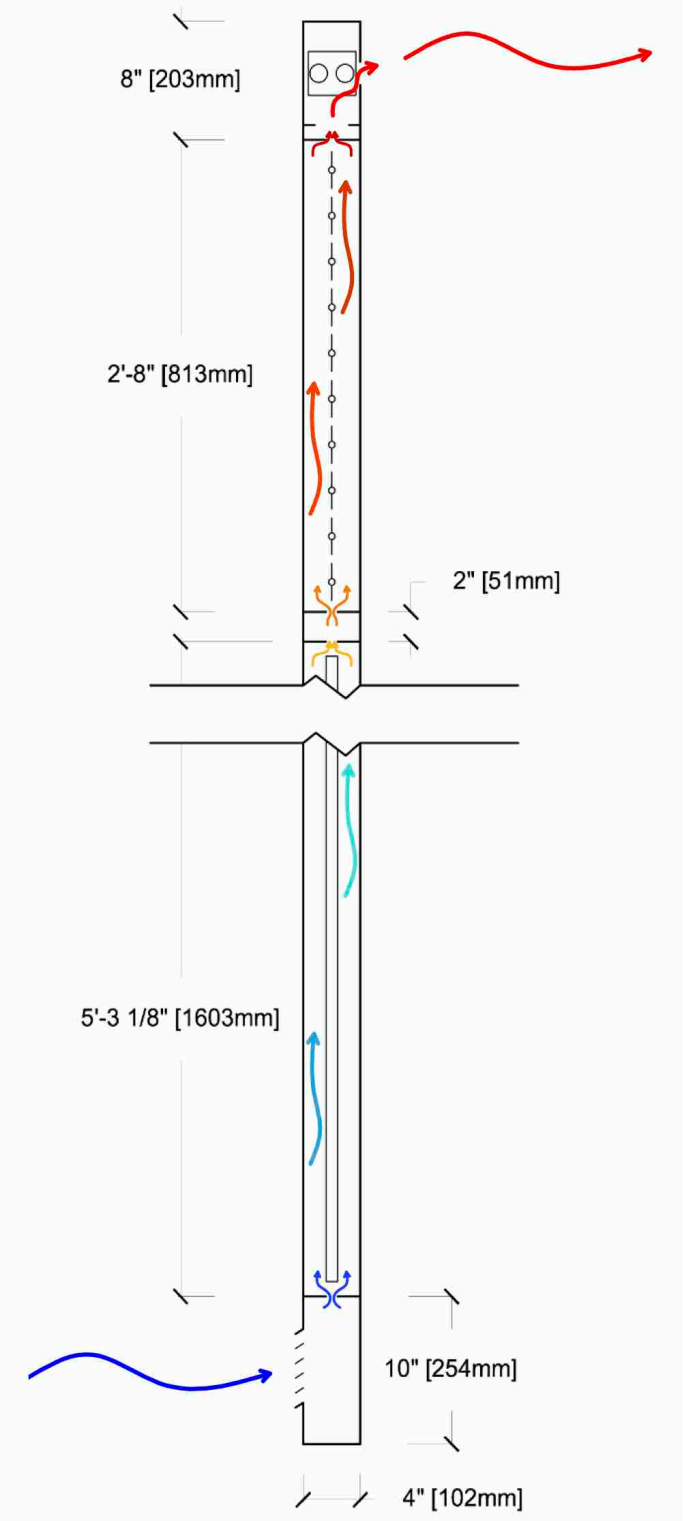

Fig. 3.7: Cross section and airflow schematic.

Chapter 4

Experimental Evaluation of Thermal and Electrical Performance

4.1 Thermal Measurement Instrumentation

Thermal measurements were taken in order to test the thermal performances of the prototype. The principal parameters of interest are the temperatures at the input and at the output of the window, the airflow properties, which includes the air velocity, air density and specific heat at constant pressure, and the solar radiation incident on the unit.

2 K-type (chromel-alumel) thermocouples were installed at the bottom vent (Fig. 4.1) to sense the input temperature, and 4 K-type at the top vent for the output air temperature (Fig. 4.2). Two more thermocouples have also been installed on the back of two PV modules on the array, located one at the second row on the top and one at

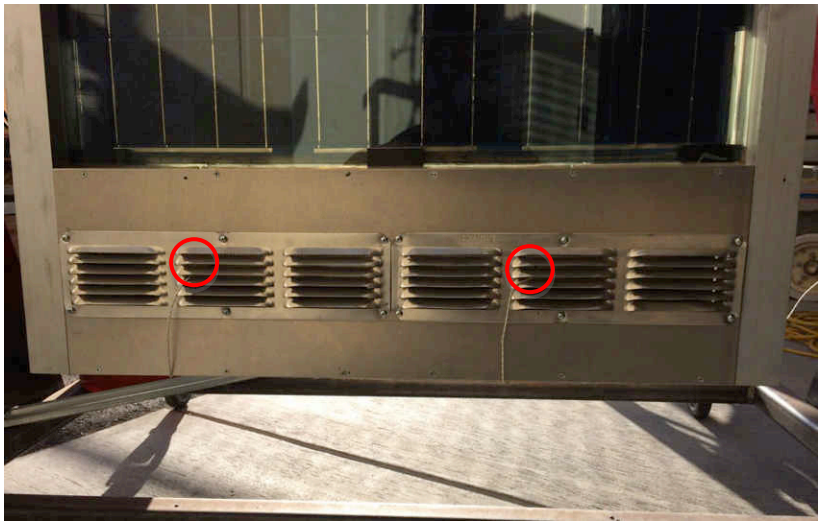

Fig. 4.1: Thermocouples placement (marked with red circles) at the bottom vent.

Fig. 4.2: Thermocouple setup on the back at the output vent and on 2 PV modules (red circles).

the second row from the bottom, in order to monitor the temperature levels reached by the array.

An Extech 410 Multimeter and two EA10 EasyView Dual Input Thermometers were used for reading and display of temperature data. The air velocity at the output has been

tested with a Kanomax Anemomaster 6006 LITE hot wire anemometer (Fig. 4.3), which reads the air speed in the direction perpendicular to the probe and has an accuracy of ±5%. To ensure this orthogonality condition, a small duct has been used to extend the output section and allow the air to come out horizontally. The measurements have been taken at nine different positions on the output section, and for each of them the probe was placed at three different height levels, so as to have a grid of 27 data points. A sample of an air velocity data recording for 3 different times is reported in Table 4.1, where v_1, v_2, … v_9 represent the 9 evenly spaced data points, which go from left to right on the top vent cross section.

Fig. 4.3: Hot wire anemometer for air velocity readings.

Table 4.1: Air velocity reading (in m/s) at 9 data points at different times.

		v_1	v_2	v_3	v_4	v_5	v_6	v_7	v_8	v_9
11:00	Top	0.26	0.75	0.98	1.18	1.1	1.1	1	1.15	0.92
	Middle	0.14	0.25	0.32	0.4	0.3	0.32	0.45	0.43	0.6
	Bottom	0.15	0.28	0.36	0.4	0.6	0.3	0.3	0.4	0.55
11.45	Top	0.24	0.7	1.08	1.05	1.15	1.15	1.08	1.25	0.8
	Middle	0.14	0.3	0.5	0.35	0.4	0.38	0.4	0.8	0.7
	Bottom	0.13	0.24	0.35	0.3	0.3	0.3	0.3	0.4	0.8
12:30	Top	0.35	0.64	1	1.1	1.2	1.15	1	1.2	1.25
	Middle	0.16	0.24	0.3	0.4	0.28	0.3	0.45	0.75	0.7
	Bottom	0.14	0.3	0.4	0.2	0.19	0.35	0.45	0.48	0.7

A pyranometer Ambient Weather TM-206, with an accuracy of ±10 W/m^2, was used to record the global irradiance incident perpendicularly to the window surface, as well as the global tilted irradiance (including beam, diffuse and reflected components) at local solar azimuth and elevation.

4.2 Electrical Measurement Set-up

4.2.1 PV Module Testing

The electrical performance was evaluated based on the generation of the top array, composed of the 60 PV modules, due to the project's main focus on PV blind elements rather than vertically installed opaque modules. To compare the actual performances with the manufacturer's data, two PV modules were individually tested first, and their I-V characteristic curves were generated. These preliminary measurements were carried out by exposing the modules perpendicularly to the sun rays and connecting them to a 350 Ω Ohmite RES350E-ND rheostat, which acts as a variable resistive load. By varying the rheostat resistance from 0 to 350 Ω, that is from a short-circuit to an

almost open-circuit condition, the PV module response (in terms of voltage and current) has been recorded. The first module was tested outside the window, while the second testing was made inside the window on one of the modules on the bottom part of the array (3rd row from bottom), tilted by 20°, which therefore received less solar radiation due to reflective losses through the glass.

The electrical output of both modules is plotted in Fig. 4.4, where the experimental data for current and power versus voltage are shown, along with their 6th order polynomial interpolation curves. The testing conditions and main data are reported in Table 4.2, where I_{PV} is the solar irradiance on the module's plane, T_{PV} is the temperature on the module's back, I_{sc} and V_{oc} are the short-circuit current and open-circuit voltage recorded, respectively, and P_{max} is the maximum power produced.

It can be seen that the module tested outside behaves very closely to the manufacturer's specifications at standard testing condition (irradiance of 1000 W/m^2 and cell temperature of 25 °C), with a I_{sc} = 190 mA (vs. 183 mA at STC) and V_{oc} = 6.9 V (vs. 7.2 V at STC).

The short-circuit current increase is caused by two factors that combine: the higher temperature of 38°C (even if current increases only slightly with temperature) and the higher solar irradiance of 1026 W/m^2. On the other hand, a higher irradiance causes a

Table 4.2: Testing conditions and data for I-V curve measurements.

	I_{PV}	T_{PV}	I_{sc}	V_{oc}	P_{max}
Outside module	1026 W/m^2	38 °C	190 mA	6.9 V	0.96 W
Inside module	920 W/m^2	49 °C	164 mA	6.4 V	0.78 W

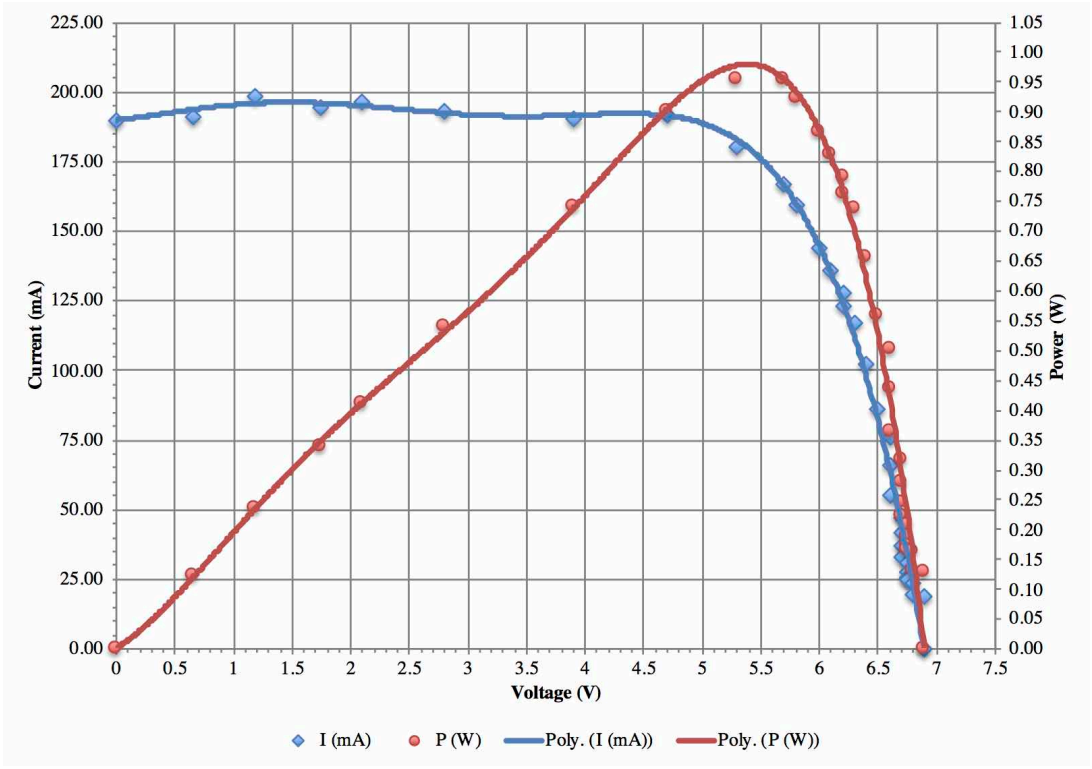

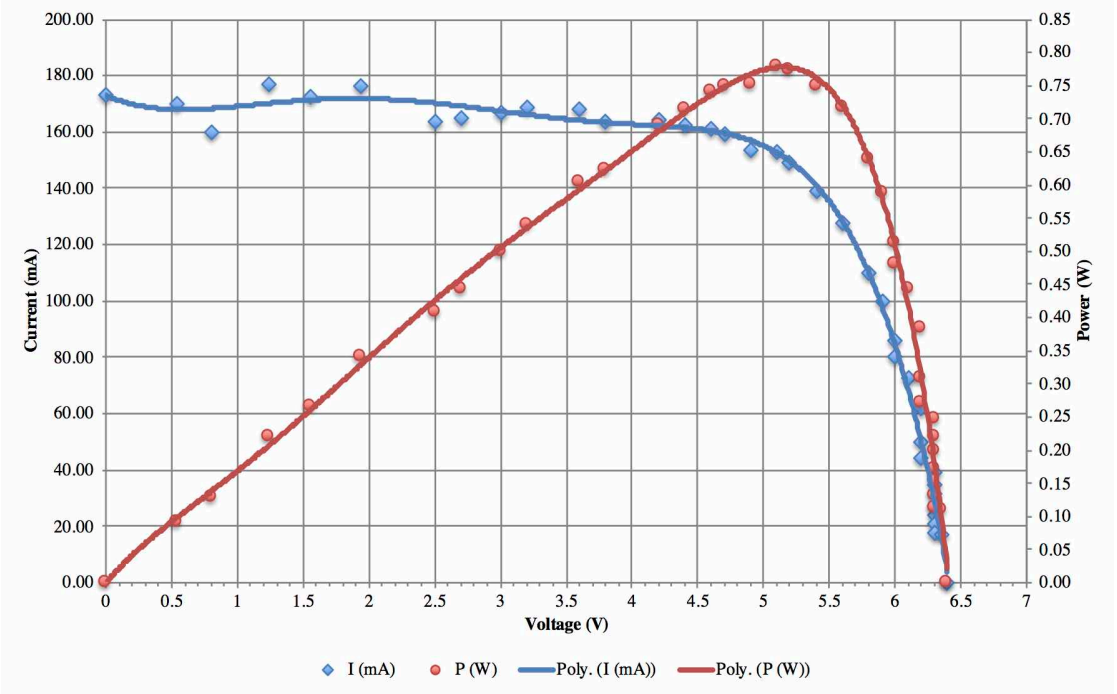

Fig. 4.4: I-V characteristics for the PV module tested outside (top graph) and inside (bottom graph) of the double glazing.

minimal increase in the voltage, while the higher temperature has a more significant impact in reducing it.

The inside module receives instead a smaller amount of radiation (I_{PV} = 920 W/m^2), which causes a smaller short-circuit current (I_{sc} = 164 mA) and, due to the fact that is placed inside the double glazing, its temperature reaches a even higher value (T_{PV} = 49 °C), which results in a further reduction in open-circuit voltage, that drops to 6.4V. In the first case, a maximum power of 0.96 W has been obtained, which decreases to 0.78 W for the second module. These values can be used to calculate the temperature coefficient for power C_P, which indicates the power reduction per degree °C with respect to a reference situation, which can be calculated as follows [105]:

$$C_P = \frac{\Delta P}{\Delta T} = \frac{P' - P_{ref}}{T' - T_{ref}} \tag{16}$$

where P' and T' are the power and temperature at the actual measured conditions, that is P_{max} and T_{PV}, respectively, in this case, while P_{ref} and T_{ref} indicates instead the same quantities calculated at a reference condition. The latter are considered to be the same as the power that a similar module at T_{ref} = 25 °C would generate with the same input solar irradiance. Under these conditions, the power P_{ref} is only dependent on the solar irradiance, and can be evaluated through the proportionality relation [106]:

$$\frac{P_{ref}}{P_{STC}} = \frac{I_{PV}}{I_{STC}} \tag{17}$$

with P_{STC} = 1 W and I_{STC} = 1000 W/m^2 are the power and current at standard testing conditions.

For I_{PV} = 1026 W/m^2 (outside module), P_{ref} = 1.026 W, and for I_{PV} = 920 W/m^2 (inside module), P_{ref} = 0.92 W.

Therefore, by considering that P_{max} = 0.96 W and T_{PV} = 38°C, Equation 16 gives in the first case a power temperature coefficient C_P = -0.00507 W/°C, while in the second case (for P_{max} = 0.78 W and T_{PV} = 49°C) it is C_P = -0.00583 W/°C, which is in line with the typical values found in commercial mono-crystalline Si modules, that is around -0.005 W/°C.

4.2.2 PV System Design and Implementation

In order to measure the power output of the top PV array, consisting of the 60 modules, a stand-alone system was set up. The system was sized to be able to run a load P_{load} = 91 W, composed of the 10 DC fans, rated at 2.6 W each, and the 65 W water pump, for a period Δt = 5 hours continuously. The required energy E_{load} is then:

$$E_{load} = P_{load} \cdot \Delta t = 455 \text{ Wh} \tag{18}$$

By choosing a 12 V DC battery, the minimum capacity that it should provide is given by [106]:

$$C_{battery} = \frac{E_{load}}{V_{rated}} = 37.9 \text{ Ah} \tag{19}$$

where $C_{battery}$ is the battery capacity and V_{rated} is the rated battery voltage. A 40 Ah battery has been chosen. Generally, a 12 V battery will have an actual voltage of 14 to 14.5 V, so in order to ensure that the array will effectively charge the battery the minimum array voltage needs to be corrected using the following relationship [106]:

$$V_{PV} = 1.2 \cdot \left\{ V_{rated} - \left[V_{rated} \cdot C_{\%V} \cdot \left(T_{\max} - T_{ref} \right) \right] \right\} \quad (20)$$

where V_{PV} is the array voltage, $C_{\%V}$ is the temperature coefficient for voltage, which is around -0.004 V/°C for most PV modules, T_{max} is the maximum expected module temperature and T_{ref} is the reference temperature, that is 25 °C. By using a rated voltage of 12 V and T_{max} = 60 °C, Equation 20 gives a minimum voltage for the PV array of 16.4 V. An array voltage of 24 VDC was chosen, in order to minimize the current involved and then reduce power losses and the conductors' size. The 60 Parallax modules have been connected 4 by 4 in series, and the resulting 15 strings were parallel connected, as shown in Fig. 4.5. The nominal voltage of the array is given by the rated module voltage (6 V) multiplied by the number of modules connected in series (4 in this case).

In order to determine the correct conductor size that is able to handle the actual operating currents, a maximum current should be evaluated. This would be the sum of the short-circuit current ratings of the parallel-connected modules (0.183 A x 15 strings) multiplied by a safety factor of 125%, which accounts for possible enhanced radiation levels that would produce higher currents, resulting in a maximum current of 3.43 A.

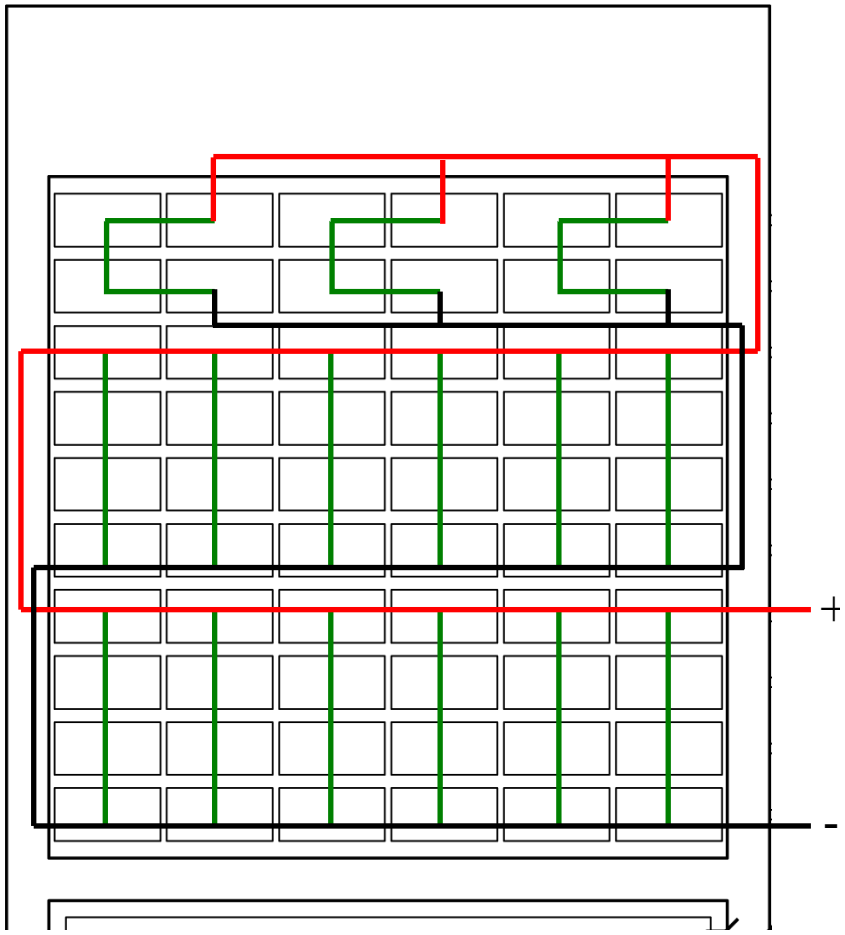

Fig. 4.5: PV connection schematics: series connection (green) and parallel connections (red and black).

For PV source circuits, as this is the case, an additional 1.25 factor is used to calculate the minimum ampacity (the current-carrying capacity) which the conductor should be sized for, that results in 4.29 A. Nominal ampacities for insulated conductors are generally based on an ambient temperature of 30 °C, and since the wires inside the air cavities of the window will experience much higher temperature levels, a temperature correction factor is used to calculate the derated capacity [106]:

$$I_{nom} = \frac{I_{\max}}{C F_{temp}} \tag{21}$$

where I_{nom} is the derated conductor nominal capacity, I_{max} is the maximum circuit current previously calculated (4.29 A) and CF_{temp} is the temperature correction factor. The latter is given for various ambient temperature intervals in NEC Table 310.15(B)(2)(a), that is reported in Fig. 4.6. By choosing a conductor with a USE-2 insulation with a 90°C rating, for a surrounding temperature above 60 °C, the CF_{temp} ranges between 0.65 (for 61 - 65 °C) and 0.29 (for 81 - 85 °C). Since previous testings have reported temperature values for the PV array not exceeding 80 °C, a value of 0.41 for CF_{temp} has been selected, which through Equation 21 gives I_{nom} = 10.46 A. The

TABLE 310.15(B)(2)(a) *Ambient Temperature Correction Factors Based on 30°C (86°F)*

For ambient temperatures other than 30°C (86°F), multiply the allowable ampacities specified in the ampacity tables by the appropriate correction factor shown below.

Ambient Temperature (°C)	Temperature Rating of Conductor			Ambient Temperature (°F)
	60°C	75°C	90°C	
10 or less	1.29	1.20	1.15	50 or less
11–15	1.22	1.15	1.12	51–59
16–20	1.15	1.11	1.08	60–68
21–25	1.08	1.05	1.04	69–77
26–30	1.00	1.00	1.00	78–86
31–35	0.91	0.94	0.96	87–95
36–40	0.82	0.88	0.91	96–104
41–45	0.71	0.82	0.87	105–113
46–50	0.58	0.75	0.82	114–122
51–55	0.41	0.67	0.76	123–131
56–60	—	0.58	0.71	132–140
61–65	—	0.47	0.65	141–149
66–70	—	0.33	0.58	150–158
71–75	—	—	0.50	159–167
76–80	—	—	0.41	168–176
81–85	—	—	0.29	177–185

Fig. 4.6: Ambient temperature correction factors. Source: NEC Table 310.15(B)(2)(a).

conductor size has been chosen to be 20 AWG (American Wire Gauge), which for conductors in free air has a rated ampacity of 13 A.

The complete PV system is composed of the 60 W rated PV array, the 40 Ah 12V DC battery and the 12V DC load represented by the fans, which have been all connected through a Tracer-2210RN MPPT solar charge controller, as shown in Fig. 4.7**.** The electrical specifications are reported in Table 4.3.

The charge controller controls the charging voltage of the battery or the current supplied from the PV array, in order to allow the battery to operate at its maximum

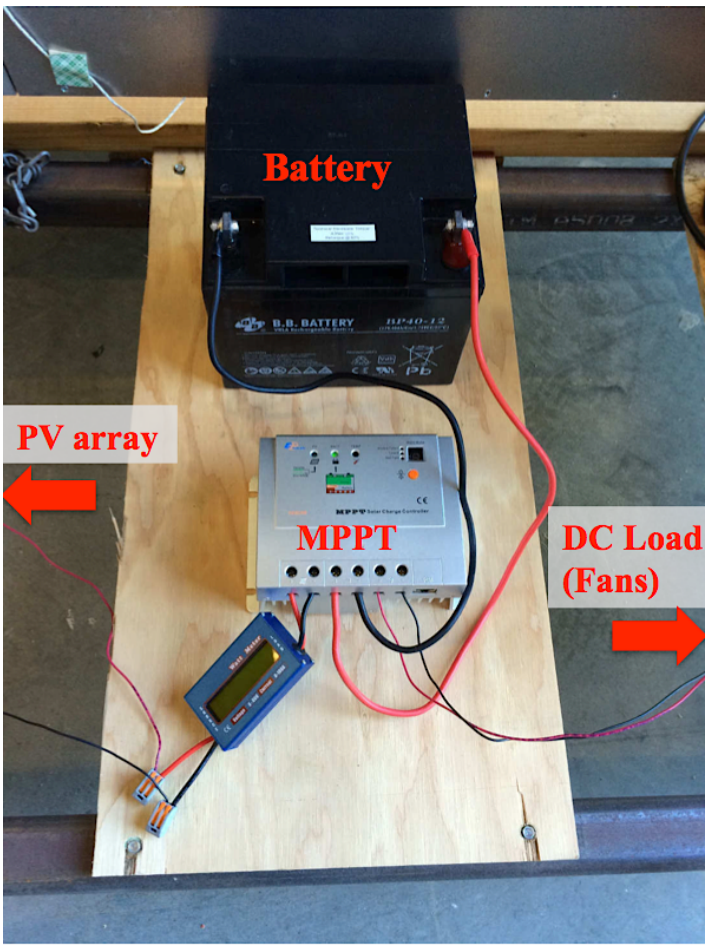

Fig. 4.7: Photograph showing the charge controller, the battery and the connections with the PV array (left conductors) and DC fans (right conductors).

state of charge as well as to prevent any overcharge or overdischarge that will cause damages to the battery. Overcharge protection is realized by interrupting or limiting the current flowing from the array when the battery reaches a high state of charge (high voltage), while overdischarge protection involves the disconnection of the load when a low state of charge (low voltage) is detected.

A maximum power point tracking (MPPT) charge controller manages the power flow between the PV array and the loads, depending on the battery charge level, and ensures that the array works at the maximum power point it could achieve at any given time. The maximum power point tracking is realized, for any given set of temperature and irradiance conditions, by changing the resistance seen by the PV array, so that it is equal to the optimal load that corresponds to the maximum power point, that is [107]:

$$R_{opt} = \frac{V_{MP}(T,I)}{I_{MP}(T,I)} \tag{22}$$

where R_{opt} is the optimal resistive load, and $V_{MP}(T, I)$ and $I_{MP}(T, I)$ are the maximum

Table 4.3: Charge controller specifications.

Model name	Tracer-2210RN
System Voltage	12 / 24 VDC
Rated Battery Current	20 A
Rated Load Current	20 A
Max PV input Voltage	100 VDC
Max PV input power	260 W (12 V system)
	520 W (24 V system)
Efficiency (for PV voltage = 24 V, PV power = 60 W and system voltage = 12 V)	95 %

power voltage and current, which depend on temperature and irradiance.

Fig. 4.8 shows 3 different loads connected to a PV module at STC, corresponding to 3 different operating points on the I-V curve. When the load is equal to R_{opt}, the module operates at its maximum power point allowed by the external conditions, but if the load would change to $R_{LA} < R_{opt}$ (or $R_{LB} > R_{opt}$), the MPPT charge controller would increase (or decrease) the circuit resistance in order to bring the operating point back at, or close to MPP.

The DC input from the PV is converted to high frequency AC and rectified back down to a different DC voltage and current, which match the battery. The voltage and current regulation follows the following relationship:

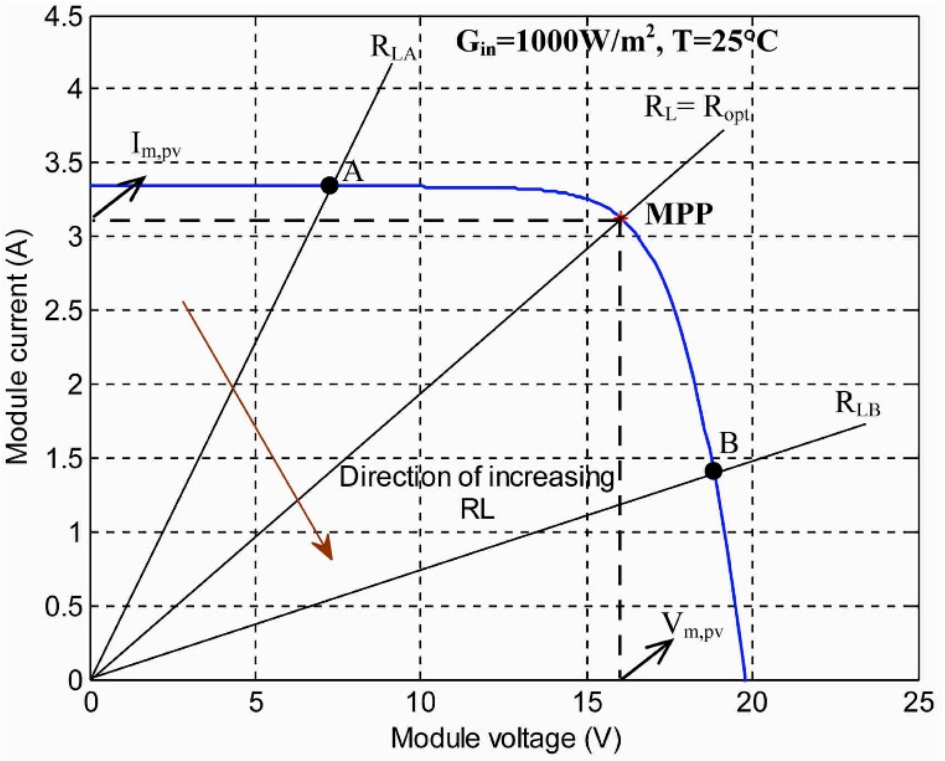

Fig. 4.8: MPPT operation [107].

$$V_{out} \cdot I_{out} = \eta \cdot V_{in} \cdot I_{in} \tag{23}$$

where the subscripts *out* and *in* refer to the output and input voltage and current, respectively, and η is the charge controller efficiency.

The charge controller converts the excess voltage from the PV array (most of the time greater than 12 V) down to a 12 VDC level, which is fed to the battery, while boosting the output current according to Equation 23, with a 95% efficiency factor.

The PV array voltage, current and power output are measured by a wattmeter, which is placed between the array and the charge controller terminals. A remote display is also connected to the charge controller, indicating the voltage and current levels of both the battery and the load, as well as the battery capacity percentage (Fig. 4.9).

A schematic of the overall BIPV/T system is shown in Fig. 4.10, where the two fluid paths are drawn.

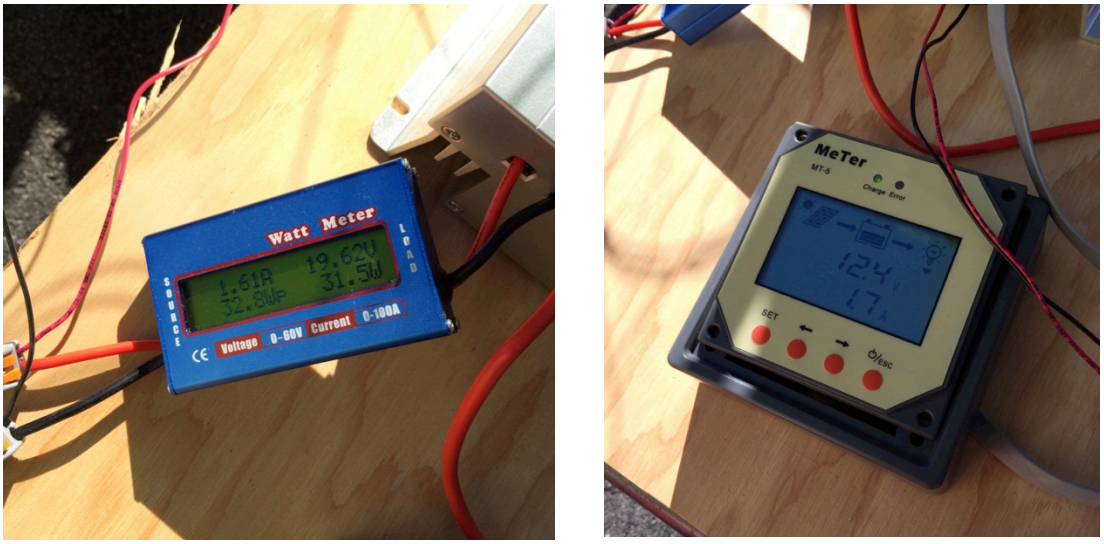

Fig. 4.9: PV array, load and battery monitoring.

The first one represents the airflow path, which enters from the air inlet at the bottom of the collector, rises to the top through the double-glazing, the fans and heat exchanger and is released through the outlet at the top. The other is the fluid circuit of the glycol, which is stored in the thermal storage tank and is pumped to the top of the collector to be input to the heat exchanger and circulated back down to the tank.

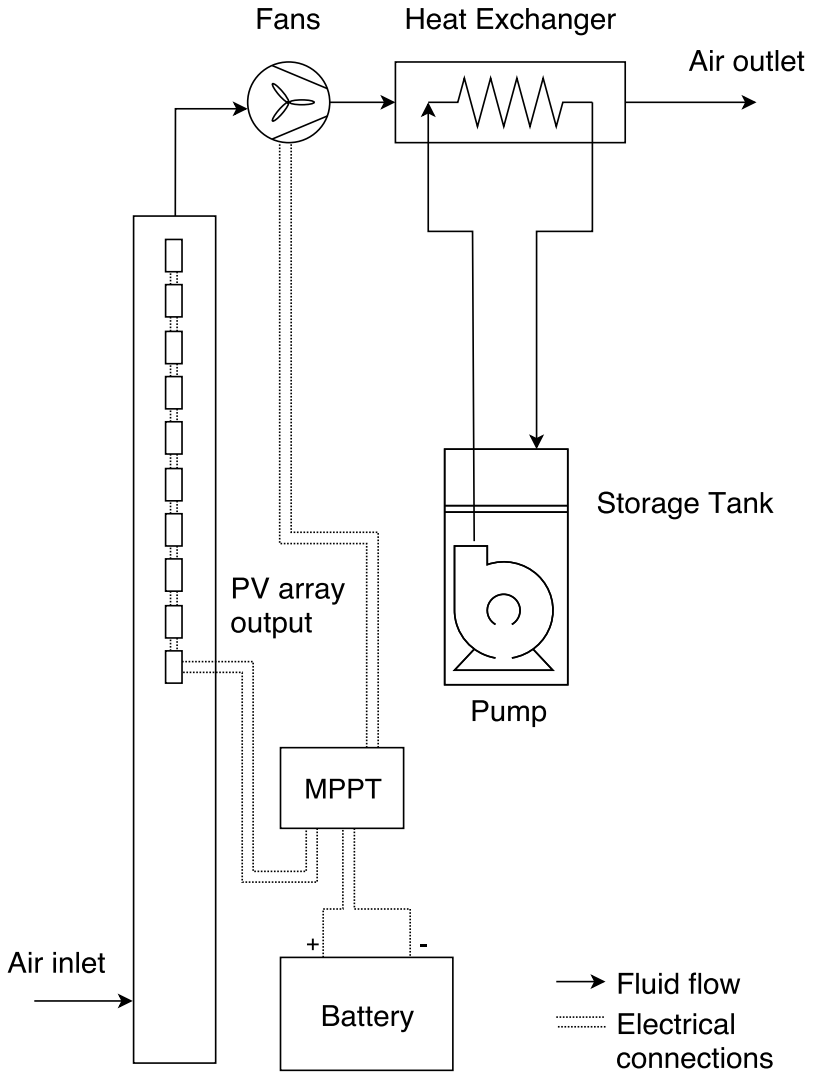

Fig. 4.10: Schematic of the PV/T system.

4.3 Thermal and Electrical Parameters

4.3.1 Thermal Output

The physical phenomena that take place when the prototype is fully operating involve all the three different types of heat transfer mechanisms, as well as a turbulent fluid flow due to the several obstacles the air encounters in its path through the unit (the input and output vents, the holes between the different sections and the PV modules). There is heat transfer by radiation between the sun and the exposed surfaces (resulting in a net heat absorption by the window), as well as radiation exchange between the different surfaces. Heat is then transferred inside by conduction from the exterior surfaces through the materials thickness, and there is convective heat transfer at the boundaries with the air, which removes the heat and carries it away in its ascending movement towards the top vent.

For the purpose of determining the prototype's thermal output, the complexity of this thermo-fluid dynamic problem can be reduced by treating the window as a black box, so that the output would include all previously mentioned effects.

Therefore, the system thermal performances has been computed based on the net heat transfer rate absorbed by the air and carried out of the window, which is considered a control volume with one inlet and one outlet, represented by the bottom and top vents. A one-dimensional flow approximation has been considered, meaning that all the properties are uniform at any cross-section perpendicular to the fluid flow, which is generally true for flows in pipes or ducts. Moreover, all the variables (temperature, solar irradiance, air properties) are considered to vary only slowly during the course of

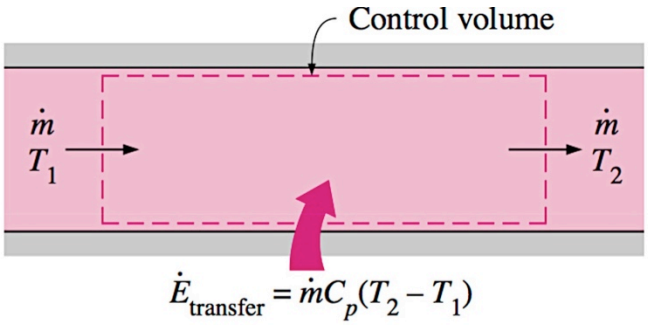

Fig. 4.11: Energy transfer and mass flow rate conservation in a control volume in steady-state conditions [18].

the day, and then for each set of measurements the fluid flow can be well approximated as a steady-state system.

Under these conditions, the mass flow rate at the input of the control volume must be equal to that flowing out of it (Fig. 4.11), and the net rate of heat transfer to the fluid $\dot{Q}$ [W] is given by [108]:

$$\dot{Q} = \dot{m} \cdot c_p \cdot \left(T_{out} - T_{in}\right) \tag{24}$$

where $\dot{m}$ [kg/s] is the mass flow rate, c_p [kJ/kg·K] is the air specific heat at constant pressure and $\Delta T = T_{\text{out}} - T_{\text{in}}$ [°C] is the temperature difference between the output temperature T_{out} and the input temperature T_{in}.

The specific heat of air between 20°C and 50°C, which is a common operating temperatures range for the window, does not change noticeably. It only varies from 1.005 kJ/kg·K at 300K to 1.007 kJ/kg·K at 330K, so the calculations have been made using an average constant value of 1.006 kJ/kg·K.

The mass flow rate $\dot{m}$ is calculated as follows [18]:

$$\dot{m} = \rho \cdot v \cdot A \tag{25}$$

where ρ [kg/m^3] is the air density, v [m/s] is the average air speed on a cross sectional area normal to the fluid flow, and A [m^2] is the area of the cross section. Since in steady-state the mass flow rate is constant at any cross-sectional area, $\dot{m}$ has been evaluated at the output vent, for which A is equal to 0.02484 m^2 and v is the velocity averaged over the measured values on the window outlet. The air density is computed for each set of data using the following relationship [18]:

$$\rho = \frac{p_a}{R_{air} \cdot T_{abs}} \tag{26}$$

where p_a [Pa] is the atmospheric pressure, R_{air} = 287.058 J/kg·K is the air gas constant, and T_{abs} [K] is the absolute temperature of the airflow.

In the estimation of the thermal efficiency, similarly to how efficiency is calculated for solar collectors, the thermal output is compared to the total solar power that the window receives, where only its component that is perpendicular to the window's plane has a useful effect, as illustrated in Fig. 4.12.

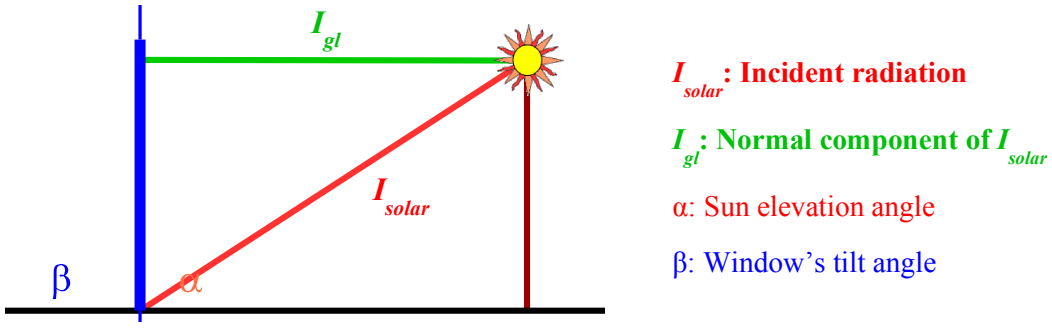

Fig. 4.12: Incident and normal radiation on the window [109].

The thermal efficiency η_{th} can therefore be expressed as [19]:

$$\eta_{th} = \frac{\dot{Q}}{I_{gl} \cdot A_{gl}} \tag{27}$$

where I_{gl} [W/m^2] is the solar irradiance incident perpendicularly to the glass panels and A_{gl} [m^2] is the total frontal glazing area, equal to 1.958 m^2, which represents the useful effective area that captures and transfer the solar radiation to the PV absorbers.

In Fig. 4.13 is reported a sample of the worksheet table used for thermal measurements and computation of the required parameters for Equations 24 – 27. I_panels represents the irradiance on the window's plane, while W_in is the total incident power, that is I_panels multiplied by the frontal glazing area A_{gl}, previously defined. The average of the two thermocouples readings at the bottom vent is also reported (T_In_Avg), along with the 4 temperature measurements at the top vent (T_1,…T_4) and their average T_out_Avg. The resulting average value V_Avg from the air velocity readings and the computed air density ρ are inputs for the calculation of the mass flow rate, here indicated as Γ. This, together with the derived temperature difference ΔT and the constant c_p, are used to calculate the thermal output and thermal efficiency (shown as Q and η).

4.3.2 Electrical Output

The PV system described in the previous chapter was used to monitor the photovoltaic array and evaluate the electrical power and generation efficiency at which the system is able to operate.

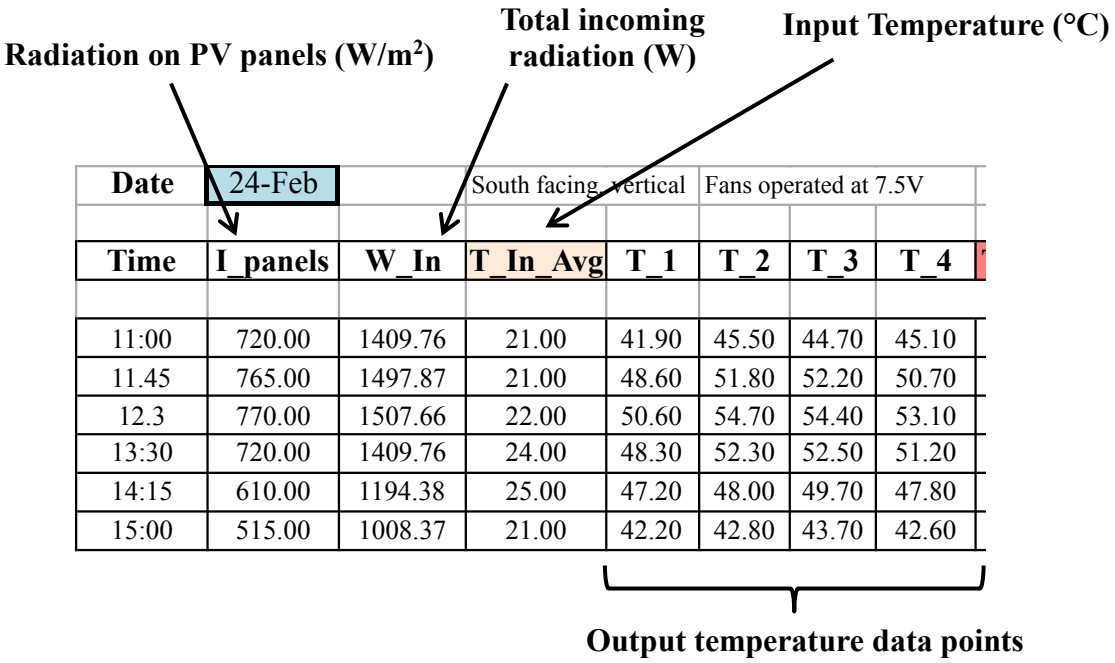

Date	24-Feb		South facing, vertical	Fans operated at 7.5V			
Time	I_panels	W_In	T_In_Avg	T_1	T_2	T_3	T_4
11:00	720.00	1409.76	21.00	41.90	45.50	44.70	45.10
11.45	765.00	1497.87	21.00	48.60	51.80	52.20	50.70
12.3	770.00	1507.66	22.00	50.60	54.70	54.40	53.10
13:30	720.00	1409.76	24.00	48.30	52.30	52.50	51.20
14:15	610.00	1194.38	25.00	47.20	48.00	49.70	47.80
15:00	515.00	1008.37	21.00	42.20	42.80	43.70	42.60

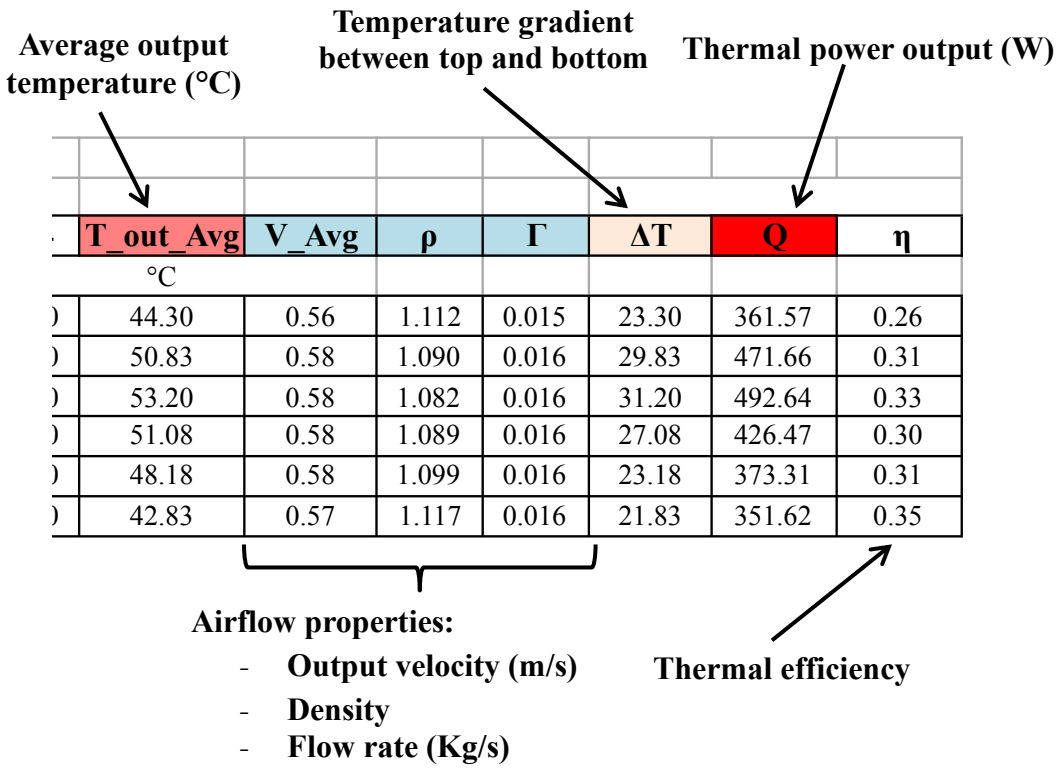

T_out_Avg	V_Avg	ρ	Γ	ΔT	Q	η
°C						
44.30	0.56	1.112	0.015	23.30	361.57	0.26
50.83	0.58	1.090	0.016	29.83	471.66	0.31
53.20	0.58	1.082	0.016	31.20	492.64	0.33
51.08	0.58	1.089	0.016	27.08	426.47	0.30
48.18	0.58	1.099	0.016	23.18	373.31	0.31
42.83	0.57	1.117	0.016	21.83	351.62	0.35

Fig. 4.13: Example of thermal measurements data worksheet and parameters computation.

The specifications for the installed Parallax modules, which were given in Fig. 3.5, can be used to calculate the rated electrical efficiency at STC, as well as the fill factor (FF). The latter is defined as the ratio of maximum power (equal to the product of maximum power voltage and current) to the product of open-circuit voltage and short-circuit current, and represents the squareness of the I-V characteristic and is a measure of the quality of a photovoltaic device. High fill factor values indicate a low equivalent series resistance and a high equivalent shunt resistance, which implies that less current is dissipated in internal losses. In terms of the I-V characteristic this means that in solar cells with a high FF the maximum power voltage and current are closer to the open-circuit and short-circuit current, respectively, as shown in Fig. 4.14. Commercial solar cells have generally a fill factor > 70%, while the maximum value for Si is around 0.83. The fill factor FF for the Parallax modules has been determined to be [110]:

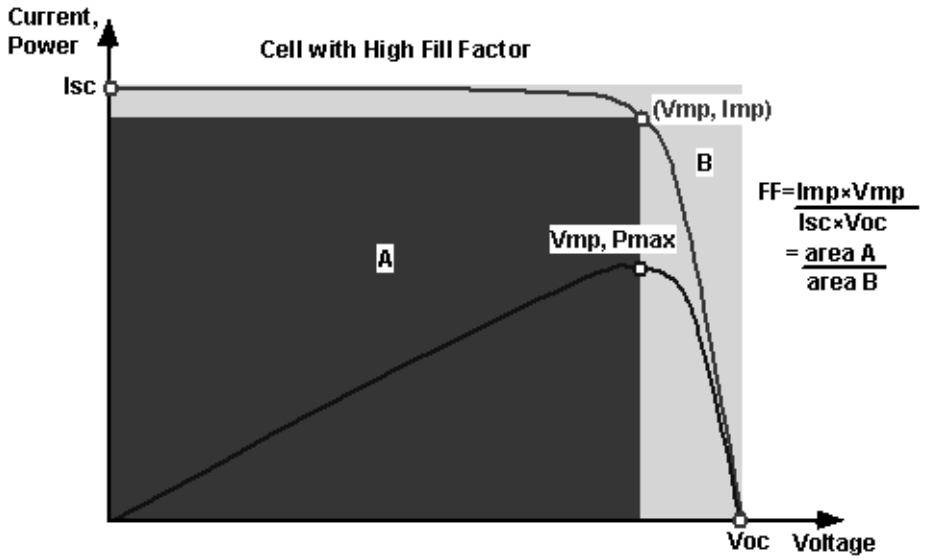

Fig. 4.14: Fill factor representation on the I-V curve [109].

$$FF = \frac{V_{MP} \cdot I_{MP}}{V_{OC} \cdot I_{SC}} = 0.756 \tag{28}$$

where V_{MP} = 6 V, I_{MP} = 0.166 A, V_{OC} = 7.2 V and I_{SC} = 0.183 A are the voltage and current at maximum power point and the open-circuit voltage and short-circuit current, respectively.

The rated electrical efficiency of a single module $\eta_{el,\,rated}$ at standard testing conditions (AM=1.5, 25°C and 1000 W/m^2) is given by [53]:

$$\eta_{el,\,rated} = \frac{V_{OC} \cdot I_{SC} \cdot FF}{I_{solar} \cdot A_{panel}} = 12.65\% \tag{29}$$

where I_{solar} is the solar irradiance, equal to1000 W/m^2, and A_{panel} is the area of a single PV panel of 7.87 x 10^{-3} m^2.

The actual operating efficiency of the array, which takes into account the effect of a lower solar irradiance (due to the modules' tilting, ambient variations though the day and reflection and transmission losses through the glazing) and a higher operating temperature, can be instead evaluated similarly to Equation 27 as follows [106]:

$$\eta_{el} = \frac{P_{el}}{I_{gl} \cdot A_{PV}} \tag{30}$$

where A_{PV} is the total area of the 60 PV modules, which is equal to 0.4725m^2, and P_{el} is the observed electrical power output. An example of the worksheet used for the electrical measurements is shown in Fig. 4.15.

Here β_1 represents the tilt angle of the normal to the window surface with respect to the

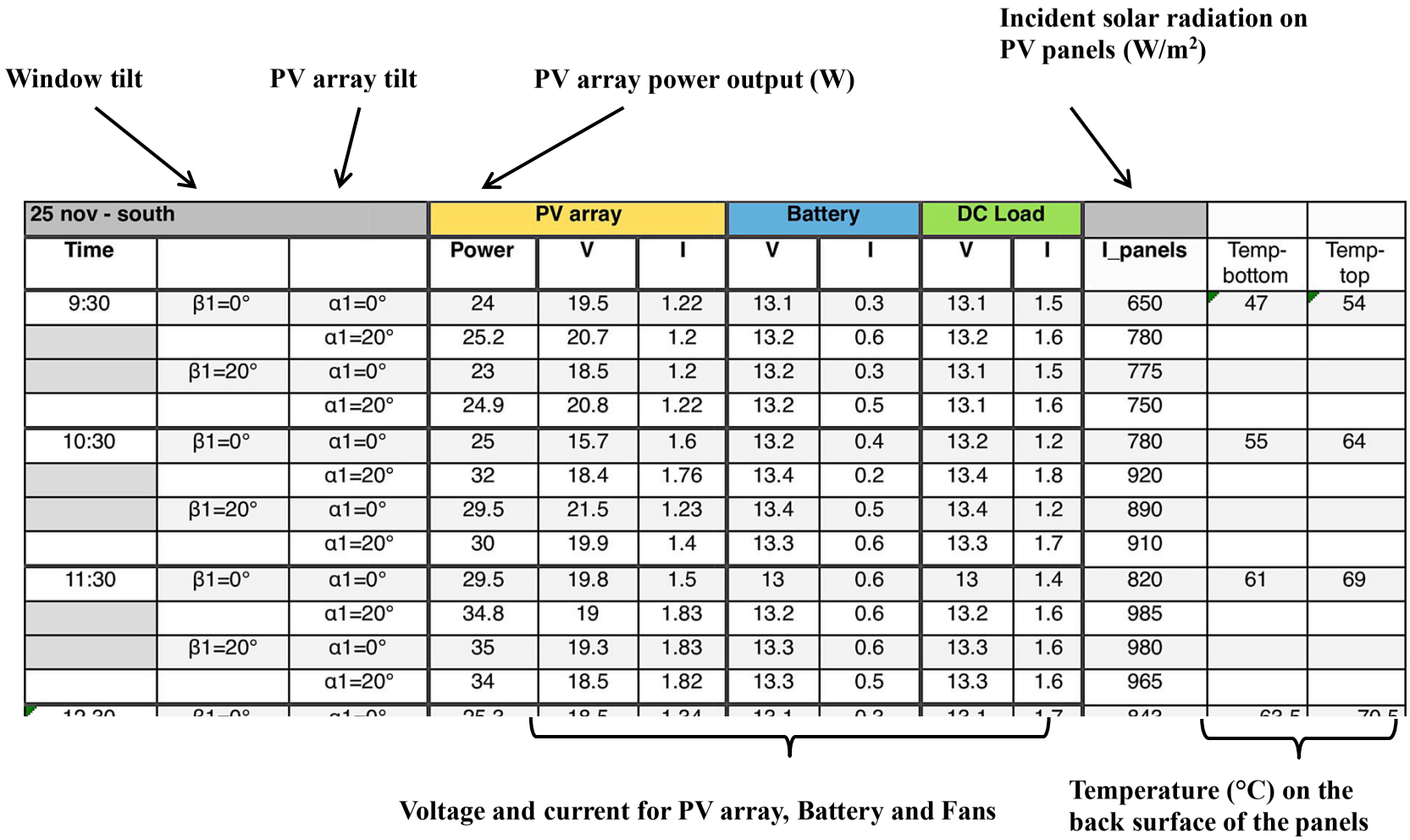

25 nov - south			PV array			Battery		DC Load				
Time			Power	V	I	V	I	V	I	I_panels	Temp-bottom	Temp-top
9:30	β1=0°	α1=0°	24	19.5	1.22	13.1	0.3	13.1	1.5	650	47	54
		α1=20°	25.2	20.7	1.2	13.2	0.6	13.2	1.6	780		
	β1=20°	α1=0°	23	18.5	1.2	13.2	0.3	13.1	1.5	775		
		α1=20°	24.9	20.8	1.22	13.2	0.5	13.1	1.6	750		
10:30	β1=0°	α1=0°	25	15.7	1.6	13.2	0.4	13.2	1.2	780	55	64
		α1=20°	32	18.4	1.76	13.4	0.2	13.4	1.8	920		
	β1=20°	α1=0°	29.5	21.5	1.23	13.4	0.5	13.4	1.2	890		
		α1=20°	30	19.9	1.4	13.3	0.6	13.3	1.7	910		
11:30	β1=0°	α1=0°	29.5	19.8	1.5	13	0.6	13	1.4	820	61	69
		α1=20°	34.8	19	1.83	13.2	0.6	13.2	1.6	985		
	β1=20°	α1=0°	35	19.3	1.83	13.3	0.6	13.3	1.6	980		
		α1=20°	34	18.5	1.82	13.3	0.5	13.3	1.6	965		
12:30	β1=0°	α1=0°	25.3	18.5	1.24	13.1	0.3	13.1	1.7	843	63.5	70.5

Fig. 4.15: Example of electrical testing.

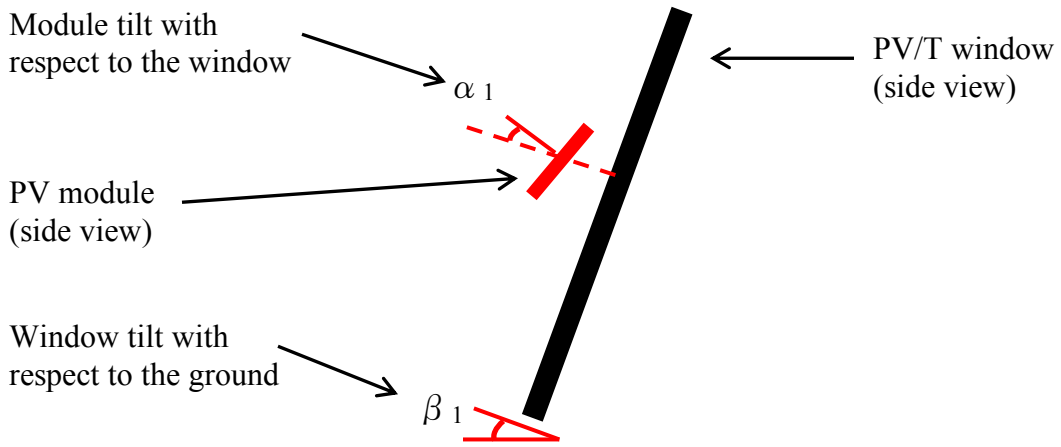

Fig. 4.16: Schematic showing the tilt angles for the prototype (black) and PV array (red).

ground, while α_1 is the angle of the PV array with respect to the window's plane, as shown in Fig. 4.16 (therefore, a situation with both β_1 and α_1 equal to 20° refers to a 40° total tilt of the array with respect to ground). On the table the voltage and current levels for the PV array, the battery and the DC fans are also reported, along with the generated power and the solar irradiance in the direction of the normal to the modules surface (I_panels). The last two columns are instead the temperature reading of the two thermocouples installed on the back of the PV modules, one on the top part and one on the bottom part of the array.

4.4 Results and Discussion

4.4.1 Summer Measurements

Measurements on the thermal system were performed in Salinas, CA (36°40′40″ N, 121°39′20″ W), in mid-July, under 4 different conditions. The window was tested in an outside environment in both south-facing position and in sun tracking mode, with

the latter meaning a continuous change of orientation of the prototype during the course of the day in order to keep it directed towards the sun. In both configurations, the window has been operated at 90° and 70° tilt angle with respect to the ground, corresponding to the window in vertical position and tilted by 20°, respectively. A picture of the window in 20° tilting position is shown in Fig. 4.17.

After the first testing trials, the weather conditions characterized by growing wind during the afternoons coming from West and North-West suggested a different location for the prototype, since it was observed that this affected both the temperature and air velocity readings, due to the cooling action of the wind on the sensors and the

Fig. 4.17: Tilting of the prototype by 20°.

added turbulence on the back of the unit. The window was then moved close to the south wall of a pocket house (Fig. 4.18), built on the same location, in order to provide shielding from the wind and ensure more stable conditions for taking data at the back of the prototype.

The results for the normal solar irradiance incident on the window plane and output air temperature are shown in Fig. 4.19, while those for the air temperature rise between the output and input vents and the heat transfer rate are reported in Fig. 4.20. It can be noticed that by keeping the window oriented south, a tilt angle of 20° almost doubles

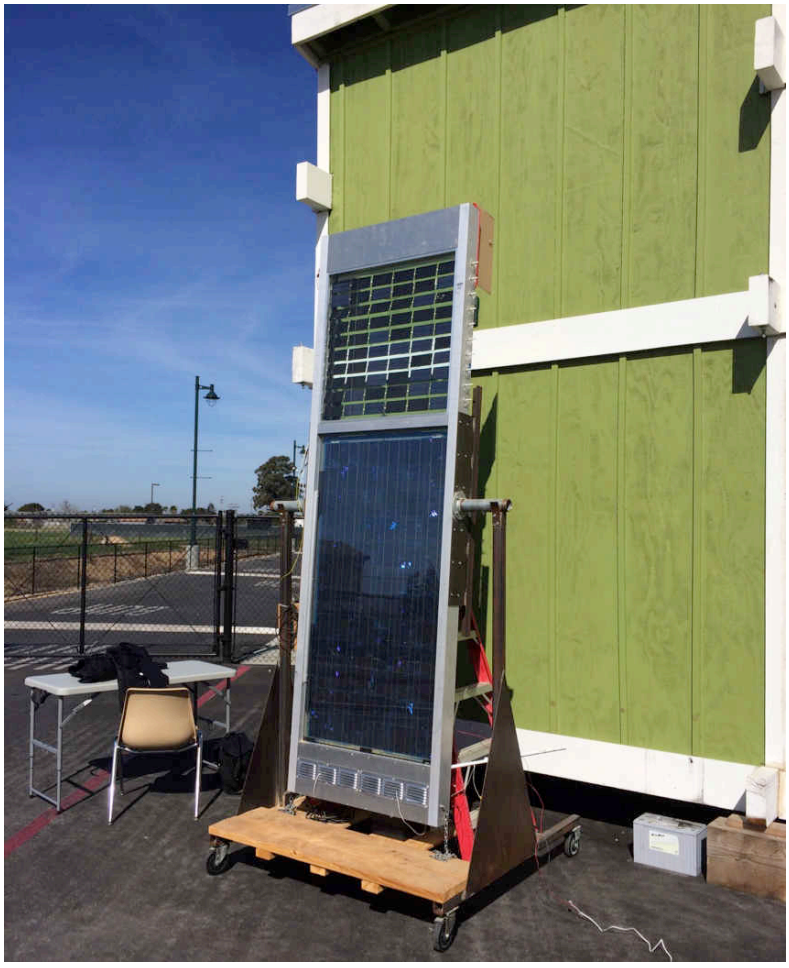

Fig. 4.18: Location for outside measurements.

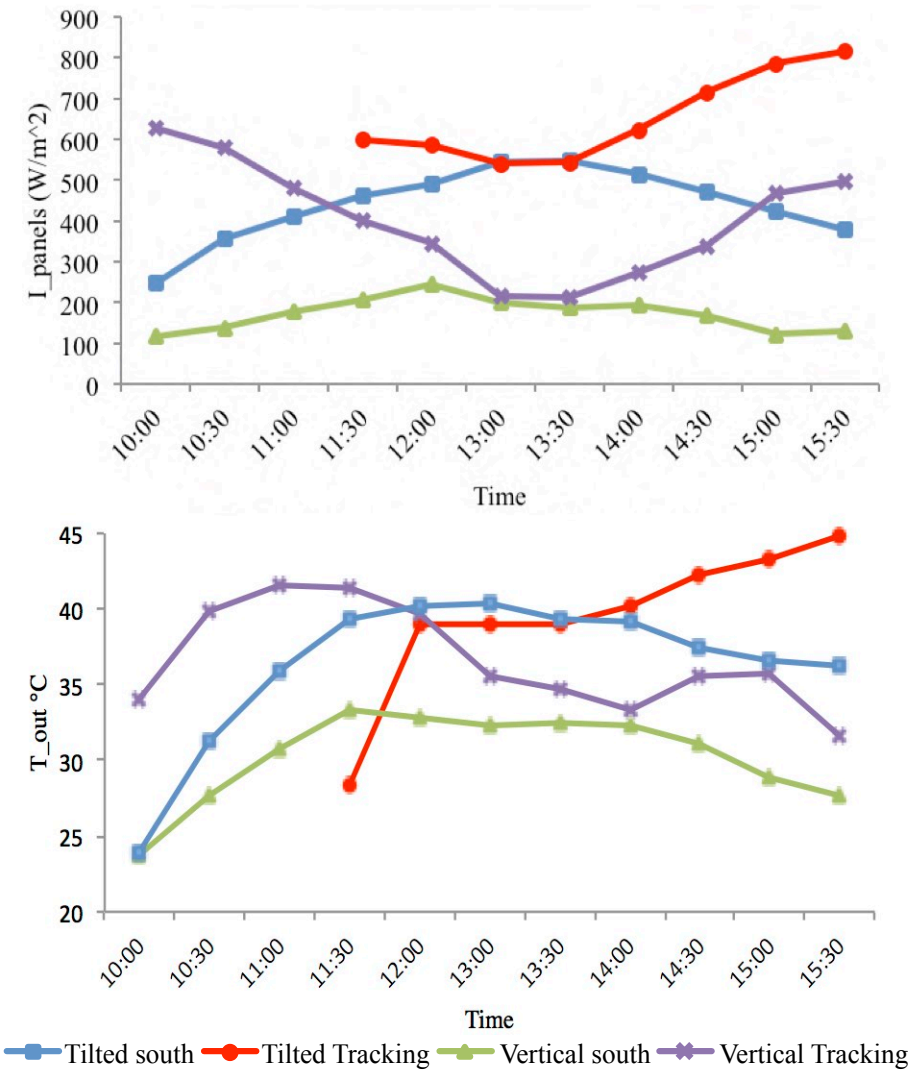

Fig. 4.19: Normal irradiance (top) and output temperature (bottom) for summer measurements.

the performances, with respect to the vertical position situation. The average temperature difference between 11:00 and 14:30 increases from 10 °C in vertical position to around 20 °C in tilted position, and as a result the heat transfer rate rises from an average of 150 W to almost 300 W. The maximum output temperature of the air increases as well from about 32 °C to slightly more than 40 °C, with a starting temperature of about 20 °C in both situations.

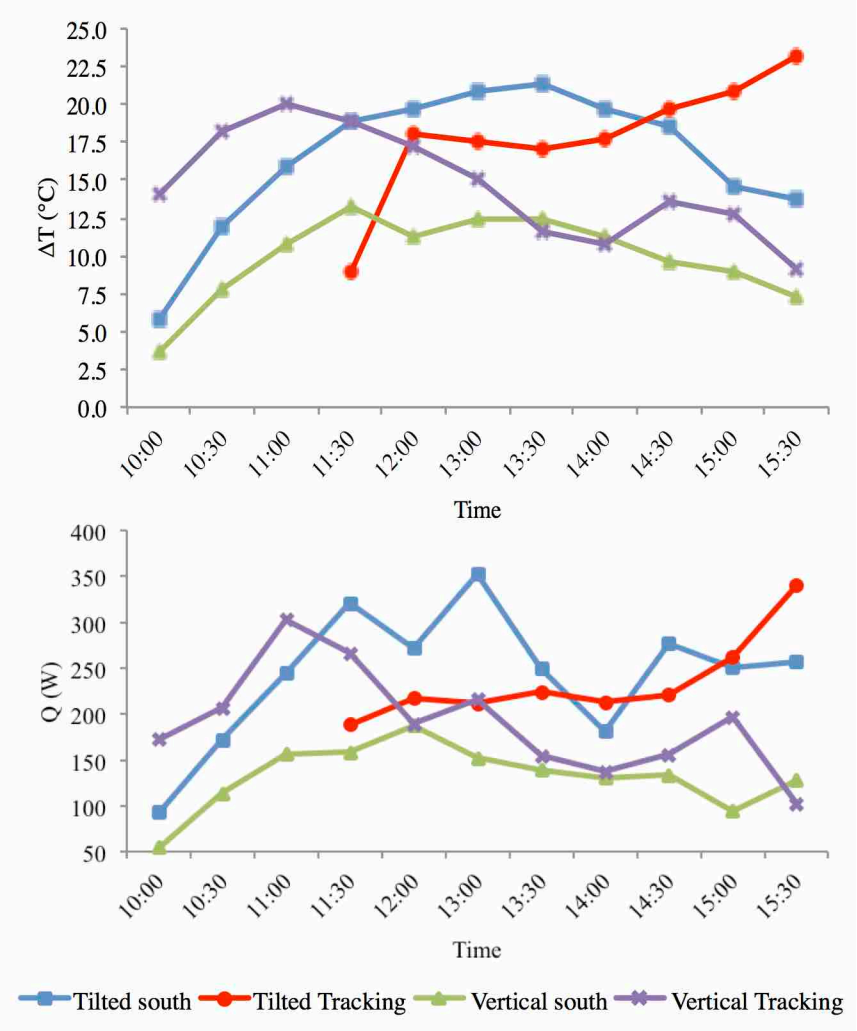

Fig. 4.20: Temperature rise (top) and heat transfer rate (bottom).

By looking at the solar irradiance profiles, it appears that the better tilting affects the radiation captured, so that the tilted south-facing configuration has the same shape of the vertical south-facing one, but it is shifted up towards higher irradiance values. At 10:00, for example, the normal irradiance is about 100 W/m^2 in the vertical case, and around 250 W/m^2 in the tilted case, and at noon is about 200 and 500 W/m^2, respectively.

Therefore, a tilting of 20° increases the incident radiation by a factor of about 2.5.

In the ideal scenario of a window always oriented in the direction of the sun, in what has been called a tracking mode, the radiation capture is further increased in morning and afternoon hours, where the elevation angle of the sun is lower, causing a bigger portion of the radiation normal component to reach the window surface. In a similar way, the performances of the tracking configurations with respect to the relative fixed south-facing counterparts are very close in the middle of the day, and much higher in earlier and later hours. As a comparison, the output temperature in tilted tracking mode maintains close to the tilted south-facing configuration (around 40 °C), and increases up to 45 °C in the afternoon. The ΔT and the heat transfer rate are instead slightly below in the central hours with respect to the fixed tilting case, even though this might be due to a different ambient temperature, as well as to a different wind speed, which affected both the cooling rate of the window and the top vent airflow measurements (resulting in an oscillating thermal power output).

4.4.2 Fall Measurements

Other measurements were taken in November and both the thermal and the electrical performances have been tested. Two sets of measurements were taken: the first set of data has been taken with the window tracking the sun during the day, and the second with the window in fixed south-facing position.

In both cases, the window was maintained vertical at an angle of 90° (with respect to the ground) for the whole day, and only during PV power measurements the tilt angles of both the window and the PV modules were changed, so as to have 4 different tilting conditions for each time data point and compare the different outputs that the array

was able to produce at the same moment. By defining β_1 as the angle between the normal to the window and the ground, and α_1 as the angle between the normal to the PV modules and the window's normal (Fig. 4.21), each PV measurement has been done by changing the tilting conditions sequentially as follows:

- $\beta_1 = 0°$, $\alpha_1 = 0°$;
- $\beta_1 = 0°$, $\alpha_1 = 20°$;
- $\beta_1 = 20°$, $\alpha_1 = 0°$;
- $\beta_1 = 20°$, $\alpha_1 = 20°$.

The results for the thermal measurements are shown in Fig. 4.22. Because of the lower elevation angle of the sun with respect to the summer testing, which resulted in a smaller radiation component reaching the collector horizontally, in fall the thermal performances in vertical position are better than the ones obtained with a 20° tilting in July, with an average ΔT of about 22 °C in both tracking and south-facing positions, and an average heat transfer rate of 400-450 W. The air at the outlet reached 50 °C in both cases, with an average of around 43-44 °C.

The testing on the photovoltaic system (Fig. 4.23) shows minimal differences in the power output. In the south-facing scenario the worst configuration is represented by the window vertical with the PV array parallel to the window's plane ($\beta_1 = 0°$, $\alpha_1 = 0°$), which gives an average power of 23 W, with a peak of 29.5 W.

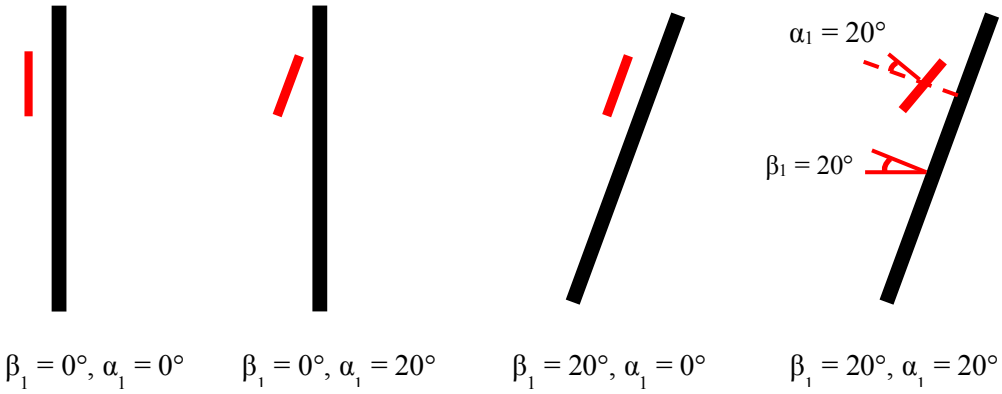

Fig. 4.21: Schematics of the 4 different tilting conditions.

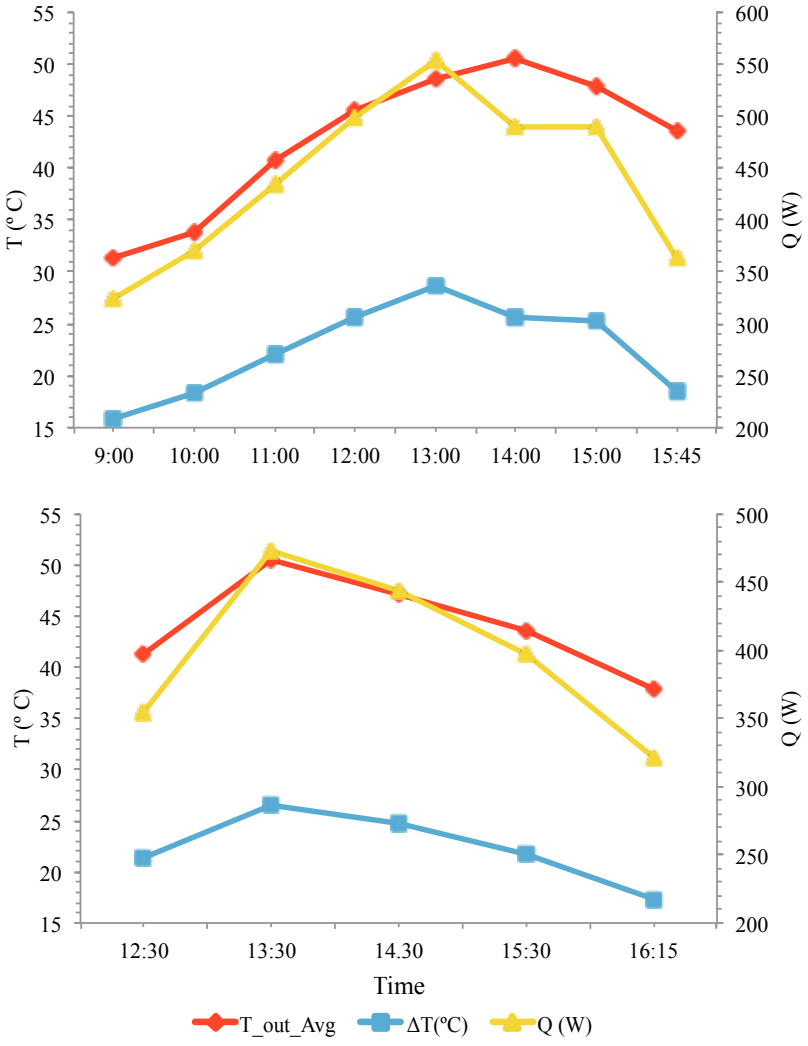

Fig. 4.22: Performance testing in fall: temperature, thermal power output and temperature difference for the south-facing (top) and tracking (bottom) conditions.

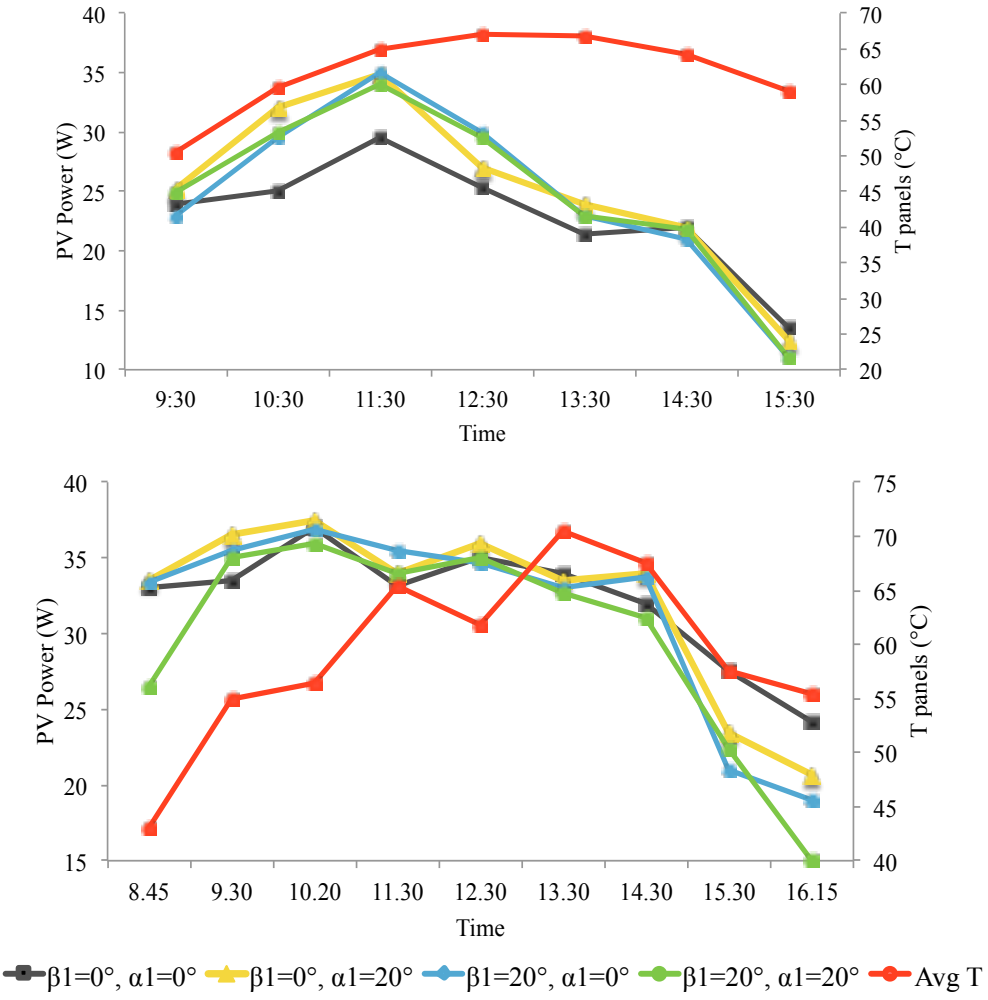

Fig. 4.23: PV array power output and temperature in different tilting conditions, for the south-facing (top) and tracking (bottom) cases.

The other configurations are instead very close, with average powers between 24.5 and 25.5 W and a peak of 34-35 W.

In tracking mode it is the most tilted configuration (β_1 = 20°, α_1 = 20°) whose performance is the poorest with respect to the others, with a peak of 36 W and an average of 29.7 W. This is due to the fact that the PV modules received less radiation in early morning and late afternoon hours, because of the high tilting (40° in total) and

low elevation of the sun. Previous configurations have instead a very similar behavior, with averages of 31.5-32 W and peaks of 37-37.5 W.

The high temperature levels, to which the PV modules are subjected, ranging from 55 to 70 °C, is one of the main causes of electrical efficiency losses. Considering the south-facing situation with $\beta_1 = 0°$, $\alpha_1 = 0°$ as an example, the peak in power is 29.5 W at 11:30, when the modules average temperature is 65 °C. The measured irradiance normal to the array plane at that time is 820 W/m^2, which results in a total input power on the whole array of 387.45 W. The actual operating efficiency can then be calculated by the ratio of power generated to the input power, which is equal to (29.5 / 387.45) x 100 = 7.6%, a result that includes optical losses through the glass, thermal losses due to the high operating modules temperatures, as well as system losses such as mismatch losses between the 60 PV modules, transmission losses through the conductors, and electronic converter losses (MPPT).

4.4.3 Winter Measurements

Other measurements were taken in February on both the thermal and the electrical system, and the impact of the airflow on the overall performances has been examined. The window was tested in vertical south-facing position, with the PV array at 90°- tilt angle, relative to the ground.

The voltage of the fans was tuned to obtain four different voltage levels. These are 6 V, 7.5 V, 9 V and 12 V, and the corresponding average air speeds measured at the output vent are, respectively, 0.5 m/s, 0.58 m/s, 0.64 m/s and 0.8 m/s, showing a linear increase of the air velocity with the voltage (Fig. 4.24).

The results for the four configurations are shown in Fig. 4.25, while the average values for the temperature rise ΔT, the electrical power P_{el}, the heat transfer rate Q, the input and output air temperature T_{in} and T_{out}, and the power consumption of the fans are reported in Table 4.4.

It can be noticed that lower air speed values result in higher temperature rises, which are close to 26°C for the 6 and 7.5 V cases, but also in lower thermal outputs, equal to 340 and 413 W, respectively. This is due to a lower convective heat transfer coefficient between the absorber surfaces (the PV modules) and the air, which results in lower heat transferred to the air and higher surface temperatures. At the highest voltage level of 12 V, corresponding to an air speed of 0.8 m/s, the ΔT drops to 24.4°C, but the heat transfer rate absorbed by the air rises to 535 W.

The electrical generation slightly increases from 20 W at 6V to 23 W at 12V, due to a drop in PV temperature (not shown in the table) from 77 °C to 71 °C, respectively.

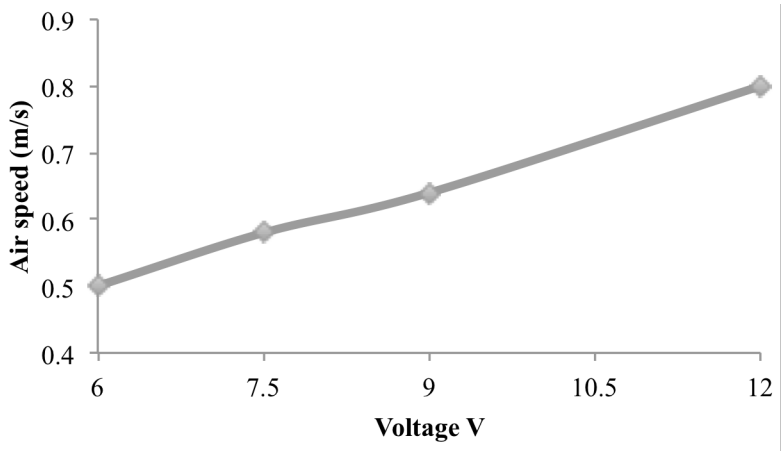

Fig. 4.24: Air velocity increment with the fans voltage.

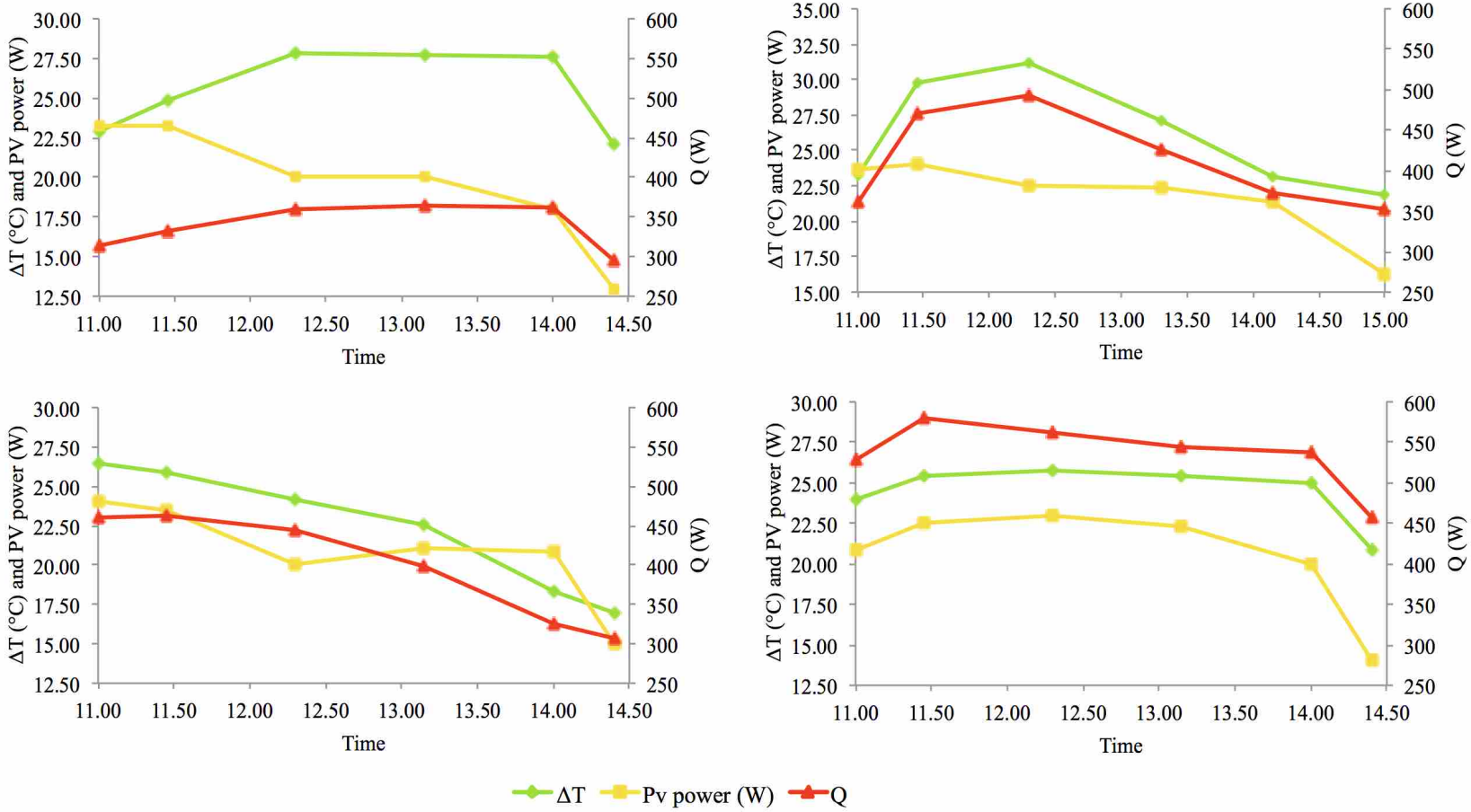

Fig. 4.25: Temperature difference, electrical and thermal power output for different voltage levels: 6V (top left), 7.5V (top right), 9V (bottom left) and 12V (bottom right).

It can also be noticed that the power consumption of the fans is maximum (19.5 W) at the rated voltage of 12 V and is less than half of this value for lower voltages.

Therefore, if thermal energy at lower temperature can be used, a higher mass flow rate is recommended, as it would improve the heat generated and the system thermal efficiency, even though the increased electrical demand for ventilation should be considered as well. For applications with a higher temperature requirement, such as space heating, a lower mass flow rate can be used, so that an air velocity of 0.58 m/s represents the optimal configuration, as it provides the highest temperature rise, and a relatively high heat transfer rate, as well as low power consumption by the fans, equal to only 8 W, resulting in a positive net electrical generation.

The thermal and electrical efficiency of the window under the different airflow conditions are reported in Fig. 4.26. As the airflow rate increases, the thermal efficiency increases as well, since a greater volume is in contact with the PV array, therefore enhancing the heat transfer coefficient between the modules and the air, which results in more heat generated for the same incident solar radiation.

Table 4.4: Average parameters under different voltage configurations: Air speed, temperature difference, electrical and thermal powers, input and output temperatures and power consumed by the fans.

Fans voltage (V)	Air speed (m/s)	ΔT (°C)	P_{el} (W)	Q (W)	T_{in} (°C)	T_{out} (°C)	Fans power consumption (W)
6	0.5	25.5	19.6	340	27.4	52.9	5
7.5	0.58	26	21.7	413	22.3	48.4	8.25
9	0.64	22.4	20.7	400	20	42.3	10.5
12	0.8	24.4	20.4	535	22.8	47.2	19.5

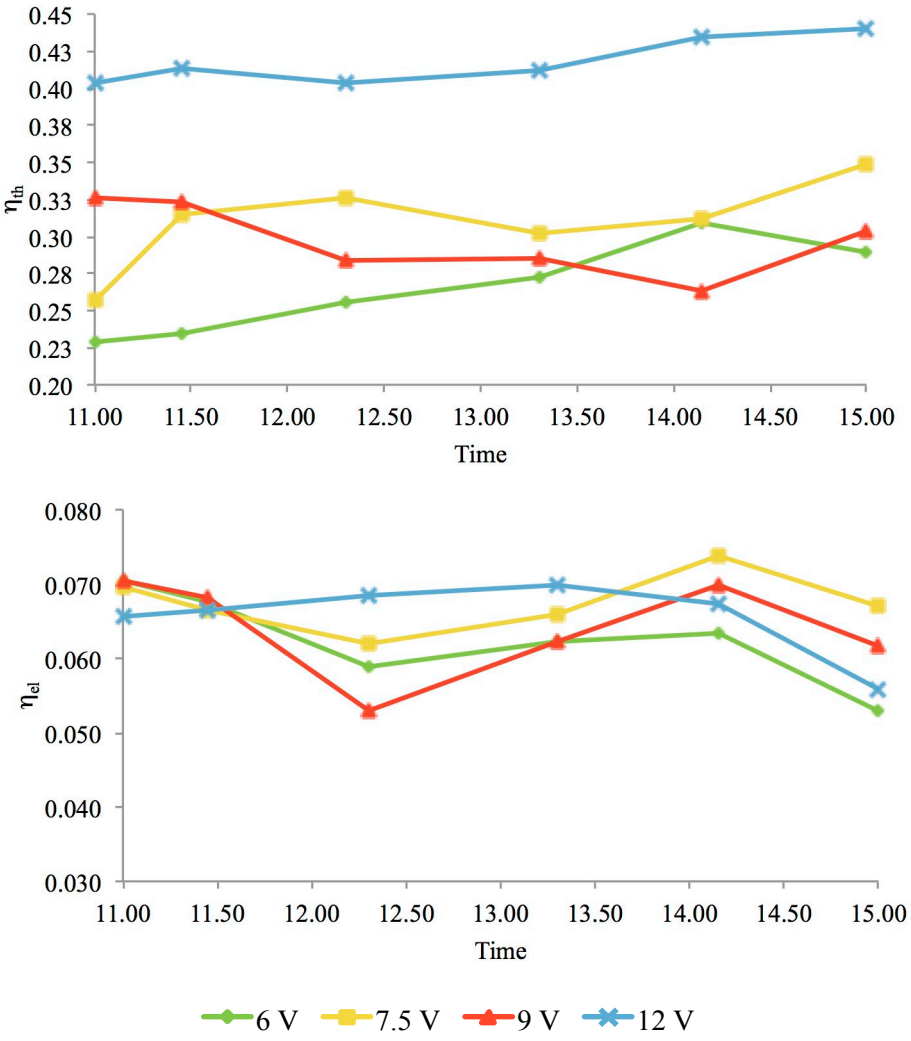

Fig. 4.26: Thermal (top) and electrical (bottom) efficiency.

A smaller temperature difference with respect to the ambient temperature also contributes to higher efficiencies at higher flow rates, because of the smaller heat losses that this implies, while at lower airflows the higher temperatures produce higher convective and radiative losses to the environment.

The values of thermal efficiency ranges between 23 - 31% for 6 V, 26 - 35% for 7.5 V, 26 - 33% for 9 V and 40 - 44% for 12 V, with average values of 27%, 31%, 30% and 42%, respectively. The optimal airflow for the temperature rise then results in a

thermal efficiency in the 31% range, while if efficiency and heat absorbed are required to be maximized, higher airflows hold better results, with an efficiency of 42%. The electrical efficiency is instead very close in both situations, and ranges between 6 and 7%, with a flatter profile for the 12V case, due to the lower temperature and higher cooling action on the PV modules by the air.

4.4.4 Comparison for the Vertical South-Facing Case

Sections 4.4.1-4.4.3 reported the several types of measurements that have been performed, which included the study of the prototype's behavior under different tilting conditions, at both fixed and tracking orientations, and under different airflow velocities. Since for the majority of residential and commercial buildings the façade are constructed vertically, the testing of the prototype in vertical position and at a fixed orientation represents the most suited configuration for common applications. In this section, a side-by-side comparison between the different seasons is provided for the vertical south-facing scenario. The results are given for the days of July 10th, November 25th and February 24th.

4.4.4.1 Thermal Results

In Fig. 4.27, the hourly change of global solar irradiance on the window surface, average air temperature output, air temperature rise between the output and input vents and heat transfer rate are shown. As it can be seen in the figure, the solar irradiance for July 10th ranges from 90 W/m^2 at 10:00 to 247.67 W/m^2 at noon, and then drops in

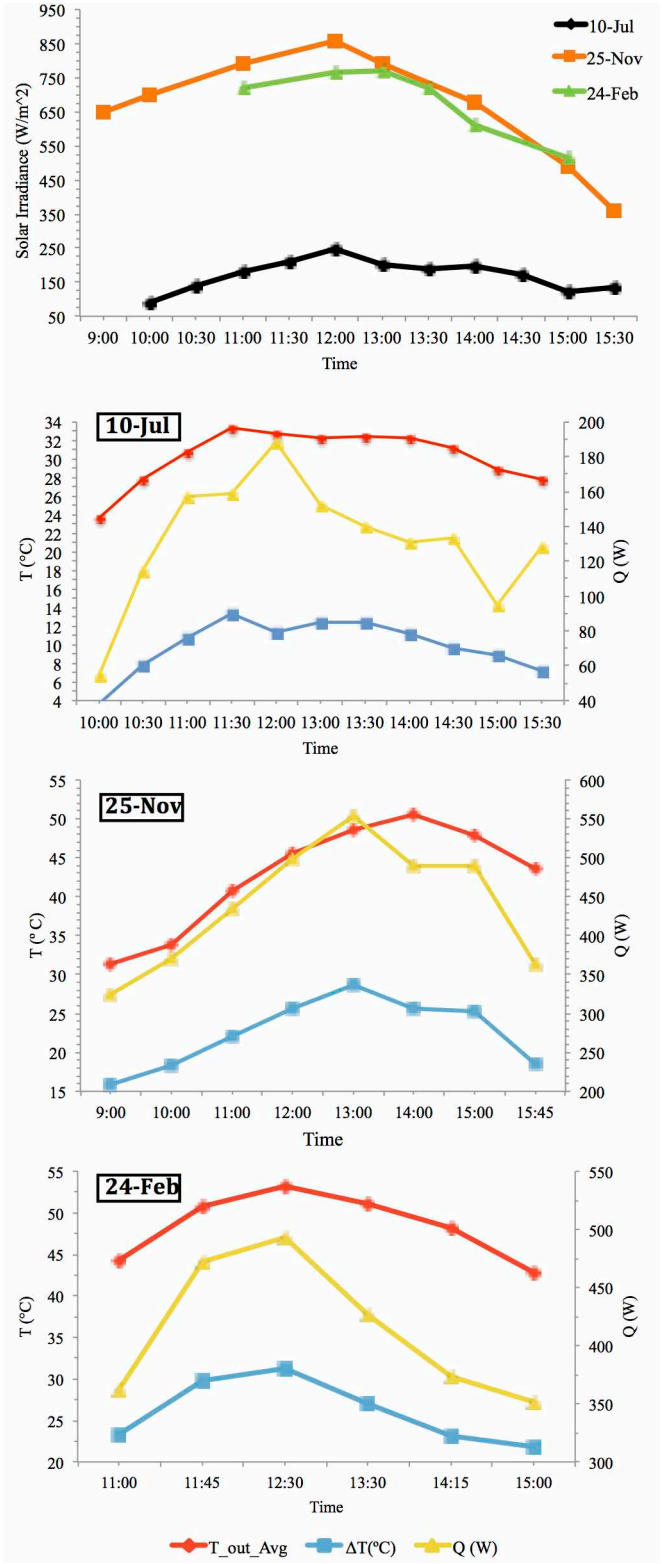

Fig. 4.27: Hourly data of the solar radiation, temperature output, temperature rise and generated heat for the days of July 10th, November 25th and February 24th.

the afternoon to values ranging from 120-200 W/m^2. The low solar input observed in the summer season is due to the high solar elevation, which was 75º at noon for July 10th, which causes a smaller horizontal component reaching the collector vertical surface. On November 25th, the solar altitude was instead 32.5º at noon, and much higher values were recorded: 650 W/m^2 is the radiation at 10:00 and 860 W/m^2 was the peak irradiance at noon, with an afternoon decrease from of 680 W/m^2 at 14:00 to 490 W/m^2 at 15:00. Very similar values were measured on February 24th, with a peak of 765 W/m^2 at noon, corresponding to a solar elevation of around 44º, and values in the 500-700 W/m^2 range from 13:30 to 15:00.

It can be seen that the different solar inputs are reflected on the temperature and heat transfer rate profiles in the results. The output temperature reaches a maximum of 33.3ºC at 11:30 on July 10th, with values ranging from 30 to 32ºC for most of the day, while the maxima are 50.5ºC for November 25th and 53.2ºC for February 24th, with average values from 11:00 to 15:00 of 46.7ºC and 48.4ºC, respectively. The average air temperature rise between 11:00 and 15:00 are 11.2ºC for the summer, 25.4ºC for the fall and 26ºC for the winter results, with peaks of 13.3ºC, 28.6ºC and 31.2ºC, respectively. The heat generated on July 10th is most of the time within a narrow range of 100-160 W, with a peak of 188W at noon, while the increased temperature rise in the fall and winter seasons makes these results more than double for November 25th and February 24th, with average values from 11:00 to 15:00 of 476.7W and 412.9W, respectively, and peaks of 553W and 492.6W, respectively.

4.4.4.2 Electrical Results

Fig. 4.28 shows the profiles of the electrical power generated and the average temperature on the back of the modules for November 25th and February 24th. The results are given for a PV array tilting of 90° with respect to the ground, that is the normal to the window and the normal to the PV array are parallel. In fall the lower solar altitude and lower modules temperature provide a higher photovoltaic generation, with an average of 24.5W from 9:30 to 14:30 and a peak of 29.5W. PV temperatures

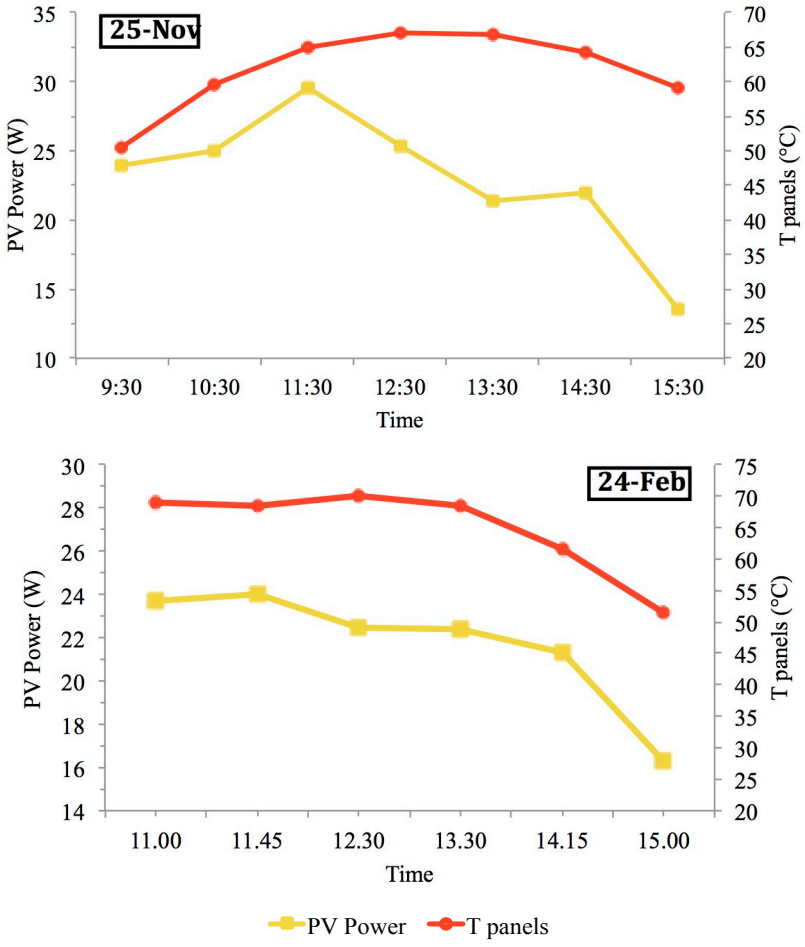

Fig. 4.28: Hourly variation of average modules temperature and PV power output for November 25 (left) and February 24 (right).

ranges from 50°C to 67°C, with an average of 64.5°C from 10:30 to 14:30. The electrical generation for 24.02.2015 is instead 22.8W on average from 11:00 to 14:15, with a peak of 24W at 11:45, and the average temperature in the same time range is 67.5°C, with a peak temperature of 70°C.

4.4.4.3 Efficiency

Fig. 4.29 shows the thermal and electrical efficiency of the prototype for the different tested seasons. On July 10 the thermal efficiency remains very close to the 37-40%

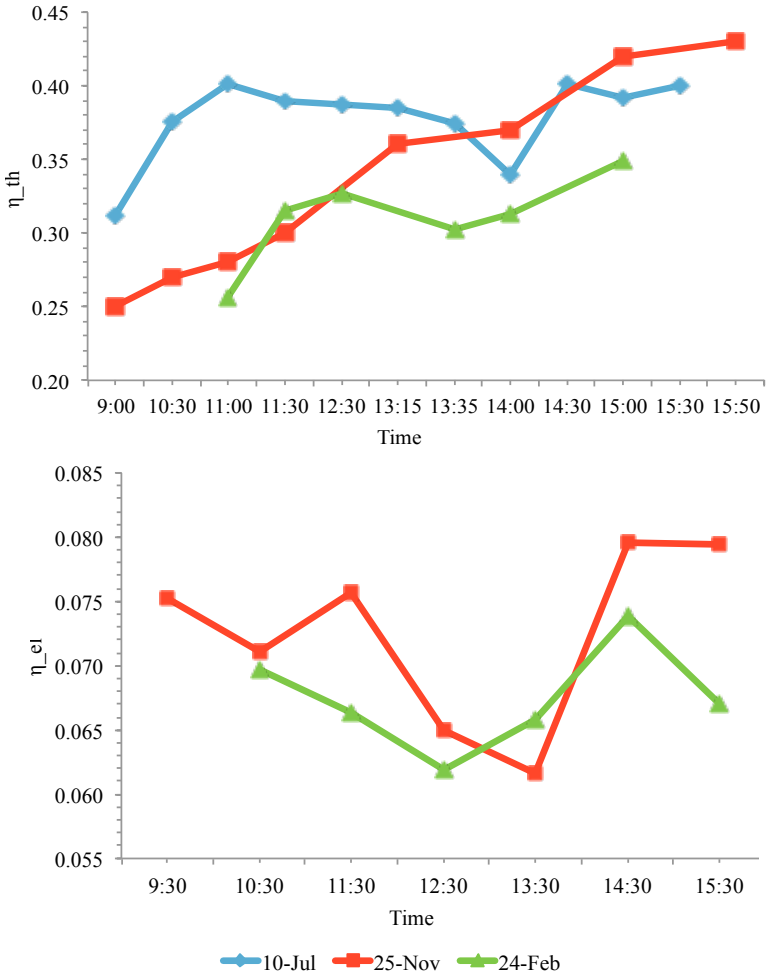

Fig. 4.29: Thermal efficiency (left) and electrical efficiency (right) for the tested seasons.

range, also due to lower operating temperatures that causes lower heat losses, while greater differences occur in fall and winter, where values between 25% and 43% for November 25th and between 26% and 35% for February 24th are achieved.

The minimum and maximum values for the electrical efficiency are 6.16% and 7.96% for November 25th and 6.2% and 7.4% for February 24th, respectively, while the averages are 7.2% in fall and 6.7% in winter.

In order to improve the efficiency and achieve higher temperatures, the features of the current prototype need to be optimized. This includes designing a better absorber, which means enhancing the radiation captured by the PV array and improving the heat transfer coefficient between the array and the air, in order to obtain higher heat collected by the airflow and lower PV temperatures, which is expected to increase both the thermal and electrical efficiency. The efficiency of the PV modules used has to be chosen according to the specific thermal and electrical requirements, since more efficient modules would convert a higher portion of radiation into electricity, but would also generate less heat and vice versa. The frame of the current design is made of aluminum, which is one of the main causes of heat losses, and therefore it requires further improvements with a better design and the use of different materials. Another component requiring optimization is the glazing system, which affects the solar radiation transmitted to the inside as well as the convective and radiative heat losses from the interior to the outside environment. The installation of additional glass panels and the use of low-emissivity or spectrally selective coatings may contribute to the system performances.

Chapter 5
CFD Modeling in COMSOL

5.1 Introduction

After the first phase of field data collection and performance assessment of the current prototype, the project main objective has been directed towards improving the collector performance. In order to determine which steps have to be taken in designing a more efficient airflow window, its thermal and fluid-dynamic behavior need to be understood. To this scope, 2D and 3D models were built in COMSOL Multiphysics v5.2a, and the heat transfer and fluid flow within the window in forced convection were analyzed through a series of CFD simulations, which were used to optimize various aspects influencing the thermal and electrical performance.

A first fundamental step has been developing a base model that would replicate the experimental findings. This served as a starting point for the subsequent models used for optimization, which will predict the system behavior upon various conditions, such as changes in the geometry, material properties, and physical parameters.

In this chapter, the development of a two-dimensional model in COMSOL to simulate conjugate heat transfer (heat transfer and fluid flow coupling) will be presented, along with a comparison between the experimental data and the results obtained from the simulation. This first model served as a starting point to build more expanded 2D and 3D models, which were then used for the optimization as well as for the design of new prototypes, by editing the prototype's features, such as geometrical layout, material properties and operational parameters.

The measured data from Feb. 24, 2015, at 11:00 in Salinas, CA (36.67ºN), were used for the input solar irradiance and the boundary conditions for the inlet air temperature, output air velocity and wind speed.

5.2 Overview of Finite Element Analysis

As a Finite Element Analysis (FEA) software, COMSOL Multiphysics uses algorithms that are based on the Finite Element Method (FEM). This is a numerical technique that works by subdividing the model domain (representing the physical medium) into a sufficient number of small elements, interconnected to each other at nodal points, whose aggregate is called a mesh. The partial differential equations (PDE), which usually describe most physical phenomena, are approximated with a set of algebraic equations or ordinary differential equations (ODE), and the dependent variables of interest, such as temperature, velocity and pressure, are solved for each node [22]. The sets of equations at each node are then combined to form a global system of equations that, together with boundary conditions and initial values, gives the final solution for the whole domain.

By approximating the PDEs with numerical model equations, numerical methods like FEM allow to handle nonlinear problems as well as complex geometries (representing the majority of real problems) that cannot be solved with analytical methods, whose solutions can easily be found only for limited cases. FEA simulations are therefore useful for better understanding and predicting real-life processes and devices, and they can be a valuable resource to reduce the number of prototypes and experiments that needs to be developed when designing or optimizing a product.

5.3 COMSOL Model

The COMSOL Multiphysics modeling workflow is summarized as follows:

- Global definitions (parameters and variables that are used through the model);
- Set up of the geometry to be studied;
- Material selection for the different parts of the geometry;
- Definition of physics interfaces (e.g. heat transfer, fluid flow);
- Mesh generation;
- Study type selection (steady state or transient) and solution computation;
- Results generation (e.g. plots, data sets and tables).

The complete model tree for the current model is reported in Fig. 5.1, where all the main nodes are displayed, with those for the physics interfaces further expanded. The principal nodes will be discussed in the following sections, including modeling assumptions and boundary conditions (B.C.).

5.3.1 Global Parameters

In the Global Definitions node, the global parameters used through the model are defined. These include ambient pressure, wind speed, glass transmittance, and solar irradiance, as well as geometrical parameters used to create the geometry (Table 5.1). The ambient parameter values (p_a, I_solar and v_air) have been taken from the reference experimental data (Feb. 24, 2015, at 11:00).

The incident irradiance has been set to the observed value of 1140W/m^2, which is above the 1000W/m^2 value that is normally used for defining STC performance of

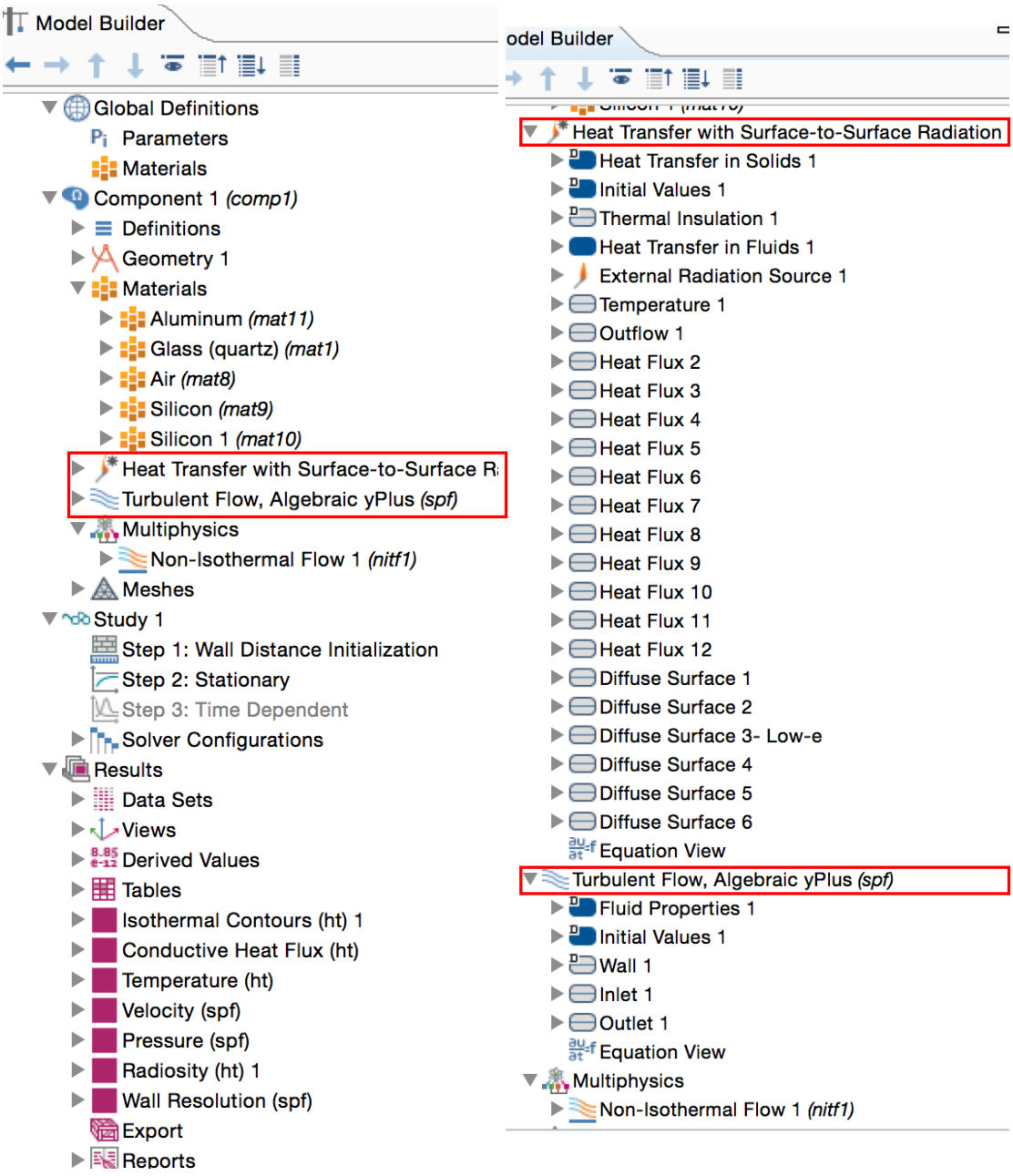

Fig. 5.1: Model tree (left), with expanded physics interface nodes (right).

solar panels. Ibrahim et al. [111] reported determinations of the global tilted irradiance for various months in a close latitude location (30.78ºN), with a maximum value of 1152.97 W/m^2 in March of 2009, that would suggest that a similar value for the global tilted irradiance at solar azimuth and elevation could be possible for 36º latitude in late

February. The measured value of the global tilted irradiance might also indicate a larger contribution of the reflected component, due to the light-colored concrete pavement of recent installation on the site (albedo values around 0.4–0.5), as well as the proximity to several metallic surfaces, which could cause extra reflections. The very clear sky and dry conditions on February 24, 2015, with a relative humidity of less than 30% at 11am, as well as a solar constant of about 1394 W/m^2 might be other contributing factors.

An assumption that was made in the model in order to account for the transmission losses through the glass has been to multiply the solar irradiance by the measured transmission coefficient of 0.937. This underestimates the solar heat flux reaching the frame (the glass is modeled as fully transparent to the solar spectrum, as it will be shown later). However, due to the limited ratio between the frame and glass area, as well as the low solar absorbance of the frame material, a difference of about 72 W/m^2 was not expected to cause appreciable changes in the temperature field.

Table 5.1: Global parameters.

Name	Expression	Value	Description
p_a	101325[Pa]	101325 Pa	Ambient pressure
t_g	0.937	0.937	Front glass solar transmittance
I_solar	1140 [W/m^2]	1140 W/m²	Solar irradiance
G_solar	I_solar*t_g	1068.18 W/m²	Effective solar irradiance
t	3.175[mm]	0.003175 m	Frame Thickness
H1	1605[mm]	1.605 m	Bottom glass height
H2	808[mm]	0.808 m	Top glass height
v_air	4[m/s]	4 m/s	Ambient wind speed

By assuming a normal solar heat flux of 1140 $W/m^2 \cdot 0.937 = 1068.2$ W/m^2 on both the glazed (1.96 m^2) and frame frontal area (0.41 m^2), the total incoming solar power is calculated to be 2532.4 W. This compares to a value of 2562 W when glass transmissivity is only accounted for the glazed portion of the total area, resulting in a relative error of 1.2%.

5.3.2 Geometry

A simplified cross-sectional geometry has been modeled, in order to reduce the computational cost for solving the internal flow through the window, as shown in Fig. 5.2, where the air domain and the solid domains (frame, glass and PV) are illustrated. The vents are placed along the vertical axis in order to facilitate vertical flow, and the holes connecting the frame cavities to the double-glazing channels were replaced with open passages. The fans were removed, which were accounted for as an output velocity boundary condition, and the heat exchanger was also not included in the model. The thicknesses for the aluminum shells, PV blinds and bottom PV module were set to 3.175mm (1/8 in), 3mm and 8mm, respectively.

5.3.3 Materials

In addition to glass, aluminum and silicon were applied to the frame and PV domains, respectively, whose properties are reported in Table 5.2. The air thermal conductivity, specific heat at constant pressure and dynamic viscosity were computed using 4^{th} order temperature-dependent polynomial expressions, while Equation 26 was used for the density as a function of temperature.

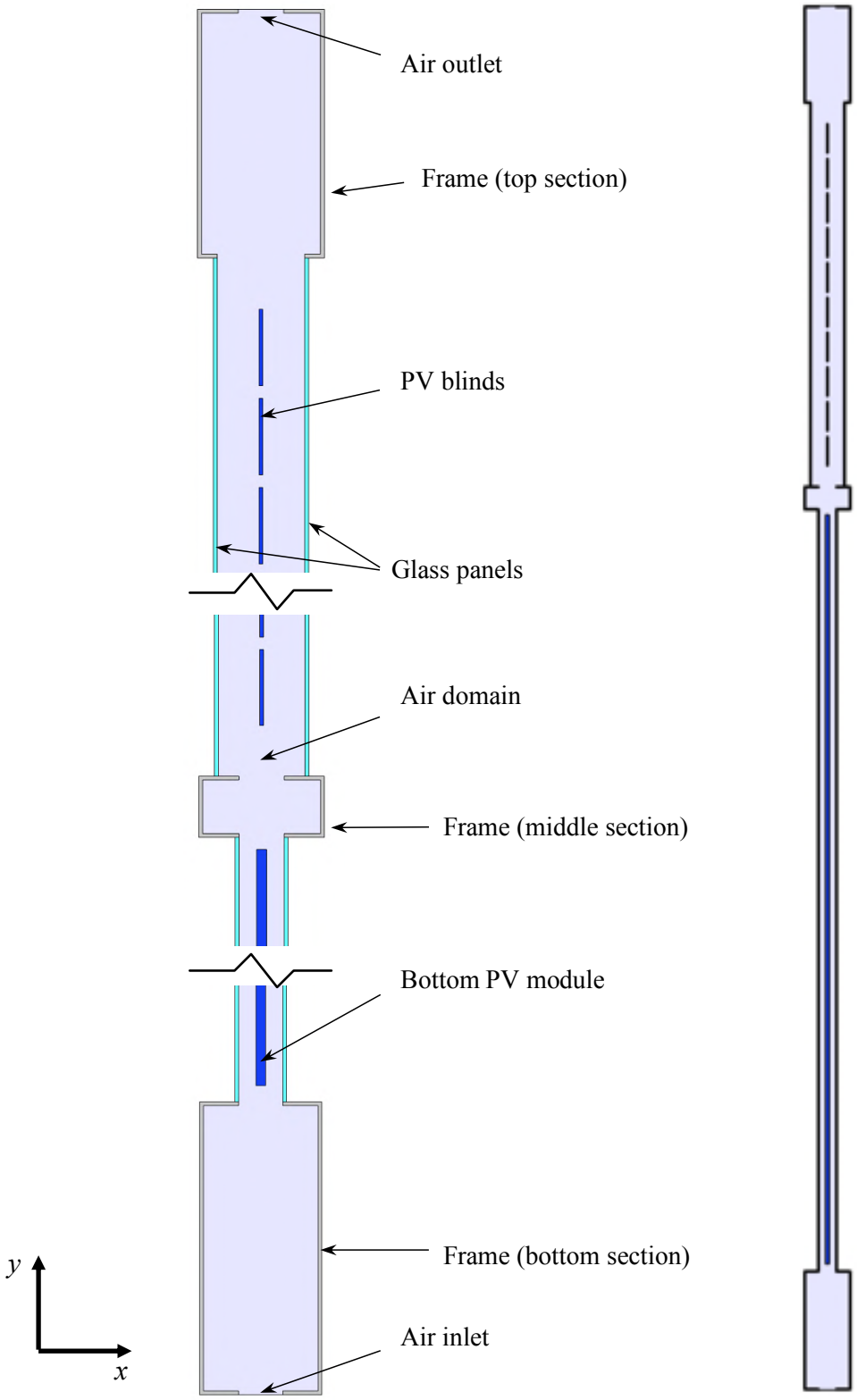

Fig. 5.2: 2D model geometry: close-up views for the bottom, middle and top parts (left), and whole geometry (right).

Table 5.2: Material properties.

Material	Density [kg/m^3]	Thermal conductivity [W/m·K]	Specific heat at constant pressure [J/kg·K]	Emissivity visible band	Emissivity NIR band	Emissivity far infrared band
Aluminum	2700	238	900	0.37	0.37	0.03
Glass	2210	1.4	730	–	–	0.84
Silicon	2329	130	700	0.85	0.85	0.9

One assumption included the modeling of the PV modules as a single domain made of silicon, having therefore a high thermal conductivity. The actual structure of the PV modules include thermally resistive layers (mostly resin for the small modules), encapsulating the solar cells, which would result in a higher temperature gradient within the module, with higher temperatures in the silicon layer and lower temperatures on the exterior boundaries. A model taking thermal resistance effects in the PV will be shown later in Chapter 6.

5.3.4 Heat Transfer Interface

The model solves the conjugate heat transfer problem where both conduction in the solid domains and convection within the airflow are involved, and couples the heat equations with the continuity and momentum equations for the fluid flow. It also accounts for the solar radiation incident on the window, the radiation exchange between surfaces, and the convective cooling by the outside environment.

5.3.4.1 Heat Transfer in Solids

The general heat conduction equation in Cartesian form can be expressed as [22]:

$$\frac{\partial}{\partial x}\left(k\frac{\partial T}{\partial x}\right)+\frac{\partial}{\partial y}\left(k\frac{\partial T}{\partial y}\right)+\frac{\partial}{\partial z}\left(k\frac{\partial T}{\partial z}\right)+\dot{q}_{gen}=\rho c_p\frac{\partial T}{\partial t} \tag{31}$$

where k, ρ and c_p are the material thermal conductivity, density and specific heat at constant pressure, respectively, T is the temperature variable, $\dot{q}_{gen}$ is the heat generation rate per unit volume within the medium, and t is time. This is an energy conservation equation, stating that the net rate of heat transfer into a unit volume plus the heat generation per unit volume equals the rate of change of the thermal energy stored within the volume [22]. In steady state, and with no heat generation, Equation 31 becomes:

$$\frac{\partial}{\partial x}\left(k\frac{\partial T}{\partial x}\right)+\frac{\partial}{\partial y}\left(k\frac{\partial T}{\partial y}\right)+\frac{\partial}{\partial z}\left(k\frac{\partial T}{\partial z}\right)=\nabla\cdot\left(k\nabla T\right)=0 \tag{32}$$

If thermal conductivity is constant, as it is the case for the solid domains in the model, Equation 31 further reduces to the Laplace equation:

$$\frac{\partial^2 T}{\partial x^2}+\frac{\partial^2 T}{\partial y^2}+\frac{\partial^2 T}{\partial z^2}=\nabla^2 T=0 \tag{33}$$

which in the two-dimensional model is solved for the x and y components.

5.3.4.2 Heat Transfer in Fluids

For the heat transfer within the air domain, the effects of fluid motion (advection) have to be taken into account. By assuming both viscous heating effects and the work done by pressure changes to be negligible (it is usually the case for low velocity flow [18], [112]), the heat equation for the air domain can be written as:

$$\rho c_p\frac{\partial T}{\partial t}+\rho c_p\left(u\frac{\partial T}{\partial x}+v\frac{\partial T}{\partial y}+w\frac{\partial T}{\partial z}\right)=\frac{\partial}{\partial x}\left(k\frac{\partial T}{\partial x}\right)+\frac{\partial}{\partial y}\left(k\frac{\partial T}{\partial y}\right)+\frac{\partial}{\partial z}\left(k\frac{\partial T}{\partial z}\right)+\dot{q}_{gen} \tag{34}$$

where the term $\rho c_p\left(u\frac{\partial T}{\partial x}+v\frac{\partial T}{\partial y}+w\frac{\partial T}{\partial z}\right)=\rho c_p\mathbf{u}\cdot\nabla T$ is added with respect to Equation 31, representing the net energy convected out of the control volume by the fluid, with **u** = (*u*, *v*, *w*) being the velocity vector. In steady state and with no heat generation within the fluid, Equation 33 reduces to:

$$\rho c_p\mathbf{u}\cdot\nabla T=\nabla\cdot(k\nabla T) \tag{35}$$

which is solved for the x and y component.

The model couples the heat transfer and fluid flow physic interfaces, so that the velocity vector **u** is computed through the fluid motion equations and inputted to Equation 35.

5.3.4.3 Radiation Settings

The radiation was divided into 3 spectral bands:

- UV and visible spectrum: $0 < \lambda < 780$ nm;
- Solar near infrared (NIR): 780 nm $< \lambda <$ 2.5 μm;
- Long-wave infrared: $\lambda >$ 2.5μm.

This enables us to specify the materials opacity for each individual spectral band, so that glass can be considered to be transparent to the visible and NIR bands (or selective in the NIR, as shown in Chapter 6), but opaque to the infrared portion, while the frame and the PV domains were set to be opaque to the whole spectrum of wavelengths.

5.3.4.4 Solar Radiation Modeling

The sun is modeled as an infinite distance external radiation source emitting radiation as a blackbody at 5780 K, and the radiation direction $\mathbf{i_S}$ was set to reproduce the incidence angle of the sun rays at the local solar elevation in Salinas, CA on February 24th, 2015 (–43.2° with respect to the *x* axis), that is $\mathbf{i_S} = 0.729\hat{x} - 0.684\hat{y}$, where $\hat{x}$ and $\hat{y}$ are the unit vectors for the *x* and *y* axis, respectively.

5.3.4.5 Radiative Boundary Conditions

Diffuse surface B.C. were set to all boundaries participating in surface-to-surface radiation, with the emissivities of the different materials for each spectral bands set to the values reported in Table 5.2. For the frame and the PV domains, which are opaque to solar radiation, the emissivity in the first two spectral bands ($0 < \lambda < 2.5$ μm) is equal to the solar absorptivity, due to the Kirchhoff's law for diffuse-grey surfaces (Equation 10). Since the first model was aimed at reproducing the current prototype design, no glass coatings were considered, and an emissivity of 0.84 in the long-wave infrared was used for all the 4 glass surfaces of the 2 panels.

The net radiative heat flux entering a surface at a certain point *P* (Fig. 5.3) is given by the difference between the incoming radiation *G* and the outgoing radiative heat flux from the surface, also called radiosity, *J* [112]:

$$q_{rad} = G - J \tag{36}$$

The radiosity is defined as the sum of the reflected radiation ρG and the emitted radiation by the surface $\varepsilon e_b(T)$:

$$J = \rho G + \varepsilon e_b(T) \tag{37}$$

where ρ is the surface reflectivity, ε is the surface emissivity and $e_b(T)$ is the blackbody emissive power. This is defined, according to the Stefan-Boltzmann law, as [27]:

$$e_b(T) = n^2 \sigma T^4 \tag{38}$$

where n is the refractive index of the medium into which the surface emits radiation (n = 1 for air), σ = 5.670·10^{-8} W/m^2·K^4 is the Stefan-Boltzmann constant and T is the absolute temperature of the surface in K.

By considering a diffuse-grey approximation for opaque surfaces (radiative properties independent of wavelength and direction), for which $\alpha = \varepsilon = 1 - \rho$, and by using Equations 36-38, the net inward radiative heat flux can be written as [112]:

$$q_{rad} = \varepsilon(G - e_b(T)) \tag{39}$$

This is the main expression used for the radiative boundary conditions in the model.

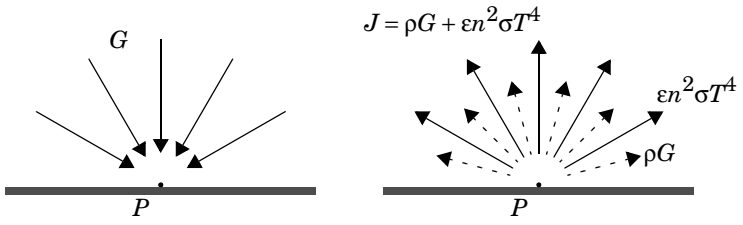

Fig. 5.3: Incoming (left) and outgoing radiation (right) at a point *P* on a surface [112].

In order to evaluate q_{rad}, the irradiation G needs to be computed. This is the sum of three contributions, expressed as:

$$G = G_m + G_{ext} + G_{amb} \tag{40}$$

where G_m is the mutual irradiation coming from other surfaces, G_{ext} is the irradiation from external radiation sources (the sun), and G_{amb} is the ambient irradiation. The last two terms, that is G_{ext} and G_{amb}, are computed, respectively, as the product of the external heat source view factor by the source irradiance and the product of the ambient view factor by the ambient emissive power (based on ambient temperature T_{amb}). The mutual irradiation term G_m, however, depends on the radiosity of the radiating surface; therefore, G is a function of the radiosity, which must be computed. The radiosity is in turn a function of G_m, resulting in the implicit expression [112]:

$$J = (1-\varepsilon)\left(G_m(J) + G_{ext} + G_{amb}\right) + \varepsilon e_b(T) \tag{41}$$

The radiation has been divided into 3 spectral bands, therefore Equations 39 and 41 become:

$$q_{rad} = \sum_{i=1}^{3} \varepsilon_{Bi}\left(G_{m,Bi}(J_{Bi}) + G_{amb,Bi} + G_{ext,Bi} - e_b(T)FEP_{Bi}(T)\right) \tag{39-1}$$

$$J_{Bi} = (1-\varepsilon_{Bi})\left(G_{m,Bi}(J_{Bi}) + G_{amb,Bi} + G_{ext,Bi}\right) + \varepsilon_{Bi} e_b(T)FEP_{Bi}(T) \quad i = 1,2,3 \tag{41-1}$$

where *Bi=B1, B2, B3* refer to the UV/visible, NIR and long-wave infrared spectral bands, respectively, and $FEP_{Bi}(T)$ is the fractional emissive power, which is computed for each spectral band as a function of surface temperature and the band endpoints [112].

The initial values for the surface radiosity are defined for each band interval as:

$$J_{Bi,init} = \varepsilon_{Bi} e_b(T_{init}) FEP_{Bi}(T_{init}) + (1-\varepsilon_{Bi}) e_b(T_{amb}) FEP_{Bi}(T_{amb}) \tag{42}$$

where T_{init} is the initial surface temperature, which was set to 293.15 K for all boundaries.

5.3.4.6 Convective Heat Flux Boundary Conditions

The convective cooling by the wind on the exterior surfaces of the window was accounted for as convective heat flux boundary conditions. The convective heat flux q_{conv} (W/m^2) is calculated by using the Newton's law of cooling [22]:

$$q_{conv} = h \cdot (T - T_{ext}) \tag{43}$$

where h [W/m^2·K] is the convective heat transfer coefficient of air, and T and T_{ext} are the surface and air temperatures, respectively. For the calculation of h, it was assumed external forced convection on a flat plate, which implies that the convective heat transfer coefficient is a function of the plate length L, the air velocity U, the ambient pressure p_A and the temperature-dependent air properties. The following correlation was used [112]:

$$h = \frac{2k}{L} \frac{0.3387 \mathrm{Pr}^{1/3} \mathrm{Re}_L^{1/2}}{\left(1 + \left(0.0468/\mathrm{Pr}\right)^{2/3}\right)^{1/4}} \quad \text{if } \mathrm{Re}_L < 5 \cdot 10^5 \tag{44}$$

where Pr and Re_L are the Prandtl and Reynolds numbers, respectively, defined as:

$$\mathrm{Pr} = \frac{\mu c_p}{k} \tag{45}$$

$$\mathrm{Re}_L = \frac{\rho U L}{\mu} \tag{46}$$

and k [W/m·K], μ [kg/(s·m)] ρ [kg/m^3] and c_p [J·kg/K] are the air thermal conductivity, dynamic viscosity, density and specific heat, respectively, which are evaluated at $(T+T_{\mathrm{ext}})/2$.

T_{ext} (K), U (m/s) and L (m) are the correlation input parameters. An ambient temperature of 293.15 K was used for the air temperature T_{ext}, and the air velocity was set to the global parameter v_air, whose value of 4 m/s is the average wind speed reported by meteorological data between 10:00 and 14:00 for the reference day and location [113]. The plate length was set to the length of the single boundary, and one heat flux B.C. was defined for each pair of symmetric boundaries with respect to the y-axis, that is the window symmetry axis, as shown in Fig. 5.4. The figure reports the settings for the two glass surfaces at the top of the window, for which L = 0.808m. In the software, Equation 43 is written in terms of the inward heat flux q_0 entering the boundary, so a negative value would represent convective cooling of the boundary to the outside environment.

The applicability of Equation 44, valid for Reynolds numbers below $5 \cdot 10^5$, can be verified for the above case, by evaluating Re_L for L = 0.808m and air properties at 20°C:

$$\mathrm{Re}_{L=0.808m} = \frac{1.2047\left(\frac{kg}{m^3}\right) \cdot 4\left(\frac{m}{s}\right) \cdot (0.808m)}{1.8205 \cdot 10^{-5}\left(\frac{kg}{m \cdot s}\right)} = 2.14 \cdot 10^5 \tag{47}$$

The maximum Re_L would be obtained for the longest boundary, which is the bottom glass surface, with L = 1.605 m. In this case, $Re_L = 4.25 \cdot 10^5 < 5 \cdot 10^5$.

5.3.4.7 Inlet and Outlet Boundary Conditions

A temperature B.C. of 21°C was set at the inlet of the air domain, which is the measured air temperature at the input vent. An outflow B.C. was applied to the outlet, which states that the only heat transfer occurring across the boundary is by convection, and sets the temperature gradient in the normal direction to zero.

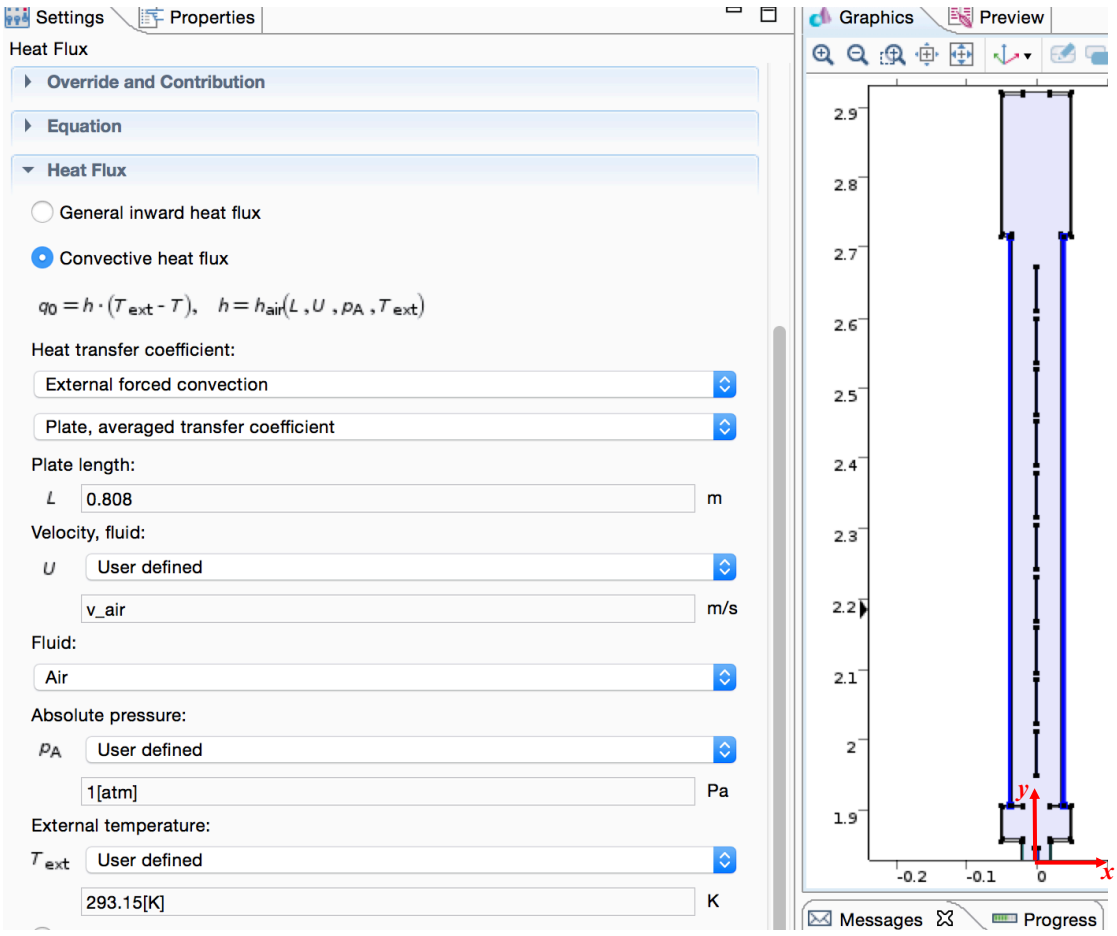

Fig. 5.4: Convective heat flux settings in COMSOL.

5.3.5 Fluid Flow Interface

The two equations of motion to be solved are the continuity and the momentum (Navier-Stokes) equations. For a non-isothermal laminar flow in steady-state, where the density changes with temperature, their fully compressible formulation can be written as [112]:

$$\nabla\left(\rho\cdot\mathbf{u}\right)=0 \tag{48}$$

$$\rho\mathbf{u}\cdot\nabla\mathbf{u}=-\nabla p+\nabla\cdot\left[\mu\left(\nabla\mathbf{u}+\left(\nabla\mathbf{u}\right)^{T}\right)-\frac{2}{3}\mu\left(\nabla\cdot\mathbf{u}\right)\mathbf{I}\right]+\rho\mathbf{g} \tag{49}$$

where ρ and μ are the fluid density and dynamic viscosity, $\mathbf{u} = (u, v, w)$ is the velocity vector, p is the pressure field**,** $\mathbf{I}$ is the identity matrix and $\mathbf{g}$ is the gravity vector.

In 2-D Cartesian form, the continuity equation can be rewritten as:

$$\frac{\partial\left(\rho u\right)}{\partial x}+\frac{\partial\left(\rho v\right)}{\partial y}=0 \tag{50}$$

and the momentum x and y components as [114]:

$$x:\quad \rho\left(u\frac{\partial u}{\partial x}+v\frac{\partial u}{\partial y}\right)=-\frac{\partial p}{\partial x}+\frac{\partial}{\partial x}\left[2\mu\frac{\partial u}{\partial x}-\frac{2}{3}\mu\left(\frac{\partial u}{\partial x}+\frac{\partial v}{\partial y}\right)\right]+\frac{\partial}{\partial y}\left[\mu\left(\frac{\partial u}{\partial y}+\frac{\partial v}{\partial x}\right)\right]+\rho g_{x} \tag{51}$$

$$y:\quad \rho\left(u\frac{\partial v}{\partial x}+v\frac{\partial v}{\partial y}\right)=-\frac{\partial p}{\partial y}+\frac{\partial}{\partial x}\left[\mu\left(\frac{\partial u}{\partial y}+\frac{\partial v}{\partial x}\right)\right]+\frac{\partial}{\partial y}\left[2\mu\frac{\partial v}{\partial y}-\frac{2}{3}\mu\left(\frac{\partial u}{\partial x}+\frac{\partial v}{\partial y}\right)\right]+\rho g_{y} \tag{52}$$

5.3.5.1 Fluid Flow and Heat Transfer Coupling

The coupling between the fluid flow and heat transfer interfaces is set in the non-isothermal flow within the multiphysics node (after the 2 physics interfaces). This allows the fluid flow to input the computed velocity field and pressure (to calculate fluid density) into the heat equation for the air domain, which in turns generates the temperature used to evaluate fluid properties used in the momentum equation (Fig. 5.5).

5.3.5.2 Compressibility

Density variations of air at low velocity (<100 m/s) are usually small (under 5%) [114], so that the density can be considered to be independent of the pressure. Since the density in a non-isothermal flow is still a function of temperature, the weakly compressible flow option was used. Equations 51-52 remain valid, with the only difference that the density is evaluated at the reference pressure (atmospheric pressure), so the green arrow in Fig. 5.5 is eliminated.

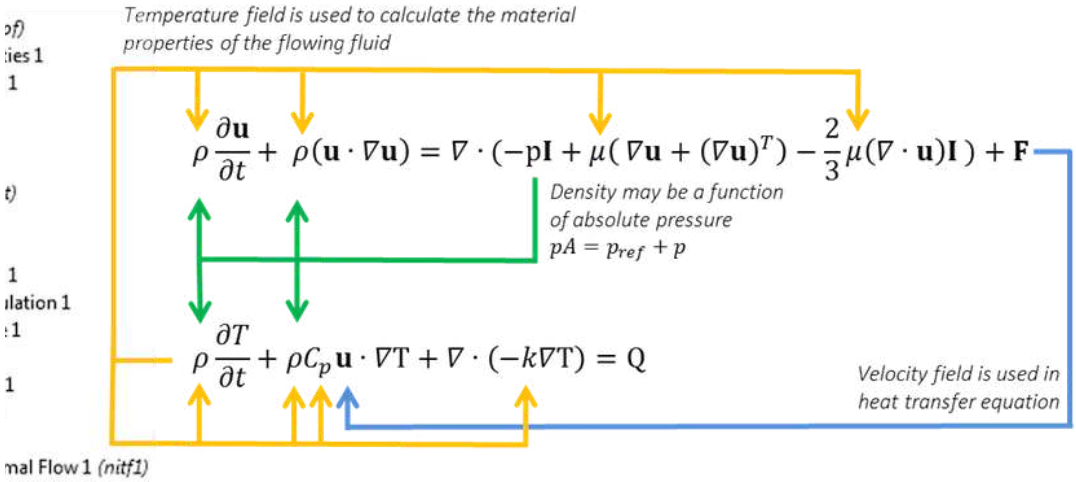

Fig. 5.5: Coupling of the energy and momentum equation for the fluid domain [115].

5.3.5.3 Turbulent Flow Modeling

Because of the presence of obstacles (PV modules) in the airflow, as well as sudden changes in the cross-sectional area of the air channel, a turbulent model was used for the fluid flow, as it is generally the case for similar cases of ventilated channels with integrated venetian blinds [116][119]. In this case, the Navier–Stokes equation is replaced by the Reynolds-averaged Navier–Stokes (RANS) equation, where the instantaneous value of the flow quantities are considered to be the sum of an average and a fluctuating part [120]:

$$\begin{aligned} u &= \overline{u} + u' \\ v &= \overline{v} + v' \\ w &= \overline{w} + w' \\ p &= \overline{p} + p' \end{aligned} \tag{53}$$

where the overbars indicates time averaged values and primes the fluctuating components. By replacing **u** and p in Equations 48-49 with the components in Equation 53, new quantities of the form $-\rho\left(\overline{u_i' u_j'}\right)$ appear, forming what is called Reynolds stress tensor $\tau_{ij,turbulent}$ [114]:

$$\tau_{ij,turbulent} = -\rho \begin{pmatrix} \overline{u'^2} & \overline{u'v'} & \overline{u'w'} \\ \overline{u'v'} & \overline{v'^2} & \overline{v'w'} \\ \overline{u'w'} & \overline{v'w'} & \overline{w'^2} \end{pmatrix} \tag{54}$$

which is a symmetric tensor, therefore introducing six additional unknown.

The Boussinesq approximation is commonly used to model the Reynolds stresses, which are calculated based on the mean velocity gradients [116]:

$$-\rho\left(\overline{u_i' u_j'}\right) = \mu_t\left(\frac{\partial u_i}{\partial x_j} + \frac{\partial u_j}{\partial x_i}\right) - \frac{2}{3}\left(\rho k_t + \mu_t \frac{\partial u_i}{\partial x_i}\right)\delta_{ij} \tag{55}$$

where δ_{ij} is the Kronecker delta, while μ_t is the turbulent viscosity and k_t is the turbulent kinetic energy, the latter defined as the mean of the turbulent components of the normal stresses ($\overline{u'^2}, \overline{v'^2}$ and $\overline{w'^2}$).

The Algebraic yPlus turbulence model has been used in this model, which computes the turbulent viscosity using algebraic expressions based on the local fluid velocity and the distance to the nearest wall. Algebraic models solve for the flow everywhere and, being less mesh-sensitive than transport-equation models like the Spalart-Allmaras or the k-ε model, it is the most robust and least computationally intensive turbulence model. It provides good approximations for internal flow, especially in electronic cooling applications [121].

The Algebraic yPlus turbulence model uses Prandtl's mixing length theory, for which the turbulent viscosity is regarded as being proportional to the product of the velocity gradient and a characteristic "mixing length", l_{mix} [122]:

$$\mu_t = \rho l_{mix}^2 \left|\frac{\partial u}{\partial y}\right| \tag{56}$$

where u is the fluid velocity parallel to the wall, and y is the coordinate normal to the wall. l_{mix} is defined as the distance traveled by a mass of fluid before its mixes with

neighboring masses and its properties get altered [120], and it is proportional to the wall distance *y*, which is computed through a wall distance algebraic equation [122].

5.3.5.4 Initial Values

The initial values for the velocity field was set to zero for the x-component, and 0.2 m/s for the y-component. This was done to facilitate the model convergence to a mainly vertical flow, and the value for the y-component was chosen to be close to the expected value of the velocity in the top double glazing. The value used for the velocity at the outlet is ~0.4 m/s, and the outlet length is about 3.65 cm, which is half of the glass-to-glass distance in the cavity enclosing the PV blinds. Therefore, within the cavity the cross-sectional area doubles, and in order to keep the mass flow rate constant (Equation 25) the average velocity has to halve.

The computed pressure is the relative pressure:

$$p = p_A - p_{ref} \tag{57}$$

where p_A and p_{ref} are the absolute and reference pressure (set to the atmospheric pressure), respectively. The initial relative pressure was set to p=0 Pa, so that the absolute pressure equals the reference pressure, while the initial value for the wall distance variable was set to 5 mm.

5.3.5.5 Wall Boundary Condition

The no-slip boundary condition was used for all the wall boundaries between the fluid and the solid domains, that is $\mathbf{u} = \mathbf{0}$.

5.3.5.6 Inlet and Outlet Boundary Conditions

At the inlet, a pressure B.C. was set, with a relative pressure p_0=0 in order to obtain atmospheric pressure, and the tangential velocity component was set to zero to model a normal inflow.

A velocity B.C. was used for the outlet, where the velocity was assumed to be normal, so that the velocity field only depends on the velocity magnitude U_0, that is $\mathbf{u} = U_0\,\mathbf{n}$, with **n** being the normal vector. The value of U_0 was set so as to provide the same mass flow rate as that experimentally measured, which is 0.0156 kg/s. In 2-D models, COMSOL considers a unitary dimension in the z-component, which is 1m in this case. Therefore, the outlet area used by the program for the calculation of the mass flow rate is 0.0365 m^2. By means of Equation 25, and using the experimental determined value for the air density of 1.082 kg/m^3, the output velocity was calculated as:

$$U_0 = \frac{\Gamma}{\rho_{out} A_{out}} = \frac{1.56 \cdot 10^{-2}\,\mathrm{kg/s}}{1.082\,\mathrm{kg/m^3} \cdot 3.65 \cdot 10^{-2}\,\mathrm{m^2}} = 0.395\ \mathrm{m/s} \tag{58}$$

5.3.5.7 Meshing

An unstructured triangular grid was created to mesh the geometry, for a total of about 95,000 elements. The air domain was calibrated for fluid dynamics, with a minimum and maximum element size of 0.2 mm and 4.57 mm, respectively, while a finer size was used on the wall boundaries, where element sizes of 0.04 mm and 2.84 mm for the minimum and maximum values, respectively, were used. Fig. 5.6 and Fig. 5.7 show the meshes for several parts of the windows, with details for zones close to the walls.

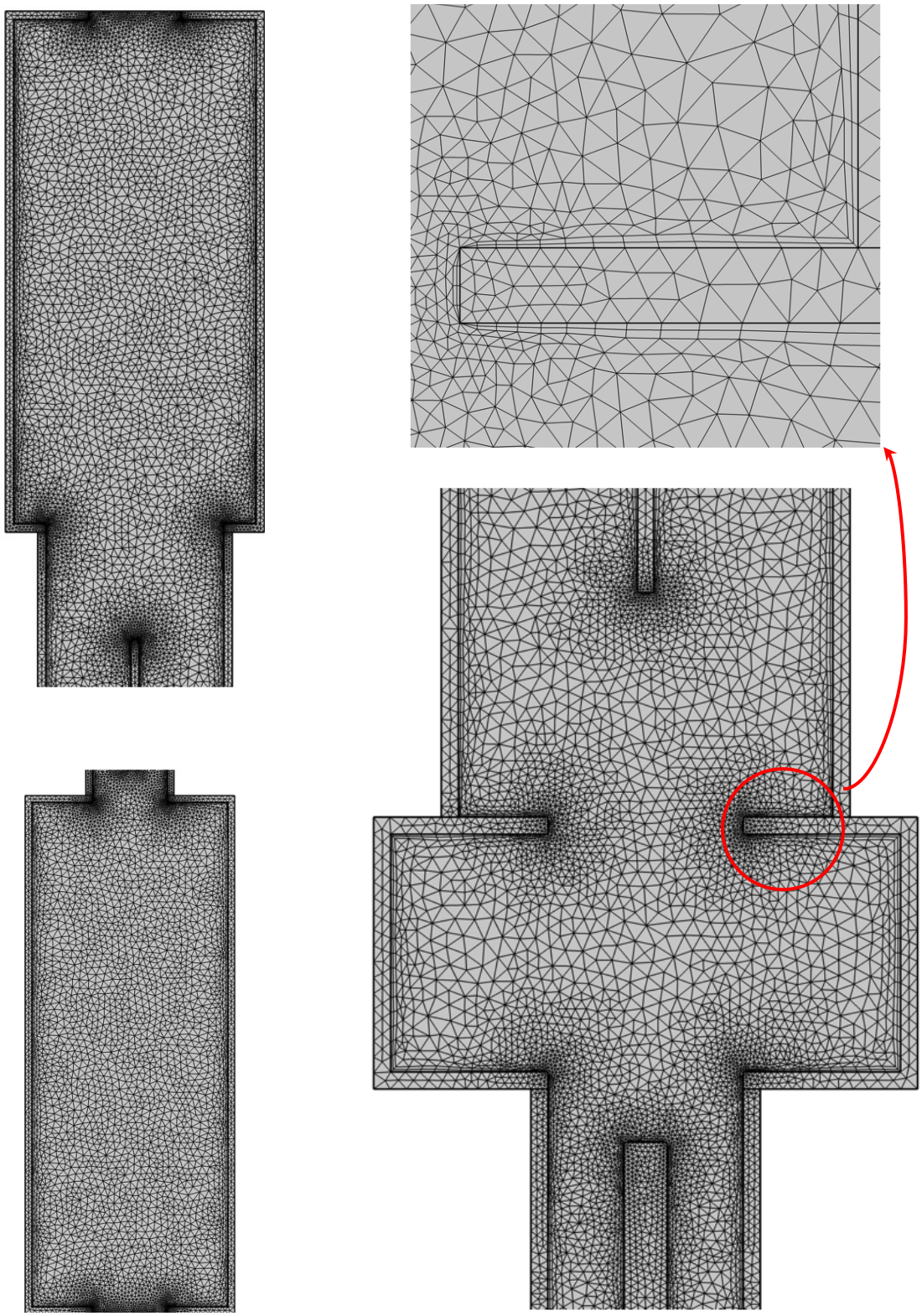

Fig. 5.6: Meshes for the top (top left), bottom (bottom left) and middle (bottom right) parts of the geometry, and close-up (top right) of the frame showing the boundary layers.

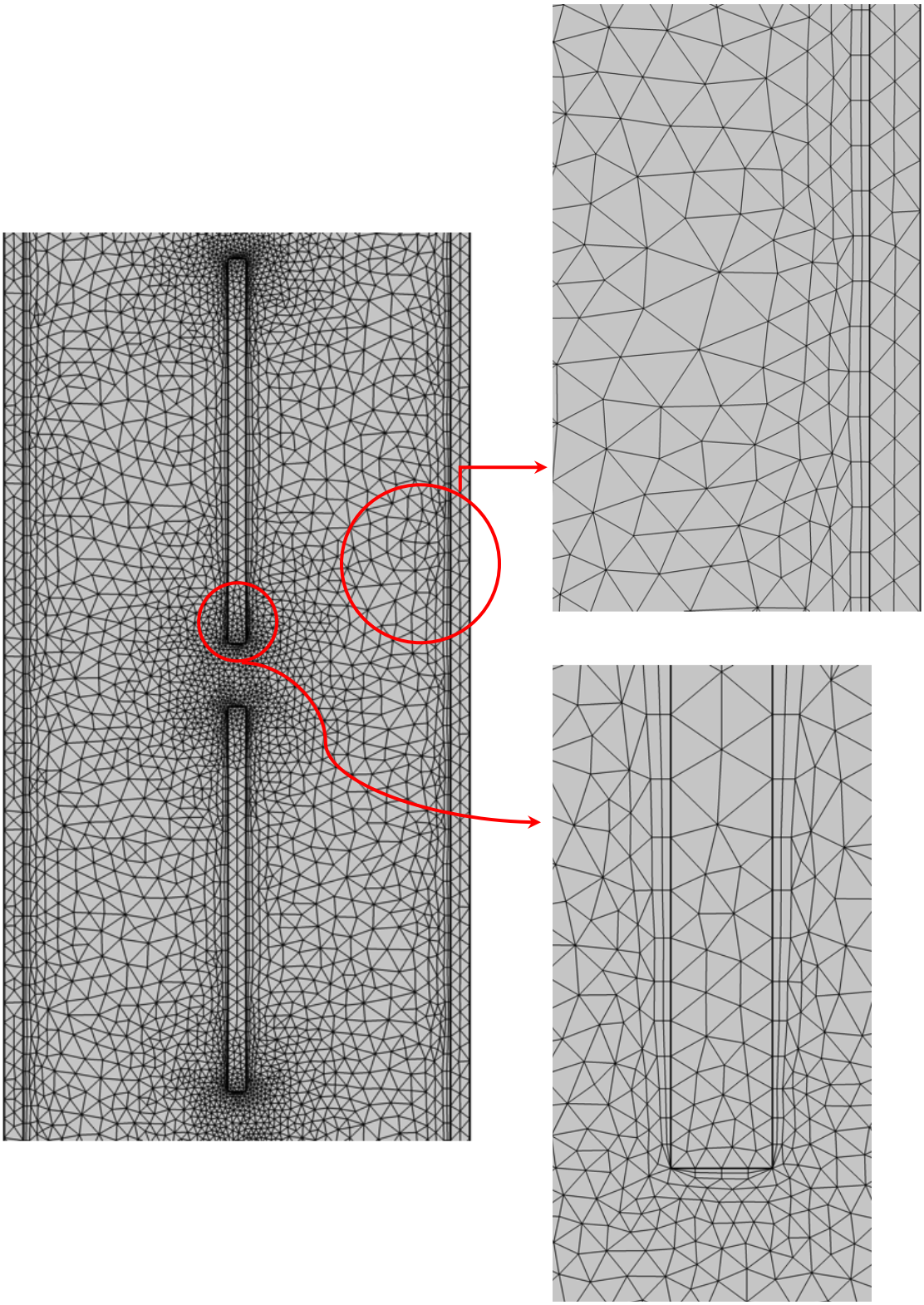

Fig. 5.7: Mesh of part of the channel hosting the PV domains (left) and close-ups showing the boundary layers at the glass (top right) and PV (bottom right) boundaries.

In order to resolve the thin boundary layers, developing in the fluid flow along the domain walls (no-slip boundaries), and where the velocity gradients are significant, a quadrilateral boundary layers mesh is used, which adds a denser element distribution in the direction normal to the boundary. The boundary layers can be observed in the close-ups of the mesh near the glass, frame and PV module in Fig. 5.6 and Fig. 5.7. Corner refinement was used to treat sharp corners at the vertices of the solid domains interfacing with the fluid domain, along with a trimming option, in order to reduce the effective resolution at the sharp corner, compared to no treatment. This makes sure that as the layer approaches the sharp edge, it decreases in height with two elements for each element that comes closer to the edge.

5.3.5.8 Study Steps

A wall-distance initialization step is used before the stationary study step, solving the wall distance equation to compute the distance to the closest wall. The stationary study step contains the main solver settings to compute the heat transfer and fluid flow physics, and it is controlled by the non-isothermal flow multiphysics coupling. When volume forces are neglected in the fluid flow interface, as this is the case, a weak coupling between the flow and the heat interfaces is assumed, and a Segregated Solver is used [112]. This works by solving each physics sequentially, and using the results of the previously solved physics to evaluate the material properties for the next physics to be solved [123]. In this model, the fluid flow ($\mathbf{u}$, p) is solved first (step 1), by using initial conditions given for the temperature field to evaluate material properties in the first iteration, and the computed velocity field is used as an input in a second step

solving for the temperature field T and radiosity J. The iterations are repeatedly computed in sequence until convergence, which is controlled by a relative tolerance of 0.1% (and by a maximum number of iterations set to 300), and the solution converges after 62 iterations. The two substeps use the direct PARDISO solver, which is best applied to 2D and small 3D models, being more robust than iterative solvers, although more computationally expensive and therefore prohibitive for large models [122].

5.3.5.9 Results

Fig. 5.8 shows the simulation results of the two-dimensional model in steady state, where the air speed and temperature fields are displayed.

It can be seen that the air enters from the bottom at 21ºC and its temperature progressively increases as it rises to the top and enters in contact with the absorbers, consisting of the larger PV module at the bottom and the PV array in the second double-glazed cavity at the top. The bottom module reaches about 67 ºC at its highest point, where the air temperature is close to 48 ºC and the velocity around 0.7 m/s. The fluid then enters the larger region where the PV array is located, where the velocity drops to 0.2–0.3 m/s, as expected.

The temperature and velocity profiles along the x-axis for several heights (as shown in Fig. 5.8) are plotted in Fig. 5.9. Right before the PV array (y=1.9m), the air velocity profile is mostly concentrated around the central region of the cavity, due to the sudden change in cross sectional area upstream. The first module therefore is impacted by a higher stream velocity at the bottom, which causes it to be cooled at a

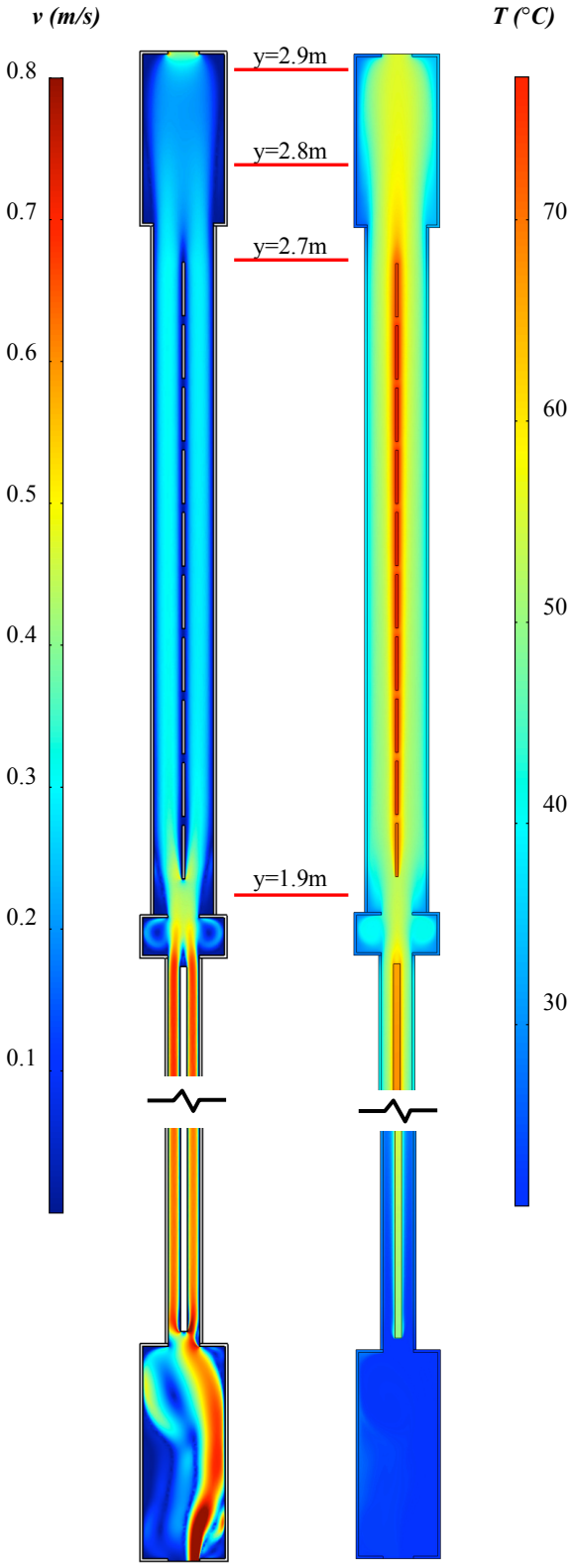

Fig. 5.8: Computed air velocity (left) and temperature field (right).

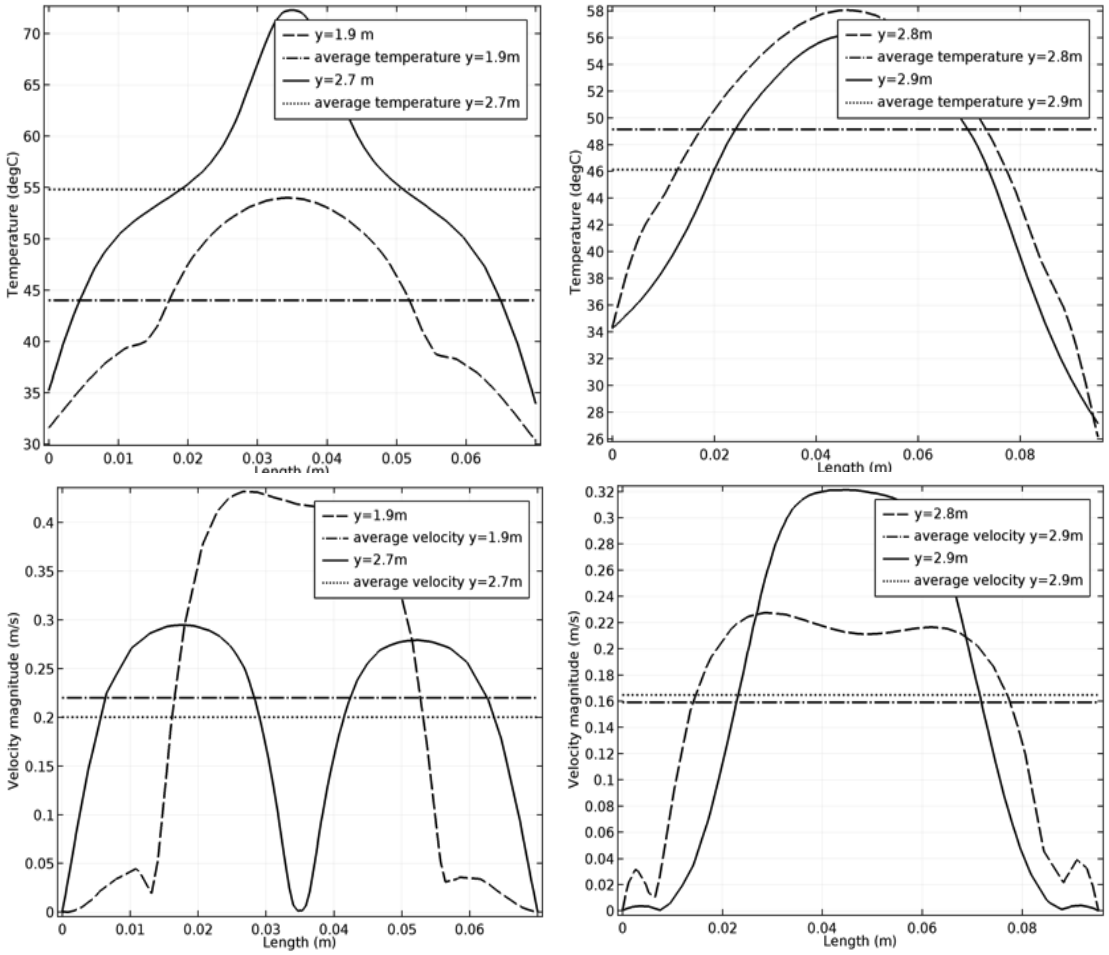

Fig. 5.9: Temperature (top row) and velocity (bottom row) profiles along the channel cross-section at different heights: before the PV array (y=1.9m), past the PV array (y=2.7m), middle and top of the frame (y=2.8m and y=2.9m).

higher rate than the other 9 modules. As a comparison, the average module temperature is around 70.6 ºC for the bottom module, 74.4 ºC for the second module, and between 75.4–77.3 ºC for the remaining ones. As the airflow enters the region containing the PV array, the flow assumes the typical channel flow profile on both sides of the cavity, as depicted by the plot for the velocity at y= 2.7 m, that is right after passing the blinds. The air temperature increases from an average value of about 44 ºC at the bottom of the array to about 55 ºC at the top of the array (top left plot). The temperature then

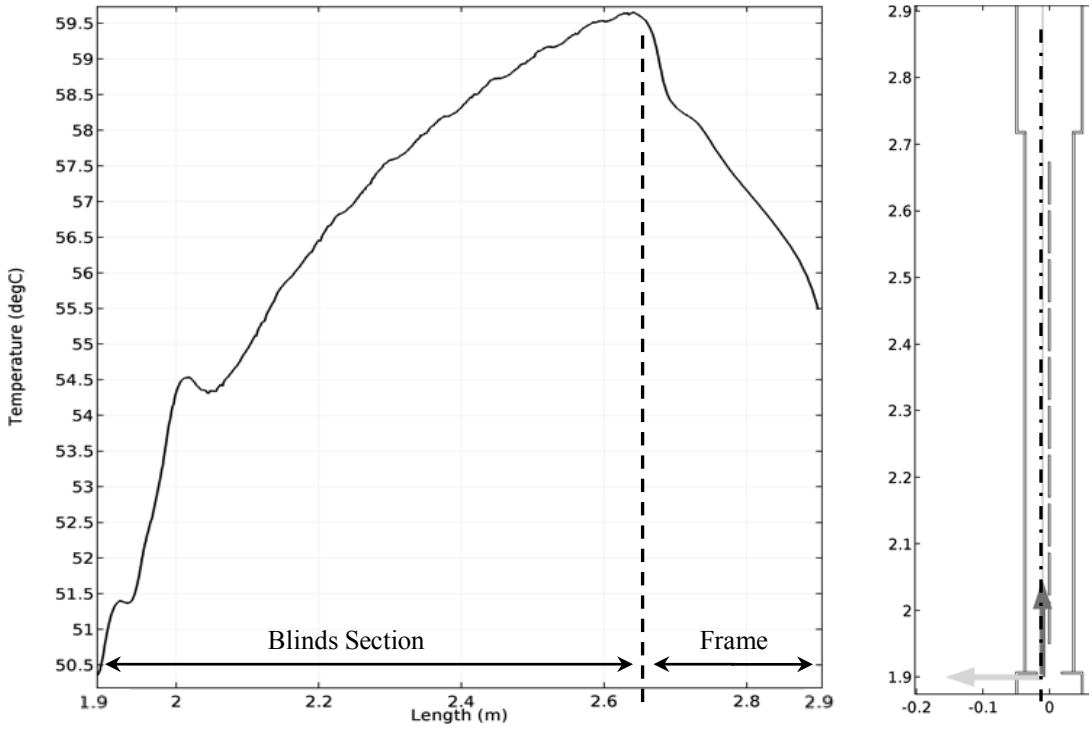

Fig. 5.10: Air temperature (left) along the vertical axis (1.9 m < y < 2.9 m), evaluated at x= -1 cm, and representation of the cut line (right).

drops as the fluid enters the last region inside the top part of the frame and loses heat through it, as it can be seen by looking at the air temperature along the y-direction (Fig. 5.10) for the last 1 m height, evaluated at a cut line placed at x= –1 cm, that is on the outer channel in front of the blinds. The average air temperature at the middle and top cross sections of the frame, shown in Fig. 5.9 are 49 ºC, for y= 2.8 m, and 46 ºC for y= 2.9 m.

A comparison between the experimental and the simulated results is given in Table 5.3. The simulated air temperature at the outlet is 52.56 ºC, while the maximum measured experimentally on the reference day was 53.2 ºC at 12:30. The other results of the simulation are 0.015609 kg/s for the mass flow rate, 1.0816 kg/m^3 for the air density, 31.56 ºC for the temperature rise, 77.18 ºC for the top PV array temperature,

Table 5.3: Comparison between experimental data and simulation results.

	Output air density (kg/m^3)	Mass flow rate (kg/s)	T_out (°C)	ΔT (°C)	T_pv_top (°C)	Heat output (W)	Thermal efficiency (%)
Experiment	1.0816	0.015603	53.2	31.2	76	492.64	32.68
Simulation	1.0842	0.015609	52.56	31.56	77.18	495.92	32.51
% Error	0.24 %	0.038 %	-1.2 %	1.15 %	1.55 %	0.66 %	-0.51 %

495.92 W for the heat transfer rate, and 32.51% for the thermal efficiency, which compare to

0.015603 kg/s, 1.0842 kg/m^3, 31.56 ºC, 76 ºC, 492.64 W and 32.68%, respectively, for the measured data, with percent errors of less than 1.55%. Therefore, the model represents the experimental data with good approximation.

Chapter 6
Optimization

6.1 Introduction

An operational parameter that can be tuned according to the requirements of integration with the building's HVAC system is the mass flow rate. The testing at different air velocities for current version of the window prototype was discussed in Section 4.4.3, where an increase in heat generation and thermal efficiency with higher velocities was observed, along with lower PV temperatures, at the expenses of the output temperature, which drops.

If thermal energy at lower temperature can be used, as in the case of space heating, where supply air temperatures below 40 ºC are needed [124], then a higher mass flow rate would provide better performance by improving the system thermal efficiency, even though the increased electrical demand for ventilation should be considered as well. However, for the integration with applications requiring a large amount of heat (therefore high mass flow rates) delivered at higher temperature, such as water heating or solar cooling (through desiccant systems or absorption chillers), further improvements to the current prototype design are needed.

The strategies to optimize the collector performance can be classified into two categories:

- Thermal insulation, which is aimed at reducing heat losses;
- Heat transfer enhancement, whose goal is to improve the rate of heat transfer at which the heat is removed from the PV.

6.2 Thermal Insulation

Heat losses occur by convection and radiation between the window exterior surfaces (frame and glazing) and the outside environment.

The glazing system affects the solar radiation transmitted to the inside PV absorbers, and a better design should include additional glass panels, with optional low-conductance gas filling in the added double-glazed cavities, as well as Low-emissivity or spectrally selective coatings. The frame of the current design is made of aluminum, which has high thermal conductivity, and therefore it requires further improvements with a better design and the use of different materials.

A better thermal insulation of the frame and the glazing system is therefore needed to limit heat losses and increase the energy content of the airflow. From the simulation of the 2-D model discussed in Chapter 5, the normal heat flux at the top frame and top glass exterior boundaries can be obtained, which are plotted in Fig. 6.1. It can be seen that the heat losses through the top part of the frame are characterized by an average heat flux of about 110 W/m^2, while the average flux through the glass is around 230 W/m^2. Therefore, while the frame insulation should be improved, the glazing system represents the main source of heat losses.

The 2-D model was further developed in order to simulate the use of Low-emissivity (Low-e) coatings and additional glass panes, as well as other options such as Argon filling and heat absorbing glass, in order to optimize the glazing system. A small 3-D model was also created for the top portion of the frame to evaluate the effects of the change of material from aluminum to wood.

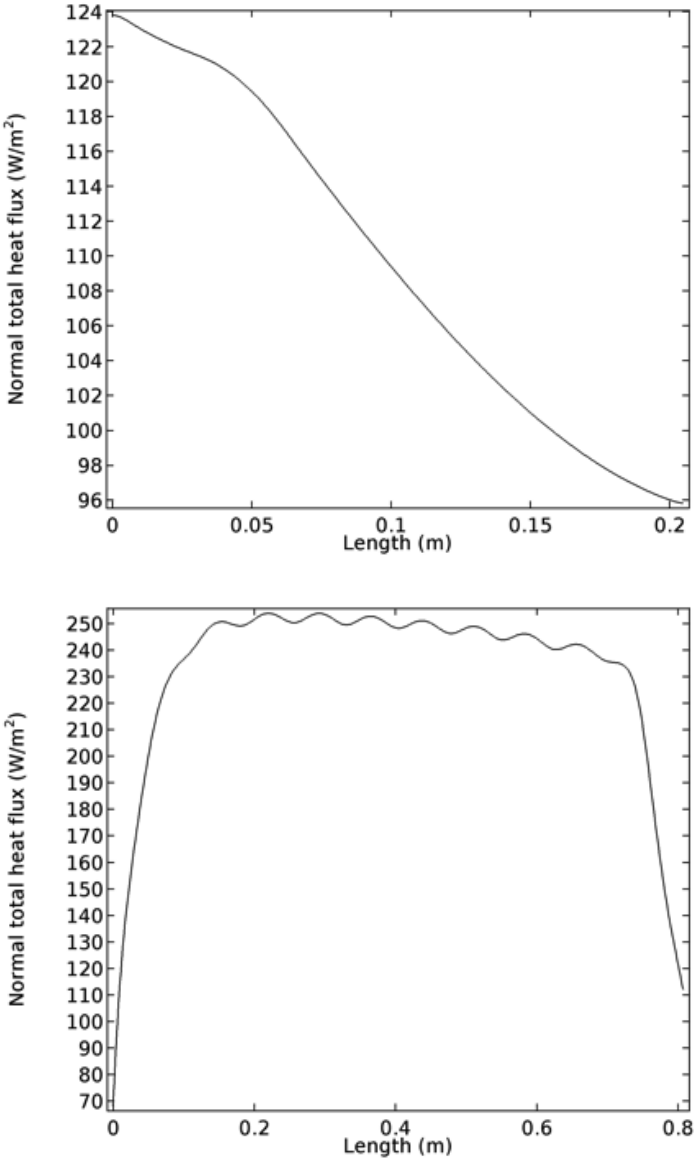

Fig. 6.1: Total heat flux in the direction normal to the boundaries interfacing with the outdoor environment, evaluated on the back side of the window at the top frame (top) and top glass (bottom) surfaces.

6.2.1 Glazing System Optimization

Different glazing system configurations, consisting of a combination of multiple glass panes, selective coatings and low-conductance gas have been simulated. These included the use of:

Table 6.1: Simulation results for different glazing system configurations.

Configuration	T_{out} (°C)	T_{out} **incr. (%)**	Q **(W)**	Q **incr. (%)**	Q_{loss} $\left(\frac{W}{m}\right)$	Q_{loss} **decr. (%)**	η_{th} **(%)**	η_{th} **incr. (%)**
2 panes uncoated	52.56	-	496	-	990	-	32.5	-
2 panes Low-e on # 3	57	8.4	558	12.5	927	6.4	36.6	12.6
2 panes Low-e on # 2, 3	58.66	11.6	581	17.1	684	30.9	38.1	17.2
3 panes Low-e on # 2, 3	62.6	19.1	634	27.8	623	37	41.6	28
3 panes Low-e on # 2, 3, 5	64.73	23.2	663	33.7	593	40	43.4	33.5
4 panes Low-e on # 4, 5, 7	64.7	23.1	662	33.5	475	52	43.4	33.5
3 panes Low-e on # 2, 3, 5, 70% NIR absorption on # 3	65.42	24.5	672	35.5	607	38.7	44.0	35.4
3 panes Low-e on # 2, 3, 5, 70% NIR absorption on # 3, Argon filling	66.43	26.4	685	38.1	593	40.1	44.9	38.1

- 2, 3 and 4 glass panes;
- Low-emissivity (Low-e) coatings;
- NIR absorbing (tinted) glass;
- Argon filling within the added cavities

The simulation results for several configurations are reported in Table 6.1 in terms of output air temperature T_{out}, thermal output Q, linear heat losses Q_{loss} and thermal efficiency η_{th}, along with their relative change with respect to the base configuration (double-pane uncoated glazing). Q_{loss} was computed by integrating the heat fluxes over the exterior boundaries, which provides the heat losses per unit width of the window. In Fig. 6.2 it is also reported a comparison between the temperature field of the various

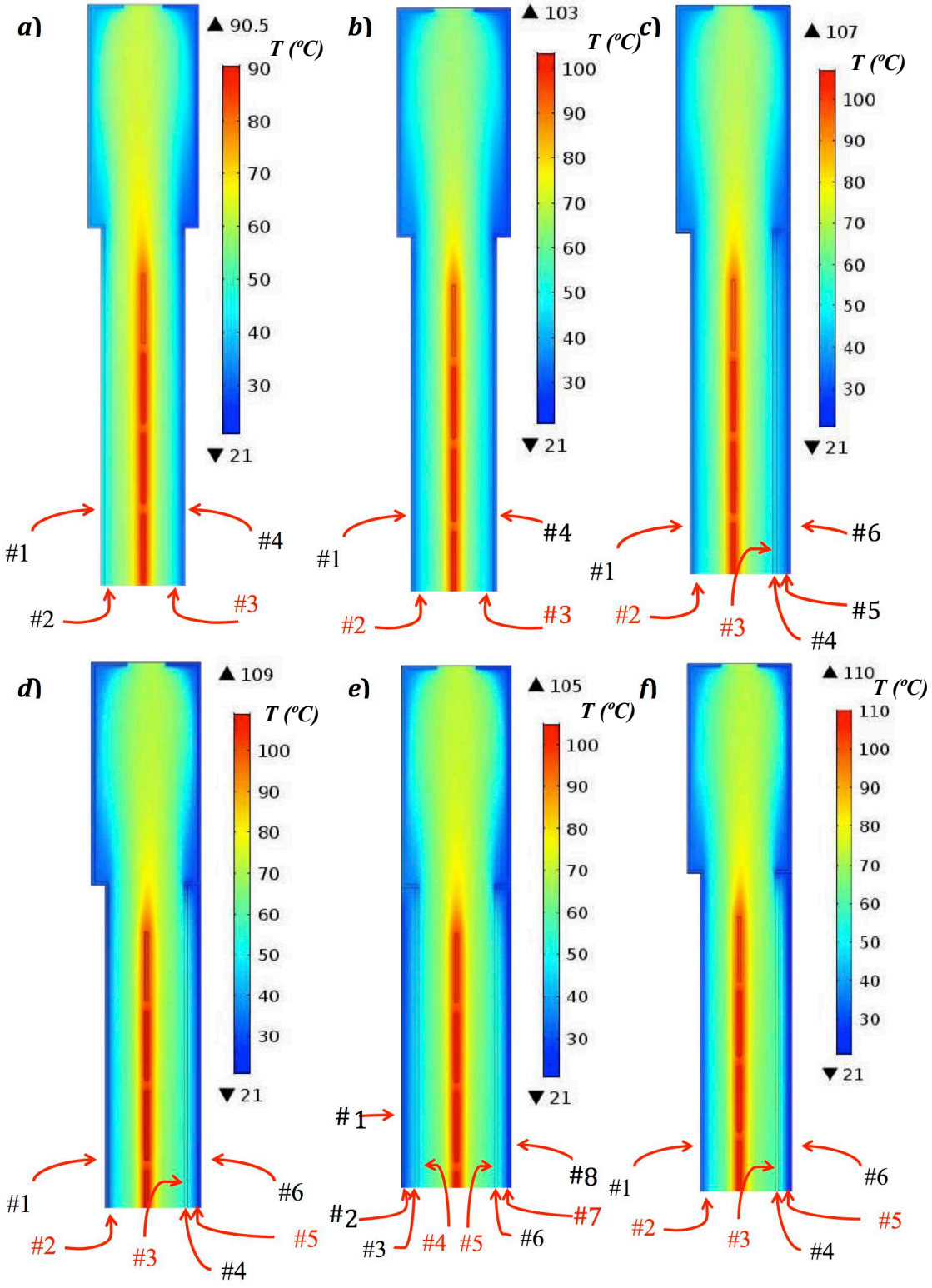

Fig. 6.2: Temperature field for 2-panes with Low-e on surface #3 (a), #2-3 (b), 3-panes with Low-e on surface #2-3 (c), #2-3-5 (d), #2-3(NIR absorbing)-5 (e), and 4-panes with Low-e on surface #4-5-7 (f). The placement of low-e coatings is indicated by labels marked in red.

configurations, where the labels #1, 2,…8 are used to define the different glass surfaces, numbered from the side of the incident solar radiation (left), with two surfaces for each glass panel, while the numbers marked in red indicate the placement of a Low-e coating on that surface. The legend for the temperature range also includes maximum and minimum values (at the top and bottom of the scale).

The value of emissivity of the Low-e surfaces used for all the simulations was set to 0.173, which was taken from the International Glazing Database (IGDB) v35.0 of the software LBNL WINDOW 7.4, assuming the use of a 3-mm Pilkington K-glass [125]. The value of the solar transmittance for the configurations using a Low-e coating on the front glass (*b–f* in Fig. 6.2) was calculated from the Pilkington Spectrum online calculator [126], where a Pilkington K-glass OW was used, which is an improved version of the previous product, where the same Low-e coating is applied to an ultra-clear (low-iron) glass substrate. This provided a solar transmittance for a single pane of glass of 0.8, which was used in the models of the triple glazing configurations. For the quadruple glazing, where an additional uncoated glass is placed at the front, an additional ultra-clear glass was added, resulting in a total transmittance of 0.72.

With reference to Table 6.1 and Fig. 6.2, it can be seen that the placing of a Low-e coating on surface #3 brings the output temperature from 52.56 ºC to 57 ºC (an 8% increase), with a consequent increase of about 12% in heat output and thermal efficiency, and 6% decrease in heat losses. This is due to the fact that the Low-e glass has low absorptivity, and therefore high reflectivity to the long-wave infrared radiation emitted by the PV modules (Section 2.5.2.3), as it is evident from Fig. 6.2*a*), where

the back glass is at a much lower temperature (about 30 ºC) than the front glass (around 45 ºC). However, the improvement in thermal insulation given by the Low-e coating comes at the expenses of the PV temperature, whose maximum value rises from 77 ºC to about 90 ºC. Therefore, the addition of a Low-e coating on the back glass has the overall effect of increasing the air temperature and the heat generated, but it increases the PV operating temperature as well. A solution to this would be to increase the airflow rate, which would reduce both air and PV temperatures, but further increase the heat generation, being the latter proportional to the airflow rate and the air temperature rise.

A Low-e coating applied to both the inner surfaces (#2 and #3, Fig. 6.2*b*)) provides an 11.6% increase in output temperature and 17% increase in thermal generation and efficiency with respect to the base configuration. The PV temperatures experience another 13ºC increase from the previous setup, for a total of 26 ºC increase by using Low-e coatings on both sides of the cavity, with respect to having uncoated double-glazing. The heat losses are reduced by 31%, which represents a significant drop compared to the 6% drop by using Low-e on surface #3. In addition to the effect of an increased thermal insulation on both sides of the window, the drop is also due to the fact that the solar transmittance is reduced from 0.937 to 0.8, therefore the solar input, as well as the heat losses, are reduced.

By keeping the coatings on surfaces #2–3, the addition of a third pane of glass (Fig. 6.2*c*) on the back side of the window further improves the performances, by limiting the back heat losses, for the same amount of solar radiation entering through the front

glass. The temperature and thermal efficiency reach 62.6 ºC (19% increase) and 41.6% (28% increase), respectively, which represents a significant improvement in performance. From the temperature field it can be seen that the exterior glazings have similar temperatures as in the previous case, but the interior glass surface is at much higher temperature, resulting in a higher average air temperature in the channel. With respect to case *b*), the heat losses reduce by another 7%, while the maximum PV temperature rise by about 4 ºC. The width of the gap used in the model has been set to 9.5 mm in order to keep the same geometry and have a comparison with the previous results.

An additional Low-e coating on surface #5 (Fig. 6.2*d*)) provides a gain of another 2 ºC, for an average output temperature of about 64.73 ºC. The thermal efficiency and maximum PV temperature in this configuration set around 43.44% and 109º C (2 ºC higher than in the previous case), respectively, while the decrease in heat losses with respect to the base configuration is around 40%.

A quadruple glazing was also simulated (case *e*)), with the Low-e coatings kept on the same surfaces. The additional glass on the front further reduces the heat losses to the outside on the front side, providing a 50% decrease in total heat losses, but it also allows for less radiation to reach the PV absorbers. The ultimate effect is a thermal efficiency of 43.41% and a heat output of 662 W, with an average output temperature of 64.7 ºC, values that are almost the same as in the 3-pane configuration. However, the maximum PV temperatures in this configuration are around 105 ºC, that is 4 ºC less than in the 3-pane case with the same coatings.

Lastly, the effects of NIR absorbing glass and argon filled gap has been simulated for the 3-pane system. The middle glass can be made of NIR absorbing material, which is typical of a tinted glass, in order to block that part of the spectrum that would otherwise be transmitted to the inside of the building, and as a result the second glass would see its temperature increased, thus enhancing the heat transferred to the air. The NIR absorption has been simulated by making the glass opaque to the corresponding spectral band, and by setting an emissivity of 0.7 on surface #3, which means that 70% of NIR radiation is absorbed and 30% reflected (the emissivity is equal to the absorptivity for an opaque surface at the same temperature and wavelength). As it can be seen in Table 6.1, this configuration (not shown in Fig. 6.2) was found to be very close to case *d*) (triple pane with Low-e on surfaces 2, 3 and 5), bringing the temperature up to only 65.42 ºC, while the thermal efficiency is increased to 44%. This relatively small improvement can be explained by the fact that with the PV modules in vertical position and such highly packed, only a small amount of radiation reaches the glass. In a situation with the blinds more spaced apart, as well as under different tilting conditions, the use of a NIR absorbing glass could provide larger improvements with respect to a regular Low-e glass. Due to the higher glass temperature (around 55 ºC), the heat losses slightly increase from 593 W/m for case *d*) to 606 W/m.

The same NIR absorbing glass has been simulated with Argon filling, instead of air, in the cavity between the second and third glass (Fig. 6.2*f*)). This provides slightly better results than the previous case, and the average output temperature and thermal efficiency rise to 66.43 ºC (26% overall increase) and 45% (38% increase),

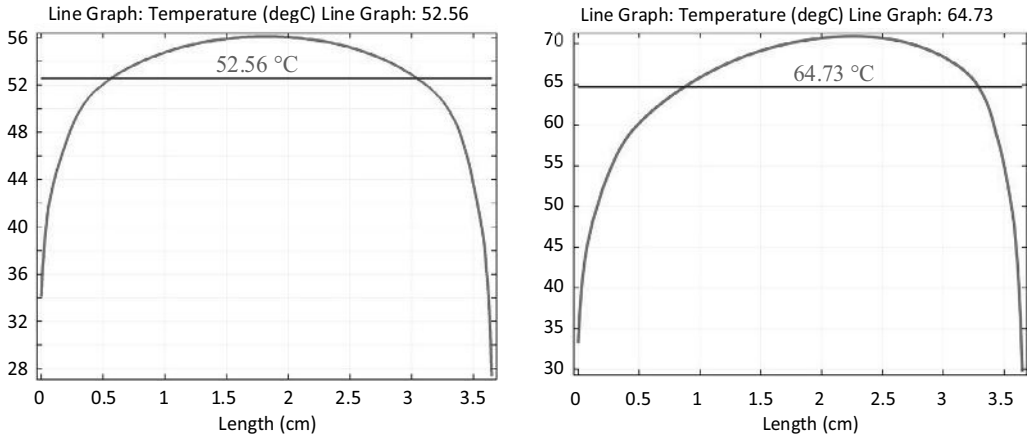

Fig. 6.3: Output temperature profile and average values before (left) and after (right) the optimization.

respectively. The Argon filling reduces the heat losses from the middle glass panel, bringing them back to a value of 593 W/m, while the maximum PV temperature is around 111 ºC, which is the highest among the previous configurations.

The triple-glazing with Low-e coatings on surfaces #2, 3 and 5, and the quadruple-glazing with the same Low-e coating placement can be considered to be the best performing configurations.

The latter can be particularly advantageous in improving the U-value of the building envelope, due to its high thermal insulation, and it is, among the best performing configurations (the last 4 in Table 6.1), the one with the lowest PV temperatures.

However, the 3-pane system represents the optimal setup in terms of cost-effectiveness, as the other solutions involving 4-pane glazing, tinted glass and argon filling do not provide enough improvements to justify the additional costs. Fig. 6.3 shows a comparison between the simulated output temperature profiles, at the output section before and after the optimization, along with the average values. This

arrangement provides an increase in temperature rise from 31.6 ºC to 43.7 ºC, while enhancing the thermal efficiency from 32.5% to 43.4%, corresponding to a percentage increase of 38.6% and 33.3%, respectively.

6.2.2 Frame Heat Losses

In order to evaluate the effects that a change in the frame material thermal conductivity, would have on the heat losses, a simplified 3-D model was built.

The channel between the two plates in the top portion of the frame was built (Fig. 6.4), where the air was assumed to enter the channel normally with an input temperature of 52 ºC at the inlet (bottom surface). To ease the simulation, the flow was modeled as laminar, with an input velocity of 0.3 m/s, and no radiation exchange was assumed. The convective cooling by the environment on the external surfaces was defined by a convective heat transfer coefficient of 20 $W/m^2 \cdot K$ and an ambient temperature of 20ºC. The frame height and the distance between the parallel plates were kept the same as in the 2-D model, that is 20 cm and 9.5 cm, respectively, and the frame length along the y-direction was set to 81.3 cm, which is the same as in the real prototype.

The materials used for comparison were Aluminum and Wood (American red oak). Both a material and a parametric sweep were set, and the model was run at different frame thicknesses (3.175 mm, 2.54 cm and 5.08 cm) for both materials.

Fig. 6.4 shows a comparison of the temperature field in 3-D and on a cross section on a x-z plane at the middle of the length, that is for y~0.41 m. It can be seen that higher temperatures occurs on the exterior surfaces of the frame for the Aluminum case, and that a wooden frame presents a higher temperature gradient along the x-direction.

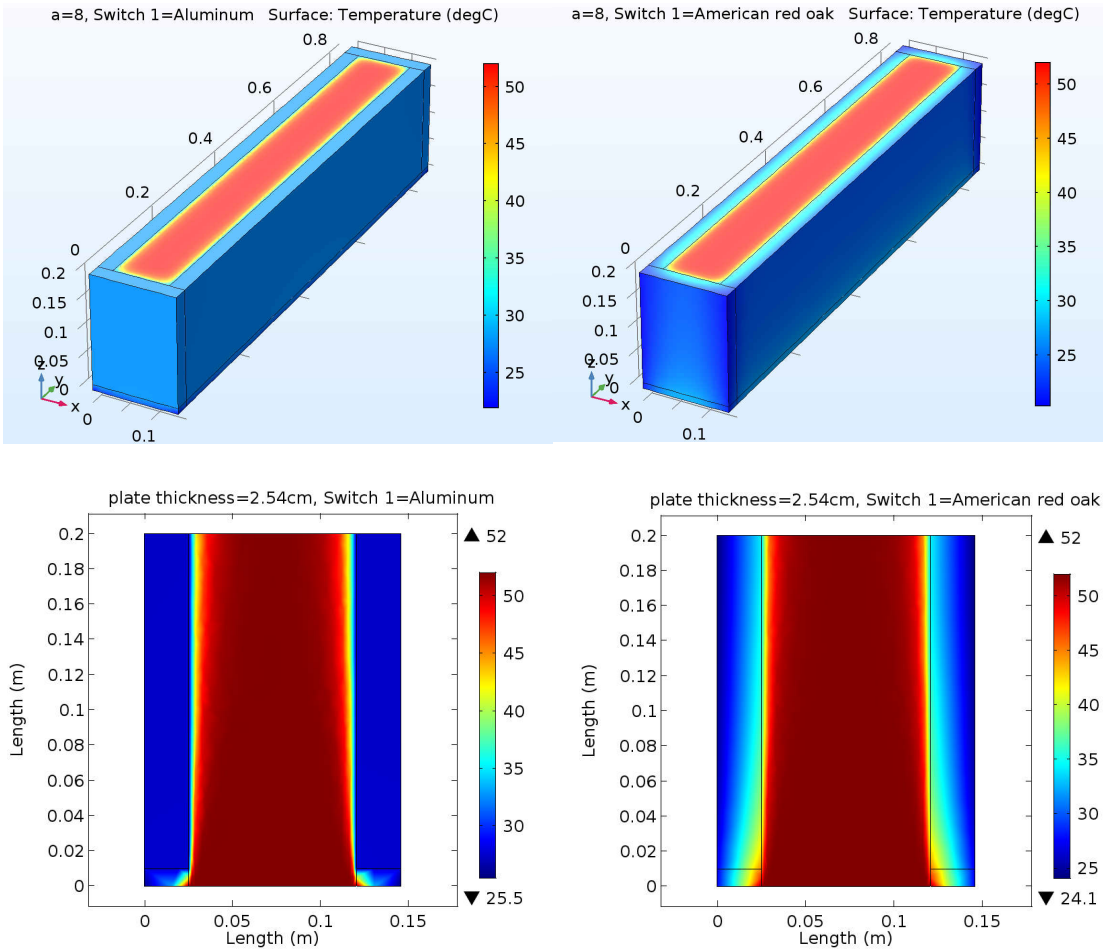

Fig. 6.4: 3D temperature field for Aluminum (top left) and Wood frame (top right), and their relative temperature (bottom) on a x-z plane at half of the frame length (y=0.41 m).

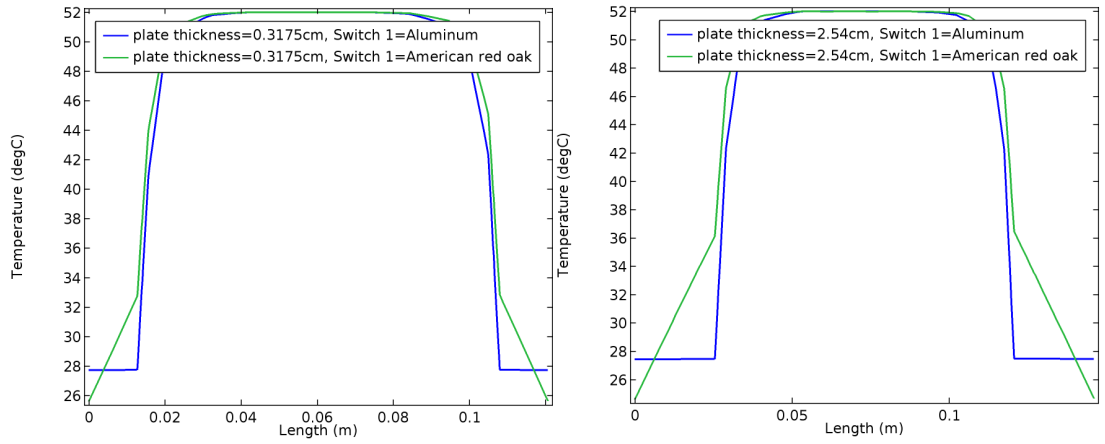

Fig. 6.5: Temperature profile comparison between Aluminum and Wood frame, along a line at z=0.1 m on the x-z plane at half of the frame length (y=0.41 m), for a plate thickness of 3.175mm (left) and 2.54 cm (right).

Table 6.2: Comparison between Aluminum and Wood frame for different thicknesses.

Frame thickness	Q_{loss} (W)		*% decr.*	T_{out} (°C)	
(mm)	*Aluminum*	*Wood*		*Aluminum*	*Wood*
3.175	55.3	41.1	25.7	48.73	49.36
25.4	55.7	33.6	39.7	48.72	49.82
50.8	56.5	24.9	55.9	48.67	50.37

This can be better evaluated by looking at the temperature profile along a line at z=0.1 m, on the same cut plane. As shown in the right plot of Fig. 6.5, the temperature at the inner surface (x=2.54 cm) is around 36 °C for wood and 27.5 °C for aluminum, and at the outer surface (x=0) the wood frame temperature drops to about 24 °C, while the aluminum frame one remains practically the same. For a smaller thickness (left plot in Fig. 6.5), the situation is very similar, but with the inner and outer wood frame temperatures approaching the almost flat aluminum temperature profile.

Table 6.2 shows the results for the output air temperature T_{out} and the total heat losses through the frame Q_{loss}. Since the heat losses for the aluminum frame remain the same at increased thickness, the percentage decrease in heat losses for the wood frame increases from 25% to over 50% by going from a 3.2 mm to 5 cm thickness. Thicknesses between 0.3–2.5 cm and 2.5–5 cm would therefore provide intermediate values, with improvement in the 25–40% and 40–55% range, respectively, with respect to a 3 mm Aluminum frame.

6.3 Heat Transfer Enhancement

As it is evident in Fig. 5.8, the PV blinds reach temperatures in the range of 70–77 ºC, while the average air temperature downstream of the blinds is around 55 ºC. Therefore, the second type of optimization is aimed at enhancing the heat transfer between the PV and the airflow, in order to remove a larger fraction of heat from the PV. This is expected to reduce the PV temperatures and increasing the heat collected by the airflow, thus increasing both the electrical and thermal efficiency.

Heat removal from the PV can be enhanced either by improving the PV-to-air convective heat transfer, or by improving the conductivity of the PV itself. In the first case, convection can be either enhanced by increasing the heat transfer coefficient, which dependents on the fluid velocity (Equations 43–44), or by increasing the contact area between the PV surface and the airflow. The different strategies are summarized in Table 6.3, where h, A and k refer to the convection coefficient, PV-air contact area, and effective thermal conductivity of the PV blinds, respectively.

6.3.1 Increase of *h* - Air Velocity Augmentation

Air velocity augmentation can either be realized by actively increasing the airflow rate,

Table 6.3: Summary of the strategies pursued to improve heat removal from the PV.

Heat transfer mode	Type of improvement	Strategy
Convection	h enhanced	Increased airflow rate
		Reduced glass spacing
	A increased	Aluminum fins on PV back
Conduction	k increased	New PV layers structure

by means of an increased fan speed (with a consequent increase in fan power consumption), or by reducing the cross-sectional area of the airflow, which increases air velocity without modifying the airflow rate. Simulations for both cases are here presented.

6.3.1.1 Increased airflow rate

As it was showed experimentally, in in Section 4.4.3, an increase of fan speed, and therefore of the air velocity, results in higher flow rate, and causes a decrease in PV and air output temperatures, and an increase in heat generation. The same effect has been simulated in COMSOL on some of the models used for the glazing system optimization, where the output velocity has been increased from 0.4 to 0.8 m/s.

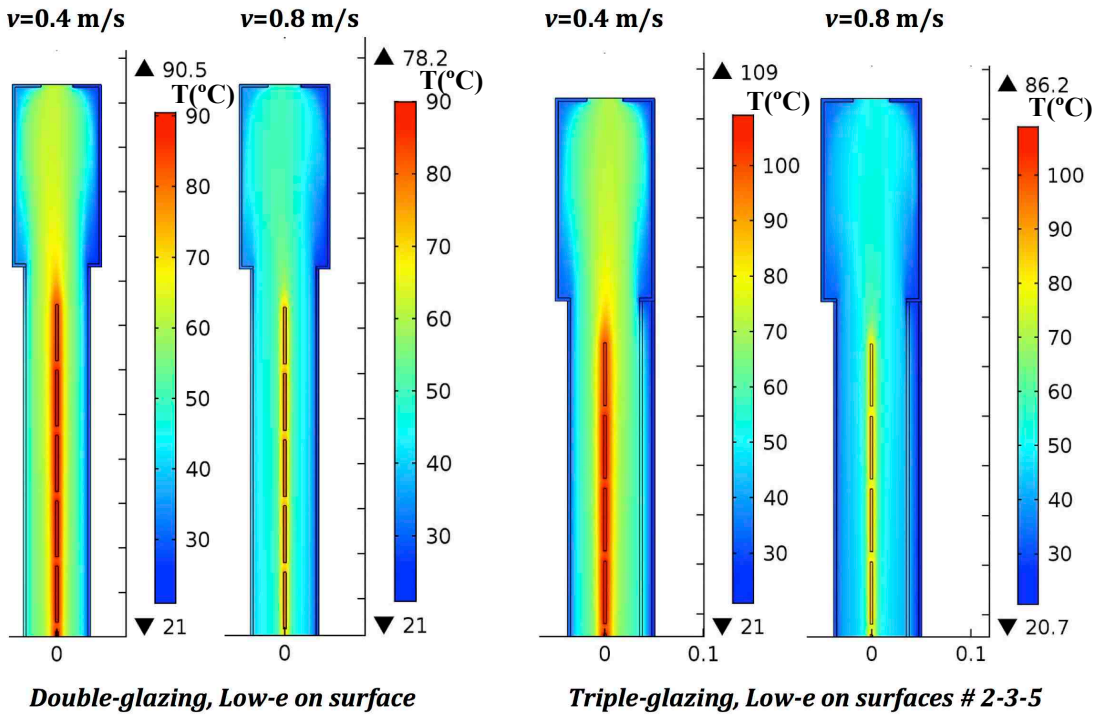

Fig. 6.6: Effects of a doubled flow rate, for a double-glazing with Low-e on surface #3 (left), and for triple-glazing with Low-e on surfaces #2-3-5 (right).

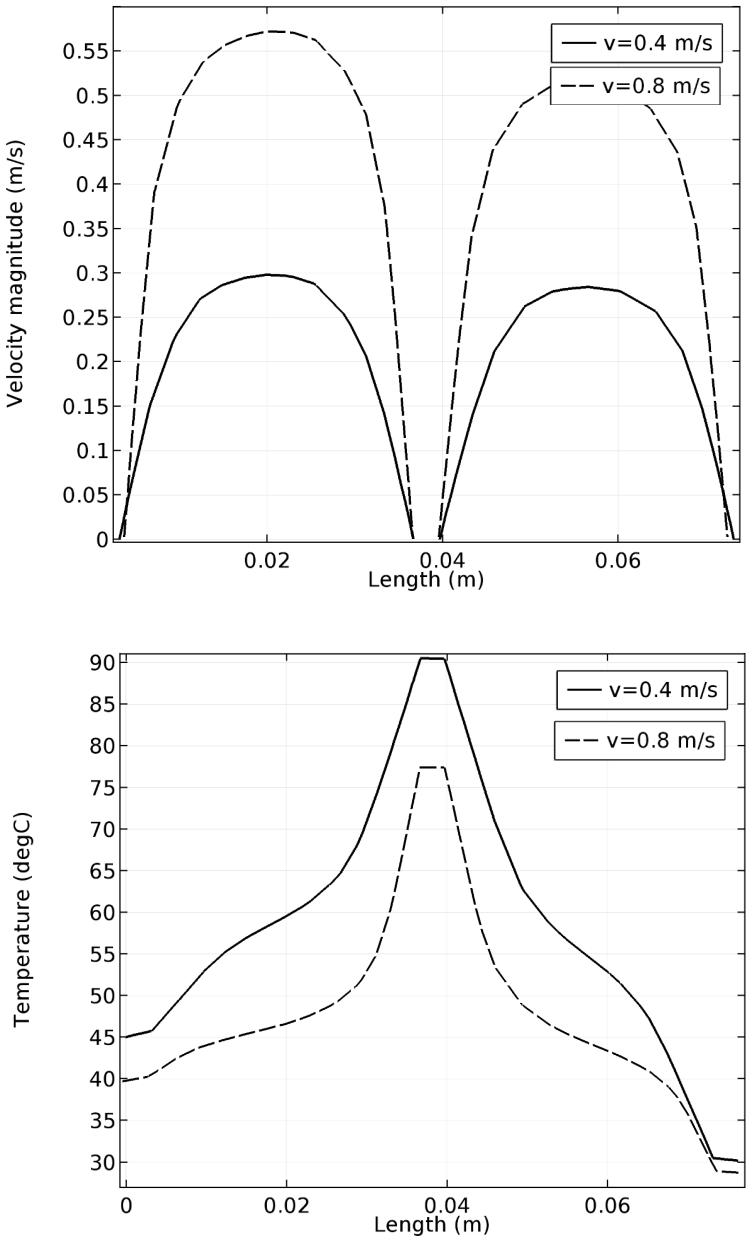

Fig. 6.7: Air velocity (top) and temperature (bottom) profiles along a cut line at y=2.5 m, for both velocities for a double-glazing configuration with Low-e on surface 3.

The results showing a comparison, with the same temperature scale, for both velocities are reported in Fig. 6.6, for the configurations *a*) and *d*) of Fig. 6.2. It can be seen from the temperature field that a double air velocity reduces the maximum PV temperatures

from 90 ºC to 78 ºC for the double-glazing case, and from 109 ºC to 86 ºC for the triple-pane configuration, but the air temperature drops as well. This means a reduction in PV temperature rise, relative to the value of 77 ºC for uncoated glass, from 13 ºC to only 1 ºC (2 panes with Low-e on surface 3) and from 32 ºC to 9 ºC (3 panes with 3 Low-e coatings). This it also evident from the temperature profile along a cut line at y= 2.5 m (middle of the third module from the top), shown in Fig. 6.7 for the double glazing, where the velocity profile is also reported. Both profiles are practically scaled up and down, and an increase in average air velocity within the channel from around 0.22 to 0.45 m/s causes a drop in both module (located at the middle of the x-axis) and air temperature.

The overall results for the output air temperature, heat generation, heat losses, thermal efficiency and maximum PV temperatures (*Max* T_{PV}) are summarized in Table 6.4 were the base configuration of double-pane uncoated glass (current prototype) is also reported for reference. By doubling the airflow rate, the output temperature for the 2 and 3 panes drops from 57 ºC to 46.9 ºC and from 64.7 ºC to 48.5 ºC, respectively,

Table 6.4: Comparison between several glazing configurations for two air velocity values

Configuration	T_{out} **(ºC)**	Q **(W)**	Q **incr. (%)**	Q_{loss} $\left(\frac{W}{m}\right)$	Q_{loss} **decr. (%)**	η_{th} **(%)**	η_{th} **incr. (%)**	***Max*** T_{PV} **(ºC)**
2 panes uncoated – 0.4 m/s	52.56	496	-	990	-	32.5	-	77
2 panes Low-e on # 3 – 0.4 m/s	57	558	12.5	927	6.4	36.6	12.6	90.4
2 panes Low-e on # 3 – 0.8 m/s	46.9	827	66.7	670	32.3	54.2	66.8	78
3 panes Low-e on # 2, 3, 5 – 0.4 m/s	64.73	663	33.7	593	40	43.4	33.5	109
3 panes Low-e on # 2, 3, 5 – 0.8 m/s	48.5	874	76.2	392	60.4	57.3	76.3	86

with a decrease of about 10.8% and 7.7% with respect to the base configuration. In turn, the thermal generation rises from 558 W to 827 W for the 2 panes, and from 670 W to 874 for the 3 panes system, while a thermal efficiency of 54– 57% is achieved. Also, the triple-glazing at double airflow rate yields a 60% reduction in heat losses relative to the base case, which is more than the reduction given by a quadruple-pane system.

Therefore, an increase in the airflow provides a significant increase (in the range of 67–76%) in thermal generation and efficiency, with respect to the uncoated configuration, while keeping the PV temperature very close to the experimental value, with a little decrease (less than about 10%) in air temperature. Thus, the adjustment of the flow rate during the actual operation of the collector allows to control the PV and air output temperature, depending on the particular application. Higher velocities are beneficial for the overall efficiency, if the produced air temperature level is acceptable, and if the latter drops (for instance, due to a drop in solar irradiance or air input temperature), the flow rate should be decreased to bring the temperatures up.

6.3.1.2 Reduced Glass – Glass Spacing

As it was previously seen, an increase in the air speed (v) during the unit operation, so without any changes in cross-sectional area A, produces a higher volumetric flow rate $\dot{V} = vA$ [m^3/s]. However, since at higher flow rates the heat is distributed over a larger volume of air per unit time, the average air temperature will be reduced.

A second strategy to increase channel velocity, which can be carried out at a design stage, is to tune the glass-to-glass distance. If the mass flow rate (Γ) is kept constant,

by keeping the fans at the same speed, a reduction in the width of the air cavity between the double-glazing would result in an increase of the air velocity.

Being the mass flow rate constant, and since the density changes only slightly with temperature, the volumetric flow rate $\dot{V}$ will remain nearly the same. Therefore, a reduction in cross sectional area causes the air velocity to increase ($\dot{V} = vA$). However, unlike the previous case, at constant flow rate more heat will be transferred to the same volume of air per unit time, resulting in higher temperature rise in the airflow. If the Γ_2 and Q_2 are the flow rate and the heat absorbed by the airflow after the cross section is reduced, and $\Gamma_1 = \Gamma_2$ and Q_1 are the same parameters evaluated for the original cross-sectional area, and it is $Q_2 > Q_1$, the respective air temperature rise for both cases, from Equation 24, are:

$$\Delta T_2 = \frac{Q_2}{\Gamma_2 c_p} > \frac{Q_1}{\Gamma_1 c_p} = \Delta T_1 \tag{59}$$

Therefore, by going from a larger to a narrower channel width, the temperature rise is expected to increase.

A 3-D model was built to evaluate the effects of a change in glass-to-glass distance. For this purpose, a small section of the ventilated double-glazing with PV blinds was reproduced. The frontal area is 18 cm wide by 24 cm high (y and z directions in the model), while the depth was parametrized based on the glass spacing *d*. Fig. 6.8 shows the definition for the various geometric entities: the PV width *w*, the pitch *c* and the spacing *s* between two PV modules. For the modules currently used in the prototype, $w = 6.3$ cm and $s = 1$ cm, so $c = w + s = 7.3$ cm. A section of the double-glazing with

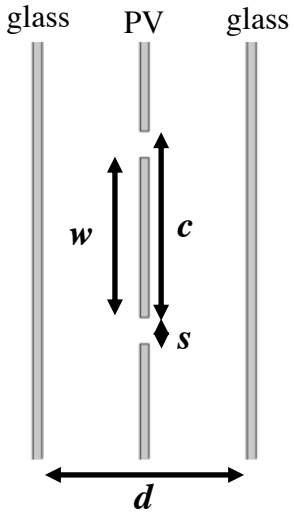

Fig. 6.8: Definition of geometrical parameters.

a height of 24 cm will host up to 3 modules, for a total length of $3 \cdot c = 3 \cdot 7.3$ cm = 21.9 cm. This value was kept the same for all simulations to maintain the same PV absorbing area. In order to scale all the geometric parameters proportionally when changing the glass spacing d, the PV width w and pitch c were also scaled down by the same factor. By using the geometric values for the current configuration, the following relations were used:

$$d = 7 \cdot a \tag{60}$$

$$w = \frac{d}{b} \tag{61}$$

$$\frac{c}{w} = 1.158 \tag{62}$$

$$n_{panels} = \frac{21.9}{c} \tag{63}$$

$$v_{air} = \frac{0.2}{a} \tag{64}$$

where n_{panels} are the number of panels within the 21.9 cm height, v_{air} is the value used for the air velocity boundary condition at the outlet, b is the glass distance to PV width ratio ($b = d/w$), and a is a scaling factor, whose values were chosen so that n_{panels} be an integer number. By keeping the same d/w ratio, a reduction of d implies an increased number of modules with shorter width w, as shown in Fig. 6.9. The air velocity was also modified by the same factor a by which the glass distance (and therefore the cross-sectional area) is scaled, in order to provide the same mass flow rate. The value of v_{air} for a=1 (current prototype layout) was assumed to be 0.2 m/s, which corresponds to the simulated average value (Fig. 5.8) within the top channel enclosing the PV blinds. Several simulations were run at different ratios d/w and scaling factors, which were the input parameters for the models.

In Fig. 6.10 the average PV temperature, the air output temperature and the heat generated in the 24 cm height are plotted, for a fixed ratio b. It can be seen that, as the distance between the two glass panes reduces, the thermal generation as well as the air temperature increase, while PV temperatures decrease. By going from about 7 cm to 2.7 cm, the heat generation increases by 33.4%, with a slight increase in air temperature of about 6%, and the PV temperatures drop by 22.7%. This is also evident from the temperature profile from glass to glass at mid-height of the channel (Fig. 6.11), plotted for 3 values of w, where the PV module temperature (the highest flat line at the middle of each profile) decreases from 50 ºC to around 38 ºC.

Similar effects are observed by changing the d/w ratio, for the same value of w (Fig. 6.12): the ratio reduces, the heat output increases and the PV temperature decreases.

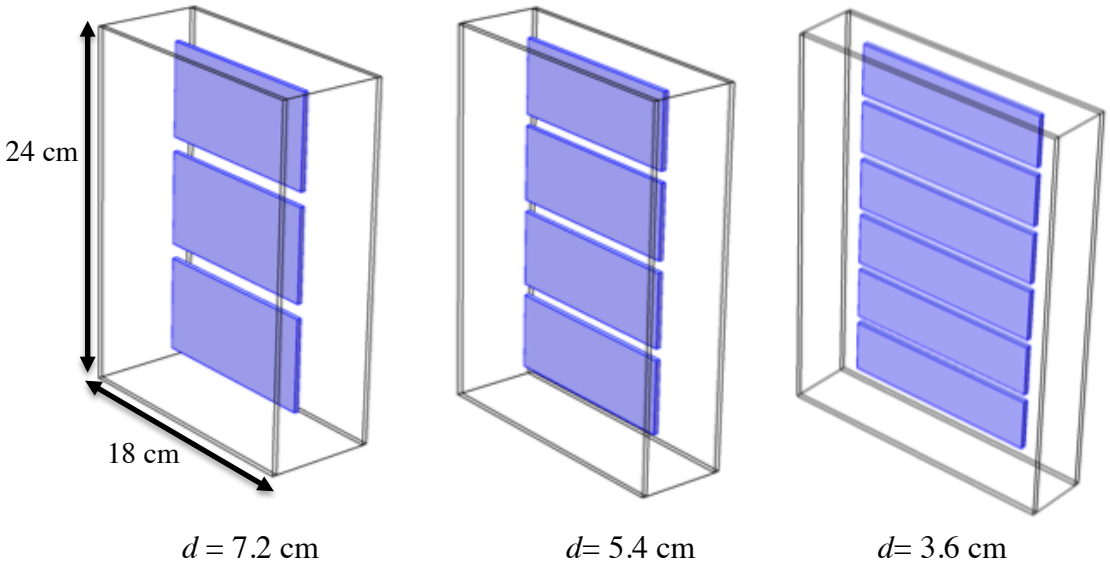

Fig. 6.9: Model setup for decreasing *d*, with 3, 4 and 6 blinds, for *d/w*=1.14.

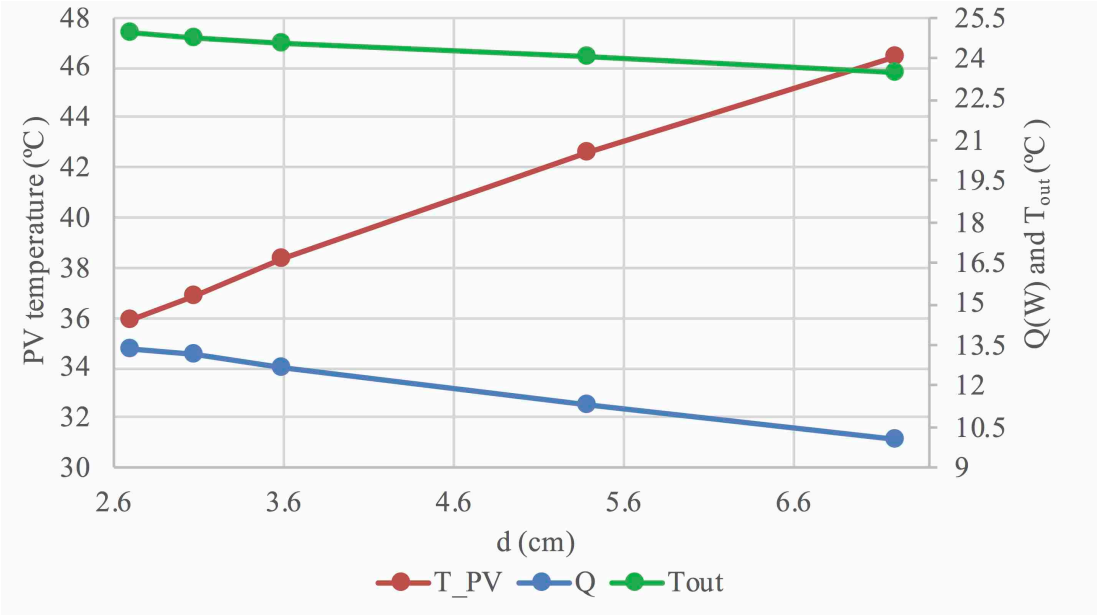

Fig. 6.10: Results for the PV temperature, heat and air temperature output, as a function of *d*, for *d/w*=1.14.

However, there is a limit in how far the ratio can be shrunk, as for $b < 1$ the PV would be larger than the cavity width, and their ability to tilt would be limited. It can be assumed that having a glass distance larger than the PV width by about 10% would

represent a reasonable safety factor to ensure that the blinds can rotate to a fully horizontal position.

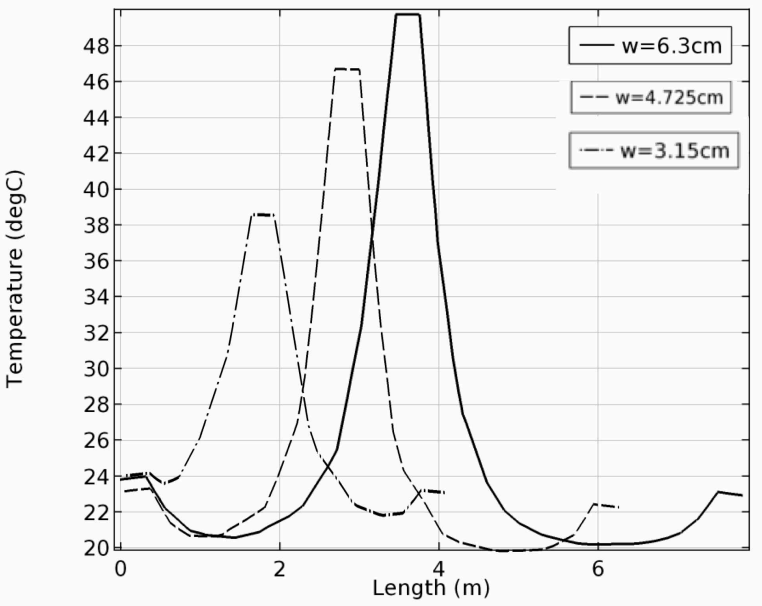

Fig. 6.11: Temperature profile at mid-height in the direction normal to the glazing surfaces, for d/w=1.14 and w = 6.3 cm, 4.725 cm and 3.15 cm.

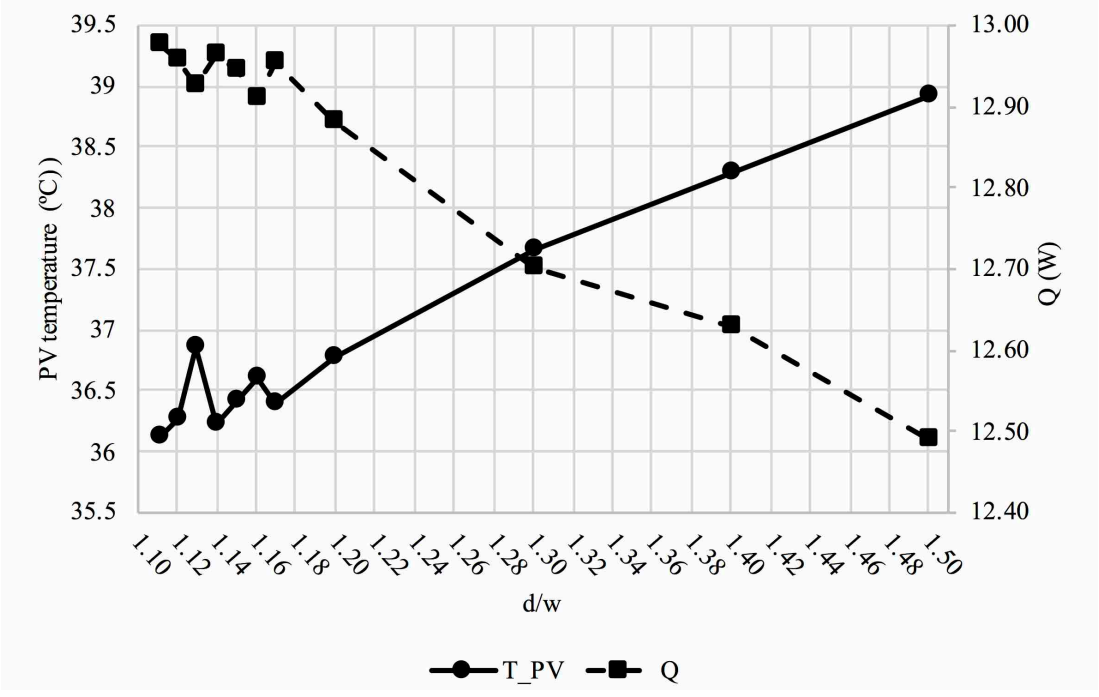

Fig. 6.12: PV temperature and heat output as a function of the ratio *d/w*, for w=3.15 cm.

The optimal d/w ratio can therefore be considered to be around 1.1.

The width of commercially available between-the-glass blinds can be as low as 12.5 mm [127], so the minimum glass spacing will depend on the minimum PV width that can actually be manufactured.

6.3.2 Increased *A* – Extended Surfaces (Finned PV/T Absorber)

It was previously seen that heat transfer augmentation by increased air velocity is limited by the required minimum temperature. A second strategy to enhance convection between the PV and the air is to increase the area through which heat transfer occurs. This can be done by adding fins on the back surface of the PV modules, and it has already proven to be an effective method to promote PV cooling [128]–[132] in hybrid PV/T collectors.

A 3D model was built in COMOSL in order to analyze the effects of additional Aluminum fins for a single PV module. A base model without fins was first developed, consisting of a 12.5 × 6.3 × 0.3 cm module placed in a double-glazed channel of dimensions 18 × 12 × 7 cm. The air was assumed to enter the bottom of the channel at 20 ºC and atmospheric pressure, with an outflow velocity at the top boundary of 0.2 m/s, and the same radiative and convective boundary conditions were applied as in the previous models. The model was further modified by adding 25 Aluminum plate-fins, with 1 mm thickness, on the back surface of the silicon domain. Fin lengths of 1 cm and 2 cm were simulated, defined as the distance by which the fins are extruded from the module surface.

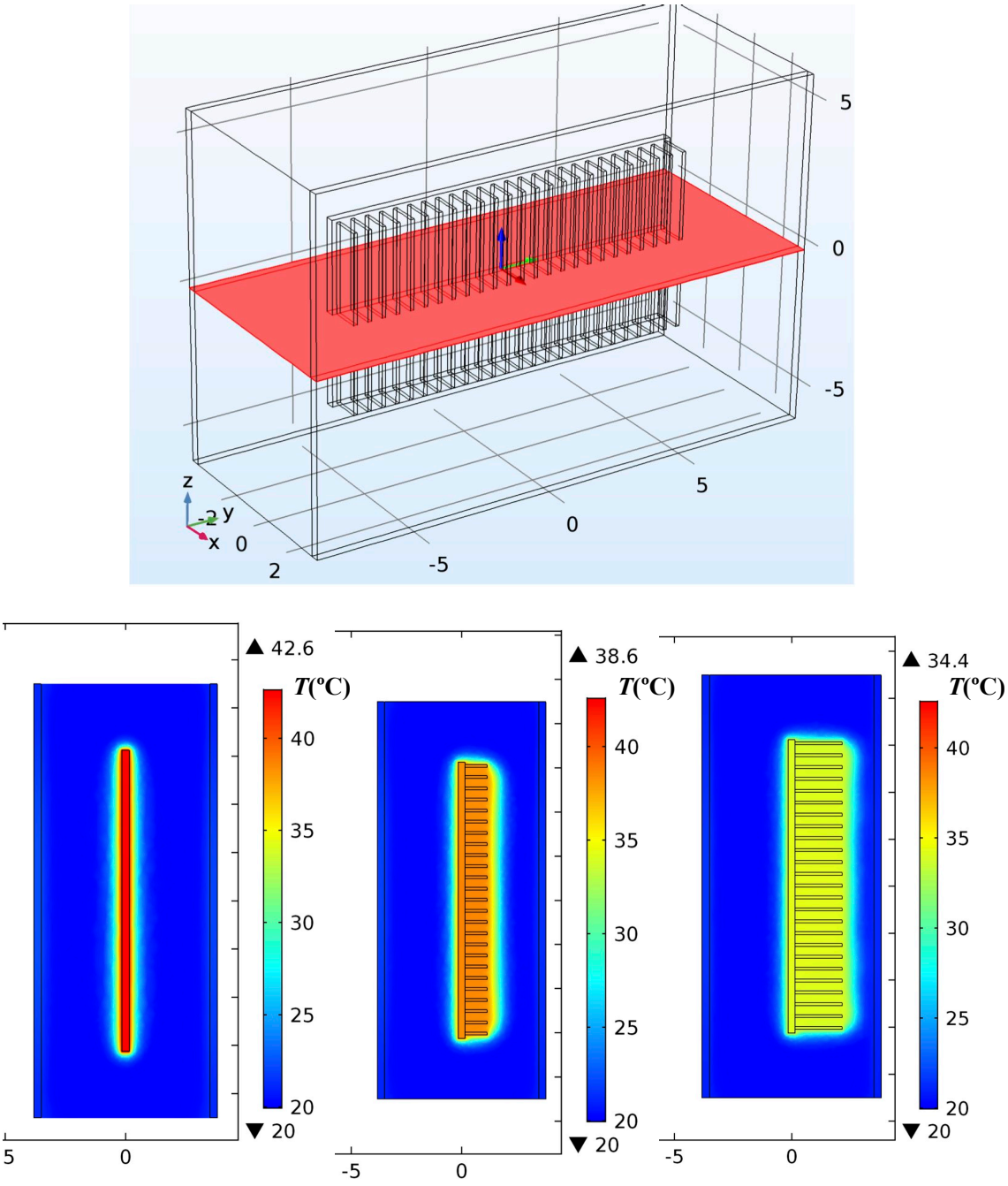

Fig. 6.13: Cut plane for data selection (top) and temperature field for the no-fins (bottom left), 1 cm fins (bottom center) and 2 cm fins (bottom right) cases.

Fig. 6.13 shows a comparison on the same temperature scale for the temperature field in the 3 cases, evaluated at the cut plane displayed at the top of Fig. 6.13. It can be

seen that the maximum PV temperature decreases from 42.6 ºC, for the base model without fins, to 38.6 ºC by using 1 cm fins, which further reduces to 34.4 ºC if 2 cm fins are used. Therefore, longer fins result in lower PV temperatures, due to the increased surface area available for the heat exchange between the module and the air. The limitation in fin length will depend on geometrical parameters, such as the spacing between the binds and the distance to the back glass. For the optimal *d*/*w* ratio from previous section, and assuming the PV width to be half of that of the currently used modules ($w = 3.15$ cm), the maximum tilting at which the blinds can be rotated without causing shading between the rows is around 20.5º. This occurs in the fall, where the solar elevation during the field-testing period was the lowest (about 32º), and the blinds can therefore be tilted more. In this case, the fins are limited to around 1 cm (Fig. 6.14), as higher values will cause the fins to interfere with the back glass.

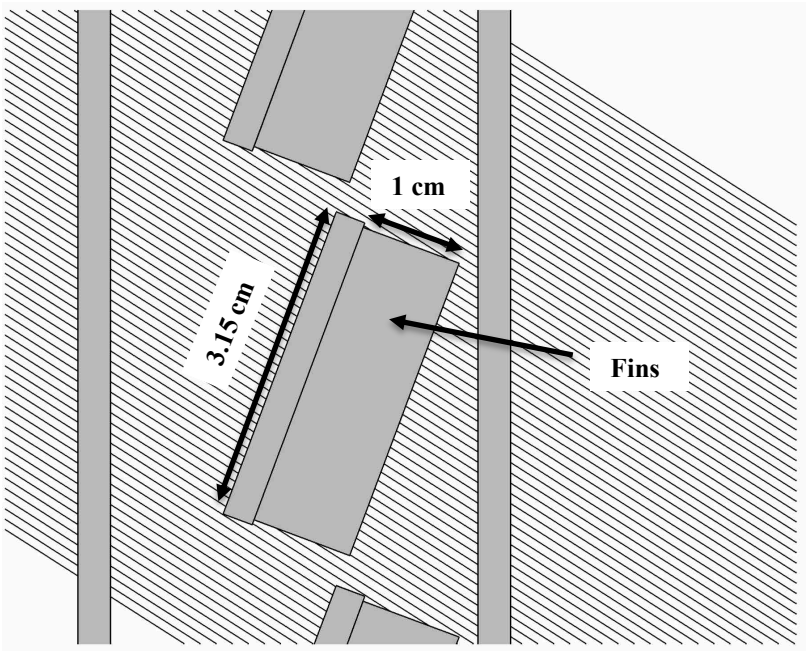

Fig. 6.14: PV tilting by 20 º in the case of 3.15 cm blinds and 1 cm fins. The straight lines represent the solar radiation beam, incident at an angle of 32 º.

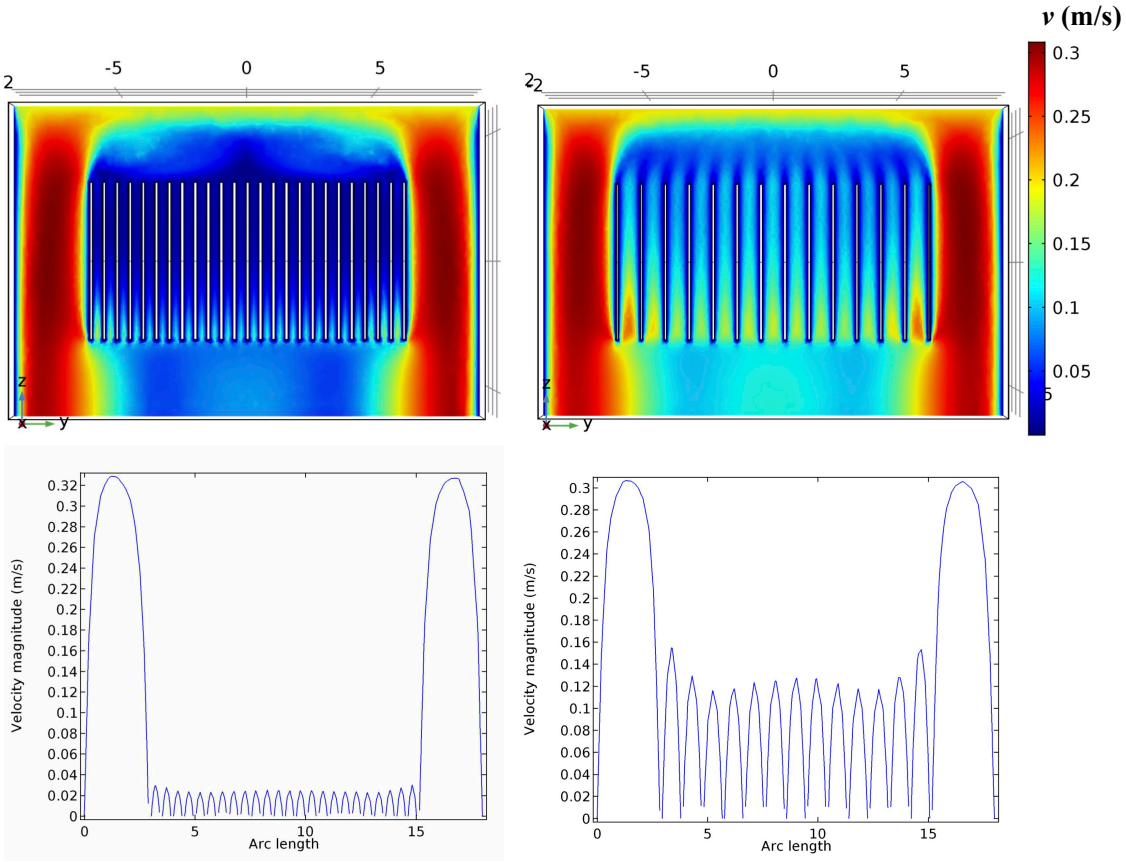

Fig. 6.15: Velocity field for 25 (top left) and 14 fins (top right) on a plane parallel to the PV module, at middle-length of the fins, and related velocity profiles along the central line of the plane (bottom plots).

Once the fins length has been determined, the next parameter to optimize is the number of fins. An increase in the number of fins will increase the heat transfer area, but it will also reduce the spacing between each pair of fins, therefore reducing the channel air velocity. A reduced number of fins will have the opposite effect. As a comparison, the velocity field on a cut plane parallel to the module, at the middle of the fin length, as well as its linear profile along the central line are plotted in Fig. 6.15. The results show a significant difference between the two cases, with the 25-fins configuration having maximum channel velocities of only 0.02–0.03 m/s, while by reducing the fins number by almost a half, the velocity increases to 0.1–0.14 m/s.

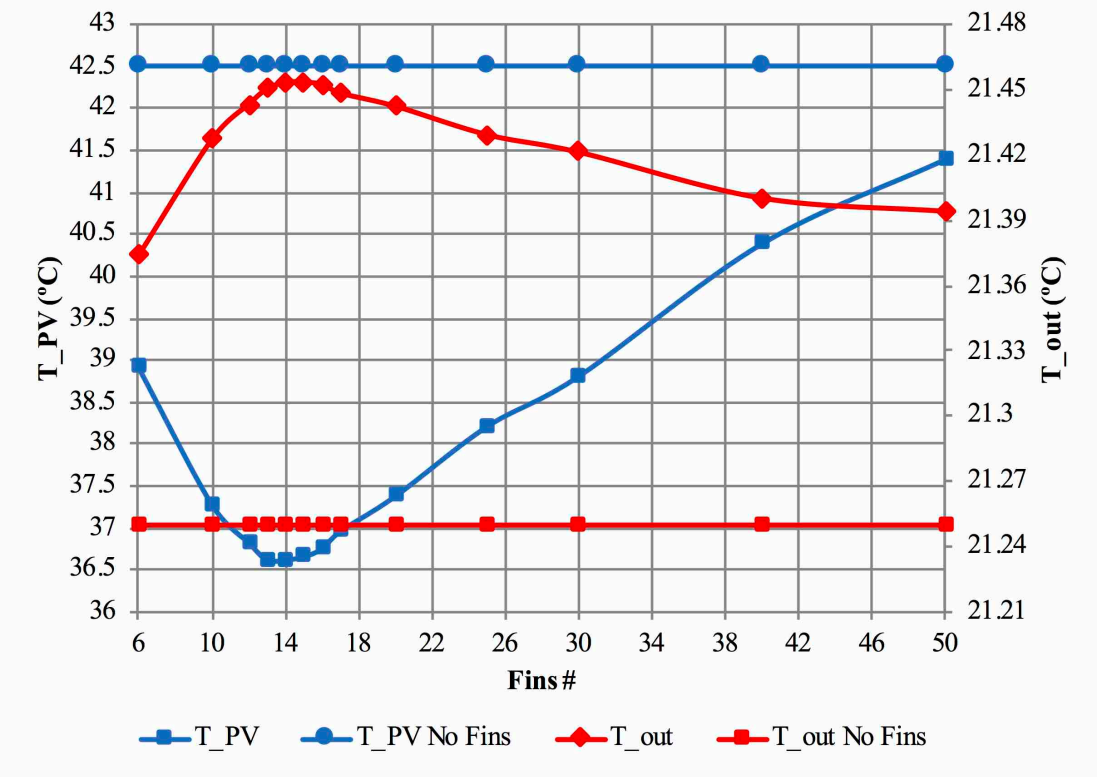

Fig. 6.16: Comparison of PV (T_PV) and air output temperature (T_out) for different number of fins. The constant profiles represent the values for the no-fins situation.

Several simulations were run for different number of fins. The results for the average air output temperature and PV temperature as a function of the fins number are reported in Fig. 6.16, where also the values for the no-fins case are shown for comparison. It can be seen that as the number of fins decreases, the output air temperature increases, resulting in higher heat generation, and the PV temperature decreases, up to a maximum and minimum value corresponding to the configuration with 14 fins. Therefore, an increase in both thermal and electrical performance can be achieved. For a fewer number of fins, the reduction in heat transfer area becomes more important than the increase in channel air velocity, and the PV and air temperature tend towards the no-fins scenario, with the first increasing and the latter decreasing.

The temperature field for the no-fins and 14 fins configurations are plotted in Fig. 6.17, where it can be seen that the maximum and minimum temperature are reduced from 42.9 ºC to 37 ºC, and from 42 ºC to 36 ºC, respectively. With respect to the module without fins, the temperature increase from the initial value for the finned module drops by 26%, while the air temperature rise from bottom to top increases by 16%.

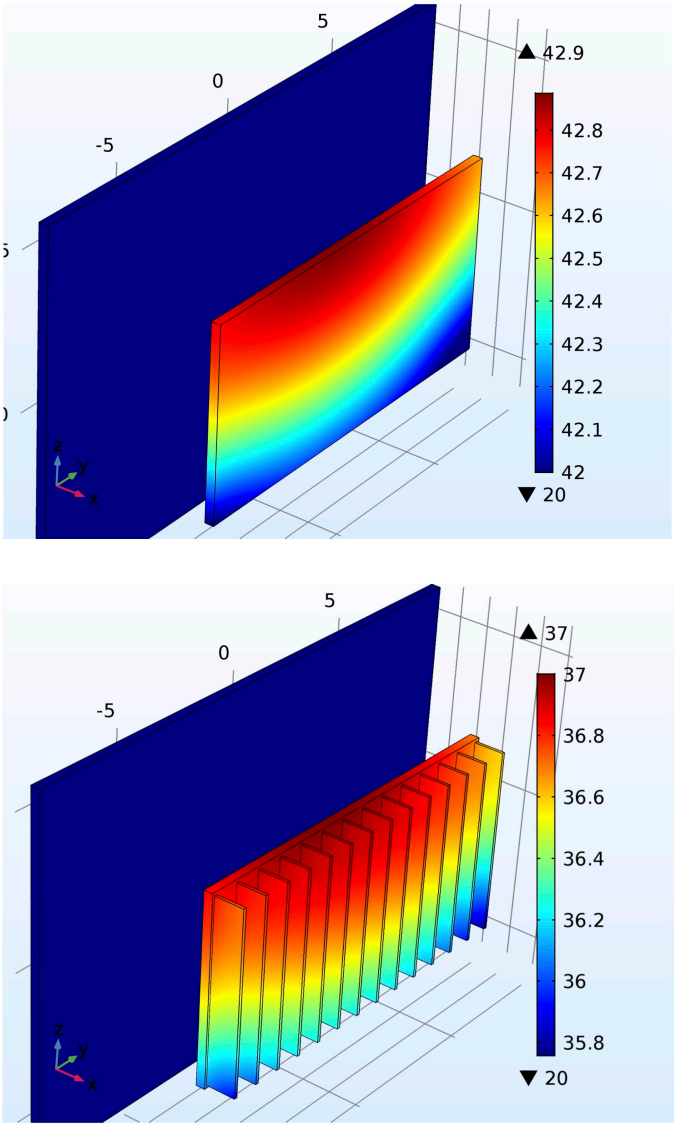

Fig. 6.17: Temperature field (ºC) for the module without fins (top) and with 14 fins (bottom).

6.3.3 Increased *k* – PV layers thermal conductivity

Some improvements can also be made in terms of conduction within the PV module layers. The current modules are mainly composed of 3 mm epoxy resin material, which has a thermal conductivity of 0.2 W/m·K and so high thermal resistance. Therefore, a new design of the PV/T absorber should include thinner and more conductive materials.

A traditional PV laminate is structured as shown in Fig. 6.18, where it can be seen that the glass cover has the highest thermal resistance per unit area (the ratio between the thickness and the thermal conductivity), due to its thickness that represents almost 75% of the total thickness of the module, while the other layer that limits heat dissipation is EVA (Ethylene-vinyl acetate). If the module is placed inside a double-glazing, the latter will provide protection from the environment, and if the module is placed on a rigid substrate providing structural support, the glass cover becomes no longer necessary. Moreover, the filling of EVA with different filler materials, such as SiC, ZnO and BN has been shown to increase EVA thermal conductivity up to 2.85 W/m·K at a filler content of 60 vol% [133]–[134].

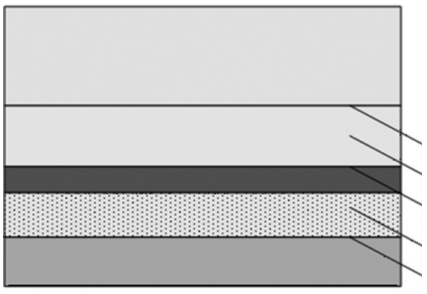

Layer	Layer thickness (mm)	Thermal conductivity (W/m·K)	Thermal resistance per unit area (m^2·K/W)
Glass	3	1.8	0.0017
EVA	0.5	0.35	0.0014
PV cells	0.225	148	$1.5 \cdot 10^{-6}$
EVA	0.5	0.35	0.0014
Tedlar	0.1	0.2	0.0005

Fig. 6.18: Structure of a PV module and layers properties [134]–[135].

The following PV layers composition has been considered:

1. Transparent thin film (e.g. Teflon®)
2. EVA
3. Solar cells (with anti-reflective coating)
4. EVA
5. Aluminum backing

A transparent thin film, such as Teflon® (ETFE or FEP), can be used as an alternative front sheet to the conventional glass cover, which serves as a moisture barrier while providing an improved light transmission. The optimal refractive index of the top layer located between air and EVA is 1.22 [136], while the glass refractive index is 1.52. As a comparison, Teflon® FEP has a refractive index of 1.39, which is therefore closer to the optimal value, and this provides a reduction in reflectivity from 8% to 4%, with respect to glass [136].

The module structural support is provided by an Aluminum back-cover, electrically insulated from the PV by the EVA interlayer, which also serves to distribute the heat uniformly across the back of the solar cells, due to its high thermal conductivity.

To evaluate the effects of the proposed configuration, two 2-D models were setup in COMSOL, which are built from the first model discussed in Chapter 5. The first (reference case) aimed to represent the current blinds composition, consisting of the solar cells, modeled as a thin Silicon layer of 0.5 mm sandwiched between two layers epoxy resin, with a thickness of 1.5 mm each (Fig. 6.19*a*). The front layer is transparent to the solar spectrum but opaque within the far-infrared spectral band ($\varepsilon = 0.9$), while

the solar cells boundary is set as opaque to solar radiation, with the same emissivity of 0.85 used in previous models. The second model used the new configuration discussed above, with both Teflon® and the solar cells modeled as a thin layer (Fig. 6.19*b*), while the top layer of EVA was set to be transparent to solar radiation. Both regular EVA and thermally conductive EVA were simulated, to see the effects of increased EVA conductivity, and the layer properties are summarized in Table 6.5.

A comparison between the reference configuration and the new setup with thermally conductive EVA (EVA* in plots) is shown in Fig. 6.20 for the conductive heat flux, evaluated within the module along the x-direction (Fig. 6.19), where it can be seen that the heat flux for the new module is improved by about 30%. As a result, the temperature gradient within the module's layers is smaller, due to the lower resistance

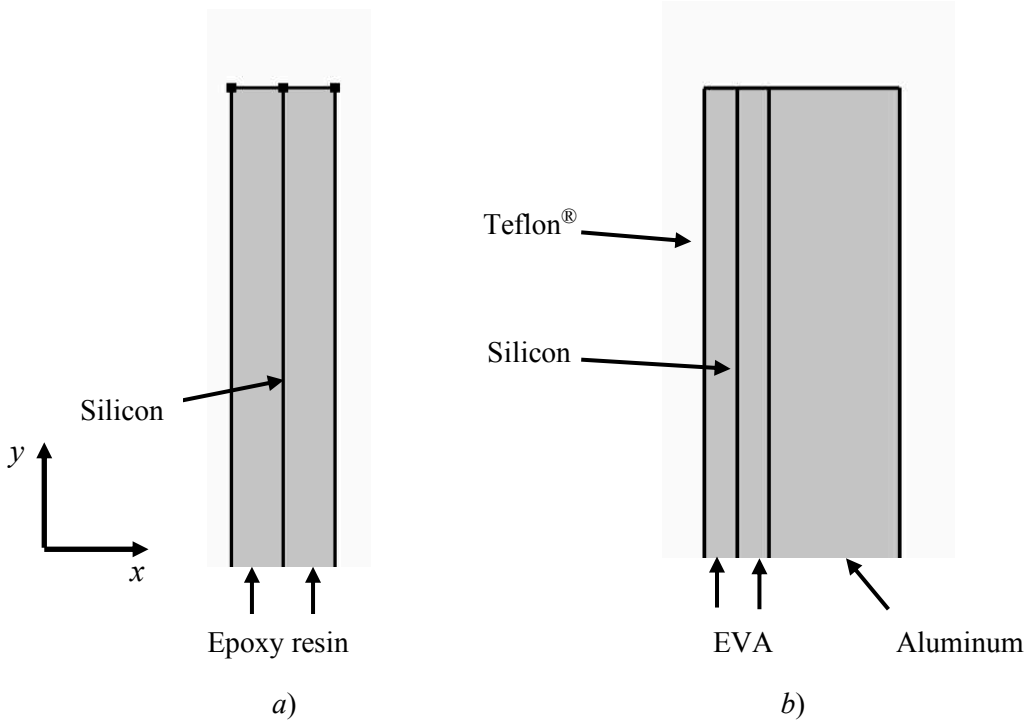

Fig. 6.19: PV module layers for current (a) and new (b) configurations, where Silicon and Teflon are applied to the displayed boundaries as thin layers.

Table 6.5: PV layer properties for the reference case and for the new configuration.

	Layer	Layer thickness (mm)	Thermal conductivity (W/m·K)	Thermal resistance per unit area (m^2·K/W)
Current PV module	Epoxy resin	1.5	0.25	0.006
	PV cells	0.225	148	$1.5 \cdot 10^{-6}$
	Epoxy resin	1.5	0.25	0.006
New configuration	Teflon®	0.1	0.195	$5.13 \cdot 10^{-4}$
	EVA	0.5	0.35 (2.85*)	0.0014 ($1.7 \cdot 10^{-4}$*)
	PV cells	0.225	148	$1.5 \cdot 10^{-6}$
	EVA	0.5	0.35 (2.85*)	0.0014 ($1.7 \cdot 10^{-4}$*)
	Aluminum	2	238	$8.4 \cdot 10^{-6}$

*thermally conductive EVA

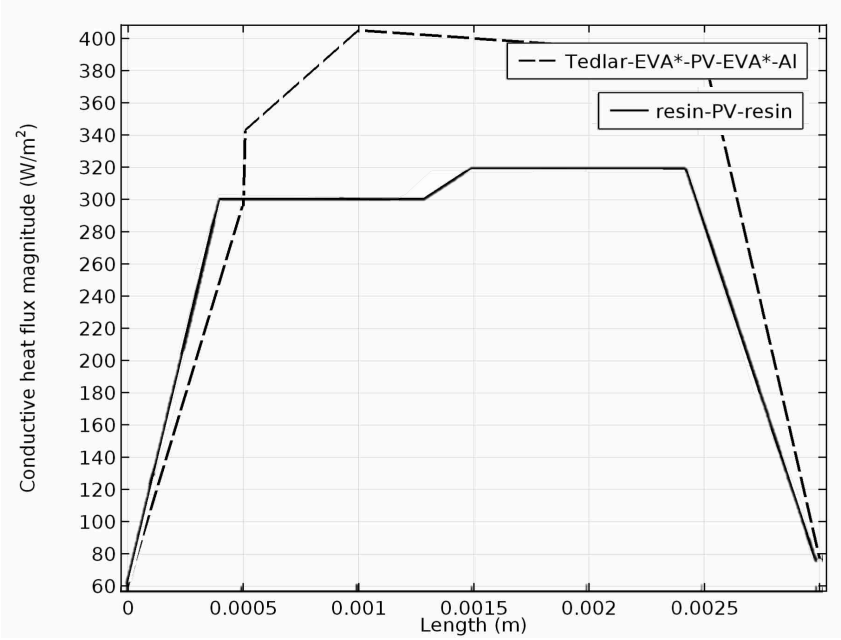

Fig. 6.20: Conductive heat flux in the direction perpendicular to the PV module's surface (x-direction).

to heat transfer from the interior heat source (PV layer) to the exterior sides of the module. This is shown in Fig. 6.21, where the temperature profiles along the same cut line are reported for the reference case and for the new arrangement with both regular and thermally conductive EVA. For the reference case, the temperature drops from

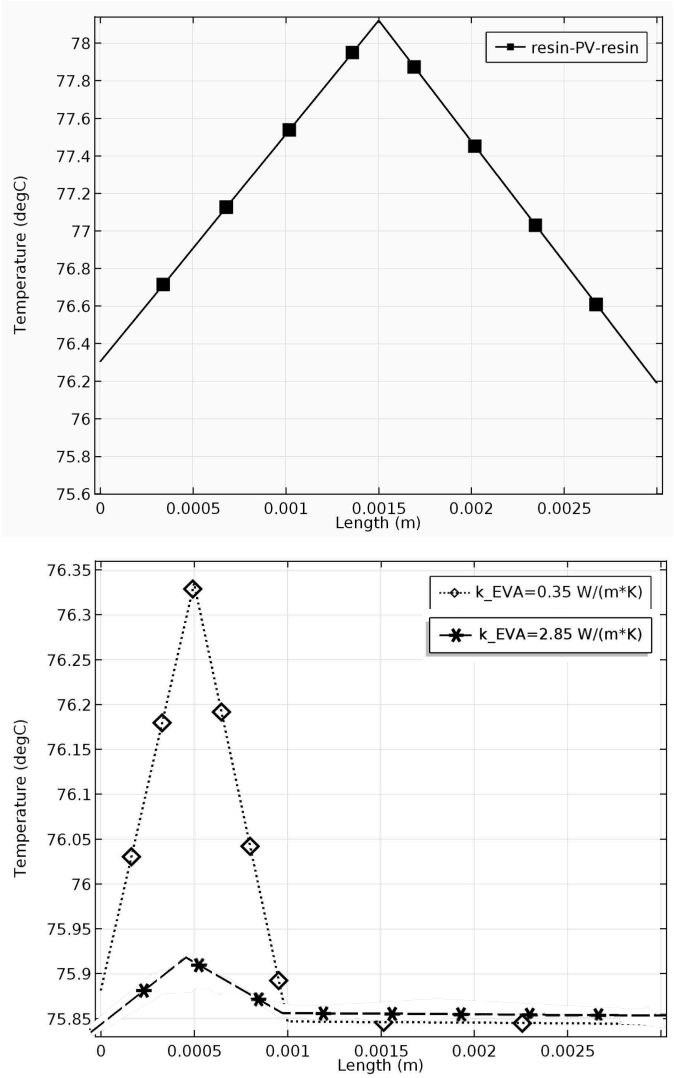

Fig. 6.21: Temperature profiles within the module's layers for the reference case (top) and for the new setup (bottom).

about 78.1 ºC in the PV layer to 76.2–76.3 ºC at the exterior boundaries, while the temperature variation in the new configurations are about 0.5 ºC with regular EVA and less than 0.1 ºC with thermally conductive EVA, with a PV layer temperature of around 76.3 ºC and 75.9, respectively.

Therefore, the new module structure provides some improvement in terms of heat dissipation, although the benefits of thermally conductive EVA are not significant.

Chapter 7
Prototype Design

As the last phase of the project, new prototype designs have been developed in SolidWorks, based on the results obtained from the optimization discussed in the previous chapter. Additional CFD models were developed to conduct several preliminary studies, which were used for design. A total of 6 different prototypes were designed, each of them being different from the other by a single change in its features. This was done so that, by testing the prototypes side by side in the same conditions, the effects of each change could be easily observed.

7.1 Preliminary Analysis

7.1.1 Effects of a Whole Array of PV Blinds

The next prototypes are intended to be fully made of blinds, and therefore the bottom PV module should be replaced with a PV array. This will reduce the total absorbing area, so the thermal performance is expected to drop.

As a three-steps iteration, Fig. 7.1 shows three configurations for double uncoated glass: case *a*) represents the current prototype, with 6.3 cm wide blinds at the top and the large PV module at the bottom, case *b*) features 6.3 cm blinds extended to the whole height, and case *c*) represents a whole array configuration with optimal ratio d/w=1.1, hosting blinds with 3.15 cm width, and having a glass-to-glass spacing of 3.5 cm. The simulation results for the output temperature and maximum PV temperature

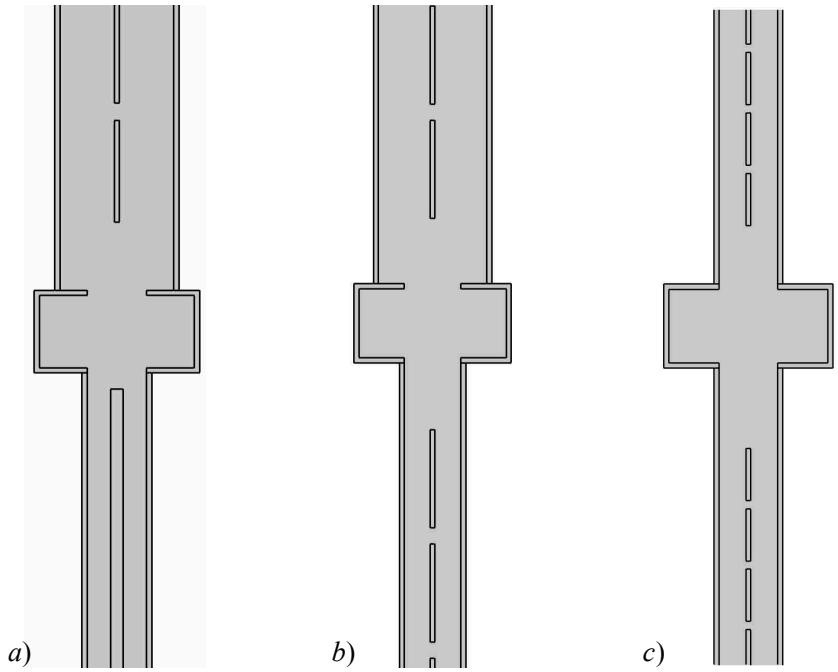

Fig. 7.1: Reference configuration (a), extended blinds to the bottom section (b) and whole PV array with 3.15 cm wide blinds and d/w=1.1 (c).

are reported in Table 7.1, where the total length of the PV absorbers is compared as well. By going from configuration *a*) to *b*), there is a drop in both output and PV temperature from 52.2 ºC to 50.7 ºC and from 77 ºC to 76 ºC, respectively, which is caused by a 11.6% reduction in the total length of the PV array. With respect to case *b*), the reduction in glass spacing and PV width by a factor of 2 (case *c*)) causes the output temperature of the air to increase to 51 ºC, and the PV temperature to drop to

Table 7.1: Comparison between cases *a*) - *c*) for the air output temperature T_{out}, maximum PV temperature $T_{PV,max}$ and total PV length.

Configuration	T_{out} (ºC)	$T_{PV,max}$ (ºC)	PV length (cm)
a)	52.2	77	221.1
b)	50.7	76	195.5
c)	51	73	195.5

73 ºC. Since configurations *b*) and *c*) have the same PV length, the slight increase in performance is due to the fact that, while the heat transfer is improved in the top portion of the window (provided by the increased air velocity), in the bottom part the ratio d/w increases from 0.58, for case *b*), to 1.1, for case *c*), which has been shown to reduce convective heat transfer (Fig. 6.12).

Overall, the use of the PV array on the whole height of the collector produces a 2.3% drop in output temperature, along with a 5.2% decrease in PV temperature, with respect to the current prototype. Therefore, the thermal and electrical performance are only slightly reduced and increased, respectively.

7.1.2 Effects of a Wood Frame

Due to the need of a wooden frame for improved thermal insulation, the model *c*) shown in Fig. 7.1 for a whole blinds configuration has been modified with a new frame geometry (Fig. 7.2), and both Aluminum and wood frame material have been simulated. Since window wood frames are usually in the order of a few centimeters, the frame thickness has been increased up to around 3.3 cm, so as to provide a constant cross-sectional area to the airflow. This would not noticeably affect the amount of heat lost through the aluminum frame, because of its high thermal conductivity, while the smaller conductivity of wood is expected to significantly reduce frame heat losses.

The optimal glazing system discussed in section 6.2.1 (triple glazing with low-e coating on surface 2-3-5) was also used, with a 20 mm air gap, and the results were compared to the reference configuration having blinds only at the top section of the window.

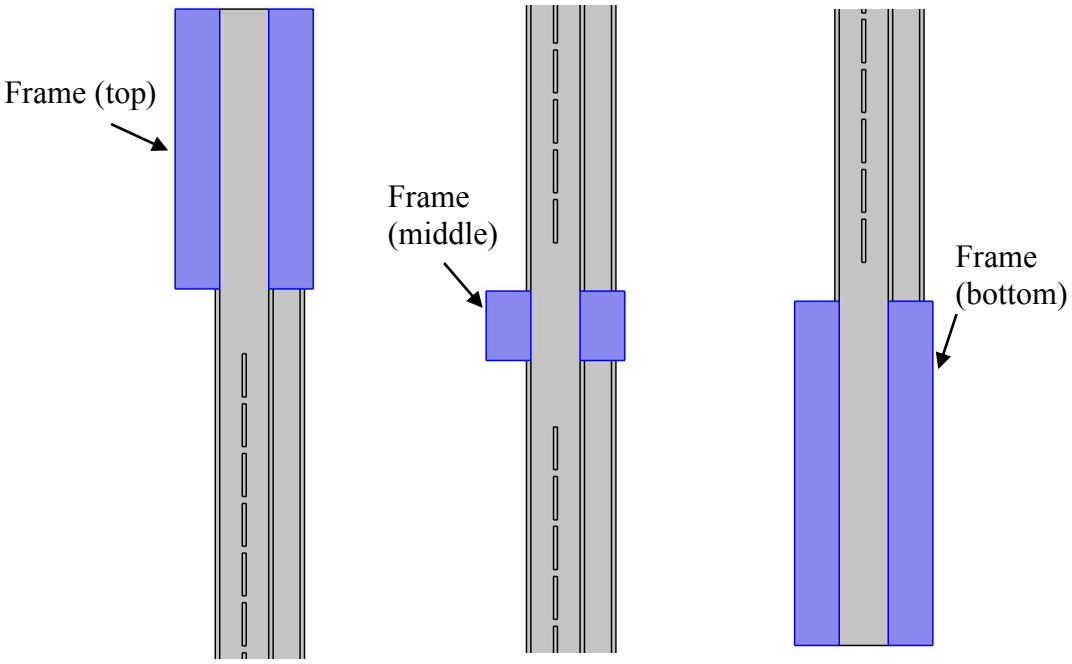

Fig. 7.2: Modified frame geometry (highlighted in blue).

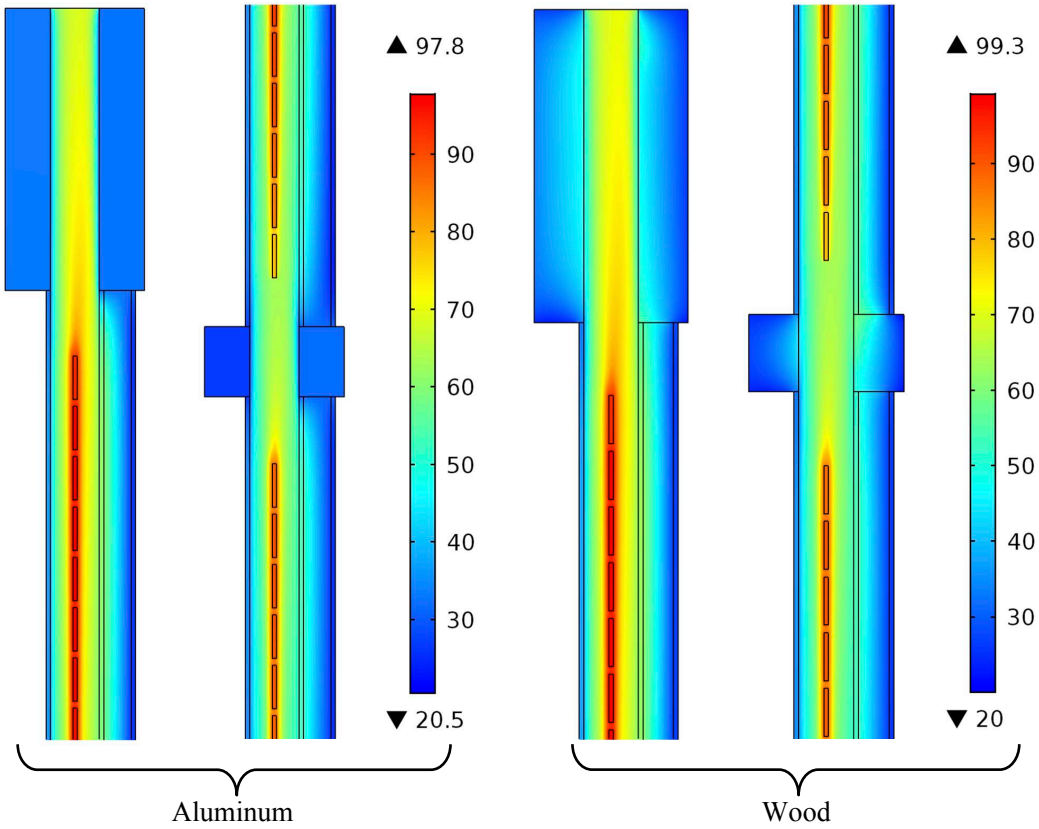

Fig. 7.3: Temperature field for 3-pane system with Low-e on surfaces # 2-3-5, with Aluminum frame (left) and Wood frame (right).

Table 7.2: Comparison between the reference case (PV array at the top and large module at the bottom) and the modified frame configurations.

Configuration	Frame material	PV length (cm)	T_{out} (ºC)	Q (W)	Q_{loss} (W/m)	η_{th} (%)	$Max\ T_{PV}$ (ºC)
Top PV array	Al	221.1	64.73	663	593	43.4	109
Whole PV array	Al (new)	195.5	62.83	646	567	42.3	97.7
Whole PV array	Wood	195.5	66.51	695	529	45.6	99.3

The temperature fields are plotted in Fig. 7.3 for the new frame configurations using Aluminum and wood, where it can be noticed how a larger temperature gradient occurs within the wood frame. While the temperature within the Aluminum domains is very uniform, and around 30-33 ºC, the temperatures of the wood frame's interior surfaces in contact with the airflow are in the 45-55 ºC range. As a result, the heat lost by the airflow is reduced, and higher temperatures are achieved.

As shown in Table 7.2, the output air temperature T_{out} for the new frame design is around 62.8 ºC for Aluminum and 66.5 ºC for wood, which compares to the 64.7 ºC value achieved by having a larger PV surface at the bottom (traditional PV). With respect to the reference case, the new Wooden frame provides an increase in heat generation and thermal efficiency from 663 to 695 W, and from 43.4 to 45.6%, respectively, as well as a reduction in heat losses (Q_{loss}) from 593 to 529 W/m and in maximum PV temperature ($Max\ T_{PV}$) from 109 to 99 ºC.

7.1.3 Hybrid Configuration

A further development of the previous section involved what it can be defined as a hybrid configuration. This consists of the same blinds' layout, but with the PV layers only used at the bottom part of the window, while the top blinds are made of traditional

aluminum venetian blinds, with a top layer of selective coating to increase solar absorptivity and reduce radiation losses. In this setup, electrical generation occurs only in the bottom part of the window, which operates at lower temperatures and therefore the PV efficiency is higher, while the top section, where the PV would experience lower efficiency due to the high temperatures, is optimized for thermal generation.

The wood framed window model used in the previous section has been modified by changing the top blinds' material from Silicon to Aluminum. The solar absorptivity and infrared emissivity at the front surface were set to 0.94 and 0.06, respectively, and the same emissivity values used for the aluminum frame were used (Table 5.2).

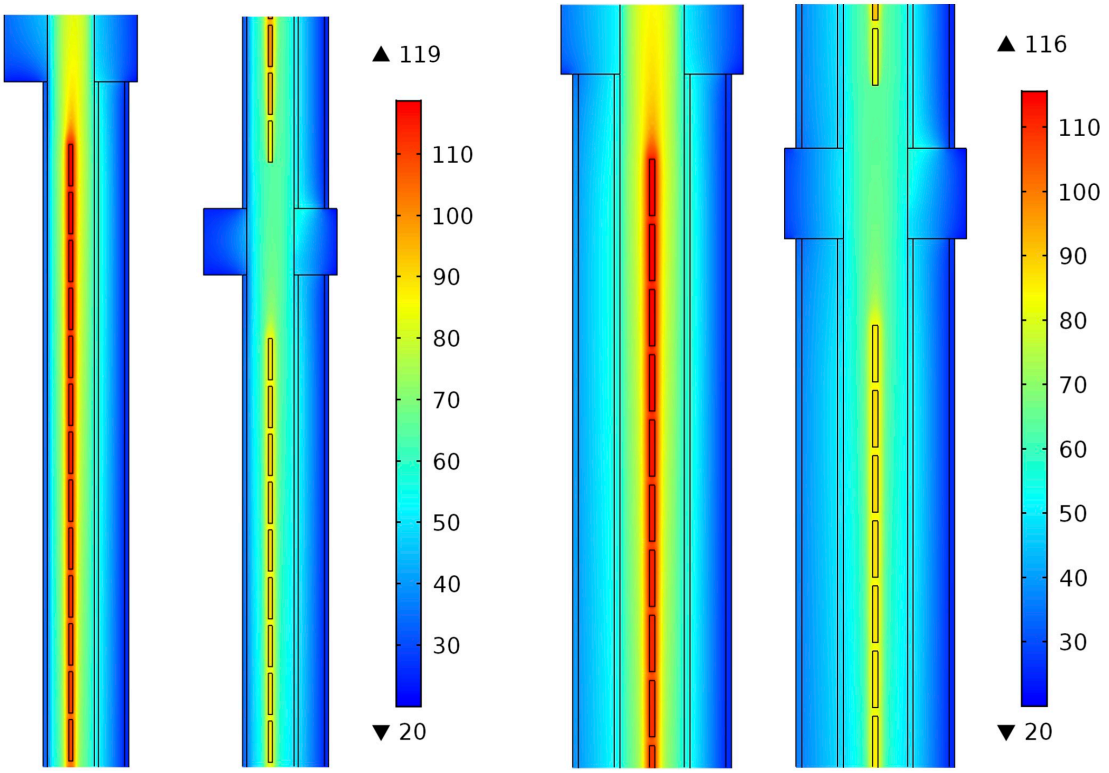

Fig. 7.4: Results for the temperature of the top portions of the Aluminum and PV blinds for a 3-pane (left) and 4-pane (right) system.

Table 7.3: Performance of triple and quadruple glazing with 3 Low-e coatings, wood frame and hybrid blinds arrangement.

Configuration	Frame material	T_{out} (ºC)	Q (W)	Q_{loss} (W/m)	η_{th} (%)	$Max\ T_{PV}$ (ºC)
3-pane Low-e #2-3-5 (hybrid)	Wood	71.7	762	501	50	90
4-pane Low-e #4-5-7 (hybrid)	Wood	74	792	337	51.9	87

The temperature field for the top sections of the Aluminum and PV blinds is shown in Fig. 7.4 for both a 3-pane and 4-pane system. Due to the higher absorptivity and lower infrared emissivity of the aluminum blinds, with respect to the PV blinds, the absorber temperature in the top section of the unit is in the range of 100–120 ºC for triple-glazing and 95–115 ºC for quadruple-glazing. As a result, the output air temperature reaches 71.7 ºC and 74 ºC, with heat generation of 762 W and 792 W and thermal efficiency of 50% and 51.9%, respectively (Table 7.3). The temperature of the PV blinds is limited to less than 90 ºC (reached at the top of the PV array in the bottom section of the window) for both cases, and ranges from 55–90 ºC and 52–87 ºC for 3-pane and 4-pane configuration, respectively.

7.1.4 Effects of Increased Blind Spacing

As the blinds are rotated, in order to capture more solar radiation, shading between the rows will occur after a certain tilt angle. For a whole array with a spacing of 0.63 cm (1/4") between the blinds, the maximum tilt angles before shading begins are 2°, 10.5° and 20.5° for solar elevations corresponding to incident angles of 75° (summer), 44° (winter) and 32.5° (fall), respectively. An increase in the spacing between the rows

would allow the blinds to rotate at larger angles. For instance, a spacing of 1.27 cm (1/2") would provide a maximum tilt of 6.5° for summer solar elevations, and it would allow the blinds surfaces to be oriented perpendicular to the winter and fall solar radiation (44° and 32.5°, respectively). However, this would come at the cost of a reduced number of blinds within the same window height.

To evaluate the effects of increase blinds spacing, 3 different configurations were simulated for uncoated double-glass, based on the same geometry shown for case c) in section 7.1.1. The first model consists of a 58-blinds array in vertical position (no tilt), with 0.5 cm spacing between the rows, while a second model, composed of an array

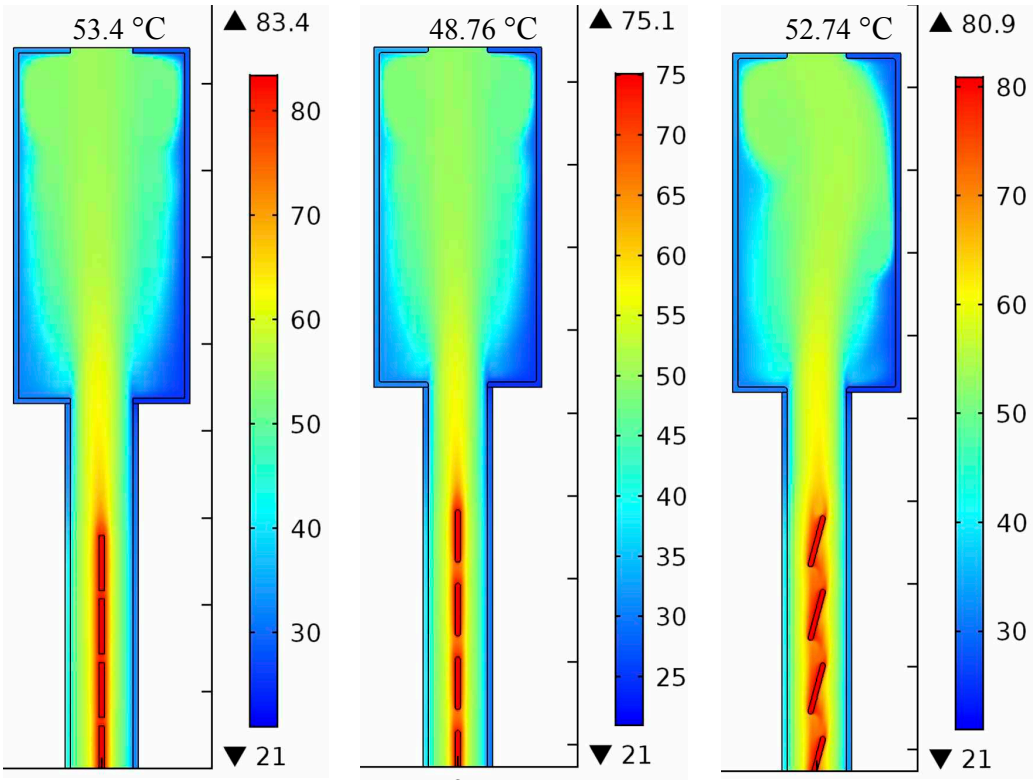

Fig. 7.5: Temperature field and output temperature for vertical blinds with spacing of 0.635 cm (left), 1.27 cm without tilting (center) and with 15° tilting (right).

of 50 blinds with 1.27 cm spacing, was simulated with blinds both in vertical position and with a 15° tilt angle.

The temperature field and the output air temperature are shown in Fig. 7.5 for the three cases. As expected a decrease in the number of blinds produces lower air and PV temperatures, due to the reduced absorbing area. A 15° increase in tilt angle, with respect to the original case with 58 blinds, produces almost the same output air temperature, while the maximum temperature experienced by the PV modules is reduced by about 2.3°C. Since the difference between the maximum tilt angles of the two configurations (0.63 cm and 1.27 cm spacing) is around 12° for fall and 33.5° for winter solar radiation, the output air temperature is expected to further increase at tilt angles larger than 15°, although the associated increase in PV temperature should be evaluated as well.

7.2 Design Variations

The following section will briefly describe the type of variations used to define the different prototypes.

7.2.1 Frame Material

The first type of feature change is the material used for the frame. While the first prototype (Prototype 1) kept the same frame as the current unit, that is Aluminum Alloy 6061 with the same geometry, Prototype 2–6 feature a wooden (Oak) frame with some modifications to the original frame geometry, as it will be shown later.

7.2.2 Blinds Layout

Two different blinds geometry are used, as shown in Fig. 7.6. Configuration 1) features a total of 60 blinds, with a spacing of 6.35 mm, while configuration 2) consists of 52 blinds spaced by 12.7 mm from each other.

7.2.3 Blinds Composition

Three different blinds structures are included in the designs, which are shown in Fig. 7.7. Variations A) and B) represent the layer composition discussed in Section 6.3.3, with the addition of Aluminum fins in configuration B). Configuration C) consists of Aluminum blinds coated with a selective material, providing high solar absorption and low emissivity.

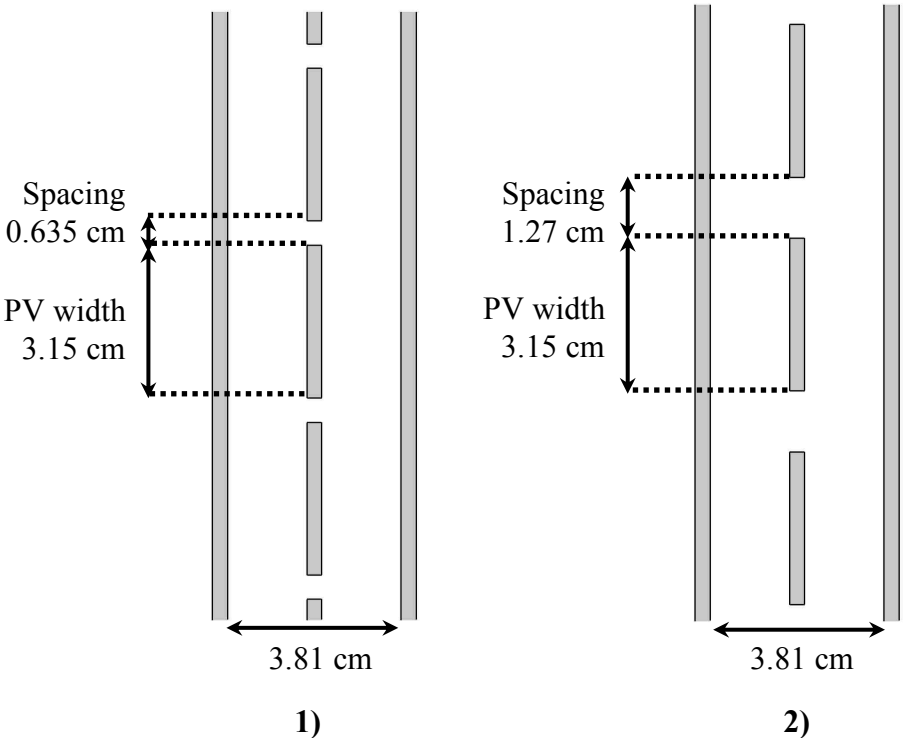

Fig. 7.6: Blinds layout configurations.

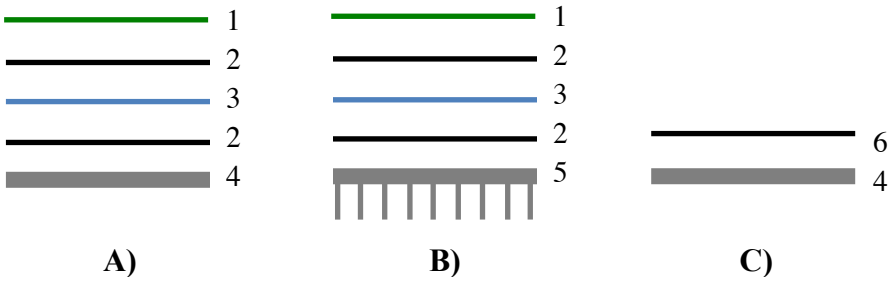

Fig. 7.7: Different arrangements of the blind's layers.

The layers shown in Fig. 7.7 are defined as follows:

1. Teflon® thin film;
2. EVA;
3. Solar cells (with anti-reflective coating);
4. Aluminum plate (1-2 mm);
5. Aluminum plate (1-2 mm) with 1 cm fins on the back;
6. Selective coating (solar absorptivity > 0.9, emissivity < 0.1).

7.2.4 Glazing system

Both triple-glazed and a quadruple-glazed configuration have been used. The two arrangements are displayed in Fig. 7.8, and the specifications for each monolithic glass panel are listed in Table 7.4, where T_{sol} and T_{vis} are the transmittances for the solar (300-2500 nm) and visible (380-780 nm) spectrum, respectively, and ε_1 and ε_2 represent the emissivity of the outer (left side in Fig. 7.8) and inner (right) surfaces, respectively.

The glazings were chosen from the IGDB (v66.0) of the LBNL WINDOW software [125] among those having both high solar and visible transmittance as well as low

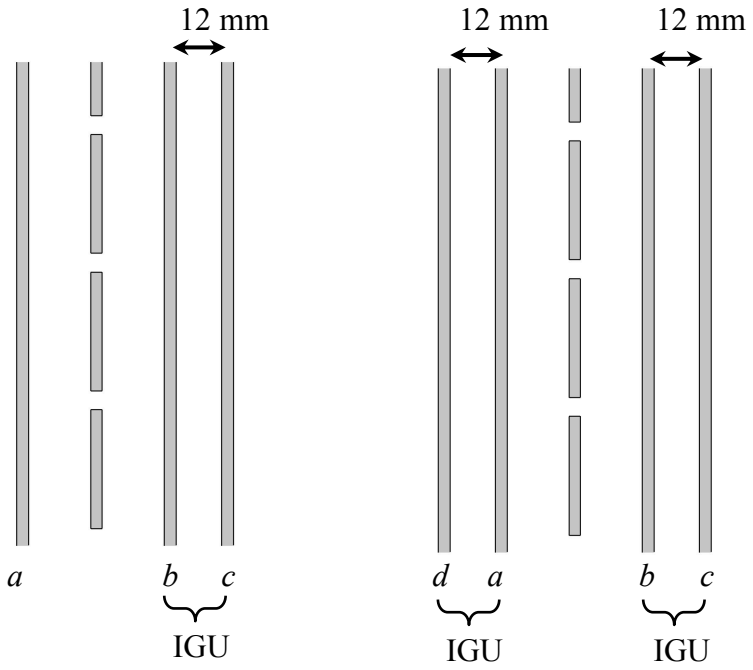

Fig. 7.8: Triple (left) and quadruple (right) glazing configurations.

emissivity, and glass products by the manufacturer Guardian Glass have been selected. All the glass panels are tempered, with a thickness of 3 mm, and measure 32" x 47 ½" (81 x 120 cm). In the triple-glazed system (*a*-*b*-*c*), glass panels *b* and *c* form an insulated glass unit (IGU), while in configuration *d*-*a*-*b*-*c* an additional ultra-clear glass (*d*) is placed as the outermost layer, adding an IGU at the front as well. The IGUs are ½" (12.7 mm) wide, and they are filled with 10% Air and 90% Argon.

Table 7.4: Details of monolithic glass products by Guardian Glass.

Position	**Product name**	T_{sol}	T_{vis}	ε_1	ε_2
a	SunGuard® IS-20 on UltraClear™	0.82	0.89	0.84	0.198
b	ClimaGuard® IS-20	0.77	0.876	0.198	0.84
c	ClimaGuard® 72/57 LE	0.488	0.784	0.045	0.84
d	UltraClear™	0.9	0.91	0.84	0.84

The innermost glass (*c*) has a soft low-e coating with an emissivity of 0.045, which is placed on the surface facing the sealed IGU cavity and offers some solar control (T_{sol} = 0.488), while still providing good visible transmittance.

Overall, the two configurations have a total visible transmittance of 0.62 for the 3-pane and 0.58 for the 4-pane system, and U-values for unventilated window of 0.85 and 0.68 $W/m^2 \cdot K$, respectively (values calculated using the Guardian Performance Calculator). If higher T_{vis} is needed, panel *c* can be substituted with Guardian Glass ClimaGuard® 80/70 (T_{sol} = 708, T_{vis} = 0.892, ε_1 = 0.095 and ε_2 = 0.84), which provides a 3-pane and 4-pane visible transmittance of 0.71 and 0.65, respectively, with an associated increase in U-value of 0.05 $W/m^2 \cdot K$ in both cases.

7.3 Prototypes Overview

The different prototype versions are summarized in Table 7.5, where the labels and configurations were defined in the previous section. The detail drawings as well as a short description of each prototype will be presented in the following subsections.

Table 7.5: Overview of the different prototypes, where the variations are highlighted in bold.

Prototype #	**1**	**2**	**3**	**4**	**5**	**6**
Frame	Al	**Wood**	Wood	Wood	Wood	Wood
Blinds layout	1)	1)	**2)**	1)	1)	1)
Blinds composition	A)	A)	A)	A)	**B)**	Top: **A)** Bottom: **C)**
Glazing system	a-b-c	a-b-c	a-b-c	**d-a-b-c**	a-b-c	a-b-c

7.3.1 Prototype 1

The first prototype (Fig. 7.9) keeps the same Aluminum frame and dimensions as the original one, while featuring the new blinds layout 1) made of single Aluminum slats with PV layers on top (configuration A)). The glazing system is also updated from

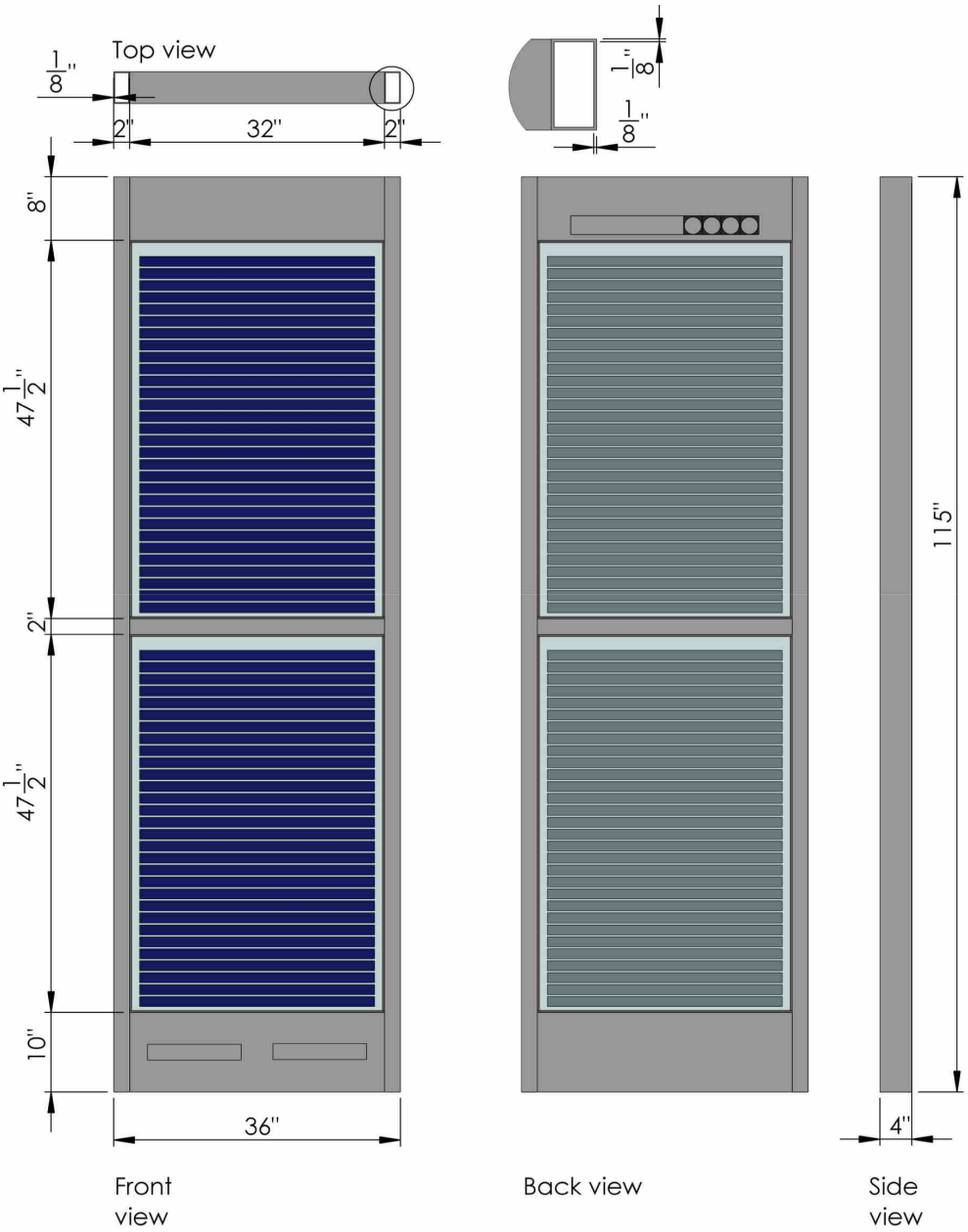

Fig. 7.9: Frontal, rear and side view of Prototype 1.

uncoated double-glazing to triple-glazing with low-e coatings, as described before (*a-b-c* setup).

The two glazed sections have been adjusted to have the same dimensions, both measuring about 120 cm in height and hosting 30 blinds each, and 10 computer fans (only 4 of which are shown in Fig. 7.9) are placed vertically at the output vent.

A cross-sectional view is shown in Fig. 7.10, where the three glass panels, warm edge spacers within the rear IGU and insulated aluminum stops are displayed, the latter serving to hold the front glass panels in place. The holes in the frame, connecting the hollow frame cavities with the glazed compartments, are replaced with rectangular openings to facilitate the airflow, as shown in the 3D cross-sections in Fig. 7.11.

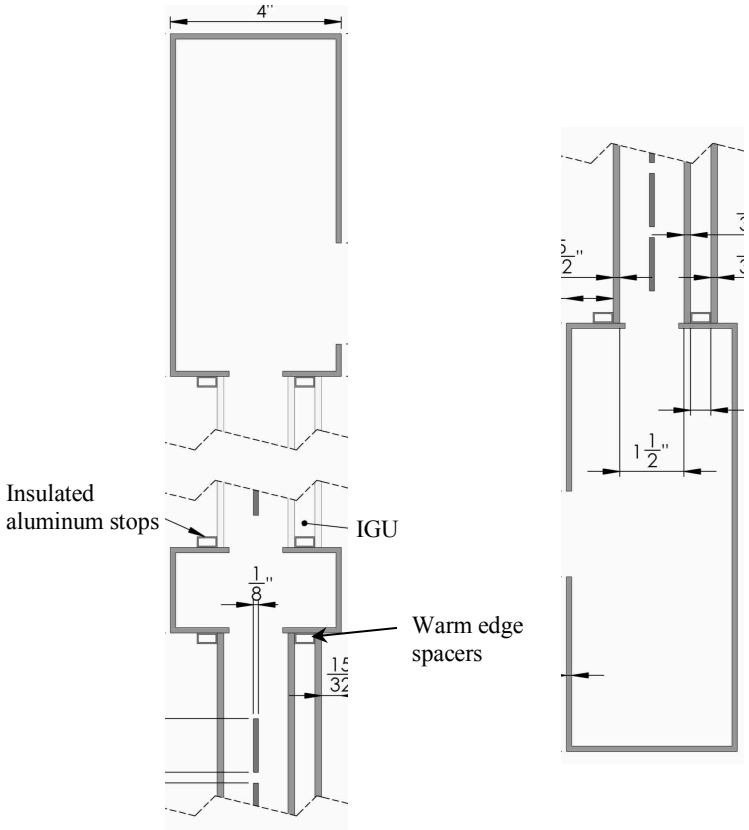

Fig. 7.10: Prototype 1 cross-sectional view.

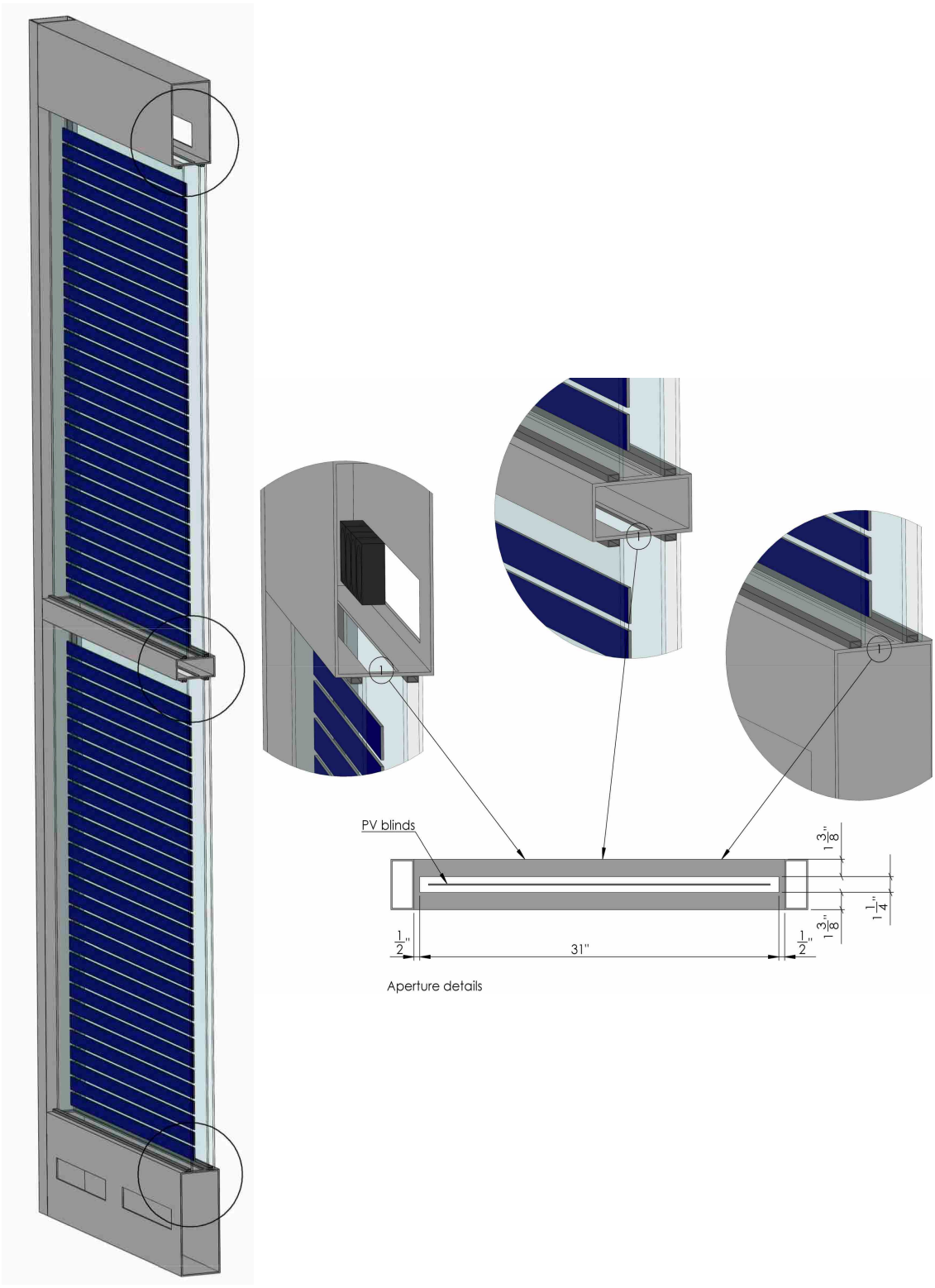

Fig. 7.11: 3D cross sectional view and close-ups showing the frame openings.

7.3.2 Prototype 2

The second prototype (Fig. 7.12) features the addition of a wooden frame, with some modifications to the frame geometry, which can be seen in the cross-sectional view of Fig. 7.13. The input vent consists of a single opening of the same size as the width of the ventilated cavity, and hosts wood stops for the front glazing.

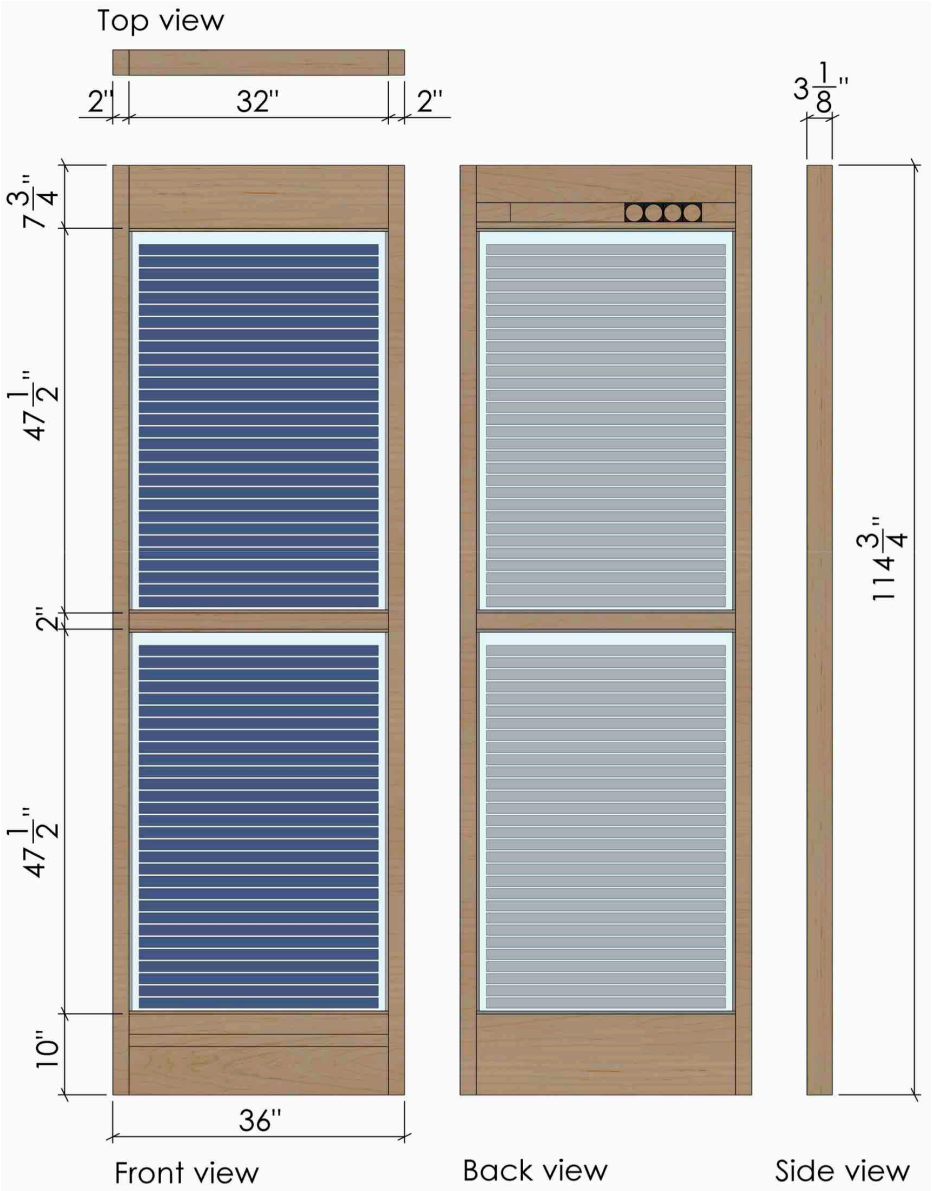

Fig. 7.12: Prototype 2 front, rear and side views.

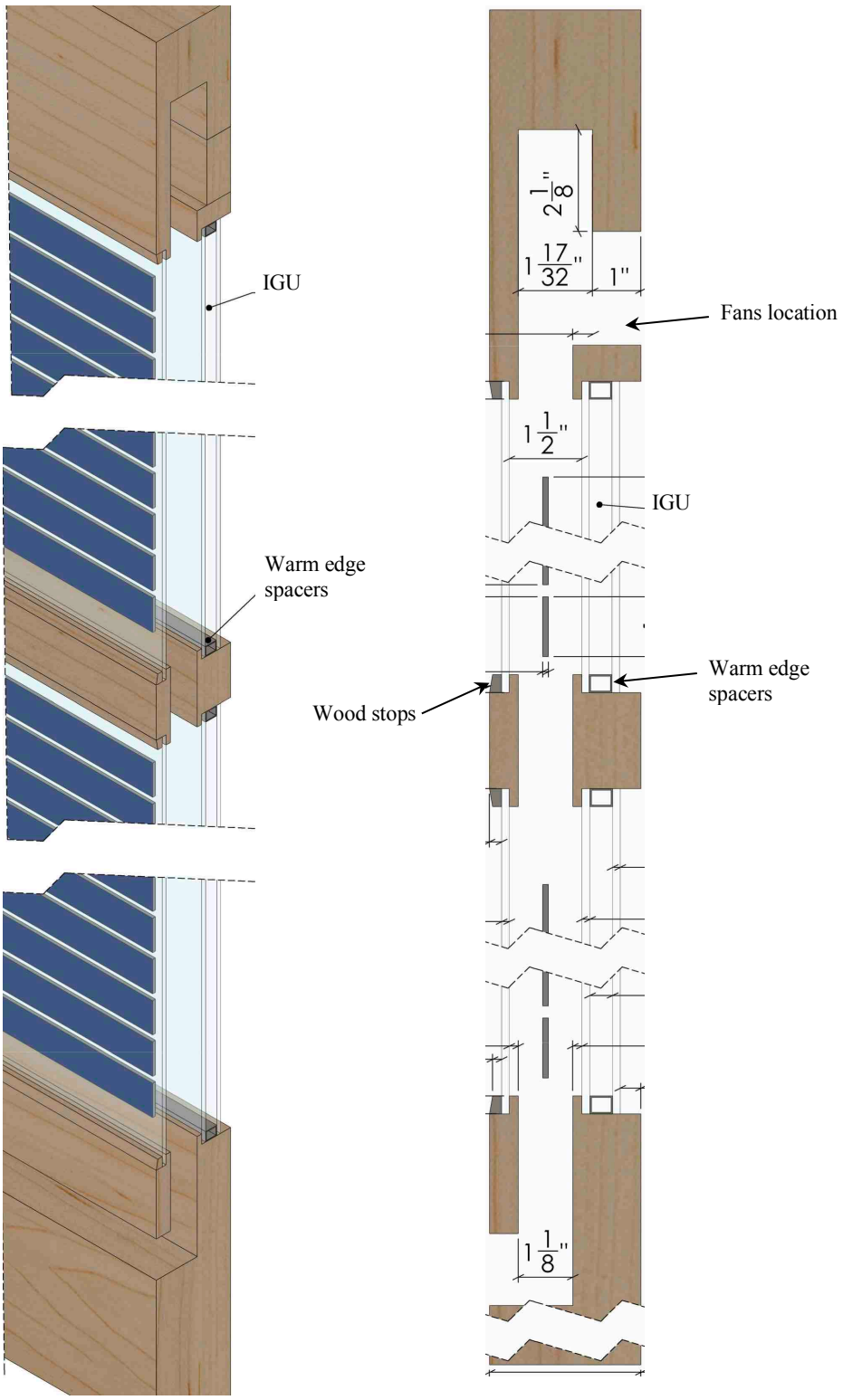

Fig. 7.13: Prototype 2 2D and 3D cross sectional view.

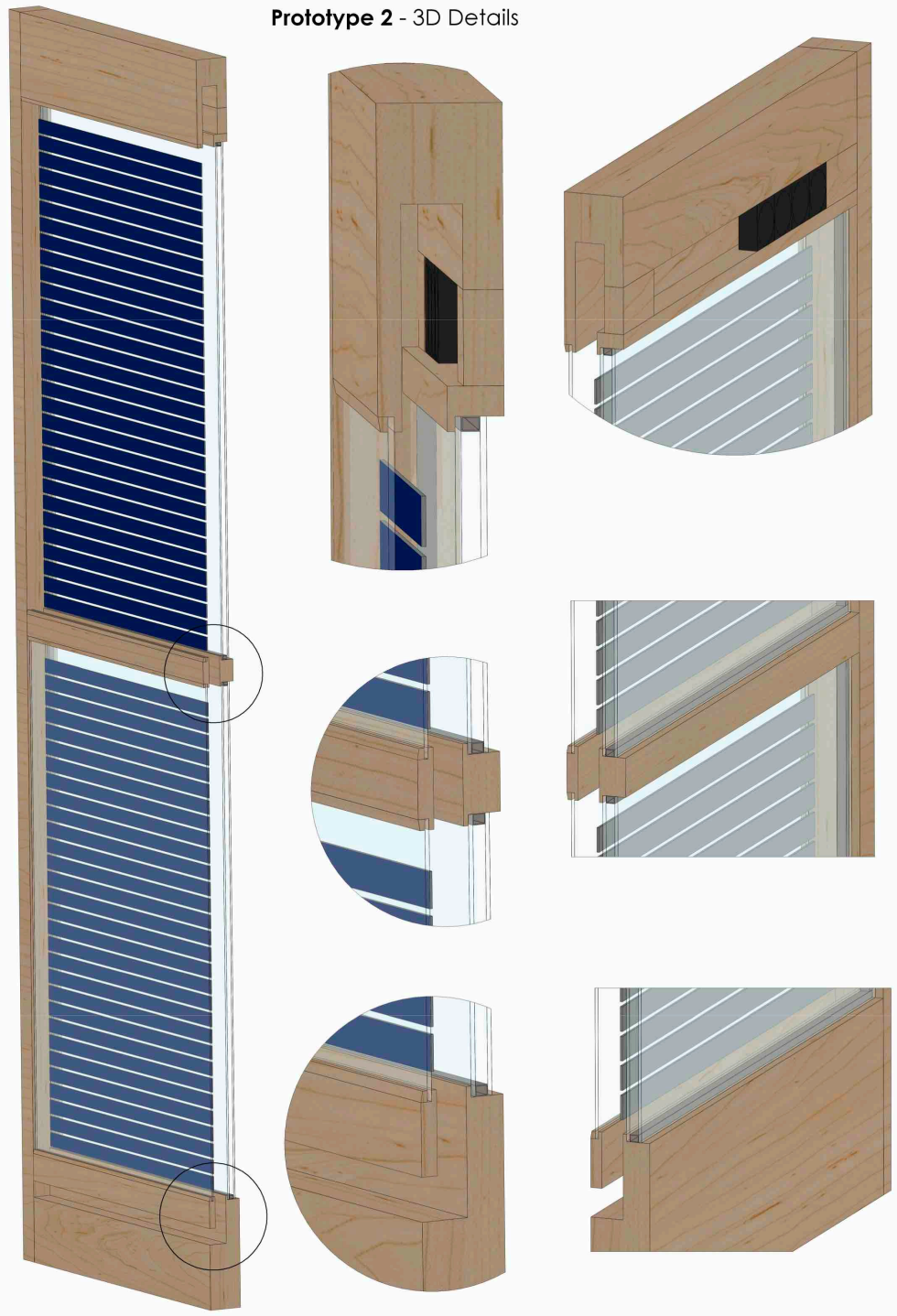

Fig. 7.14: 3D details for Prototype 2.

The offset of the frame with respect to the front glass has been reduced in order to decrease shading on the top blinds by the frame for high solar elevations, which makes

the overall window depth to decrease by about 2.2 cm with respect to Prototype 1.

The size of the gap between the outlet section and the top portion of the frame will depend on the actual dimensions of the blinds head rail (not shown in the drawings).

A cross-sectional 3D view of the overall prototype, as well as some close-up views, is also shown in Fig. 7.14

Prototype 2 is the reference configuration from which the other 4 iterations are developed, and each of them represents a further modification of Prototype 2, as it will be discussed in the rest of the chapter.

7.3.3 Prototype 3

Prototype 3, shown in Fig. 7.15, features the configuration 2) for the blinds' layout, therefore having 26 blinds for each glazed section, with a slat spacing of 1.27 cm. This arrangement will serve to evaluate the effects of a reduced absorbing area (at increased PV tilting) during side-by-side testing with Prototype 2.

7.3.4 Prototype 4

This version has an additional glass panel at the front for each glazing section, and therefore differs from the other prototypes by being characterized by the *d-a-b-c* glazing system layout.

Due to the additional IGU at the front, the frame is thicker than the other wood framed prototypes (around 9.5 cm), but it does not exceed the depth of Prototype 1, which is 10.2 cm.

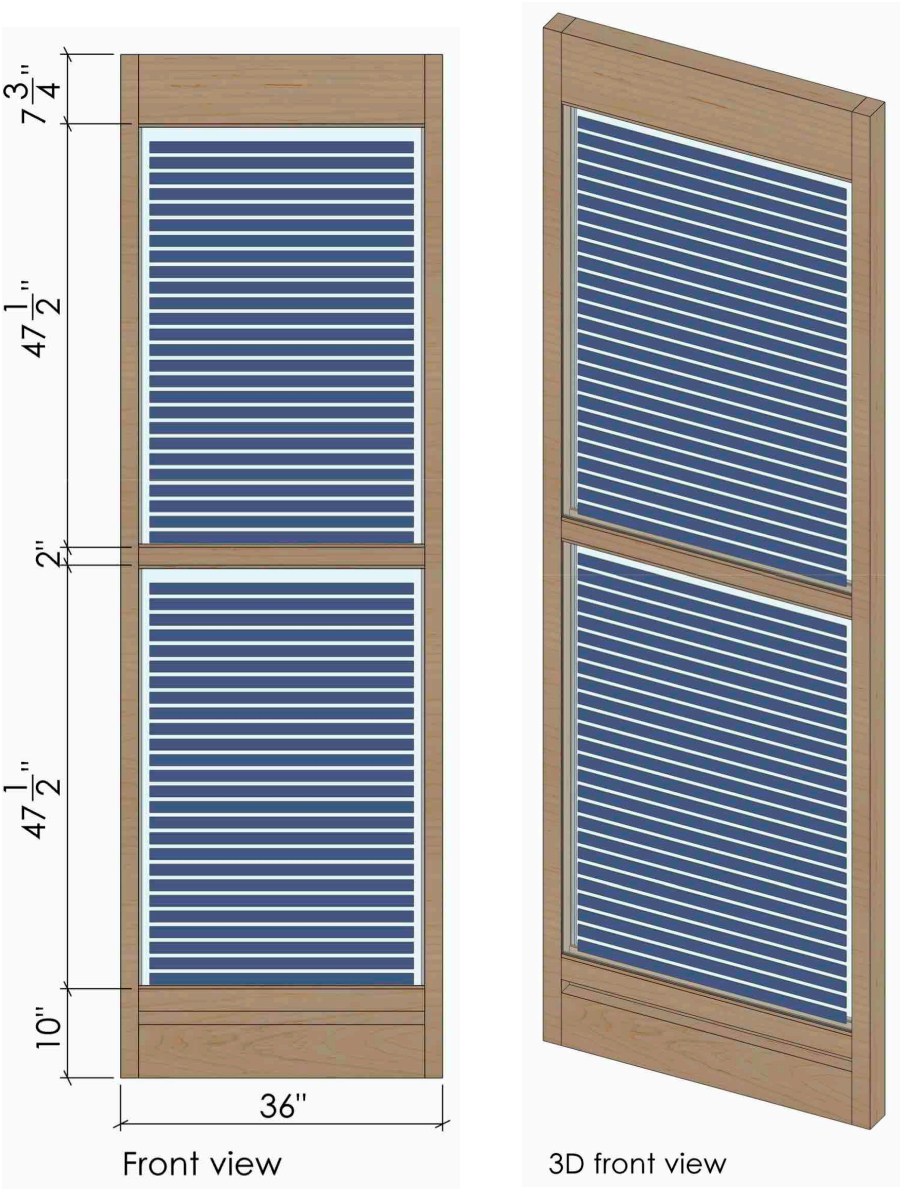

Fig. 7.15: Prototype 3 2D and 3D front view.

A comparison between the cross-sectional views for Prototypes 3 and 4 is shown in Fig. 7.16, where it can be seen how the triple-glazed and quadruple-glazed window differ in terms of glazing arrangement and frame thickness. The different blinds' spacing of layout 1) can be also compared to that of configuration 2), which is represented by the 4-pane system.

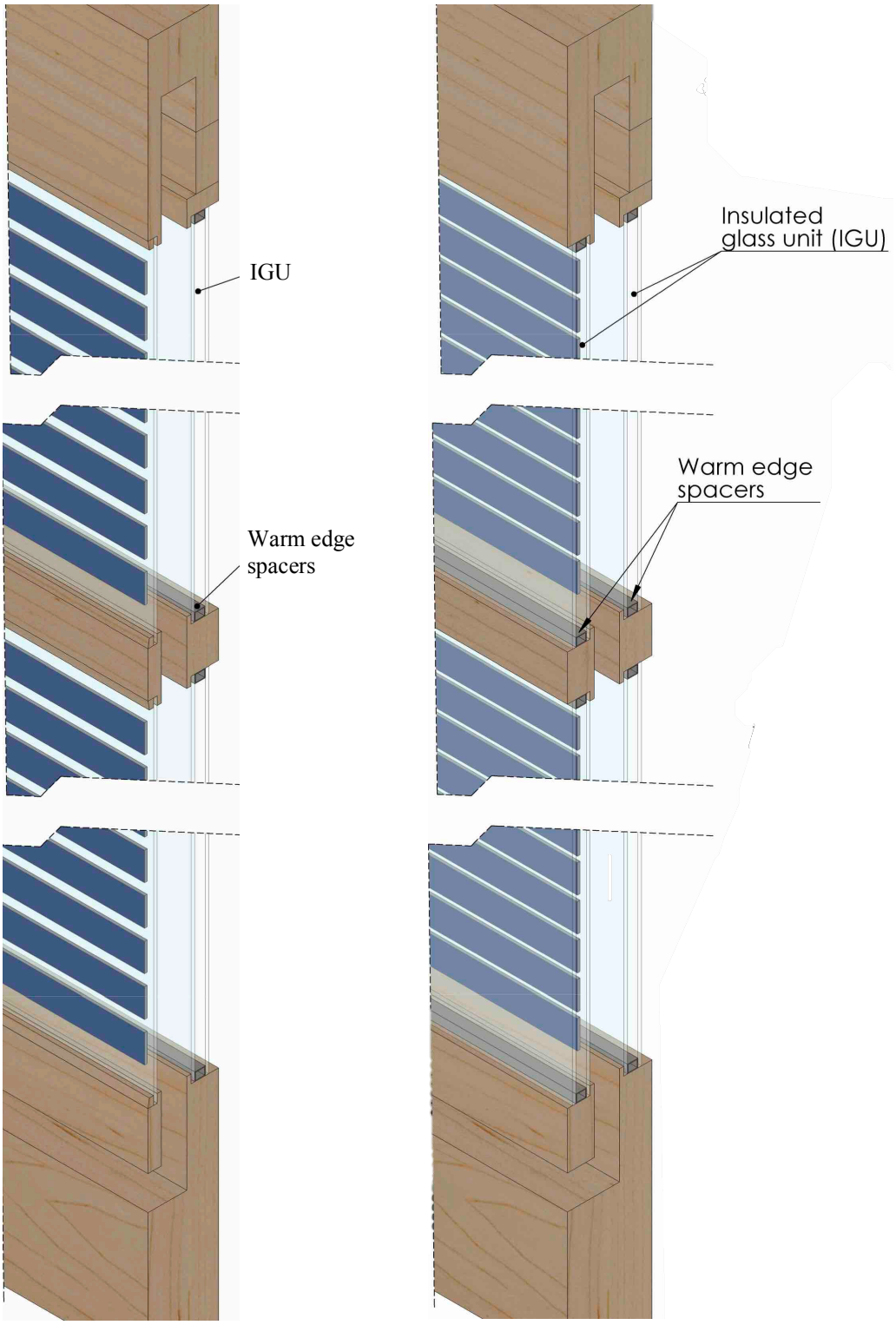

Fig. 7.16: 3D cross-section of Prototype 3 (left) and Prototype 4 (right).

7.3.5 Prototype 5

Prototype 5 has the same features as Prototype 2, with the exception of aluminum fins attached to the back of the PV blinds (blinds composition B) in Table 7.5).

A 3D drawing of a finned PV blind is shown in Fig. 7.17, which consists of 74 fins with 1 cm length and about 1 mm thick.

7.3.6 Prototype 6

The last variation involves a type C) blinds' configuration, consisting of selectively coated Aluminum blinds at the top section (black slats in Fig. 7.18), and PV blinds at the bottom section, while keeping all the other features of Prototype 2.

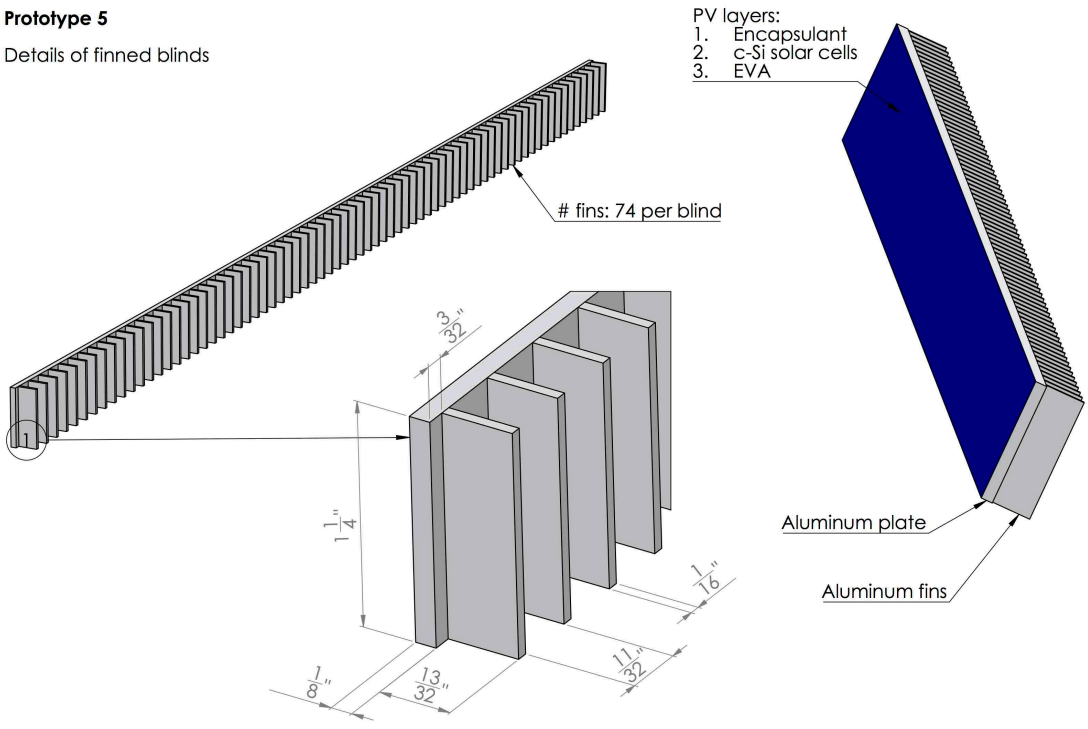

Fig. 7.17: Details of a PV blinds with fins used for Prototype 5.

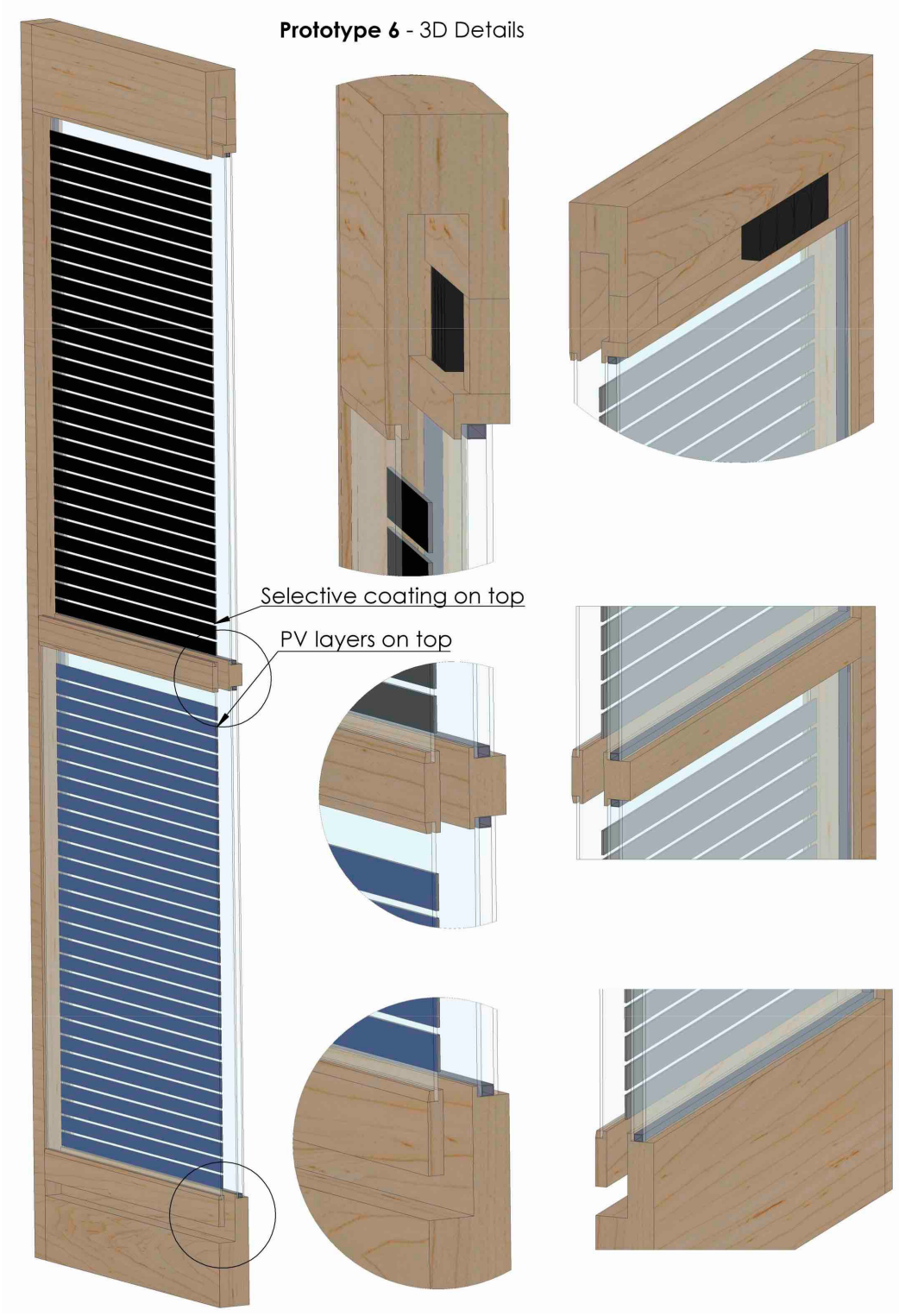

Fig. 7.18: 3D cross-sectional views of Prototype 6.

Chapter 8
Conclusion and Summary of Results

In this work, a novel BIPV/T solar air collector for integrated heat and power generation has been presented, which consists of a double-glazed airflow window with PV blinds installed within the ventilated cavity.

The thermal and electrical performances of a prototype were first evaluated by testing the collector in outdoor conditions, and the results showed maximum output temperatures up to 53.2°C during the winter, corresponding to a temperature rise of 31°C. The thermal efficiency ranges between 25 and 40%, while the electrical efficiency remains around 6–8%, with an average power generation of 20–25 W and peaks up to 35 W for the top PV array, which operates at temperatures up to 77 ºC. Higher PV generation could be achieved by using higher efficiency modules, or by the use of thin-film solar cells, which have a lower sensitivity to high temperatures [65].

The experimental data have been used to build and validate a two-dimensional CFD model in COMSOL Multiphysics, which was used to build more expanded 2D and 3D models in order to optimize the collector performance.

Different strategies were presented, in terms of thermal insulation improvements and heat transfer enhancement.

The use of a triple-glazed system with Low-e coatings provides a 38.6% and 33.5% increase in temperature rise and thermal efficiency, respectively. This results in an air output temperature of 64.7 ºC and thermal efficiency of 43.4%, as well as in maximum

PV temperature of 109 ºC and a 40% decrease in heat losses, with respect to the reference case.

The air and PV temperature can be controlled by adjusting the air flow rate, and by doubling the air velocity the air and PV temperatures drops to 48.5 ºC and 86 ºC, respectively, while the heat generated increases to 874 W, with respect to a value of 496 W for the original prototype configuration. The heat losses are reduced by 60%, with an associated increase in thermal efficiency increases up to 57.3%.

Three-dimensional models for a portion of the ventilated cavity were developed to simulate the effects of a reduced glass spacing and additional fins on the back of the PV modules. In the first case, a reduction of the air gap from about 7 cm to 2.7 cm produces a 33.4% increase in heat generation, with a 6% increase in air output temperature and a 22.7% decrease in PV temperature. The use of aluminum fins has the potential to further increase the amount of heat transferred from the PV to the airflow, and to reduce PV temperatures. An optimal number of 14 fins for a 12.5 cm module's length has been found to increase the temperature rise by 16% and decrease the module temperature rise from its initial value by 26%, with respect to the module without fins. A new structure of the PV layers was also proposed, which provides a 30% increase in conductive heat flux within the module, and a decrease of the solar cells' temperature by 2 ºC.

Some additional analysis and simulations were performed to aid the design of new prototypes. The use of blinds on the whole height of the window was not found to

significantly affect the performance, and a 2% decrease in air temperature and 5% drop in PV temperature was observed.

A new wooden frame design provides a 5% increase in heat generation, with a thermal efficiency of 45.6% and output temperature of 66.5 ºC, as well as a reduction in maximum PV temperature from 109 to 99 ºC, when coupled with the extension of PV blinds on the bottom section.

A hybrid solution, with Aluminum blinds at the top and PV blinds at the bottom of the window, was also simulated, which was found to further increase the output temperature and thermal efficiency up to 74 ºC and 52%, respectively, while keeping the PV temperatures below 90 ºC.

Lastly, additional CFD models were developed and, together with the results from the previous studies and optimizations, they were used for the design of 6 new prototypes in SolidWorks. The prototypes are intended to be tested side-by-side, in order to evaluate the single changes between the various prototype variations, therefore more work is needed for future testing.

In conclusion, this study showed that PV/T airflow windows have the potential to significantly impact the building energy performance, by providing on-site combined heat and power generation as well as thermal insulation at the same time, which is further improved by the airflow with respect to a same size high-performance window. Furthermore, they can provide space heating, solar control, visible light transmission and shading with a single element, which can result in cost reduction with respect to having separate systems performing the same functions.

Although the market is currently focused on either the PV or the solar thermal sector, and despite the added complexity of such system, BIPV/T technologies are expected to become increasingly important in the future energy scenario.

Bibliography

[1] M. Dabaieh and A. Elbably, "Ventilated Trombe wall as a passive solar heating and cooling retrofitting approach; a low-tech design for off-grid settlements in semi-arid climates", *Solar Energy*, vol. 122, pp. 820-833, 2015.

[2] U. Eicker, Energy Efficient Buildings with Solar and Geothermal Resources, 1st ed. West Sussex, U.K.: Wiley, 2014.

[3] EIA, *Monthly Energy Review - U.S. Energy Information Administration*, 2017. [Online]. Available: https://www.eia.gov/totalenergy/data/monthly/. [Accessed: 06 - Jun - 2017].

[4] EIA, *Annual Energy Outlook 2017*, 2017. [Online]. Available: https://www.eia.gov/outlooks/aeo/. [Accessed: 06- Jun- 2017].

[5] *Thermal Insulation*. [Online]. Available: https://www.solardirectory.com.au/power-saving/thermal-insulation. [Accessed: 14 - Dec- 2016].

[6] J. Carmody, *Residential Windows: a Guide to New Technologies and Energy Performance*, 3rd ed. New York: W.W. Norton, 2007, pp. 9-14, 73-104, 131-133.

[7] Wychavon District Council, *History of Windows & Glass, a Guide for Owners & Occupiers*, Pershore, Worcestershire, U.K., 2007.

[8] "*Glassmaking - History of Glass Making*", 2017. [Online]. Available: http://www.historyofglass.com/glass-history/glass-making/. [Accessed: 24- Oct- 2017].

[9] Londoncrownglass, *History of Glass*", 2017. [Online]. Available: http://londoncrownglass.com/History.html. [Accessed: 24- Oct- 2017].

[10] A. Polak, *Glass: its Tradition and its Makers*. New York: G.P.Putnam's Sons, 1975, p. 169.

[11] The American Society of Mechanical Engineers, "The American Society of Mechanical Engineers designates the Owens "AR" bottle machine as an International Historic Engineering Landmark", 1983.

[12] L. Pilkington, "Review Lecture. The Float Glass Process", in *Proc. R. Soc. Lond. A: Mathematical, Physical and Engineering Sciences*, vol. 314, no. 1516, pp. 1-25, 1969.

[13] A. Friedman, *Fundamentals of Sustainable Dwellings*, 3rd ed. Washington: Island Press, 2012, pp. 105-114.

[14] "*Trasmittanza Infissi, Taglio Termico e Vetro Basso Emissivo: La Guida Definitiva sui Serramenti*", 2016. [online]. Available: http://biblus.acca.it/speciale-guida-ai-serramenti/. [Accessed: 07- Apr- 2018].

[15] J. Carmody and K. Haglund, "Measure Guideline: Energy-Efficient Window Performance and Selection", NorthernSTAR, St. Paul, MN, 2012.

[16] Commercialwindows.org, *Windows for High-Performance Commercial Buildings*. [Online] Available at: http://www.commercialwindows.org/ [Accessed 3 Mar. 2018].

[17] RDH Building Science Inc., "Window Energy Performance: a Reference Guide for Energy Advisors", BC Hydro Power Smart, 2017.

[18] Y. Çengel and A. Ghajar, *Heat and Mass Transfer: Fundamentals & Applications*, 5th ed. New York, NY: McGraw-Hill Education, 2015, pp. 6-13, 397-399, 732-754, ch. 16.

[19] J. Duffie and W. Beckman, *Solar Engineering of Thermal Processes*, 4th ed. Hoboken, N.Y.: Wiley, 2013, pp. 3-41, 138-139, 215-216, 238.

[20] Data from American Society for Testing and Materials (ASTM) G-173-03 reference spectra.

[21] L. Wald, "Basics in Solar Radiation at Earth Surface", Sophia Antipolis, France, 2018.

[22] F. Incropera et al., *Fundamentals of Heat and Mass Transfer*, 5th ed. New York: Wiley, 2002, pp. 6-12, 82-85, 230-256, 768-773, 885.

[23] J. Lienhard IV and J. Lienhard V, *A Heat Transfer Textbook*. Cambridge, Massachusetts: Phlogiston Press, 2016, pp. 535-581.

[24] C. Chen, *Physics of Solar Energy*. Hoboken, N.J.: Wiley, 2011, p. 229.

[25] COMSOL Multiphysics Reference Manual, COMSOL AB, 2017.

[26] M. Modest, *Radiative Heat Transfer*, 3rd ed. Nowy Jork [etc.]: Academic Press, 2013, p. 102.

[27] J. Howell, R. Siegel and P. Mengüç, *Thermal Radiation Heat Transfer*, 5th ed. Boca Raton: CRC Press, 2010, pp. 28, 485-488.

[28] Fioretti Infissi srl, *Finestra Legno Alluminio*, 2017. [Online]. Available: http://www.fioretti-infissi.it/portfolio/finestra-legno-alluminio/. [Accessed: 05- Dec- 2017].

[29] "*Prodotti - Finestre Legno + Sughero* ", 2017. [Online]. Available: http://www.eurofinestra.it/ita/prodotti/finestre-legno-sughero.html. [Accessed: 05- Dec- 2017].

[30] Efficientwindows.org, *Efficient Windows Collaborative*, 2018. [online] Available at: http://www.efficientwindows.org [Accessed 9 Feb. 2018].

[31] Bejan, A. and Kraus, A. (2003). *Heat Transfer Handbook*. Hoboken, N.J.: Wiley, p.123.

[32] N. Baker, *The Handbook of Sustainable Refurbishment*. London: Earthscan, 2009, pp. 47-51.

[33] *About Insulated Glass Units: Vitro Residential Glass*, 2018. [Online]. Available: http://www.vitrowindowglass.com/window_glass/understanding_IGU.aspx. [Accessed: 13- Jun- 2018].

[34] D. Harvey, *A Handbook on Low-Energy Buildings and District-Energy Systems*. Abingdon, UK: Routledge, 2015, pp. 64-65, 479-482.

[35] *2013 ASHRAE Handbook: Fundamentals*, American Society of Heating, Refrigerating and Air-Conditioning Engineers, Atlanta, 2013, Chapter 15.

[36] S. Van Den Bergh, R. Hart, B. Jelle and A. Gustavsen, "Window spacers and edge seals in insulating glass units: A state-of-the-art review and future perspectives", *Energy and Buildings*, vol. 58, pp. 263-280, 2013.

[37] F. Patania et al., "Thermofluid-dynamic analysis of ventilated facades", *Energy and Buildings*, vol. 42, no. 7, pp. 1148-1155, 2010.

[38] D. Saelens, "Energy Performance Assessment of Single Storey Multiple-Skin Facades", Ph.D. Dissertation, Katholieke Universiteit Leuven, 2002.

[39] O. Mørck and S. Hastings, *Solar Air Systems: a Design Handbook*. London: James & James, 2000, pp. 146-149.

[40] T. Zhang, Y. Tan, H. Yang and X. Zhang, "The application of air layers in building envelopes: A review", *Applied Energy*, vol. 165, pp. 707-734, 2016.

[41] M. Ghadimi et al., "Analysis of free and forced convection in airflow windows using numerical simulation of heat transfer", *International Journal of Energy and Environmental Engineering*, vol. 3, no. 1, p. 14, 2012.

[42] K. Brandle and R.F. Boehm, "Airflow windows: performance and applications", in *Proc. of the ASHRAE/DOE Conf.: Thermal Performance of the Exterior Envelopes of Buildings II*, Clearwater Beach, 1982, pp. 361–379.

[43] S.D. Park, H.S. Suh and S.H. Cho, "The Analysis of Thermal Performance in an Airflow Window System Model", in *Proc. of the ASHRAE/DOE/BTECC/CIBSE Conf.: Thermal Performance of The Exterior Envelopes of Buildings IV*, vol. 14, 1989, pp. 361-375.

[44] S. R. Hastings, *Passive Solar Commercial and Institutional Buildings*, 1st ed. Chichester: Wiley, 1994, pp. 93-111.

[45] P. Baker and M. McEvoy, "Test cell analysis of the use of a supply air window as a passive solar component", *Solar Energy*, vol. 69, no. 2, pp. 113-130, 2000.

[46] J.L. Wright, "Effective U-value and shading coefficients of preheat/supply air glazing systems", in *Proceedings of the Renewable Energy Conference*, Winnipeg, Manitoba, 1986.

[47] J. Haddad and A.H. Elmahdy, "Comparison of the monthly thermal performance of a conventional window and a supply-air window", *ASHRAE Transactions*, vol. 104 (Part 1B), pp. 1261-1270, 1998.

[48] J. Gosselin and Q. Chen, "A Dual Airflow Window for Indoor Air Quality Improvement and Energy Conservation in Buildings", *HVAC&R Research*, vol. 14, no. 3, pp. 359-372, 2008.

[49] P. Hersch and K. Zweibel, *Basic Photovoltaic Principles and Methods*. Golden, CO: Technical Information Office, Solar Energy Research Institute, 1982, p. 14.

[50] M. Green et al., "Solar cell efficiency tables (version 51)", *Progress in Photovoltaics: Research and Applications*, vol. 26, no. 1, pp. 3-12, 2018.

[51] S. Rühle, "Tabulated values of the Shockley–Queisser limit for single junction solar cells", *Solar Energy*, vol. 130, pp. 139-147, 2016.

[52] F. Alharbi and S. Kais, "Theoretical limits of photovoltaics efficiency and possible improvements by intuitive approaches learned from photosynthesis and quantum coherence", *Renewable and Sustainable Energy Reviews*, vol. 43, pp. 1073-1089, 2015.

[53] A. Luque and S. Hegedus, *Handbook of Photovoltaic Science and Engineering*, 1st ed. Chichester, West Sussex, U.K.: Wiley, 2012, p. 113, 298.

[54] J. Pern, "Module Encapsulation Materials, Processing and Testing, National Renewable Energy Laboratory (NREL)", APP International PV Reliability Workshop, SJTU, Shanghai, China, 2008.

[55] SunPower, *SunPower® X-Series Residential DC: X22-370*, 2018. [Online]. Available: https://us.sunpower.com/solar-resources/sunpower®-x-series-residential-dc-x22-370/. [Accessed: 13- Jun- 2018].

[56] H. Haberlin, *Photovoltaics System Design and Practice*, 1st ed. Hoboken, N.J.: Wiley, 2012, p. 135.

[57] A. Smets, K. Jäger, O. Isabella, R. Swaaij and M. Zeman, *Solar Energy: The Physics and Engineering of Photovoltaic Conversion, Technologies and Systems*. Cambridge, England: UIT Cambridge Ltd, 2016, pp. 255-259.

[58] Y. Tian, and C.Y. Zhao, "A review of solar collectors and thermal energy storage in solar thermal applications." *Applied Energy*, vol. 104, pp. 538-553, 2013

[59] D. Goswami, *Principles of Solar Engineering*, 3rd ed. Hoboken: CRC Press, 2015, p. 130.

[60] "*Solar hot water collectors*", 2017. [Online]. Available: http://www.greenspec.co.uk/building-design/solar-collectors/. [Accessed: 16 - Mar - 2017].

[61] A. Rabl, *Active Solar Collectors and their Applications*, 1st ed. New York: Oxford Univ. Press, 1985, pp. 8-23.

[62] Deutsche Gesellshaft für Sonnenenergie, *Planning and Installing Solar Thermal Systems*, 2nd ed. London: Routledge, 2010, pp. 223-230.

[63] G. Tiwari, A. Tiwari and Shyam., *Handbook of Solar Energy*, 1st ed. Singapore: Springer Science+Busines Media, 2016, pp. 369-373.

[64] H. Henning, M. Motta and D. Mugnier, *Solar Cooling Handbook*, 1st ed. Vienna: Ambra V, 2013, pp. 61-63.

[65] S. Kalogirou, *Solar Energy Engineering: Processes and Systems*, 2nd ed. Academic Press, 2013, pp. 125-133, 498-500.

[66] M. Wolf, "Performance analyses of combined heating and photovoltaic power systems for residences", *Energy Conversion*, vol. 16, no. 1-2, pp. 79-90, 1976.

[67] M. Alonso García and J. Balenzategui, "Estimation of photovoltaic module yearly temperature and performance based on Nominal Operation Cell Temperature calculations", *Renewable Energy*, vol. 29, no. 12, pp. 1997-2010, 2004.

[68] S. Kalogirou and Y. Tripanagnostopoulos, "Hybrid PV/T solar systems for domestic hot water and electricity production", *Energy Conversion and Management*, vol. 47, no. 18-19, pp. 3368-3382, 2006.

[69] J. Tonui and Y. Tripanagnostopoulos, "Improved PV/T solar collectors with heat extraction by forced or natural air circulation", *Renewable Energy*, vol. 32, no. 4, pp. 623-637, 2007.

[70] M. Hasan and K. Sumathy, "Photovoltaic thermal module concepts and their performance analysis: A review", *Renewable and Sustainable Energy Reviews*, vol. 14, no. 7, pp. 1845-1859, 2010.

[71] P. Charalambous, G. Maidment, S. Kalogirou and K. Yiakoumetti, "Photovoltaic thermal (PV/T) collectors: A review", *Applied Thermal Engineering*, vol. 27, no. 2-3, pp. 275-286, 2007.

[72] M. Debbarma, K. Sudhakar and P. Baredar, "Comparison of BIPV and BIPVT: A review", *Resource-Efficient Technologies*, vol. 3, no. 3, pp. 263-271, 2017.

[73] Schüco International KG, *Schüco Building-Integrated Photovoltaics*, Bielefeld, Germany, 2018. [Online]. Available:

https://www.schueco.com/web2/de-en/architects/products/bipv/schueco_bipv. [Accessed: 15- Sep- 2018].

[74] Romag, *Building Integrated Photovoltaics*, Leadgate Industrial Estate, Consett, United Kingdom, 2018. [Online]. Available: https://www.romag.co.uk/solar/building-integrated-pv/ [Accessed: 15- Sep- 2018]

[75] PV-Tech Solar Media Limited, *Tesla and RGS set for solar roof tile market share battle in US*, America House, London, United Kingdom, 2018. [Online]. Available: https://www.pv-tech.org/news/tesla-and-rgs-set-for-solar-roof-tile-market-share-battle-in-us. [Accessed: 15- Sep- 2018].

[76] Onyx Solar, *Amorphous Silicon Photovoltaic Glass*, Ávila, Spain, 2018. [Online]. Available: https://www.onyxsolar.com/product-services/amorphous-pv-glass. [Accessed: 15- Nov- 2018].

[77] Soliculture, LUMO: The First Commercially Available, Mass Produced Luminescent Solar Collector (LSC), Scotts Valley, CA, USA, 2018, Available: http://www.soliculture.com/lumo-technology/ [Accessed: 15- Sep- 2018].

[78] Pilkington, *The NSG Group and Solaria announce collaboration*, Bartlett, IL, USA, Sept 12, 2016. [Online]. Available: http://www.pilkington.com/en/us/news-insights/latest/the-nsg-group-and-solaria-announce-collaboration. [Accessed: 16- Sep- 2018].

[79] Solaria Corporation, *Solaria PowerVision™, Power Producing Insulated Glass Unit*, Oakland, CA, USA, 2018. [Online]. Available: https://static1.squarespace.com/static/568f7df70e4c112f75e6c82b/t/599b3d22be6594d3c856dddd/1503345955948/Datasheet_SolariaPowerVision_IGU_Rev_1C_8-21-17.pdf. [Accessed: 16- Sep- 2018].

[80] C. Good, J. Chen, Y. Dai and A. Hestnes, "Hybrid Photovoltaic-Thermal Systems in Buildings – A Review", *Energy Procedia*, vol. 70, pp. 683-690, 2015.

[81] Conserval Engineering, *SolarWall® Systems*, Toronto, ON, Canada, 2018. [Online]. Available: https://www.solarwall.com [Accessed: 4- Mar- 2018].

[82] R. Kumar and M. Rosen, "A Critical Review of Photovoltaic–Thermal Solar Collectors for Air Heating", *Applied Energy*, vol. 88, no. 11, pp. 3603-3614, 2011.

[83] DualSun, *Spring, the photovoltaic and thermal solar panel*, Marseille, France, 2018. [Online]. Available: https://dualsun.com/en/product/panels/. [Accessed: 16- Sep- 2018].

[84] Solator GmbH, "*Use the sun twice: PV+THERM INROOF*", Wolfurt, Austria, 2018. [Online]. Available: http://www.solator.cc/en/products/collectors/pv-therm-inroof/#c489. [Accessed: 16- Sep- 2018].

[85] Aesthetic Green Power, Inc, *"Products – Welcome to Aesthetic Green Power"*, Poughkeepsie, NY, USA, 2018. [Online]. Available: http://aestheticgreenpower.com/products/. [Accessed: 16- Sep- 2018].

[86] Tractile, *"The Designer Solar Roof"*, Southport, Australia, 2018. [Online]. Available: http://tractile.com.au. [Accessed: 16- Sep- 2018].

[87] T. Yang and A. Athienitis, "A review of research and developments of building-integrated photovoltaic/thermal (BIPV/T) systems", *Renewable and Sustainable Energy Reviews*, vol. 66, pp. 886-912, 2016.

[88] E.C. Kern and M.C. Russell, "Combined photovoltaic and thermal hybrid collector systems", in *The 13th IEEE Photovoltaic Specialists' Conference*, 1978, pp. 1153–1157.

[89] L. Florschuetz, "Extension of the Hottel-Whillier model to the analysis of combined photovoltaic/thermal flat plate collectors", *Solar Energy*, vol. 22, no. 4, pp. 361-366, 1979.

[90] B. Agrawal and G. Tiwari, "Optimizing the energy and exergy of building integrated photovoltaic thermal (BIPVT) systems under cold climatic conditions", *Applied Energy*, vol. 87, no. 2, pp. 417-426, 2010.

[91] T. Fujisawa and T. Tani, "Annual exergy evaluation on photovoltaic-thermal hybrid collector", *Solar Energy Materials and Solar Cells*, vol. 47, no. 1-4, pp. 135-148, 1997.

[92] J. Clarke, J. Hand, C. Johnstone, N. Kelly and P. Strachan, "Photovoltaic-integrated building facades", *Renewable Energy*, vol. 8, no. 1-4, pp. 475-479, 1996.

[93] B. Brinkworth, R. Marshall and Z. Ibarahim, "A validated model of naturally ventilated PV cladding", *Solar Energy*, vol. 69, no. 1, pp. 67-81, 2000.

[94] L. Gaillard, S. Giroux-Julien, C. Ménézo and H. Pabiou, "Experimental evaluation of a naturally ventilated PV double-skin building envelope in real operating conditions", *Solar Energy*, vol. 103, pp. 223-241, 2014.

[95] E.S. Morse, "Warming and ventilating apartments by the sun's rays", U.S. Patent 246,626, Sept. 6, 1881.

[96] J. Jie, Y. Hua, H. Wei, P. Gang, L. Jianping and J. Bin, "Modeling of a novel Trombe wall with PV cells", *Building and Environment*, vol. 42, no. 3, pp. 1544-1552, 2007.

[97] W. Sun, J. Ji, C. Luo and W. He, "Performance of PV-Trombe wall in winter correlated with south façade design", *Applied Energy*, vol. 88, no. 1, pp. 224-231, 2011.

[98] B. Koyunbaba, Z. Yilmaz and K. Ulgen, "An approach for energy modeling of a building integrated photovoltaic (BIPV) Trombe wall system", *Energy and Buildings*, vol. 67, pp. 680-688, 2013.

[99] K. Nagano, T. Mochida, K. Shimakura, K. Murashita and S. Takeda, "Development of thermal-photovoltaic hybrid exterior wallboards incorporating PV cells in and their winter performances", *Solar Energy Materials and Solar Cells*, vol. 77, no. 3, pp. 265-282, 2003.

[100] A. Athienitis, J. Bambara, B. O'Neill and J. Faille, "A prototype photovoltaic/thermal system integrated with transpired collector", *Solar Energy*, vol. 85, no. 1, pp. 139-153, 2011.

[101] S. Pantic, L. Candanedo and A. Athienitis, "Modeling of energy performance of a house with three configurations of building-integrated photovoltaic/thermal systems", *Energy and Buildings*, vol. 42, no. 10, pp. 1779-1789, 2010.

[102] N. Aste, G. Chiesa and F. Verri, "Design, development and performance monitoring of a photovoltaic-thermal (PVT) air collector", *Renewable Energy*, vol. 33, no. 5, pp. 914-927, 2008.

[103] R. Charron and A. Athienitis, "Optimization of the performance of double-façades with integrated photovoltaic panels and motorized blinds", *Solar Energy*, vol. 80, no. 5, pp. 482-491, 2006.

[104] N. Singh Kapany, "Solar Window apparatus and method", U.S. Patent 8,046,960 B1, issued November 1, 2011.

[105] P. Kamkird, N. Ketjoy, W. Rakwichian and S. Sukchai, "Investigation on Temperature Coefficients of Three Types Photovoltaic Module Technologies under Thailand Operating Condition", *Procedia Engineering*, vol. 32, pp. 376-383, 2012.

[106] J. Dunlop, *Photovoltaic Systems*, 3rd ed. Orland Park, IL: American Technical Publishers, Inc., 2012, pp. 131-142, 260-269, 308-318.

[107] S. Kolsi, H. Samet and M. Amar, "Design Analysis of DC-DC Converters Connected to a Photovoltaic Generator and Controlled by MPPT for Optimal Energy Transfer throughout a Clear Day", *Journal of Power and Energy Engineering*, vol. 02, no. 01, pp. 27-34, 2014.

[108] O. Mørck and S. Hastings, *Solar Air Systems*, 1st ed. London: James & James Ltd, 2000, p. 133.

[109] Pveducation.org, "*Solar Radiation on a Tilted Surface*" , 2013. [Online]. Available: https://www.pveducation.org/pvcdrom/properties-of-sunlight/solar-radiation-on-a-tilted-surface [Accessed: 21 - Nov- 2016]

[110] E. Skoplaki and J. Palyvos, "On the temperature dependence of photovoltaic module electrical performance: A review of efficiency/power correlations", *Solar Energy*, vol. 83, no. 5, pp. 614-624, 2009.

[111] A. Ibrahim, A. El-Sebaii, M. Ramadan and S. El-Broullesy, "Estimation of solar irradiance on tilted surfaces facing south for Tanta, Egypt", *International Journal of Renewable Energy Research*, vol. 1, no. 1, pp. 18-25, 2011.

[112] Heat Transfer Module User's Guide, v5.2a, pp. 85-93, 121-123, 158-173, 186-193, 215-223, 372-377, COMSOL AB, 2016.

[113] Weather underground, "Weather History for Salinas, CA", 2016. [Online]. Available: https://www.wunderground.com/history/airport/KSNS/2009/5/10/DailyHistory.html

[114] Y. Çengel and J. Cimbala, *Fluid Mechanics: Fundamentals and Applications*, 4th ed. New York: McGraw-Hill Education, 2018, pp. 10-11, 886-929.

[115] COMSOL Multiphysics, "*Compressibility Options and Buoyancy Forces for Flow Simulations*", 2016. [Online]. Available: https://www.comsol.com/blogs/compressibility-options-and-buoyancy-forces-for-flow-simulations/. [Accessed: 12- Sep- 2017].

[116] N. Safer, M. Woloszyn and J. Roux, "Three-dimensional simulation with a CFD tool of the airflow phenomena in single floor double-skin facade equipped with a venetian blind", *Solar Energy*, vol. 79, no. 2, pp. 193-203, 2005.

[117] T. Jiru, Y. Tao and F. Haghighat, "Airflow and heat transfer in double skin facades", *Energy and Buildings*, vol. 43, no. 10, pp. 2760-2766, 2011.

[118] W. He et al., "Thermal and hydraulic analysis on a novel Trombe wall with venetian blind structure", *Energy and Buildings*, vol. 123, pp. 50-58, 2016.

[119] B. Janssens and W. Bosschaerts, "Study of the Airflow Window", *Energy Procedia*, vol. 85, pp. 303-310, 2016.

[120] R. Bird, W. Stewart and E. Ligthfoot, Transport Phenomena, 2nd ed. New York: Wiley, 2002, pp. 156-159, 163.

[121] COMSOL Multiphysics, "*Which Turbulence Model Should I Choose for My CFD Application?*", 2017. [Online]. Available: https://www.comsol.com/blogs/which-turbulence-model-should-choose-cfd-application. [Accessed: 23- Nov- 2017].

[122] CFD Module User's Guide, v5.2a, pp. 34-35, 146-153, COMSOL AB, 2016.

[123] COMSOL Multiphysics, "*Solving Multiphysics Problems*", 2013. [Online]. Available: https://www.comsol.com/blogs/solving-multiphysics-problems/. [Accessed: 06- Dec- 2017].

[124] O. Kazanci, "Low Temperature Heating and High Temperature Cooling in Buildings", Ph.D, Technical University of Denmark, 2016.

[125] Berkeley Lab, "*IGDB | Windows and Daylighting*", 2019. [Online]. Available: https://windows.lbl.gov/software/igdb.

[126] Pilkington, "*Pilkington Spectrum*", 2019. [Online]. Available: https://www.pilkington.com/en/global/commercial-applications/specification-tools/pilkington-spectrum.

[127] Pilkington, "*Pilkington Insulight™ with ScreenLine® blinds*". 2016. [Online] Available: http://www.pilkington.com/en-gb/uk/products/product-categories/special-applications/pilkington-insulight-with-screenline#brochures [Accessed: 18- Jan- 2017]

[128] J. Tonui and Y. Tripanagnostopoulos, "Improved PV/T solar collectors with heat extraction by forced or natural air circulation", *Renewable Energy*, vol. 32, no. 4, pp. 623-637, 2007. Available: 10.1016/j.renene.2006.03.006.

[129] N. Sukesh, P. Lakshmisagar and G. Kumar, "Heat Transfer Analysis of Fin Performance for PVT Absorber", *Journal of Mechanical Engineering and Automation*, vol. 5, no. 3, pp. 1-4, 2015. Available: 10.5923/c.jmea.201502.01.

[130] R. Kumar and M. Rosen, "Performance evaluation of a double pass PV/T solar air heater with and without fins", *Applied Thermal Engineering*, vol. 31, no. 8-9, pp. 1402-1410, 2011. Available: 10.1016/j.applthermaleng.2010.12.037.

[131] M. Hj. Othman, B. Yatim, K. Sopian and M. Abu Bakar, "Performance analysis of a double-pass photovoltaic/thermal (PV/T) solar collector with CPC and fins", *Renewable Energy*, vol. 30, no. 13, pp. 2005-2017, 2005. Available: 10.1016/j.renene.2004.10.007.

[132] E. Cuce, T. Bali and S. Sekucoglu, "Effects of passive cooling on performance of silicon photovoltaic cells", *International Journal of Low-Carbon Technologies*, vol. 6, no. 4, pp. 299-308, 2011. Available: 10.1093/ijlct/ctr018.

[133] B. Lee, J. Liu, B. Sun, C. Shen and G. Dai, "Thermally conductive and electrically insulating EVA composite encapsulant for solar photovoltaic (PV) cell", *Express Polymer Letters*, vol. 2, no. 5, pp. 357-363, 2008. Available: 10.3144/expresspolymlett.2008.42.

[134] J. Allan, H. Pinder and Z. Dehouche, "Enhancing the thermal conductivity of ethylene-vinyl acetate (EVA) in a photovoltaic thermal collector", *AIP Advances*, vol. 6, no. 3, p. 035011, 2016. Available: 10.1063/1.4944557.

[135] S. Armstrong and W. Hurley, "A thermal model for photovoltaic panels under varying atmospheric conditions", *Applied Thermal Engineering*, vol. 30, no. 11-12, pp. 1488-1495, 2010. Available: 10.1016/j.applthermaleng.2010.03.012.

[136] P. Dupeyrat, C. Ménézo, H. Wirth and M. Rommel, "Improvement of PV module optical properties for PV-thermal hybrid collector application", *Solar Energy Materials and Solar Cells*, vol. 95, no. 8, pp. 2028-2036, 2011. Available: 10.1016/j.solmat.2011.04.036.

[137] Guardian Glass, "*Guardian Glass Analytics™* ". 2018. [Online] Available: https://glassanalytics.guardian.com/PerformanceCalculator.aspx [Accessed: 18- Jul- 2018]